



Mechanical and microstructural study of biocemented soils: application to hydraulic earthworks.

Abdelali Dadda

► To cite this version:

Abdelali Dadda. Mechanical and microstructural study of biocemented soils: application to hydraulic earthworks.. Solid mechanics [physics.class-ph]. Université Grenoble Alpes, 2017. English. NNT : 2017GREAI103 . tel-03934613

HAL Id: tel-03934613

<https://theses.hal.science/tel-03934613>

Submitted on 11 Jan 2023

HAL is a multi-disciplinary open access archive for the deposit and dissemination of scientific research documents, whether they are published or not. The documents may come from teaching and research institutions in France or abroad, or from public or private research centers.

L'archive ouverte pluridisciplinaire **HAL**, est destinée au dépôt et à la diffusion de documents scientifiques de niveau recherche, publiés ou non, émanant des établissements d'enseignement et de recherche français ou étrangers, des laboratoires publics ou privés.

THÈSE

Pour obtenir le grade de

DOCTEUR DE LA COMMUNAUTE UNIVERSITE GRENOBLE ALPES

Spécialité : **Matériaux, Mécanique, Génie civil, Electrochimie**

Arrêté ministériel : 25 mai 2016

Présentée par

Abdelali DADDA

Thèse dirigée par **Fabrice EMERIAULT**
et codirigée par **Christian GEINDREAU**

préparée au sein du **Laboratoire Sols, Solides,
Structures - Risques (3SR)**
dans l'**École Doctorale Ingénierie – Matériaux Mécanique
Énergétiques Environnement Procédés Production**

Étude mécanique et microstructurale des sols bio-cimentés : application aux ouvrages hydrauliques en terre

Thèse soutenue publiquement le « **7 Décembre 2017** »,
devant le jury composé de :

Mr Pierre-Yves HICHER

Professeur Emérite à l'Ecole Centrale de Nantes, Président

Mr Pierre BREUL

Professeur à l'Université Blaise Pascal – Clermont – Ferrant II, Rapporteur

Mr Claudio TAMAGNINI

Professeur à l'Université degli Studi di Perugia, Rapporteur

Mme Rebecca LUNN

Professeur à l'Université de Strathclyde Glasgow, Examinatrice

Mme Annette ESNAULT FILET

Chef de projet à Solétanche-Bachy, France, Examinatrice

Mme Aurélie GARANDET

Ingénieur à la Compagnie Nationale du Rhône, France, Examinatrice

Mr Fabrice EMERIAULT

Professeur à Grenoble INP, Directeur de thèse

Mr Christian GEINDREAU

Professeur à l'Université Grenoble Alpes, Co-directeur de thèse



Ces travaux de thèse ont bénéficié du soutien financier de
la Compagnie Nationale du Rhône (CNR) dans le cadre
du projet **FUI BOREAL**



Elle a été préparée au sein du **Laboratoire Sols, Solides,
Structures - Risques** (3SR)



*À mon cher père
À ma chère mère
À mes frères
À mes soeurs
À ma future femme*

Remerciements

Ce travail a été réalisé au sein du laboratoire 3SR à l'Université Grenoble Alpes, avec une collaboration entre l'équipe Géomécanique et l'équipe Comhet. Je souhaite vivement remercier les personnes qui ont contribué à accomplir avec succès l'ensemble de mes tâches.

Je remercie très chaleureusement mes directeurs de thèse Pr. Fabrice EMERIAULT et Pr. Christian GEINDREAU pour m'avoir accordé une grande disponibilité, leurs encouragements et leur confiance. Leur expérience, leur rigueur scientifique, leur pédagogie ont constitué un soutien indispensable à la réalisation de cette étude.

Je remercie sincèrement Dr. Sabine ROLLAND DU ROSCOAT pour m'avoir initié et formé à l'utilisation de différents outils d'imagerie, pour ces idées brillantes et pour son aide à la réalisation de certains travaux.

Je remercie sincèrement Dr. Jean MARTIN, Pr. Lorenzo SPADINI, Pr. Laurent OXARANGO, Dr. Emilie FRANCOIS et Mme. Alix DUMAY pour leurs collaborations surtout dans la partie biologique et chimique de ce travail. Je les remercie aussi pour leurs idées précieuses et les échanges fructueux qu'on a eus.

Je souhaite remercier Pr. Pierre BREUL et Pr. Claudio TAMAGNINI qui ont accepté d'être rapporteurs de ma thèse, ainsi que Pr. Pierre-Yves HICHER et Pr. Rebecca LUNN d'avoir accepté de faire partie de mon jury.

Je remercie chaleureusement Mme. Annette ESNAULT FILET, Mme. Aurélie GARANDET, Mme. Leslie SAPIN et tous nos collaborateurs du projet BOREAL pour les discussions très enrichissantes lors des réunions.

Je remercie également l'ensemble des chercheurs de l'équipe Geomécanique et Comhet pour leur générosité scientifique et les connaissances qu'ils ont pu me transmettre lors de nos multiples discussions et échanges quotidiens.

Je tiens à remercier mes chers amis et collègues de 3SR notamment mes collègues de bureau Deepak, Payam et Aleksandr et mes stagiaires Annalisa et Oltion. Et, enfin, j'adresse toute ma gratitude à ma chère famille, et très particulièrement mon père, pour leurs encouragements et soutiens permanents.

Abdelali.

Résumé

Le procédé de bio-cimentation est une technique prometteuse pour renforcer les sols lâches et de faible résistance mécanique. Cette technique a montré une très bonne efficacité pour plusieurs types de sols lors d'essais en laboratoire, dans des modèles physiques ou lors d'essais sur site. Par contre, elle a montré une forte sensibilité aux conditions de traitement telles que concentrations des réactifs, bactéries, vitesse d'injection, type de sols, température, etc... Ces facteurs influencent principalement la distribution spatiale de la calcite précipitée, sa forme et sa morphologie, ce qui influence par la suite les propriétés effectives des sols traités. Ces travaux de thèse ont été réalisés dans le cadre du projet BOREAL qui vise à renforcer par cette technique des digues et barrages en terre existants contre l'érosion interne des noyaux et la liquéfaction des fondations. L'objectif de cette thèse est d'étudier l'évolution des propriétés physiques et mécaniques du sable bio-cimenté (perméabilité, résistance mécanique) par la réalisation d'essais mécaniques et de mesures de perméabilité en laboratoire, et de lier cette évolution aux changements microstructuraux via des observations par micro-tomographie RX. Le travail a commencé par des essais de bio-cimentation de colonnes de sable de Fontainebleau afin de vérifier la faisabilité de la bio-cimentation en laboratoire. Suite à ces essais de faisabilité, des essais triaxiaux drainés ont été réalisés sur le sable bio-cimenté afin d'estimer l'évolution de ses paramètres de résistance tels que la cohésion et l'angle de frottement. Des petits volumes de sable bio-cimenté présentant différentes teneurs en calcite ont été extraits des échantillons triaxiaux et observés par micro-tomographie aux rayons-X à l'ESRF sous une très haute résolution ($0,65 \mu\text{m}/\text{pixel}$). Des méthodes quantitatives d'imagerie 3D ont été développées pour calculer les propriétés microstructurales moyennes (quantité de calcite, porosité, surface spécifique et surface spécifique de calcite) et les propriétés de contact (surface de contact, nombre de coordination, type de contacts, orientation des contacts, etc...) pour les différents échantillons observés. Cette étude a montré une forte évolution de la résistance du sable bio-cimenté (évolution non-linéaire de la cohésion, évolution quasi-linéaire de l'angle de frottement, légère augmentation de la résistance résiduelle, etc...) et une diminution de la perméabilité par la précipitation de la calcite à l'intérieur de l'échantillon. L'étude quantitative de l'évolution de la microstructure a montré une stabilité de la surface spécifique de la calcite à partir d'un certain niveau de calcification, une forte évolution quasi-linéaire de la surface de contact cohésive entre les grains ainsi qu'une légère évolution du nombre de coordination par la création de nouveaux contacts. La comparaison de ces évolutions avec celles obtenues pour un arrangement périodique de type cubique simple en utilisant deux scenarii de précipitation (uniforme et localisée au niveau du contact) a montré que la précipitation de la calcite se produit principalement dans les zones de contact inter-granulaire. L'utilisation de ces informations microstructurales dans des modèles micromécaniques a permis d'estimer avec succès les propriétés effectives du sable bio-cimenté (cohésion, perméabilité, modules élastiques). Enfin, les mêmes outils ont été utilisés pour étudier la durabilité chimique du sable bio-cimenté. Cette étude a montré une dégradation de la résistance du sable par la dissolution de la calcite à l'intérieur des échantillons. Les mesures quantitatives sur les images 3D ont montré une dégradation de la surface de contact sans hystérésis par rapport à l'évolution de ces surfaces de contacts pendant le processus de bio-cimentation.

Mots-clés : Bio-cimentation, calcite, triaxial, perméabilité, rayon-X, MEB, surface de contact, nombre de coordination, cohésion, angle de frottement, modules élastiques, durabilité.

Abstract

The biocementation process is considered as a promising technique for strengthening loose and weak soils. This technique has shown very good efficiency for several types of soil through laboratory tests and large scale models. On the other hand, it has shown a high sensitivity to the treatment conditions such as reactant concentrations, bacteria, injection rate, type of soil, temperature, etc.... These factors influence mainly the spatial distribution of the precipitated calcite, its shape and morphology, which subsequently influences the effective properties of the treated soils. This thesis is part of the French research project BOREAL, which aims at reinforcing old dykes and earth dams with this technique against internal erosion of the core and liquefaction of foundations. The objective of this thesis is to study the evolution of the physical and mechanical properties of biocemented sands (permeability, mechanical strength) by performing mechanical tests and permeability measurements in the laboratory and linking this evolution to microstructural changes by using quantitative 3D X-ray imaging tools. To do this, this work began with biocementation tests on Fontainebleau sand to verify the feasibility of the biocementation process in the laboratory. After these feasibility tests, drained triaxial tests have been carried out on the biocemented sand in order to estimate the evolution of its resistance parameters such as cohesion and friction angle. Small sub-samples of biocemented sand with different calcite contents have been then extracted and observed using X-ray micro-tomography at ESRF at a very high resolution ($0.65 \mu\text{m} / \text{pixel}$). Quantitative methods of 3D imaging have been developed to compute mean microstructural properties (amount of calcite, porosity, specific surface area and specific surface area of calcite) and contact properties (contact surface area, coordination number, type of contacts, contact orientation, etc...) for the different observed sub-samples. This study has shown a strong evolution of the resistance of biocemented sand (non-linear evolution of the cohesion, quasi-linear evolution of the friction angle, a slight increase of the residual resistance, etc...) and a decrease of the permeability by the precipitation of the calcite inside the sample. The quantitative study of the evolution of the microstructure has shown a stability of the specific surface area of the calcite beyond a certain level of calcification, a strong quasi-linear evolution of the cohesive contact surface between the grains as well as a slight evolution the coordination number (creation of new contacts). The comparison of these evolutions with those obtained considering a simple cubic periodic arrangement using two precipitation scenarii (uniform and localized at the contact) has shown that the precipitation of the calcite mainly occurs in the zones of inter-granular contact. This microstructural information has been then used successfully in micromechanical models to estimate the effective properties of biocemented sand (cohesion, permeability, elastic moduli). Finally, the same tools have been used to study the chemical durability of biocemented sand. This study has shown a degradation of sand resistance by dissolving calcite within the samples. The quantitative measurements on the 3D images have shown a degradation of the contact surface area without hysteresis with respect to the evolution of these contact surfaces during the biocementation process.

Keywords: Biocementation, calcite, triaxial, permeability, X-ray, SEM, contact surface area, coordination number, cohesion, friction angle, elastic moduli, durability.

TABLE DES MATIÈRES

1 General introduction	1
2 Étude bibliographique	7
2.1 Introduction	9
2.2 Bio-cimentation par bio-précipitation de calcite (CaCO_3)	10
2.3 Facteurs contrôlant le processus de bio-cimentation	12
2.3.1 Type et concentration de microorganismes	13
2.3.2 Concentration de solution calcifiante	14
2.3.3 Influence du pH initial	15
2.3.4 Température	16
2.3.5 Type de sol	18
2.3.6 Salinité	19
2.4 Modifications des propriétés des matériaux bio-cimentés	19
2.4.1 Changements microstructuraux	19
2.4.2 Evolution de la perméabilité	21
2.4.3 Evolution des propriétés mécaniques	22
2.5 Durabilité de la bio-cimentation	31
2.5.1 Durabilité chimique	31
2.5.2 Durabilité mécanique	33
2.6 Stratégie de traitement	36
2.6.1 Méthode d'injection	36
2.6.2 Pré-mixing	37
2.6.3 Percolation de surface	37
2.7 Conclusion	38
3 Evolution of strength properties of biocemented sand with the cementation level	41
3.1 Introduction	42
3.2 Material and Method	45

3.2.1	Sample preparation and treatment	45
3.2.2	Experimental procedure	47
3.2.3	Calcite measurements and microstructural observations	48
3.2.4	Permeability measurement	49
3.3	Results and discussion	50
3.3.1	Physical properties	50
3.3.2	Mechanical properties	52
3.3.3	SEM and X-ray observations	56
3.4	Conclusion	58
4	Characterization of microstructural and physical properties changes in biocemented sand using 3D x-ray microtomography	61
4.1	Introduction	62
4.2	Material and Method	64
4.2.1	Biocemented samples preparation	64
4.2.2	Permeability measurement	66
4.2.3	Mass fraction of calcite	66
4.2.4	Microstructural and physical properties computed on 3D images	67
4.3	Results and discussion	74
4.3.1	Microstructural and physical properties from 3D X-ray microtomography	74
4.3.2	Correlation lengths	75
4.3.3	Permeability and effective diffusion	77
4.4	Comparison with analytical estimates and numerical values	79
4.4.1	Models	79
4.4.2	Correlation lengths and total specific surface area (SSA)	80
4.4.3	Permeability and effective diffusion	81
4.5	Conclusions	81
5	Characterization of contact properties in biocemented sand using 3D x-ray microtomography	83
5.1	Introduction	84
5.2	Material and Method	86
5.2.1	Samples and image acquisition	86
5.2.2	Image treatments	86
5.2.3	Computed contact properties	89
5.3	Results and discussion	94
5.3.1	Coordination number	94
5.3.2	Contact surface area	94
5.3.3	Contacts orientation	96
5.3.4	Contact types and distribution	98
5.3.5	Precipitation pattern and modeling	99

5.4 Conclusion	103
6 Relationship between the microstructural parameters and the macroscopic properties of biocemented sand	107
6.1 Introduction	108
6.2 Material and Method	111
6.2.1 Image acquisition and processing	111
6.2.2 Effectives properties estimates	112
6.3 Results and discussion	116
6.3.1 Elastic properties	116
6.3.2 Cohesion	117
6.4 Conclusion	119
7 Mechanical and microstructural changes of biocemented sand subjected to aggressive solution : chemical durability	121
7.1 Introduction	122
7.2 Material and Method	125
7.2.1 Specimens and chemical solution preparations	125
7.2.2 Dissolution device and protocol	126
7.2.3 Calcite dosage and microstructural observations	127
7.3 Results and discussion	128
7.3.1 Chemical durability of biocemented sand	128
7.3.2 Mechanical response	130
7.3.3 Microstructural observations	132
7.3.4 Calcification versus dissolution	140
7.4 Conclusions	141
8 Conclusions and perspectives	145
8.1 Conclusions	145
8.2 Perspectives	149
A Essais traxiaux et mesure de calcite	151
Bibliographie	159

LISTE DES FIGURES

1.1	Structure of BOREAL project	3
1.2	Plan of thesis work and its position in BOREAL project.	3
2.1	Morphologies du carbonate de calcium induites par des activités bactériennes (Ivanov and Stabnikov, 2017).	10
2.2	Biocalcification dans les espaces inter-granulaires et dans les anfractuosités du grain (Girinsky, 2009)	10
2.3	Schéma représentatif des réactions chimiques durant le processus de biocalcification (DeJong et al., 2010a).	11
2.4	Schéma représentatif des facteurs qui contrôlent le procédé.	12
2.5	Schéma des étapes de biocalcification à côté d'une cellule bactérienne (De Muynck et al., 2010a).	13
2.6	Observations au MEB de deux échantillons de sable bio-cimenté pour différentes concentrations bactériennes , a) $\text{CaCO}_3 = 0,061 \text{ g/g}$ sable et la résistance à la compression simple ($R_c = 713 \text{ kPa}$), b) $\text{CaCO}_3 = 0,039 \text{ g/g}$ sable $R_c = 709 \text{ kPa}$, et (Cheng et al., 2016).	14
2.7	Observation MEB pour des échantillons de sable traités avec différentes concentrations de solution calcifiante (Al Qabany and Soga, 2013).	15
2.8	Influence du pH initial sur la résistance mécanique à la compression simple (R_c) et la quantité de la calcite précipitée (neutre : pH=7, acide : pH=3,5, basique : pH=9.5) (Cheng et al., 2014).	16
2.9	Observation MEB pour des échantillons de sable calcifiés sous différentes températures, a) $\text{CaCO}_3 = 0.021\text{g/g}$ de sable, $R_c = 108 \text{ kPa}$, b) $\text{CaCO}_3 = 0.028 \text{ g/g}$ de sable, $R_c = 245 \text{ kPa}$, c) $\text{CaCO}_3 = 0.034 \text{ g/g}$ de sable, $R_c = 121 \text{ kPa}$ (Cheng et al., 2016).	17
2.10	Comparaison entre la taille les grains de sol et les microorganismes (Mitchell and Santamarina, 2005).	18

2.11 Relation entre la salinité d'eau et la structure cristalline de la calcite (Iwatsuki et al., 2002)	20
2.12 Configuration réelle de précipitation de calcite (DeJong et al., 2010a)	21
2.13 Configurations extrêmes (précipitation uniforme et préférentielle) de précipitation de la calcite et configuration réelle (DeJong et al., 2010a)	21
2.14 Evolution de la conductivité hydraulique en fonction de la teneur en CaCO_3 précipité dans différents sol (Ivanov and Stabnikov, 2017)	22
2.15 Réduction de la perméabilité normalisée par la perméabilité initiale pour 3 niveaux de concentration de la solution calcifiante (0.25, 0.5 et 1 M) (Al Qabany and Soga, 2013)	23
2.16 Vitesse de cisaillement et Module de cisaillement vs quantité de calcite dans l'échantillon de sable (Duraisamy and Airey, 2015)	24
2.17 Evolution de la vitesse d'onde de cisaillement (V_S) en fonction de la quantité de la calcite précipitée pour différents protocole d'injection (Al Qabany et al., 2011b) .	24
2.18 Résistance à la compression simple des sables bio-cimentés à différents niveaux de cimentation (Ivanov and Stabnikov, 2017)	25
2.19 Résistance à la compression des sable bio-cimentés en fonction de niveau de calcification sous différents concentrations de la solution calcifiante (Al Qabany and Soga, 2013)	25
2.20 Résistance à la compression des sable bio-cimentés sous différents niveaux de saturation (Cheng et al., 2013)	26
2.21 Observation MEB pour des échantillon de sable biocalcifié à différente degrés de saturation (Cheng et al., 2013)	26
2.22 Influence de l'activité enzymatique sur l'amélioration de la résistance mécanique du sable (Cheng et al., 2016)	27
2.23 Evolution de la résistance à la compression en fonction de la quantité de calcite pour 3 différentes températures (Cheng et al., 2016)	27
2.24 Résistance à la compression en fonction de la quantité de calcite précipitée pour 3 sables de granulométrie différentes (Cheng et al., 2016)	28
2.25 Comportement triaxial (résistance mécanique et comportement volumique) d'un sable avec différents niveaux de cimentation et sous différentes pressions de confinement (Feng and Montoya, 2015)	29
2.26 Comportement triaxial non-drainé d'un sable bio-cimenté avec différents niveaux de cimentation (Montoya and DeJong, 2015)	29
2.27 Influence du pH sur la solubilité de CaCO_3 à une pression d'air (100 kPa) et à une température ambiante de 25°C (Coto et al., 2012)	32
2.28 Influence simultanée de la pression et de la température sur la solubilité du CaCO_3 (Coto et al., 2012)	32
2.29 Résistance à la compression simple (R_C) et masse de calcite dissoute vs le volume de la solution injectée (Cheng et al., 2013)	33
2.30 Chargement cyclique triaxial sur un sable bio-cimenté (Dura, 2013)	34

2.31	Dégradation de module de cisaillement de différents échantillons sur un l'amplitude de 100 kPa pour les premiers 700 cycles (Dura, 2013)	35
2.32	Dégradation de la résistance à la compression simple d'un sable d'une granulométrie étalée subi à des cycles gel-dégel Cheng et al. (2016)	35
2.33	Dégradation de la résistance à la compression simple des sable d'une granulométrie uniforme subis à des cycles gel-dégel Cheng et al. (2016)	36
2.34	a) renforcement de sol par l'injection de coulis de ciment, b) réalisation d'une paroi étanche (Canal de Lens - Lille - France)	36
2.35	Schéma de des travaux de thèse et sa position dans le projet BOREAL.	39
3.1	Treatment schema for the small amount of calcite, b) treatment schema for the medium amount of calcite, c) treatment schema for the higher amount of calcite .	46
3.2	Schema of the treatment procedure (low, medium and high cementation level), the left figure represents the reference sequence of treatment	47
3.3	Schema of the sample dividing and complementary analysis after the triaxial tests	49
3.4	Average profile of calcite for each group of specimens in each calcification level .	50
3.5	Permeability of the tested specimens vs the amount of calcite	52
3.6	Triaxial samples after failure a) untreated sand (T1), b) moderately cemented sand (specimen 11T : 5.9%), c) moderately cemented sand (specimen 11B : 8.1%), d) heavily cemented sand (specimen 13B : 10.3%), e) heavily cemented sand (specimen 13M : 11.4%)	52
3.7	Triaxial results of different treated specimens under 25 kPa of confinement, a) mechanical response, b) volumetric response	54
3.8	Evolution of the elastic modulus of different tested biocemented sand under various confining pressure (25, 50 and 100 kPa)	55
3.9	Evolution of the different mechanical properties with the degree of biocalcification, a) cohesion , b) peak friction angle, c) dilatancy angle, d) critical friction angle .	55
3.10	Microstructural observations of biocemented sand specimens (specimen 14M), a) SEM observation of untreated sand grains (scale = 100 μ m) b) SEM observation of cemented agglomeration sand (scale = 100 μ m), c) X-ray micro-tomography observation (black : void, grey : sand and white : calcite), d) SEM observation grain to grain contact (scale = 20 μ m)	57
4.1	Injection protocol for biocementation process.	65
4.2	Injection protocol for biocementation process.	66
4.3	SEM observation of the biocemented sand (subsample 13MB).	68
4.4	X-ray micro-tomography images of biocemented sand subsamples (column 2). . .	68
4.5	Image treatments applied on 2D images and the corresponding 3D volume.	69
4.6	Total specific surface area : $SSA = (S_g + S_c)/V$; Specific surface of calcite : $SSA_c = S_c/V$	70

4.7	Two-points correlation function $S_2(x)$ for the air phase computed on a 2D image of the sub-sample “13MB”. Correlation lengths computed on the total 3D volume of the sub-sample “13MB” within the three main planes (x,y), (y,z) and (x,z) (b) without calcite, (c) with calcite. The green surface was adjusted on the numerical values (red mark).	72
4.8	Microstructural properties computed on the sub-sample “13MB” by using the REV approach (a,c,e,g) and the statistical approach (b,d,f,h).	73
4.9	Evolution of the physical properties computed on the 3D images of the sub-sample “13MB” versus the number of subvolumes under consideration : (a) and (b) permeability components, (c) and (d) dimensionless effective diffusion components. .	74
4.10	Experimental versus the numerical results computed on 3D images : (a) initial porosity, (b) mass fraction of calcite. The vertical error bar represents the minimum and the maximum of 4 measurements.	76
4.11	Evolution of the ratio of the mean correlation lengths with and without calcite versus the volume fraction of calcite.	77
4.12	Evolution of the ratio of the SSA with and without calcite versus the volume fraction of calcite computed on 3D images. Comparison with analytical estimate (SMC) and numerical values (BCC, FCC).	77
4.13	Evolution of the ratio $SSAc/SSA$ versus the volume fraction of calcite computed on 3D images.	78
4.14	Evolution of the permeability ratio of the same sub-sample with and without calcite versus the volume fraction of calcite computed from 3D images. Comparison with experimental values, analytical estimate (SCM) and numerical values (BCC, FCC). The vertical and horizontal bars represent the minimum and the maximum values of three different measurements.	78
4.15	Evolution of the effective diffusion ratio of the same sub-sample with and without calcite versus the volume fraction of calcite computed from 3D images. Comparison with analytical estimate (SCM) and numerical values (BCC, FCC).	79
4.16	Periodic lattices of coated shperes with calcite : a) body-centred cubic arrangement (BBC), b) face-centred cubic arrangement (FCC), c) bi-compisite sphere constituted by a coated grain Ω_s (sand (Ω_g) + calcite) surrounded by a spherical shell Ω_f full of fluid.	80
5.1	Different steps of the image treatment (subsample “13BT”).	88
5.2	Distribution of the coordination numbers (c) within the image (a) before and after biocementation, Distribution of the coordination numbers (d) within the image (b) before and after biocementation, without edge effects (subsample “12MB”).	90
5.3	Geometry of the grain to grain contacts : (a) 2D labeled grains image, (b) example of two grains in contact, (c) contact surface between the two grains in contact, (d) distribution of the contact surface area before and after calcification (subsample “12MB”).	91

5.4	Definition of the different types of contact.	92
5.5	Distribution of the different types of contact. (a) number of contacts, (b) contact surface area. (subsample “12MB”).	92
5.6	Contact orientation before (a) and after (b) biocalcification (subsample “12MB”).	93
5.7	(a) 2D trinarized images, (b) Distribution of the coordination number within the six samples, (c) Distribution of the contact surface areas within the six samples, before and after biocalcification.	95
5.8	Evolution of the ratio \bar{Z}_a/\bar{Z}_b of the mean coordination number after and before biocalcification with respect to the volume fraction of calcite.	96
5.9	Evolution of the ratios (\bar{S}_a/\bar{S}_b) and (\bar{S}_c/\bar{S}_a) with respect to the volume fraction of calcite.	96
5.10	Orientation of the contacts within the six samples under consideration, (a) 2D trinarized images, (b) before and (c) after biocalcification.	97
5.11	Distribution of the different types of contact, in each sample after biocementation, in terms of (b) number of contacts, (c) contacts surface area.	100
5.12	Evolution of the distribution of the different types of contact with respect the volume fraction of calcite, in terms of (a) number of contacts, (b) contact surface area. (c) Typical protocol for the biocementation process : number of injections of bacterial solution (BS) and calcification solution (CS).	101
5.13	(a) distribution of the calcite at the grain scale, (b) evolution of the ratio between the mean cohesive contact surface area and the mean contact surface area after calcification (\bar{S}_c/\bar{S}_a) , and the ratio between the specific surface area of calcite and the total specific surface area (SSA_c/SSA) with the volume fraction of calcite . .	102
5.14	Granular media is made of periodic simple cubic (SC) arrangements of grains. (a) the calcite is localized at the contact, (b) the calcification is uniform at the grain surface.	103
5.15	Comparison between the analytical estimates and the numerical results from 3D image. (a) Evolution of the ratio (\bar{S}_c/\bar{S}_a) , (b) Evolution of the ratio (SSA_c/SSA) with respect to the volume fraction of calcite.	103
6.1	a) 3D images in grey levels, b) 3D trinarized image which contains grains (orange), calcite (purple) and pores, c) 3D images which contains separated grains (subsample “13BT”).	112
6.2	Contact between 2 grains deduced from 3D images and idealized contact used in the contact cement theory.	113
6.3	Computation schema of the elastic properties of the biocemented sand specimens. .	115
6.4	Evolution of the dimensionless estimated elastic properties of the biocemented sand (a) Young’s modulus (b) Shear modulus, and (c) the evolution of Poisson’s ratio.	118
6.5	Estimation of the cohesion evolution compared with experimental results.	119
7.1	Dissolved calcite depending on output pH.	126

7.2	Schematic representation of the dissolution device.	126
7.3	Schema of the sample dividing and complementary analysis after the triaxial tests.	128
7.4	a) calcite profile of all the tested specimens before and after dissolution, b) pH variation of output water.	129
7.5	Triaxial results of different dissolved and undissolved specimens under 50 kPa of confinement, a) mechanical response, b) volumetric response.	131
7.6	Triaxial samples after failure.	131
7.7	Peak deviatoric stress vs volume of injected solution.	132
7.8	SEM observation of different undissolved (SS_0) and dissolved specimens (SS_{3b1} , SS_{3b2} and SS_{3b3}).	133
7.9	Microstructural properties of the four scanned subsamples (SS_0 , SS_{3b1} , SS_{3b2} and SS_{3b3}), a) 2D treated images, b) final porosity and volume fraction of calcite, c) the specific surface area with and without calcite and the specific surface area of calcite.	134
7.10	Microstructural properties of the four scanned subsamples (SS_0 , SS_{3b1} , SS_{3b2} and SS_{3b3}), a) measured and computed initial porosity, b) measured and computed mass fraction of calcite, c) ratio between the specific surface area of calcite (SSA_c) and the total specific surface area with calcite (SSA_a).	136
7.11	Contact properties of the four scanned subsamples (SS_0 , SS_{3b1} , SS_{3b2} and SS_{3b3}), a) 2D treated images, b) coordination number distribution with and without calcite c) contact surface area with and without calcite.	137
7.12	Contact properties of the four scanned subsamples (SS_0 , SS_{3b1} , SS_{3b2} and SS_{3b3}), a) measured and computed mass fraction of calcite, b) coordination number, c) contact surface.	138
7.13	Contact properties of the four scanned subsamples (SS_0 , SS_{3b1} , SS_{3b2} and SS_{3b3}), a) 2D treated images, b) type of contact distribution, c) type of contact surface distribution.	139
7.14	Orientation of the different types of contact within the subsamples (SS_0 , SS_{3b1} , SS_{3b2} and SS_{3b3}), Contact properties of the four scanned subsamples (SS_0 , SS_{3b1} , SS_{3b2} and SS_{3b3}), a) 2D treated images, b) contact distribution before calcification c) contact distribution after calcification	140
7.15	Microstructural properties computed on 3D images of calcified and dissolved specimens, a) mean cohesive contact surface area (\bar{S}_c/\bar{S}_a), b) Calcite specific surface area (SSA_c/SSA) and c) coordination number evolution (\bar{Z}_a/\bar{Z}_b).	142
A.1	Triaxial compression tests results of group 1 specimens (untreated sand)	152
A.2	Triaxial compression tests results of group 2 specimens	153
A.3	Triaxial compression tests results of group 3 specimens	154
A.4	Triaxial compression tests results of group 4 specimens	155
A.5	Triaxial compression tests results of group 5 specimens	156
A.6	Triaxial compression tests results of group 6 specimens	157

A.7 Triaxial compression tests results of group 7 specimens	158
---	-----

LISTE DES TABLEAUX

2.1	Récapitulatif de l'évolution des paramètres de résistance des sables bio-cimentés mis en évidence dans la littérature.	31
3.1	Fontainebleau sand characteristics.	45
3.2	Experimental characteristics of the tested samples.	48
3.3	Measured permeability and calcite dosage.	51
4.1	Fontainebleau sand characteristics.	65
4.2	List of the scanned sub-samples with its associated properties.	67
5.1	Characteristics of the scanned sub-samples (Dadda et al., 2017b).	87
6.1	Characteristics of the observed sub-samples.	111
7.1	Characteristics of the performed tests.	127
7.2	Computed microstructural properties of the subsamples.	135

CHAPITRE 1

GENERAL INTRODUCTION

Several soil improvement techniques have been invented to enhance and increase their bearing capacity for civil engineering projects. These reinforcement techniques are based mainly on mechanical energy (dynamic compaction/vibroflotation), adding chemical additives (cement, epoxy, and lime, etc.) and/or materials such as : synthetic fibers (recycled glass fibers, tires and geosynthetics) (Mujah et al., 2017). However, most of these techniques require a considerable amount of energy for the production of materials and the installation of equipments (DeJong et al., 2010a), making these techniques polluting, in particular because of the CO₂ emissions required for the manufacture of cement (about 5% of the world's anthropogenic CO₂ emissions) (John, 2003), and the use of fossil energy for mechanical equipments *in-situ*, but also because of the noise generated by mechanical reinforcement. In addition, most of the chemical adjuvants used in reinforcement operations are considered as toxic and environmentally aggressive (Karol, 2003). From a mechanical point of view, these reinforcement techniques are considered very effective for most traditional problems such as the reinforcement of soils foundation for new structures. Today, much of the projects constructed during the 20st century have aged, and locally present pathologies linked to their ageing, which can ultimately lead to risks of rupture. The evolution of the current regulations calls for increased monitoring of these structures (in particular with respect to seismic hazards and those related to internal erosion for earthen hydraulic structures) and their treatment in case of proven risks. On the other hand, the techniques of reinforcement that exist today are very limited to reinforce old dams or other earth structures ; because of their sensitivities to these harmful methods (e.g., soil mixing and thin wall), or the uncertainty and inefficiency of these techniques at great depths (e.g., grouting) (DeJong et al., 2010a).

This critical situation has forced the community of researchers and engineers to find alternative and effective solutions to reinforce these old structures while minimizing financial costs and ecological impacts. Biology is a promising candidate to establish a partnership between certain natural and technical processes of reinforcement and/or prevention against certain natural risks. This partnership has been superficial for many years, and has been summarized in the applications of

implantation and slope coverage by vegetalized soils (reinforcement by root system) (Gray and Sotir, 1996). In the early 21st century researchers confirmed that some bacteria have the potential to accelerate the calcium carbonate precipitation process (CaCO_3) in natural environments (Castanier et al., 2000). Several types of microorganisms that have existed in natural soils for a long time (more than three billion years) can crystallize different types of minerals such as : calcium carbonates (CaCO_3), calcium phosphates ($\text{Ca(PO}_4)_2$), silicates (SiO_4) (DeJong et al., 2006; Girinsky, 2009). These phenomena have always been present in nature. One of the most representative and spectacular examples in this field is a phenomenon encountered in Australia with the formation of stromatolites on the surface of saline waters (Castanier et al., 2000), but there are other phenomena of the same type in France and in the world.

The observation of this phenomenon in nature paved the way for a new branch in geotechnical engineering called « geobiology ». This branch focuses on the biotransformation of sand to sandstone to improve its mechanical properties, using microorganisms such as urease bacteria (Mujah et al., 2017). This technique has advantages over traditional reinforcement techniques (e.g., injection of cement grout), in particular because of the capacity of micro-organisms to infiltrate into the soil on large distances or depths, which can ensure volume treatments, and reduce the cost of installing injection wells in a structure. Moreover, the energy required for the manufacture of a bio-cement by bacteria represents 10% of the total energy required for the manufacture of the same quantity of conventional cement (Torgal et al., 2015). From the environmental point of view, this technique is considered ecological, capable of reducing CO_2 emissions in the atmosphere, thus contributing to the reduction of global warming. The use of micro-organisms as a potential biocatalyst in the soil biocementation process was first proposed by Whiffin (2004) and Mitchell and Santamarina (2005). Since then, research in this field has developed in several ways. The performed studies have recommended the use of this promising technique to mitigate several problems of instability in geotechnics and geomechanics (internal erosion of earth hydraulic structures, liquefaction of soils, landslides, crack closure, etc.) (Phillips et al., 2013).

The work presented in this thesis has been carried out within the framework of the « BOREAL project » (Bio-renforcement des OuvRagEs hydrAuLiques en remblais) which was launched in 2014 in France. The aim of this project is to reinforce the hydraulic structures against two geotechnical problems (internal erosion and liquefaction), using the Microbial-Induced Calcite Precipitation (MICP) process. Two zones in the earthen hydraulic dams are concerned in this study ; the foundation exposed to the liquefaction hazards and the core subjected to the internal erosion. These regions correspond to different types of soils ; fine soil in the core and coarse soil with large gap of particle size distribution in the foundation. As a first step in the BOREAL project, the Fontainebleau (NE34) sand has been used as a reference in order to study the different aspects of biocementation. This project brings together all the skills needed to lift technical and scientific locks. The partners of the project are : [3SR](#), [IGE](#), [LETG](#), [CNR](#), [EDF](#), [Soletanche Bachy](#), [geophyConsult](#) and [ENOVEO](#). This project is mainly divided into 7 parts (Figure 1.1).

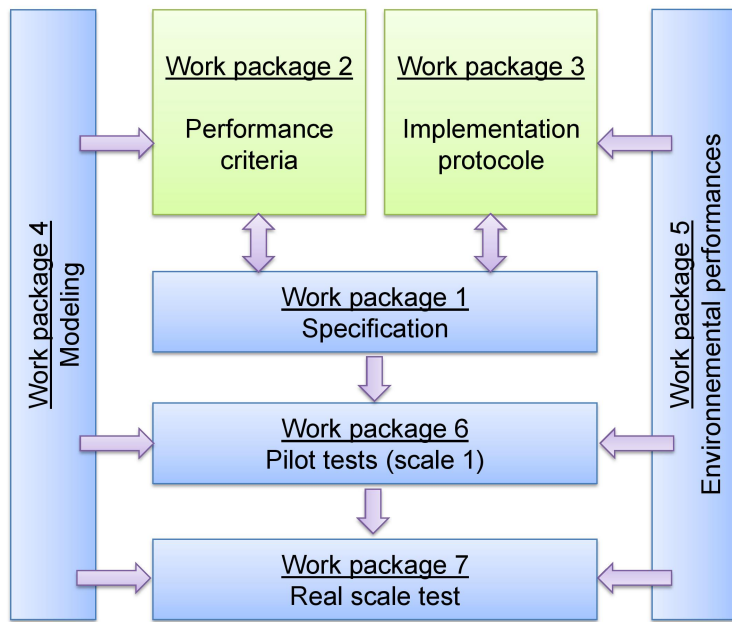


FIGURE 1.1: Structure of BOREAL project.

Each part represents a task for one or more partners in the project according to their specialities. The different tasks in this project are preliminary steps to an *in-situ* test of reinforcement (real dike). The work presented in this document fits in work package 2 and 3 of BOREAL project, which concentrates on the mechanical and microstructural aspects of biocemented soils. In this context, an experimental study was carried out to (1) characterize the evolution of the mechanical and physical properties of biocemented sand in the laboratory, (2) interpret qualitatively and quantitatively the microstructural changes by the 3D imaging technique (3) to establish a link between the microstructural properties and the effective (mechanical and physical) properties of biocemented sand, and (4) to study the durability of biocemented sand (degradation of mechanical and microstructural properties under the effect of an aggressive chemical solution) (Figure 1.2).

This thesis contains six chapters.

The **chapter 2** is devoted to a detailed bibliographic study on the biocementation technique. In this chapter, an extensive literature review of biocalcification technique is presented. This study focuses particularly on the factors controlling the process, the mechanical and microstructural changes in bio-cemented soils, the mechanical and chemical durability of this process, and the challenges and limitations for real applications.

After the chapter of bibliographic research, the different chapters are written in the form of accepted articles or submitted to international journals to facilitate the valorization of the research work carried out during this thesis work. Some notations and specimens names have been chan-

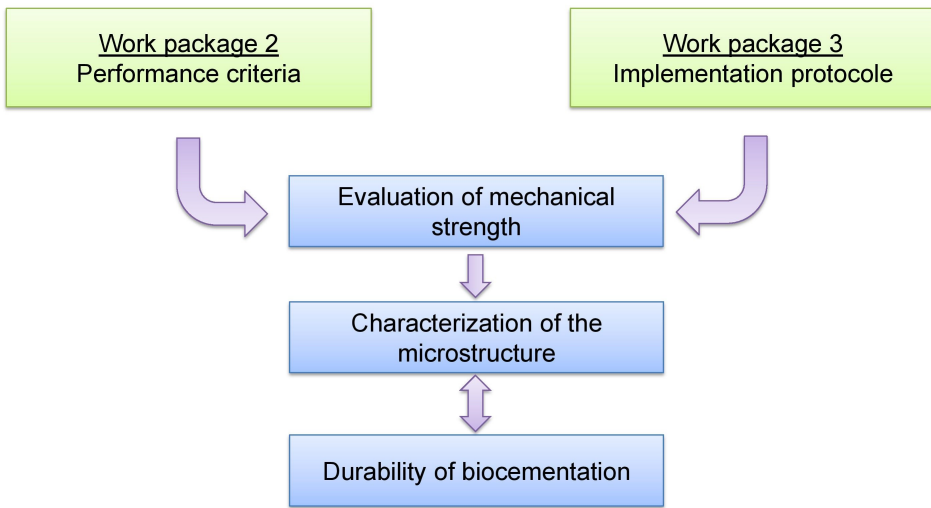


FIGURE 1.2: Plan of thesis work and its position in BOREAL project.

ged in the present document compared to published articles in order to facilitate the reading of this document. The **chapter 3** focuses on the effectiveness of a laboratory treatment protocol and the induced changes in the mechanical strength and permeability of bio-cemented sand by carrying out drained triaxial tests and permeability measurements at constant load (Mariotte system). In this study, a range of cementation wider than that considered in previous investigations was analyzed (from 0 to 11,9% of calcite in mass). Micro-tomographic and microscopic observations have been also carried out on several samples in order to qualitatively explore the change in microstructure, the spatial distribution of calcite crystals and their morphology. This chapter is submitted as a scientific paper in the Canadian Geotechnical Journal.

The **chapter 4** is devoted to the quantitative exploitation of 3D images reconstructed from a set of X-ray scans. Samples of sand with different levels of calcification were thus observed at the synchrotron ([ESRF-ID19](#)) at a very high resolution ($0.65 \mu\text{m}/\text{pixel}$) in order to (1) observe the distribution of calcite at the pore scale and (2) to characterize the evolution of the microstructure (volume fraction of calcite, surface area, etc.) and physical properties (permeability, effective diffusion tensor) of the biocemented sand as a function of the level of cementation. The numerical results calculated on Representative Elementary Volumes extracted from the 3D images are compared with experimental data, analytical models (self-consistent estimates) and numerical values obtained with simple periodic arrangements of calcite-coated spheres (BCC, FCC). This chapter is published in *Acta Geotechnica* as scientific paper (Dadda et al., 2017b).

The **chapter 5** is a logical sequel to the chapter 4. In this chapter, we propose to determine and quantify the evolution of the contact properties (contact surface are, number of coordination, contact orientation, contact type, etc.) of the bio-cemented sand according to the cementation level using the same 3D images obtained by micro-tomography. The numerical results calculated on Representative Elementary Volumes extracted from the 3D images are then compared with

the numerical values obtained on a simple periodic arrangement (simple cubic), assuming that the precipitation is located at the contacts between grains or uniform in order to identify the most probable precipitation scenario of the calcite (localized, uniform or an intermediate scenario). This chapter is submitted as paper in Granular Matter.

The chapter 6 is an attempt to use the microstructural properties computed in the chapters 4 and 5 such as : the cohesive contact surface area, the coordination number, the solide fraction, etc. in order to estimate the effective macroscopic properties such as the cohesion and the elastic properties, using simple micromechanical models.

The last chapter (**chapter 7**), is devoted to the study of chemical durability of bio-cemented sands. In this study, biocalcified sand samples were rinsed with an aggressive (acid) solution. The degradation of the mechanical strength of these samples was estimated by triaxial compression tests. SEM and X-ray micro-tomography observations have been performed in order to explore qualitatively and quantitatively the calcite degradation process at the microscopic scale. Calculations on these 3D images have been carried out, using the methods developed in the previous chapters (chapters 4 and 5) in order to be able to follow the degradation of the microstructural properties (number of coordination, contact surface area, etc.) with respect to the chemical treatment.

This manuscript ends with a general conclusion (**chapter 8**) which summarizes the main results of this research work together and draws some perspectives for future studies.

CHAPITRE 2

ÉTUDE BIBLIOGRAPHIQUE

Sommaire

2.1	Introduction	9
2.2	Bio-cimentation par bio-précipitation de calcite (CaCO_3)	10
2.3	Facteurs contrôlant le processus de bio-cimentation	12
2.3.1	Type et concentration de microorganismes	13
2.3.2	Concentration de solution calcifiante	14
2.3.3	Influence du pH initial	15
2.3.4	Température	16
2.3.5	Type de sol	18
2.3.6	Salinité	19
2.4	Modifications des propriétés des matériaux bio-cimentés	19
2.4.1	Changements microstructuraux	19
2.4.1.1	Cristallographie de la calcite	19
2.4.1.2	Distribution spatiale de la calcite	20
2.4.2	Evolution de la perméabilité	21
2.4.3	Evolution des propriétés mécaniques	22
2.4.3.1	Propriétés élastiques (très petites déformation)	23
2.4.3.2	Résistance à la compression simple	24
2.4.3.3	Résistance au cisaillement et déformabilité mesurées à partir d'essais triaxiaux	28
2.4.3.4	Paramètres de résistance	30
2.5	Durabilité de la bio-cimentation	31
2.5.1	Durabilité chimique	31
2.5.2	Durabilité mécanique	33
2.6	Stratégie de traitement	36
2.6.1	Méthode d'injection	36
2.6.2	Pré-mixing	37
2.6.3	Percolation de surface	37

2.1 Introduction

Dans la littérature, les travaux publiés sur la technique de bio-cimentation sont extrêmement riches surtout en ce qui concerne les protocoles de traitement et l'évolution de la résistance mécanique des sols bio-cimentés. Les recherches sur ce domaine ont probablement débuté avec la découverte des bactéries qui peuvent accélérer potentiellement le processus de précipitation de calcite (CaCO_3) dans les milieux naturels (Castanier et al., 2000). Cette découverte a initié l'idée de la biocalcification des sols pour améliorer ses propriétés mécaniques.

Whiffin (2004) et Mitchell and Santamarina (2005) sont les premiers à avoir suggéré l'utilisation de ces bactéries en tant que biocatalyseur potentiel pour cimenter les sols. Depuis lors, la recherche dans ce domaine n'a fait que croître suivant plusieurs voies. Au début, la plupart des études ont été consacrées à la validation des capacités de ce procédé à augmenter les propriétés mécaniques des sols renforcés, sans diminuer la perméabilité (Whiffin et al., 2007; van Paassen et al., 2010; Al Qabany et al., 2011b). Vu la complexité de ce procédé qui est basé sur une réaction biogéochimique, les résultats des premières études ont montré une grande variabilité, ce qui a obligé les chercheurs à travailler sur les protocoles de traitement et la microstructure des sols bio-cimentés. Dans ces études, des observations microscopiques au microscope électronique à balayage (MEB) ont été réalisées sur différents sols après différents protocoles de traitement. Ces observations ont montré que l'augmentation de la résistance mécanique ainsi que la chute de perméabilité sont très dépendantes de la microstructure, qui résulte elle-même du protocole de traitement (concentration de bactéries et des réactifs, vitesse d'injection, saturation, etc.) (Cheng et al., 2013; Al Qabany and Soga, 2013). Après ces constatations, les travaux de recherche réalisés se sont concentrés sur les liaisons entre le protocole de traitement, la microstructure et la résistance mécanique du sol, afin de pouvoir déterminer les conditions optimales pour cette technique (Zhao et al., 2014; Cheng et al., 2014, 2016). En parallèle, d'autres travaux de recherche ont été lancés pour pousser cette technique vers des applications *in-situ* comme le renforcement contre la liquéfaction, l'érosion interne, la suppression de poussières (DeJong et al., 2014a; Jiang et al., 2014; Montoya and DeJong, 2015; Han et al., 2016; Jiang and Soga, 2016; Gomez et al., 2016; Venuleo et al., 2016).

Généralement, ces travaux ont beaucoup enrichi les approches théoriques et expérimentales à différentes échelles (microscopique, macroscopique et à l'échelle du site). Les difficultés rencontrées dans ces études se trouvent dans la grande variété des paramètres influençant le processus de biocalcification tels que le protocole de traitement (concentration des réactifs et des bactéries), les conditions *in-situ* (type de sols, température, acidité, etc.). C'est pour cela que le processus de bio-cimentation reste encore relativement mal maîtrisé. Dans ce chapitre, une synthèse bibliographique approfondie de la technique de biocalcification est présentée. Elle se concentre particulièrement sur les facteurs contrôlant ce processus, les changements mécaniques et microstructuraux des sols bio-cimentés, la durabilité mécanique et chimique de ce procédé, et les défis et les limitations de ce procédé pour des applications *in-situ*.

2.2 Bio-cimentation par bio-précipitation de calcite (CaCO_3)

La bio-cimentation par précipitation du carbonate de calcium (CaCO_3) est induite par des activités bactériennes en présence d'autres substances (1) source de calcium et (2) urée (source de dioxyde de carbone). Ce processus est appelé également MICP (Microbially Induced Calcite Precipitation) ou biocalcification. Elle génère généralement trois morphologies différentes de carbonate de calcium (calcite, aragonite et vatérite), en fonction des conditions physico-chimiques du milieu de réaction (Figure 2.1) (Ivanov and Stabnikov, 2017).

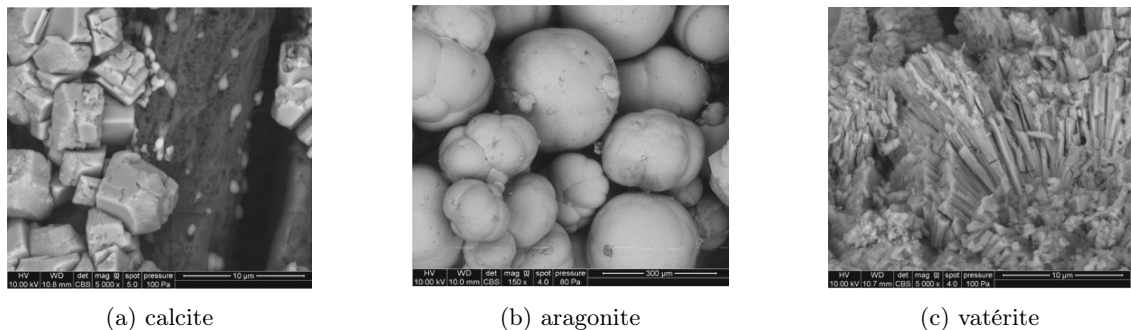


FIGURE 2.1: Morphologies du carbonate de calcium induites par des activités bactériennes (Ivanov and Stabnikov, 2017).

Les cellules bactériennes représentent des sites de nucléation pour le processus de bio-cimentation. En effet, dans un sol ces cellules bactériennes vont se fixer aux endroits où les forces de cisaillement produites par l'écoulement d'injection sont faibles, et les endroits riches en nutriment (zones de contact inter-granulaire et au niveau des microrugosités des grains) (Figure 2.2), ce qui conduit à une bio-précipitation préférentielle du carbonate de calcium au niveau des contacts inter-granulaires dans les sols traités. Ceci présente un avantage pour cette technique de renforcement puisque la cohésion du sol va augmenter de façon significative par la précipitation de la calcite dans les zones de contact inter-granulaire, sans diminution notable de la conductivité hydraulique (Girinsky, 2009; DeJong et al., 2010a).

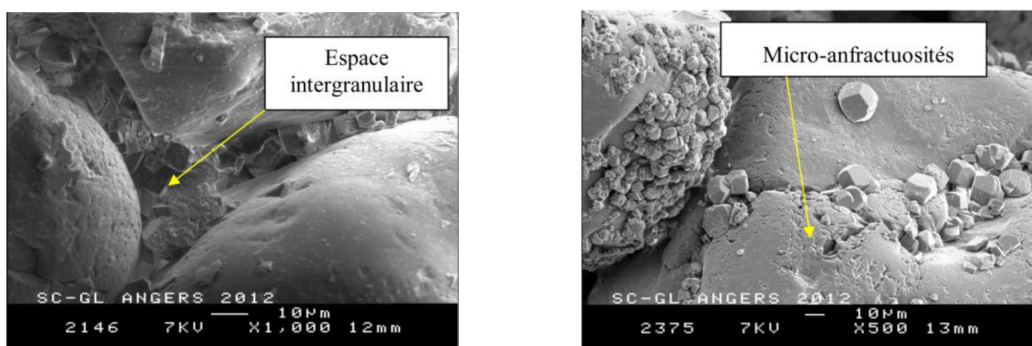


FIGURE 2.2: Biocalcification dans les espaces inter-granulaires et dans les anfractuosités du grain (Girinsky, 2009)

L'activité métabolique des microorganismes conduit à sécréter des enzymes comme l'uréase, qui sont capables d'hydrolyser l'urée dans les cellules microbiennes, en le décomposant en ammoniac NH₃ et en dioxyde de carbone CO₂ (Equation 2.1). Ces produits chimiques se diffusent à travers la paroi cellulaire du microorganisme dans la solution environnante (Figure 2.3).

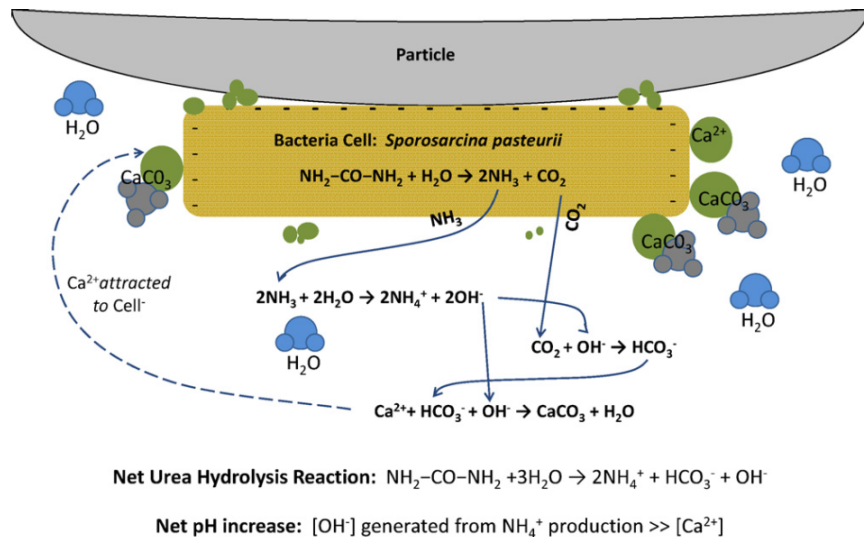
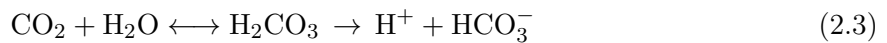


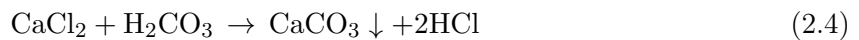
FIGURE 2.3: Schéma représentatif des réactions chimiques durant le processus de biocalcification (DeJong et al., 2010a).



Deux réactions se produisent spontanément en présence d'eau dans la solution environnante ; l'ammoniac est convertie en ions ammonium NH₄⁺ (Equation 2.2), et le dioxyde de carbone s'équilibre avec l'acide carbonique, les ions de carbonates, et bicarbonates (Equation 2.3) en fonction du pH.



L'augmentation du pH est due à des ions hydroxyle OH⁻ générés lors de la production du NH₄⁺. L'activité enzymatique des bactéries est favorisée par l'alcalinité du milieu (pH : 8,5-10) produisant alors les carbonates requis pour la précipitation de calcite (Equation 2.4) (DeJong et al., 2010a).



La réaction géochimique totale (Equation 2.5) de la biocalcification donne la précipitation du produit minérale (CaCO₃) qui peut augmenter de façon importante la résistance mécanique

des sols. L'ammoniaque est un sous-produit de cette réaction biochimique en parallèle avec le carbonate de calcium. Ce produit est toxique et nocif pour l'environnement aquatique et l'atmosphère, ceci représente un inconvénient pour ce procédé (Pacheco-Torgal and Labrincha, 2013).

2.3 Facteurs contrôlant le processus de bio-cimentation

Etant donné la complexité de ce processus biogéochimique, plusieurs travaux de recherche ont été réalisés pour comprendre et améliorer cette technique de bio-cimentation pour des futures applications *in-situ*. À partir de ces études, trois facteurs ont été identifiés comme les principaux paramètres de contrôle de ce procédé : (1) le type et la concentration de microorganismes ; (2) la concentration de solution calcifiante (concentration d'ion de calcium et le carbone inorganique dissous) ; (3) les facteurs environnementaux tels que : PH, température, salinité, type de sols (granulométrie et minéralogie) (Figure 2.4) (Nemati et al., 2005; Maier et al., 2009; De Muynck et al., 2010b).

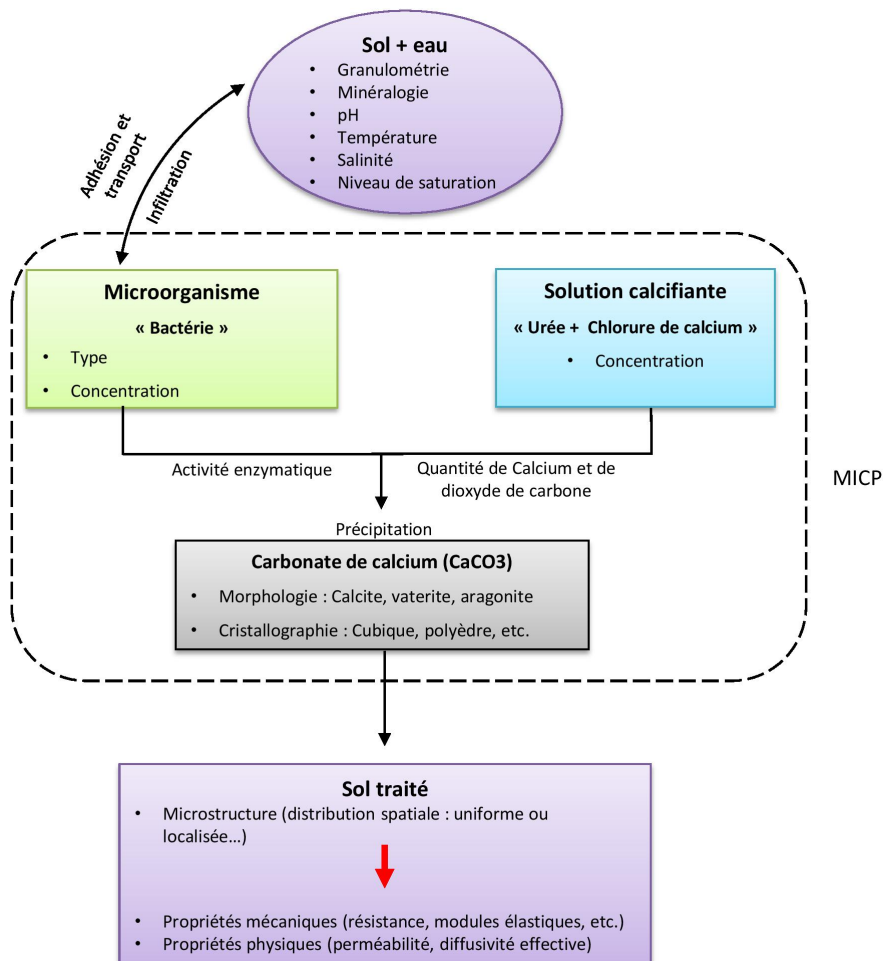


FIGURE 2.4: Schéma représentatif des facteurs qui contrôlent le procédé.

Dans les paragraphes suivants, les différents facteurs contrôlant ce processus sont présentés en

détails ainsi que leurs influences sur la technique de MICP.

2.3.1 Type et concentration de microorganismes

Les principales tâches de la bactérie dans le processus de bio-cimentation sont (1) la sécrétion de l'enzyme de l'uréase et (2) la création des sites de nucléation pour la réaction biochimique (Figure 2.5). Plusieurs études réalisées au laboratoire ont montré que l'enzyme de l'uréase peut être produit dans des quantités différentes par plusieurs microorganismes (*in-situ*, *B. lentus*, *B. cereus*, *B. megaterium*, *B. sphaericus*, *S. succinus*) (Castanier et al., 2000; Dhami et al., 2014; Dick et al., 2006; Bang et al., 2001; Achal and Pan, 2011; Stabnikov et al., 2013) et par différentes plantes dans la nature (*Canavalia ensiformis*, *Soja*, *Cajanus*) (Dilrukshi and Kawasaki, 2016). Cependant, le processus de bio-cimentation est plus compliqué *in-situ* qu'en laboratoire. L'injection sur place dans un environnement donné, des bactéries cultivées au laboratoire peuvent faire face à des problèmes de compétition et prédation par des bactéries indigènes, ce qui réduit l'efficacité du traitement *in-situ* (Burbank et al., 2011). Les règlements dans de nombreux pays exigent aussi la non-toxicité et la non-nocivité des produits utilisés dans les travaux de construction, ce qui limite les choix des micro-organismes qui peuvent être utilisés dans des travaux de renforcement par bio-cimentation. Par conséquent, les critères de choix du type de microorganisme à utiliser dans la bio-cimentation se résument à (1) l'activité enzymatique, (2) l'adaptabilité au milieu environnemental (salinité, pH, bactéries indigènes, température etc.), (3) la toxicité et/ou nocivité.

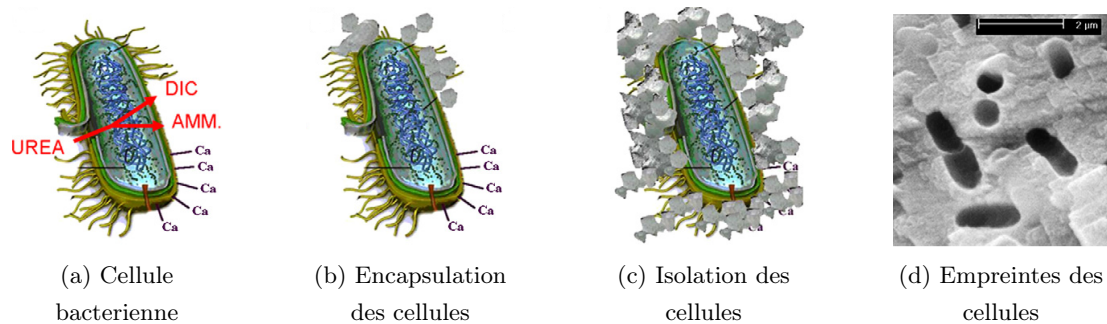
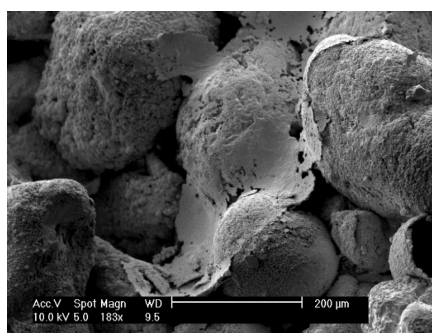


FIGURE 2.5: Schéma des étapes de biocalcification à côté d'une cellule bactérienne (De Muynck et al., 2010a).

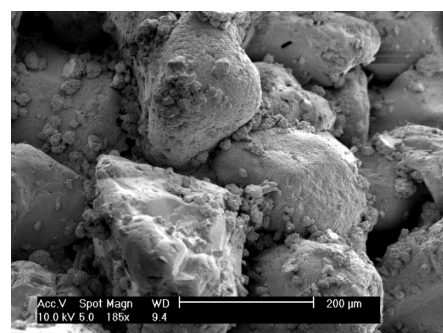
Type des microorganismes : La plupart des recherches en calcification biologique utilisent la bactérie *Sporosarcina pasteurii* qui représente un choix optimal pour ces trois critères. Cette bactérie est caractérisée par une activité enzymatique élevée. Elle est considérée comme ubiquiste dans l'environnement (largement disponible) ce qui facilite son adaptabilité et diminue sa compétition et sa prédation par d'autres bactéries indigènes sur site. Cette souche bactérienne est caractérisée aussi par une bonne adaptabilité aux milieux basiques (pH supérieur à 8,5) et aux fortes concentrations de calcium, ce qui représente un avantage pour la MICP (Torgal et al., 2015). Ce type de bactérie est non pathogène, et elle est de petite taille, en forme de bâtonnet de

longueur entre 1 à 4 μm et de diamètre entre 0.7 à 1 μm , ce qui lui permet de rentrer facilement dans les pores des sols à traiter (Girinsky, 2009). D'autres espèces similaires peuvent être utilisées pour la biocalcification telles que : *B. lentus*, *B. cereus*, *B. megaterium* et *B. sphaericus*. Certaines espèces, comme la *S. succinus*, possèdent une activité enzymatique très élevée par rapport à la souche *Sporosarcina pasteurii*, ce qui donne une capacité de précipitation de calcite plus élevée (Stabnikov et al., 2013). Cependant, cette souche bactérienne est souvent toxique (Zell et al., 2008).

Concentration des microorganismes : La concentration bactérienne représente un facteur majeur pour l'efficacité du traitement, à cause de la relation directe entre l'activité enzymatique, la disponibilité des sites de nucléation, et le nombre de bactéries dans le milieu (Whiffin, 2004; DeJong et al., 2010a). Une densité optique (DO) entre 0.8 et 1.2 de la bactérie *Sporosarcina pasteurii* est généralement utilisée pour le procédé MICP pour des concentrations de solution calcifiante comprises entre 0.05 et 1.5 M (Mitchell and Ferris, 2006; Harkes et al., 2010; Al Qabany and Soga, 2013; Martinez et al., 2013; Feng and Montoya, 2015). Les travaux réalisés sur cet aspect ont montré que l'utilisation de fortes concentrations bactériennes produit une grande quantité de calcite ; ce qui conduit à une résistance mécanique (résistance à la compression) plus importante par rapport aux faibles concentrations (Zhao et al., 2014). Cependant, Cheng et al. (2016) ont montré que pour un même niveau de calcification, des faibles concentrations bactériennes peuvent conduire à une plus grande efficacité mécanique du traitement par rapport aux plus fortes concentrations (Figure 2.6). L'utilisation de faibles concentrations de bactéries nécessite un nombre d'injections plus important pour atteindre une grande quantité de calcite précipitée, ce qui n'est pas très pratique pour des applications de renforcement sur site.



(a) Forte concentration bactérienne



(b) Faible concntration bactérienne

FIGURE 2.6: Observations au MEB de deux échantillons de sable bio-cimenté pour différentes concentrations bactériennes , a) $\text{CaCO}_3 = 0,061 \text{ g/g sable}$ et la résistance à la compression simple ($R_c = 713 \text{ kPa}$), b) $\text{CaCO}_3 = 0,039 \text{ g/g sable}$ $R_c = 709 \text{ kPa}$, et (Cheng et al., 2016).

2.3.2 Concentration de solution calcifiante

Le processus de biocalcification nécessite une source de calcium et une source de dioxyde de carbone pour la réaction biochimique de précipitation de la calcite. Généralement, dans le pro-

cessus de bio-cimentation on utilise le chlorure de calcium (CaCl_2) comme une source de calcium et l'urée comme une source de carbone ($\text{CO}(\text{NH}_2)_2$) (Equation 2.5). Nemati et al. (2005) ont montré qu'une solution calcifiante équimolaire (même quantité molaire de chlorure de calcium et d'urée) conduit à une meilleure conversion en calcite (efficacité maximale de précipitation). Les études réalisées sur l'influence de la concentration de la solution calcifiante montrent un effet significatif sur la cristallographie (taille et morphologie des cristaux) et la distribution spatiale de la calcite (CaCO_3) précipitée dans le squelette solide ; ce qui influence par la suite la résistance mécanique des sols traités (Al Qabany and Soga, 2013). L'utilisation d'une faible concentration (0.05 à 0.25 M) conduit à une répartition plus homogène de la calcite dans les échantillons de sols traités avec des cristaux de calcite de plus petites tailles (Nemati et al., 2005; De Muynck et al., 2010b). En revanche, l'utilisation d'une concentration élevée de solution calcifiante (0.5 à 1 M) peut donner une quantité considérable de calcite avec de grands cristaux ; par contre la précipitation dans ce cas est très hétérogène à l'intérieur de l'échantillon du sol traité (Figure 2.9c), ce qui réduit l'efficacité mécanique de ce procédé (Cheng et al., 2016).

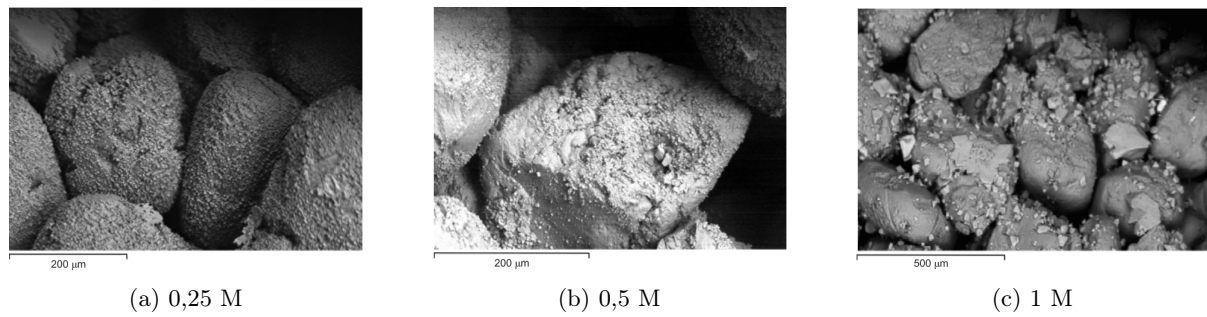


FIGURE 2.7: Observation MEB pour des échantillons de sable traités avec différentes concentrations de solution calcifiante (Al Qabany and Soga, 2013).

L'influence de ces concentrations sur l'efficacité mécanique a été étudiée par Al Qabany and Soga (2013). Ils ont montré qu'une solution de faible concentration introduite en plusieurs opérations d'injection permet d'obtenir des échantillons calcifiés par des petits cristaux de calcite et plus résistants pour une même quantité de calcite obtenue avec des concentrations plus grandes.

2.3.3 Influence du pH initial

Le pH des sols varie généralement entre 4 et 10. Cette variation dépend de plusieurs paramètres comme la composition minéralogique du sol, le type de précipitation dans la région (ex : pluie acide), et l'existence des polluants acides ou basiques dans le sol. Par conséquent, l'étude de l'influence de l'acidité des sols est indispensable pour des applications *in-situ* de la technique de bio-cimentation. D'après des études réalisées sur cet aspect, le pH du sol ou du milieu peut affecter différemment (1) la croissance et l'activité enzymatique des bactéries, (2) les propriétés de transport et d'adhésion des bactéries et (3) la cristallisation du carbonate de calcium (Stocks-Fischer et al., 1999; Achal et al., 2009; DeJong et al., 2010a; Bang et al., 2001; Harkes et al., 2010; Tobler et al., 2011; Cheng et al., 2014).

Croissance bactérienne et activité enzymatique : Les micro-organismes peuvent vivre dans des milieux acides avec un pH inférieur à 2 et dans des milieux basiques d'un pH supérieur à 10 (Mitchell and Santamarina, 2005). Cependant, un milieu avec un pH inférieur à 5 peut être préjudiciable pour l'enzyme et les cristaux de calcite (Mobley et al., 1995; Phillips et al., 2013). Le micro-organisme le plus utilisé dans le traitement des sols par bio-cimentation (*Sporosarcina pasteurii*) préfère les milieux basiques pour la croissance et la sécrétion de l'enzyme de l'uréase (pH entre 6.5 et 9.3) (Ferris et al., 2004). Différentes valeurs de pH ont été testées afin d'explorer l'évolution de l'activité enzymatique des bactéries. Une activité enzymatique maximale et des conditions de croissance optimales ont été trouvées dans un environnement de pH entre 8,7 et 9 pour la souche *Sporosarcina pasteurii* (Dupraz et al., 2009). Cette valeur optimale de pH peut changer d'une bactérie à une autre (*B. Megaterium* "pH : 7", *B. Sphaericus* "pH : 8", et *B. sphaericus* "pH : 9").

Transport et adhésion : L'adhésion et le transport des bactéries dans les milieux poreux sont contrôlés principalement par la surface de charge négative des microorganismes qui aide à attirer les ions calcium (Ca^{2+}). Vu que les sols ont généralement des charges négatives, ces ions calcium peuvent jouer le rôle d'intermédiaires pour fixer les bactéries sur les surfaces des grains. La charge électrostatique des cellules bactériennes est très sensible à la variation du pH du milieu. Un pH entre 5 et 7 donne une charge négative importante sur les surfaces des bactéries, proche de celles des sols en surface, cette charge électrique peut être diminuée par la diminution de pH du milieu, elle peut atteindre une charge nulle pour un pH entre 4 et 5 pour la souche (*Sporosarcina pasteurii*), ce qui peut influencer l'adhésion et la fixation des bactéries dans le milieu poreux (Mitchell and Santamarina, 2005).

Cristallisation du carbonate de calcium : Bien que la formation des ions hydroxyle (OH^-) dans la réaction biochimique de précipitation augmente de façon significative le pH initial du milieu (Figure 2.3), la valeur initiale du pH du milieu peut influencer la morphologie et la distribution des cristaux de carbonate de calcium dans le sol. Cheng et al. (2014) ont testé le processus de biocalcification sur des sables de différents pH initiaux (acide, neutre et basique) (Figure 2.8). Les résultats préliminaires de cette étude ont montré une grande influence du pH initial sur les propriétés mécaniques du sable traité. Un pH initial neutre conduit à une petite quantité de calcite, mais à une grande efficacité mécanique par rapport à un pH initial acide ou basique. Cette différence est probablement liée à la cristallographie des cristaux et leur distribution spatiale à l'intérieur de l'échantillon.

2.3.4 Température

La température sur la terre change d'une région à une autre et d'une saison à l'autre, et elle dépend de plusieurs paramètres comme l'altitude, la latitude, le type de sols, la saturation, la conductivité, la radiation solaire, etc. (Ng et al., 2012). Différentes études ont été réalisées pour caractériser l'effet de la température sur l'efficacité du traitement par biocalcification. Généra-

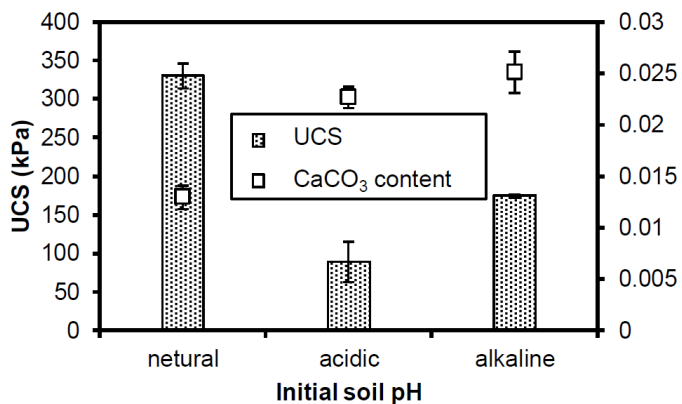


FIGURE 2.8: Influence du pH initial sur la résistance mécanique à la compression simple (Rc) et la quantité de la calcite précipitée (neutre : pH=7, acide : pH=3,5, basique : pH=9,5) (Cheng et al., 2014).

lement, ces études montrent que la température du milieu influence (1) l'activité enzymatique, ce qui influence aussi la quantité de carbonate de calcium précipitée, (2) la distribution et la morphologie du carbonate de calcium précipité et (3) la croissance et la survie des bactéries.

Activité enzymatique : L'activité enzymatique des bactéries représente généralement le taux d'urée hydrolysée qui peut être mesuré expérimentalement par l'augmentation de la conductivité électrique du milieu. Van Paassen (2009) a montré que l'activité enzymatique était négligeable pour une température inférieure à 5°C. Cette activité enzymatique est multipliée par dix lorsque la température est augmentée de 10°C à 20°C (Mitchell and Santamarina, 2005). Plusieurs travaux de recherche ont montré que la valeur optimale de l'activité enzymatique des bactéries se situe dans l'intervalle de 20 et 37°C (Mitchell and Ferris, 2006). Dhami et al. (2014) ont montré que l'activité enzymatique diminue de 47% à une température de plus que 55°C par rapport à une température ambiante. Cependant, Van Paassen (2009) a mis en évidence que dans un environnement qui a une température comprise entre 25 et 70°C, l'activité enzymatique augmente linéairement jusqu'à une valeur optimale à 70°C.

Morphologie et distribution de la calcite : Cheng et al. (2014) ont montré qu'une température élevée (50°C) conduit à une quantité de CaCO₃ plus importante par rapport à une calcification à une température ambiante (25°C). Cependant, l'efficacité mécanique de la calcification à température ambiante était meilleure pour le même niveau de calcification. Cheng et al. (2016) ont testé trois températures différentes dans le processus de bio-cimentation (4, 25, et 50°C). Cette étude a confirmé que la température a un effet significatif sur l'efficacité mécanique du traitement. La résistance mécanique pour des échantillons calcifiés avec le même niveau de calcification présente une valeur maximale pour une température ambiante de 25°C et une valeur minimale pour une température maximale de 50°C. L'observation microscopique de ces échantillons biocalcifiés à différentes températures (4, 25 et 50°C), montre que les différences en terme de résistance mécanique sont dues à la microstructure (Figure 2.9). De larges cristaux (20

et $50\ \mu\text{m}$) localisé dans des zones de contact inter-granulaires ont été obtenus à une température ambiante. Par contre, une distribution uniforme de petits cristaux d'une taille entre 2 et $5\ \mu\text{m}$ a été obtenue pour les deux autres températures (4 et 50°C), ce qui peut illustrer la faible efficacité mécanique trouvée pour les échantillons calcifiés à ces deux températures (Figure 2.9).

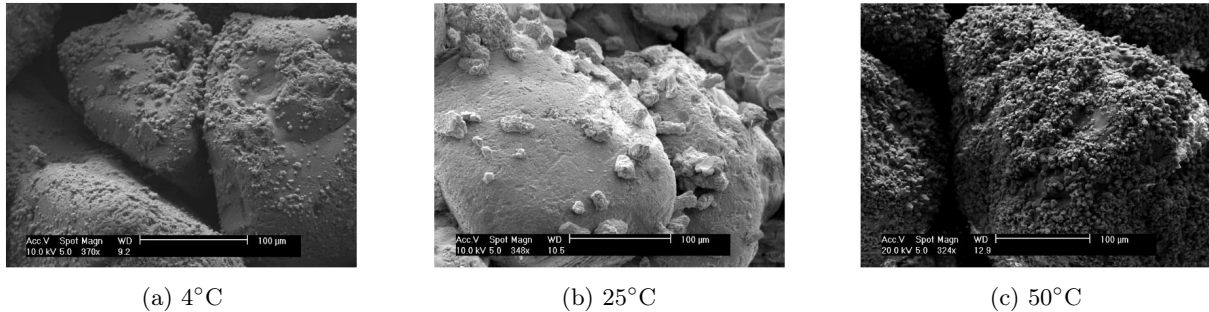


FIGURE 2.9: Observation MEB pour des échantillons de sable calcifiés sous différentes températures, a) $\text{CaCO}_3 = 0.021\text{g/g}$ de sable, $R_c = 108\ \text{kPa}$, b) $\text{CaCO}_3 = 0.028\ \text{g/g}$ de sable, $R_c = 245\ \text{kPa}$, c) $\text{CaCO}_3 = 0.034\ \text{g/g}$ de sable, $R_c = 121\ \text{kPa}$ (Cheng et al., 2016).

Croissance et survie des bactéries : Plusieurs études ont été réalisées pour définir l'intervalle de température optimale pour la croissance et la survie des cellules bactériennes. Ng et al. (2012) ont montré une faible sensibilité de la croissance des cellules bactériennes dans un intervalle de températures entre 20 à $30\ \text{C}^\circ$. Cependant, à partir d'une valeur de $60\ \text{C}^\circ$ les cellules bactériennes commencent à mourir et perdre leurs activités biologiques (Rebata-Landa, 2007).

2.3.5 Type de sol

Dans les projets de génie civil, les ingénieurs peuvent rencontrer plusieurs problèmes d'instabilité des sols (glissement, risque de liquéfaction sous des activités sismiques, effondrement par érosion, etc.). Ces sols sont de différentes granulométries et de différentes minéralogies (argile, limons, sable, etc.), ce qui influence les propriétés d'infiltration, de transport et d'adhésion des bactéries dans les sols, et par conséquent l'efficacité mécanique du traitement.

Infiltration : Les bactéries ont généralement des formes différentes (rond, tige et spirale) et des tailles entre 0.5 et $3\ \mu\text{m}$; cette taille est sensible à la pression et les propriétés physico-chimiques du milieu (salinité, pH, etc.). Une première comparaison a été présentée par Mitchell and Santamarina (2005) entre les tailles des grains dans les différents types de sols et celles des microorganismes (Figure 2.10). Ils ont montré que l'infiltration des bactéries dans des sols sableux est possible, alors que celle-ci peut présenter des difficultés dans les sols limoneux et est quasi-impossible pour les sols argileux.

Maier et al. (2009) ont confirmé que le *Sporosarcina pasteurii* peut se déplacer facilement dans un sol sableux avec une granulométrie entre 0.05 à $2\ \text{mm}$. Rebata-Landa (2007) a constaté qu'un

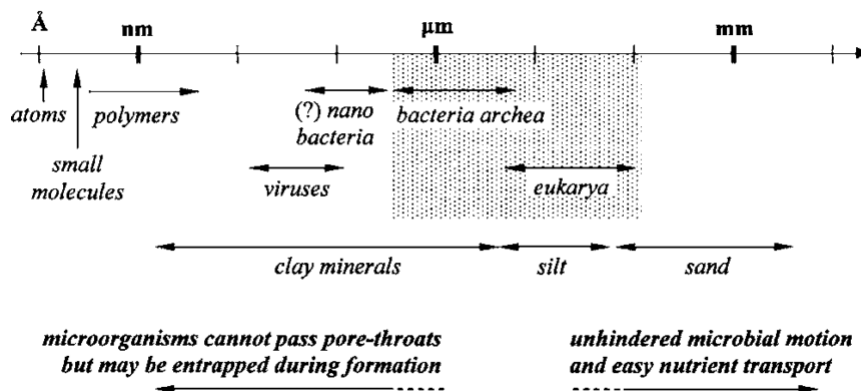


FIGURE 2.10: Comparaison entre la taille les grains de sol et les microorganismes (Mitchell and Santamarina, 2005).

sol qui a une granulométrie entre 50 et 400 μm a une compatibilité géométrique optimale, entre la taille des bactéries et la taille de ses pores. Cependant, les cellules individuelles des bactéries peuvent s'agglomérer et former des filaments, qui peuvent avoir des tailles supérieures à 100 μm (Kadhim and Zheng, 2017), ce qui peut conduire à un colmatage éventuel des pores des sols. Les sols fins qui contiennent des particules de petite taille (argile et limon) peuvent perturber l'infiltration des microorganismes à l'intérieur des milieux poreux. D'autre part, les sols grossiers ont besoin d'une quantité importante de bactéries et de solution calcifiantes pour augmenter leur résistance et leur rigidité par le processus de bio-cimentation, à cause de la grande taille des grains et des pores, qui laisse les bactéries s'infiltrer sans fixation importante. Ces faits ont été confirmés par des essais mécaniques réalisés sur des sables fin et grossier cimentés par la même procédure de bio-cimentation (Cheng et al., 2016).

Transport et adhésion : Les sables et les sols grossiers sont généralement constitués de quartz qui présente des charges électriques négatives en surface. Dans ce type de sols, la fixation et l'adhésion des bactéries se fait par l'intermédiaire du Ca^{2+} (comme expliqué dans le paragraphe 2.3.3). Cependant, dans les argiles et les sols qui ont des minéraux argileux comme les limons, l'adhésion peut être assurée par l'attraction électrostatique entre les argiles (chargées positivement) et les bactéries (chargées négativement) (Stevik et al., 2004). La grande surface spécifique des sols fins (argile et limons) peut aussi jouer un rôle très important pour la fixation et l'adhésion des bactéries par rapport aux sols grossiers qui ont des petites surfaces spécifiques.

2.3.6 Salinité

La salinité des eaux souterraines varie en fonction de plusieurs paramètres géologiques, géographiques et climatiques. Plusieurs études ont été réalisées pour analyser l'influence de la salinité du milieu sur le processus de bio-cimentation. Ces études ont montré que la salinité peut influencer certains paramètres tels que la croissance des bactéries, l'activité enzymatique, l'adhésion, et le transport. Généralement, les milieux de forte salinité ont un effet inhibiteur sur l'activité microbienne et la cristallisation du carbonate de calcium (Ng et al., 2012). Cependant, les bactéries

halotolérantes (*Sporosarcina pasteurii*) sont moins influencées par les milieux fortement salés. Ces bactéries sont capables de croître dans des milieux salés, ce qui les rend efficaces pour des opérations de renforcement dans des milieux salés *in-situ*. L'augmentation de la salinité du milieu peut augmenter l'alcalinité du milieu ce qui augmente systématiquement l'activité enzymatique des bactéries *in-situ*. L'utilisation d'une solution salée dans le processus de bio-cimentation peut augmenter aussi l'adhésion des bactéries dans le milieu poreux par l'augmentation de la force ionique de la solution, ce qui permet d'optimiser la masse injectée de bactérie et par conséquent une précipitation de calcite optimale dans le milieu (Harkes et al., 2010).

2.4 Modifications des propriétés des matériaux bio-cimentés

2.4.1 Changements microstructuraux

Les études précédentes (Feng and Montoya, 2015; DeJong et al., 2010a; Cheng et al., 2014; Terzis et al., 2016; Cheng et al., 2016, 2013; Tobler et al., 2012; Sel et al., 2015) ont montré que les changements observés, en terme mécanique et physique des sols traités par ce processus sont directement liés aux modifications de leurs propriétés microstructurales (taille et structure des cristaux de carbonate de calcium, distribution spatiale du CaCO₃ dans le réseau poral).

2.4.1.1 Cristallographie de la calcite

Structure cristalline de la calcite : Généralement, la calcite représente la forme morphologique la plus répandue du carbonate de calcium dans les travaux antérieurs de bio-cimentation. Elle est aussi la forme la plus stable du carbonate de calcium en terme mécanique et chimique. Les études réalisées sur la bio-cimentation avec différentes conditions de traitement ont permis d'observer la formation de cristaux de calcite de différentes structures cristallines (cubique, polyèdre, etc.) (Feng and Montoya, 2015; DeJong et al., 2010a; Cheng et al., 2014; Terzis et al., 2016; Cheng et al., 2016, 2013; Tobler et al., 2012; Sel et al., 2015). Cette structure cristalline de la calcite peut être influencée par plusieurs facteurs environnementaux comme le type d'eau et sa salinité (Folk, 1974). Folk (1974) a montré qu'une forte salinité du milieu peut diminuer le temps de formation de cristaux, ce qui favorise la formation des cristaux d'une forme allongée. Cependant, une eau douce accélère la formation des cristaux et favorise la formation de cristaux de calcite moins allongés (Figure 2.11).

Taille des cristaux : Différentes tailles de cristaux de calcite ont été trouvés dans les études antérieures (1 à 15 µm) (Feng and Montoya, 2015; DeJong et al., 2010a; Cheng et al., 2014; Terzis et al., 2016; Cheng et al., 2016, 2013; Tobler et al., 2012; Sel et al., 2015). La taille des cristaux est très dépendante des conditions initiales de traitement comme montré dans la partie 2.3 de ce chapitre. Généralement, l'utilisation de grandes concentrations de bactéries, de faibles concentrations de solution calcifiante, une température plus élevée ou plus faible que la température ambiante conduisent à la précipitation de petits cristaux de calcite. Des petites concentrations de bactéries, des fortes concentrations de calcium, et une température ambiante

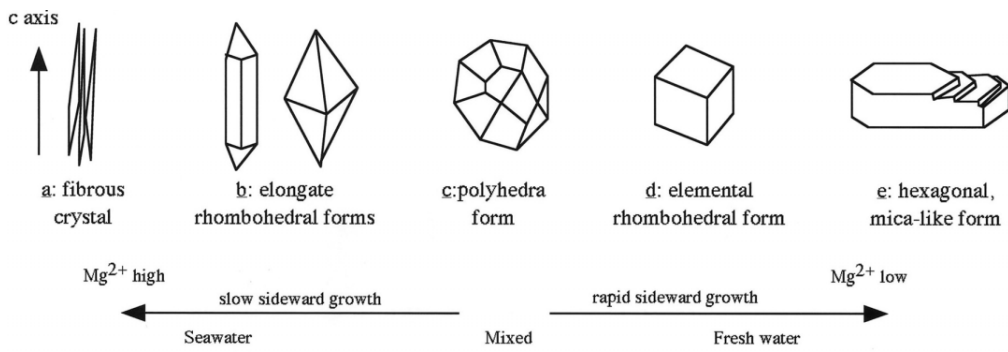


FIGURE 2.11: Relation entre la salinité d'eau et la structure cristalline de la calcite (Iwatsuki et al., 2002).

sont des conditions qui conduisent souvent à des cristaux de calcite de grande taille.

2.4.1.2 Distribution spatiale de la calcite

La plus part des études réalisées sur la bio-cimentation ont montré que la calcite se précipite de manière localisée dans les zones de contact inter-granulaire (calcite active) (DeJong et al., 2010a; Terzis et al., 2016; Tobler et al., 2012; Rong et al., 2013; Sel et al., 2015) et augmente ainsi considérablement la cohésion du sol, avec une légère évolution de la rugosité par la précipitation de cristaux de calcite sur la surface des grains (calcite passive), comme le montre les observations au MEB présentées (Figure 2.12).

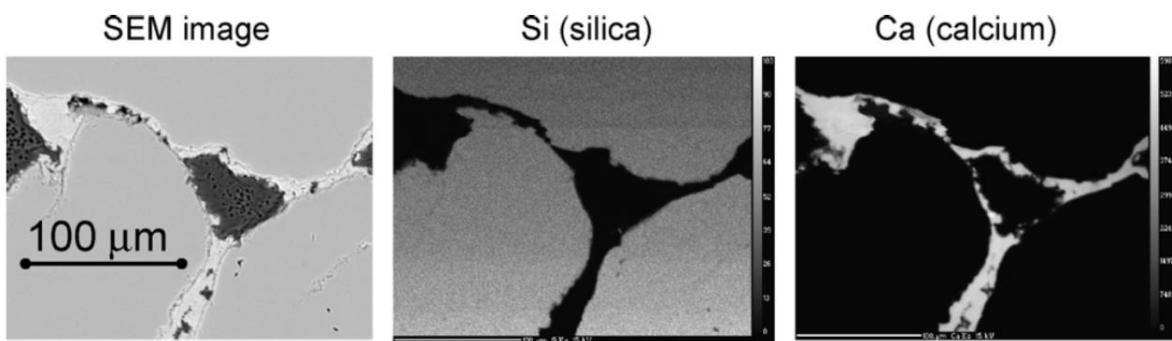


FIGURE 2.12: Configuration réelle de précipitation de calcite (DeJong et al., 2010a).

Cependant, cette localisation n'est pas parfaite. En effet, une partie de calcite peut être précipitée sur la surface des grains. Le scenario réel de precipitation de la calcite est un couplage d'une precipitation uniforme et parfaitement localisée comme montré dans les travaux de DeJong et al. (2010a) (Figure 2.13). Plusieurs facteurs peuvent influer sur la quantité de calcite active (degré de localisation de précipitation) comme la saturation, la concentration des bactéries, la température, etc. (Cheng et al., 2016, 2013).

Suite au processus de biocalcification, d'autres paramètres microstructuraux peuvent également évoluer, qui n'ont pas été abordés dans les études antérieures, et qui devraient jouer un rôle

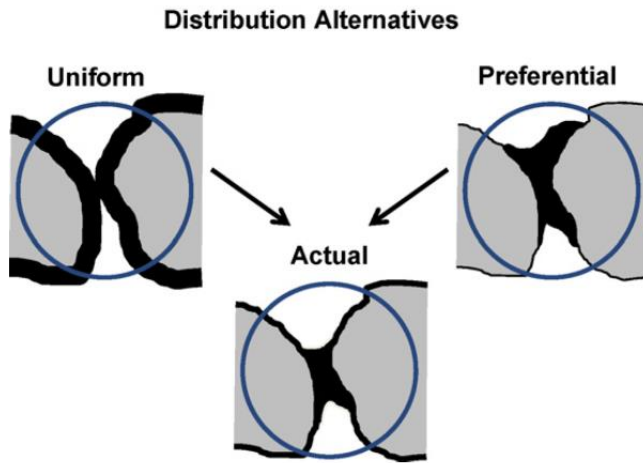


FIGURE 2.13: Configurations extrêmes (précipitation uniforme et préférentielle) de précipitation de la calcite et configuration réelle (DeJong et al., 2010a).

majeur dans l'évolution de la résistance mécanique (cohésion, angle de frottement, etc.). C'est le cas par exemple du nombre de coordination, la création ou non de nouveaux contacts, l'augmentation des surfaces de contacts ou bien de la rugosité de la surface des grains. Les observations de la microstructure réalisées jusqu'à aujourd'hui sont essentiellement des observations en 2D et très localisées (DeJong et al., 2010a; Girinsky, 2009; DeJong et al., 2010b), qui ne permettent pas à quantifier l'évolution des paramètres ci-dessus en fonction du niveau de calcification. Comme nous le verrons dans les chapitres suivants, notamment les chapitres 4 et 5, l'ensemble de ces paramètres sont accessibles par tomographie RX à haute résolution. Ces informations sont bien sur précieuses pour bien comprendre le processus de bio-cimentation, mais aussi dans les modélisations analytiques ou numériques (DEM, homogénéisation, etc.) du comportement hydromécanique des sols traités.

2.4.2 Evolution de la perméabilité

En général, la réduction de perméabilité des sols traités par des techniques traditionnelles de renforcement (ciment, chaux, etc.) est légèrement plus élevée que celle observée après biocalcification. En effet, le ciment de Portland injecté va généralement boucher des pores du sol traité, alors que la biocalcification conduira essentiellement à des précipitations à la surface des grains ou localisées au niveau des contacts. La réduction de la porosité par la précipitation de la calcite à l'intérieur des échantillons bio-cimentés contribue bien sûr à la réduction des propriétés de transferts (perméabilité et diffusivité). Différentes études ont été réalisées pour quantifier la diminution de perméabilité par le processus de bio-cimentation. Les résultats obtenus sont résumés sur la Figure 2.14 (Ivanov and Stabnikov, 2017). Ce graphe montre que la perméabilité décroît de façon exponentielle en fonction du taux de calcite. Cette décroissance est plus importante pour des taux de calcite supérieurs à 20% en masse. Dans ce cas, certains pores peuvent être entièrement colmatés. Enfin, on peut noter que la réduction de la perméabilité d'échantillons faiblement bio-cimentés (3%) ne dépasse pas 10%. Cette réduction dépasse 30% après une

calcification de 5%. En pratique, la perméabilité des sols traités par la calcification biologique dépend de plusieurs facteurs (vitesse d'injection, concentration de la solution calcifiante et des bactéries, etc.) (Al Qabany and Soga, 2013). Dans leur étude, Al Qabany and Soga (2013) ont montré que l'utilisation de fortes concentrations pour la solution calcifiante conduit à une chute de perméabilité plus importante que des faibles concentrations (Figure 2.15).

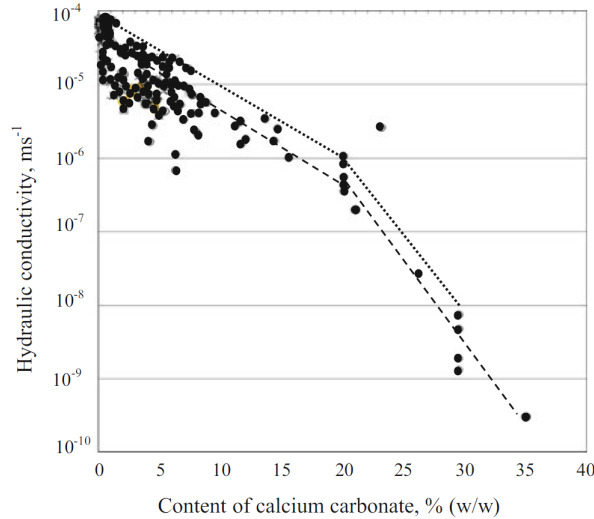


FIGURE 2.14: Evolution de la conductivité hydraulique en fonction de la teneur en CaCO_3 précipité dans différents sol (Ivanov and Stabnikov, 2017).

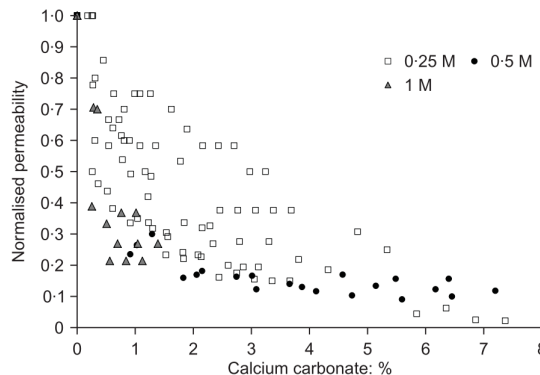


FIGURE 2.15: Réduction de la perméabilité normalisée par la perméabilité initiale pour 3 niveaux de concentration de la solution calcifiante (0.25, 0.5 et 1 M) (Al Qabany and Soga, 2013).

2.4.3 Evolution des propriétés mécaniques

Les études expérimentales antérieures ont montré que la résistance mécanique et la rigidité des sols bio-cimentés augmentent linéairement avec le degré de calcification. Cette augmentation est due à deux facteurs principaux : (1) à l'augmentation de la cohésion en « collant » les grains entre eux avec la précipitation de la calcite dans les zones de contact inter-granulaire (2) à l'augmentation du frottement avec la précipitation de la calcite sur la surface des grains. Cette augmentation

est contrôlée par plusieurs facteurs : (1) le processus du traitement (vitesse d'injection, concentration des bactéries et de la solution calcifiante) et (2) les facteurs environnementaux du sol (température, pH, salinité, type de sol, saturation, etc.).

2.4.3.1 Propriétés élastiques (très petites déformation)

La précipitation de la calcite sur et entre les grains du sol change fortement les propriétés de contact (rigidité normale et tangentielle, nombre de coordination, etc.) et la densité du sol. Ceci va naturellement induire des modifications des propriétés élastiques des sols bio-cimentés. En géotechnique, les propriétés élastiques des sols peuvent être divisées en deux grandes parties : (1) le domaine des petites déformations (entre 10^{-3} et 10^{-5} de déformation axiale) et (2) domaine de très petites déformations (inférieure à 10^{-5} de déformation axiale). Pour exploiter précisément ces deux domaines de déformations, il faut utiliser des dispositifs expérimentaux avancés comme le dispositif triaxial des petites déformations ou des capteurs piézoélectriques (mesures géophysiques) (Dano, 2001). Les mesures géophysiques sont les plus utilisées pour déterminer les propriétés élastiques des sols au laboratoire. Dans les sols cimentés, différentes études ont utilisé les mesures de vitesse de propagation d'ondes de cisaillement (V_s) et d'ondes de compression (V_p). Ces études ont montré une augmentation importante de ces deux paramètres géophysiques avec le niveau de cimentation, ce qui montre aussi l'augmentation des modules élastiques (module de cisaillement, module de Young, etc.) (Martinez et al., 2013; Montoya, 2012; Montoya and DeJong, 2015; Al Qabany et al., 2011b; Sharma et al., 2011; Gomez et al., 2016; Yang and Salvati, 2010; Dvorkin et al., 1994).

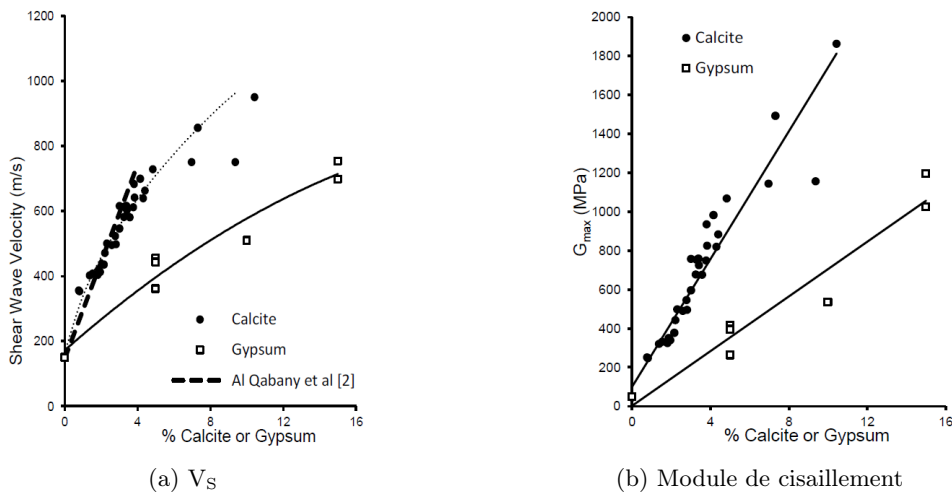


FIGURE 2.16: Vitesse de cisaillement et Module de cisaillement vs quantité de calcite dans l'échantillon de sable (Duraisamy and Airey, 2015).

Duraisamy and Airey (2015) ont réalisé des mesures de V_s à l'aide de capteurs piézo-électriques installés dans un dispositif triaxial (Figure 2.16). Cette figure confirme une augmentation de la vitesse en fonction du niveau de calcification, qui se traduit par une augmentation du module de

cisaillement (G_{max}). Pour une fraction massique de 10% de calcite, ce module de cisaillement du sable bio-cimenté est 18 fois plus important que celui du sable initial (pulvérulent).

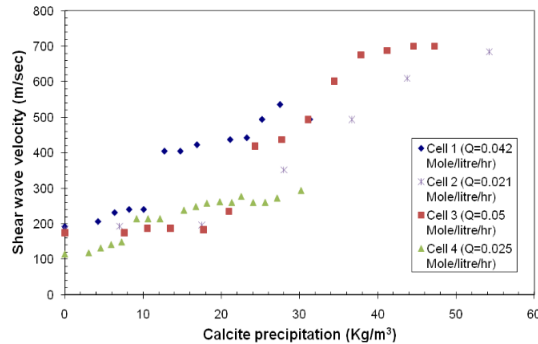


FIGURE 2.17: Evolution de la vitesse d'onde de cisaillement (V_s) en fonction de la quantité de la calcite précipitée pour différents protocole d'injection (Al Qabany et al., 2011b).

Al Qabany et al. (2011b) ont mesuré l'évolution de la vitesse d'onde de cisaillement pour plusieurs échantillons avec différents niveaux de calcification obtenus par différents protocoles de traitement (vitesse d'injection, concentrations de la solution calcifiante, fréquence d'injection) (Figure 2.17). Les résultats de cette étude montre que les paramètres du protocole ne sont pas sans effet sur les valeurs des vitesses d'onde et par conséquent sur les modules, même si il est difficile de dégager une tendance (Figure 2.17).

2.4.3.2 Résistance à la compression simple

La détermination de la résistance à la compression simple est l'un des premiers tests qui a été réalisé pour quantifier l'évolution de la résistance mécanique de sols biocalcifiés (Whiffin et al., 2007; van Paassen et al., 2010; Dekuyer et al., 2012; Cheng et al., 2013; Al Qabany and Soga, 2013; Zhao et al., 2014; Ivanov et al., 2015b). Ivanov and Stabnikov (2017) ont collecté la résistance à la compression simple de sols traités par différents processus de traitement, afin d'avoir une tendance globale de l'évolution de ce paramètre en fonction du taux de calcite (Figure 2.18).

Cette figure montre une évolution non-linéaire de la résistance à la compression en fonction du taux de calcite. Pour des taux compris entre 0 et 20% de calcite en masse, la résistance (R_C) augmente quasi-linéairement avec le taux de calcite. Une résistance à la compression de quelques centaines de kPa est obtenue pour un taux de calcite de 5% en masse. Cette évolution (dans les faibles pourcentages de calcite) est due principalement à l'évolution de la cohésion par la précipitation de la calcite entre les grains. Pour des taux de calcite supérieurs à 20%, la résistance à la compression augmente très rapidement. La résistance est de l'ordre de 12 MPa pour un taux de calcite proche de 25%. Comme pour la perméabilité (Figure 2.14), à ces niveaux de calcification, certains pores sont remplis de calcite, ce qui augmente considérablement le niveau de résistance.

Généralement, la résistance à la compression a montré dans différentes études une forte dépendance au protocole de traitement et à la microstructure (concentration de la solution calcifiante,

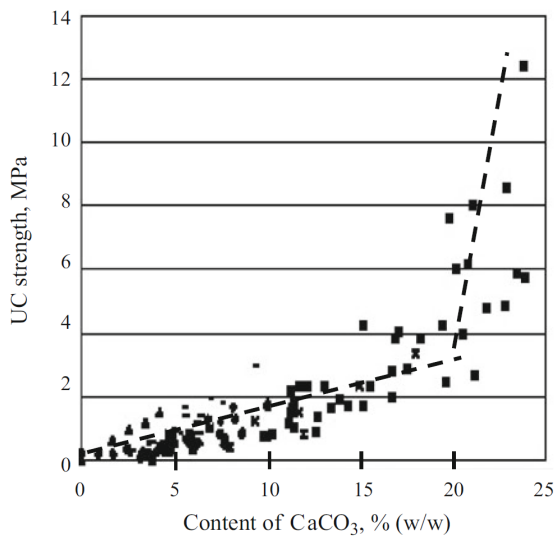


FIGURE 2.18: Résistance à la compression simple des sables bio-cimentés à différents niveaux de cimentation (Ivanov and Stabnikov, 2017).

saturation, concentration de bactéries, température, granulométrie, etc.).

Influence de la concentration de la solution calcifiante : L'influence du processus de bio-cimentation et des conditions initiales sur ce paramètre a été investiguées dans plusieurs travaux de recherche (Cheng et al., 2013; Al Qabany and Soga, 2013; Cheng et al., 2016). Dans les travaux de Al Qabany and Soga (2013) quatre niveaux de concentration de solution calcifiante ont été testés (0.1, 0.25, 0.5 et 1 M) sur l'influence de la résistance mécanique.

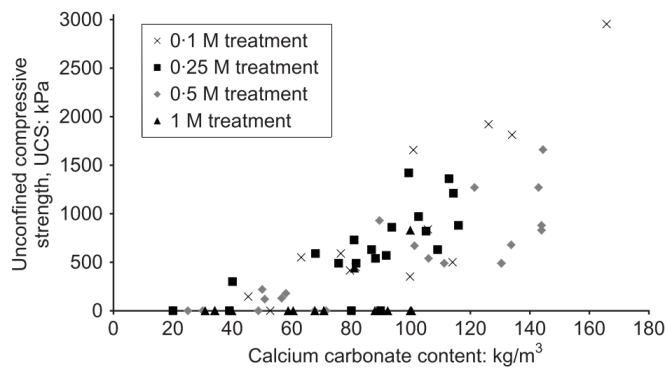


FIGURE 2.19: Résistance à la compression des sable bio-cimentés en fonction de niveau de calcification sous différents concentrations de la solution calcifiante (Al Qabany and Soga, 2013).

La Figure 2.19 montre une évolution non linéaire de ce paramètre de résistance en fonction du taux de calcite pour toutes les valeurs de concentration utilisées. Cependant, on peut remarquer que l'utilisation de concentrations faibles conduit à des résistances plus importantes. Comme déjà mentionné, ces faibles concentrations sont favorables à la formation de petits cristaux distribués de façon homogène le long de l'échantillon et sur les grains, et favorables à la création de surfaces

de contact plus grandes que celles obtenues avec de grands cristaux.

Influence de saturation initiale : Cheng et al. (2013) ont réalisé des échantillons biocalcifiés avec différents niveaux de saturation (Figure 2.20). La précipitation dans les sols non-saturés se passe généralement au niveau des ménisques d'eau formés entre les grains, qui contiennent les bactéries et la solution calcifiante (Figure 2.21). Cette localisation permet d'augmenter de façon significative la surface cohésive entre les grains de sable, en diminuant le niveau de saturation.

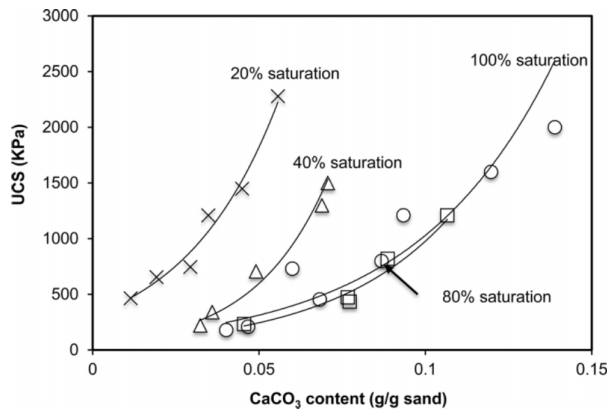


FIGURE 2.20: Résistance à la compression des sable bio-cimentés sous différents niveaux de saturation (Cheng et al., 2013).

Les essais de compression simple réalisés dans cette étude confirment cette hypothèse, où les échantillons calcifiés avec des faibles niveaux de saturation (20%) ont une résistance mécanique plus importante que les autres échantillons traités avec des niveaux de saturation plus élevés (80% à 100%).

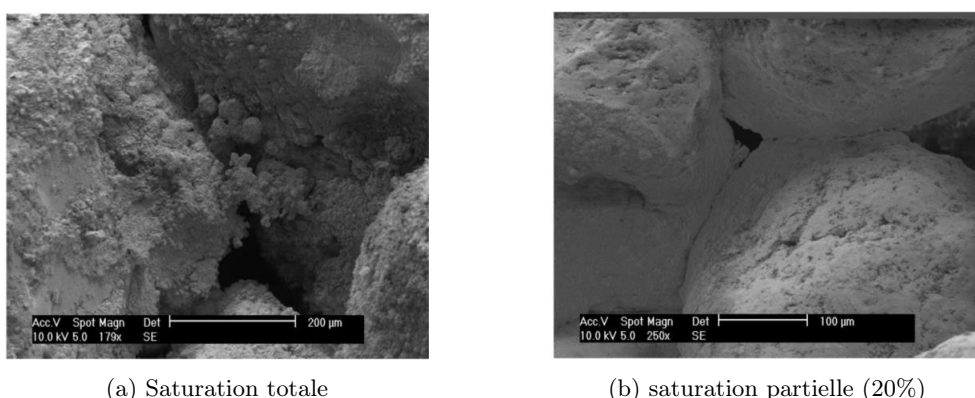


FIGURE 2.21: Observation MEB pour des échantillon de sable biocalcifié à différente degrés de saturation (Cheng et al., 2013).

Influence de l'activité enzymatique : Cheng et al. (2016) ont étudié aussi l'influence de l'activité enzymatique des bactéries sur l'efficacité mécanique du traitement sur les sables (Figure 2.22). D'après cette étude une activité enzymatique plus faible donne une efficacité mécanique plus grande. Cette efficacité de traitement est due à la formation plus lente des cristaux de cal-

cite, favorisant ainsi la formation des ponts entre les grains (Cheng et al., 2016).

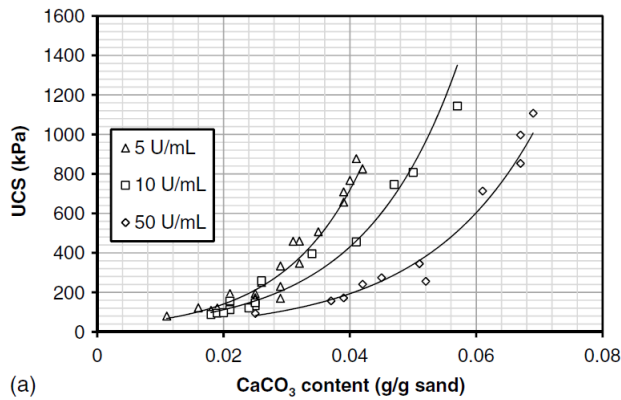


FIGURE 2.22: Influence de l'activité enzymatique sur l'amélioration de la résistance mécanique du sable (Cheng et al., 2016).

Influence de température : Dans les travaux de Cheng et al. (2016) l'influence de la température sur l'efficacité mécanique du traitement a été analysée, en variant la température pendant le processus de bio-cimentation. La Figure 2.23 montre l'évolution de la résistance à la compression pour 3 températures différentes (4, 25 et 50°C). Cette Figure montre qu'une température ambiante conduit à une meilleure efficacité mécanique du traitement.

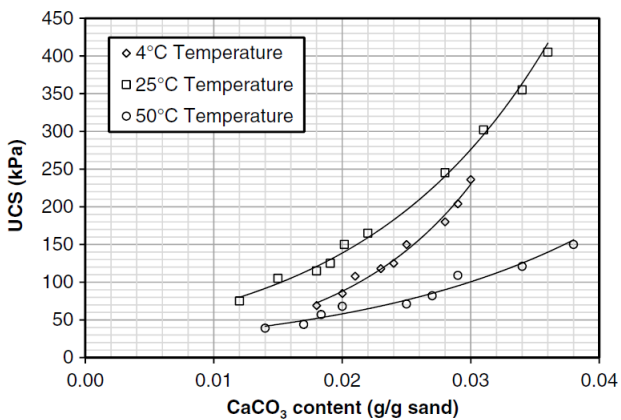


FIGURE 2.23: Evolution de la résistance à la compression en fonction de la quantité de calcite pour 3 différentes températures (Cheng et al., 2016).

Les observations MEB de ces échantillons ont montré qu'une température ambiante favorise la précipitation dans les zones de contact au contraire des autres températures. Les fortes et basses températures conduisent à la précipitation de l'aragonite ou de la vaterite dans certaines conditions de pH et de concentration de magnésium et de calcium (Al-Thawadi, 2011), ce qui peut changer la réponse mécanique et influencer l'efficacité du traitement.

Influence de la granulométrie : L'influence de la granulométrie du sol a été étudiée aussi dans les travaux de Cheng et al. (2016), par l'application de la même procédure de bio-cimentation pour différentes granulométries de sable (un sable fin avec une granulométrie uniforme, un sable grossier avec une granulométrie uniforme, un sable avec une granulométrie étalée) (Figure 2.24). Cette étude a montré que le sable grossier avec une granulométrie serrée a la plus faible résistance mécanique. Le sable fin avec la granulométrie serrée a présenté la plus grande efficacité mécanique par rapport aux autres sables. Dans ce cas, une faible quantité de calcite semble suffisante pour accroître le nombre de coordination et les surfaces de contact, et augmenter la cohésion globale du sable traité.

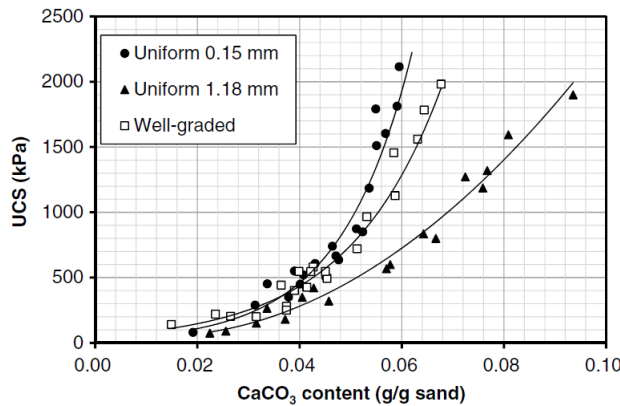


FIGURE 2.24: Résistance à la compression en fonction de la quantité de calcite précipitée pour 3 sables de granulométrie différentes (Cheng et al., 2016).

2.4.3.3 Résistance au cisaillement et déformabilité mesurées à partir d'essais triaxiaux

Les études réalisées sur le comportement triaxial ont montré un comportement très similaire aux sols cimentés par un produit chimique (ciment, chaux, etc.) (Abdulla and Kiousis, 1997; Schnaid et al., 2001; Wang and Leung, 2008a; Ajorloo et al., 2012; Li et al., 2015; Duraisamy, 2016; Montoya and DeJong, 2015; Thomas O'Donnell and Kavazanjian Jr, 2015; Feng and Montoya, 2015; Lin et al., 2015). Ces essais ont mis en évidence une augmentation de la rigidité, de la résistance au cisaillement maximale et ultime, une augmentation de la dilatance des sols initialement denses, et un changement de comportement volumique de la contractance vers la dilatance pour les sols initialement lâches.

Résistance maximale : Feng and Montoya (2015) ont réalisé des essais triaxiaux drainés sous différentes pressions de confinement (100, 200 et 400 kPa) sur un sable lâche traité de 0 à 5.3% de calcite en masse. Les résultats de ces essais ont été comparés avec ceux obtenus sur le même sable dans un état initial dense. La résistance au cisaillement évolue de façon monotone avec la quantité de calcite précipitée dans chaque échantillon de sable comme le montre les Figures 2.25a et 2.25b (la résistance du sable fortement cimenté (4,3%) est 4 fois plus grande que la résistance

du sable non-traité), ce qui confirme les résultats trouvés lors des essais triaxiaux non-drainés sur le même sable par Montoya and DeJong (2015) (Figure 2.26a).

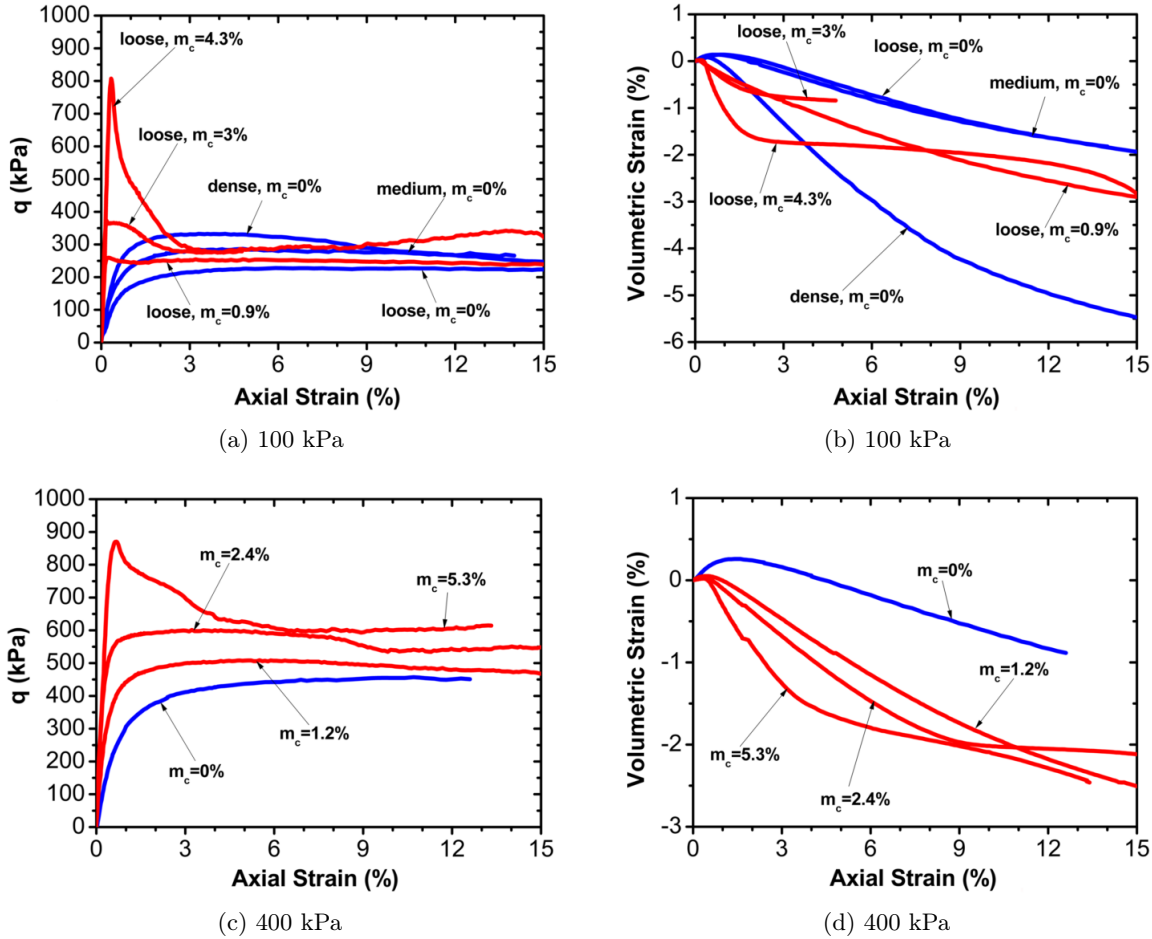
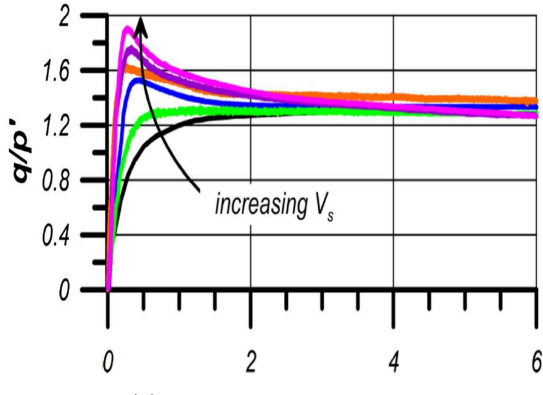


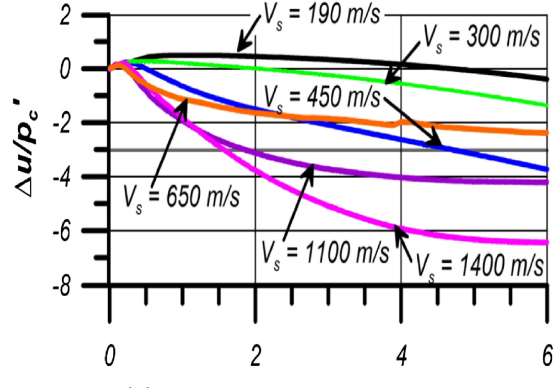
FIGURE 2.25: Comportement triaxial (résistance mécanique et comportement volumique) d'un sable avec différents niveaux de cimentation et sous différentes pressions de confinement (Feng and Montoya, 2015).

Cette évolution de la résistance est due principalement à l'évolution de la cohésion du sable traité avec la précipitation de calcite entre les grains. Dans le domaine des petites déformations, l'échantillon fortement cimenté présente une raideur plus importante par rapport aux échantillons moyennement bio-cimentés et non traités. L'augmentation de cette raideur est due à la présence de ponts de calcite intacts qui forment un réseau de forces actives à l'intérieur de l'échantillon. Près du pic, le comportement volumétrique change de direction, passant de la contractance à la dilatance, en raison de la forte densité et de la grande cohésion de l'échantillon cimenté.

Résistance ultime : Après le pic, la dilatance augmente de façon monotone avec la quantité de calcite. La rupture fragile des ponts de calcite provoque une baisse rapide de la résistance, qui doit être compensée par la dilatation associée dans les échantillons cimentés. Pour un petit incrément de déformation après le pic (supérieure à 3% de déformation axiale), le sable atteint son état de résistance ultime, légèrement supérieur à celui du sable non traité (Figure 2.25).



(a) Contrainte-déformation



(b) Comportement volumique

FIGURE 2.26: Comportement triaxial non-drainé d'un sable bio-cimenté avec différents niveaux de cimentation (Montoya and DeJong, 2015).

Ce phénomène a été mis en évidence dans d'autres études (Montoya and DeJong, 2015; Lin et al., 2015). Cette légère différence de résistance peut être interprétée par deux mécanismes différents : une rugosité supplémentaire générée par la calcite précipitée sur la surface des grains et l'existence d'agglomérats formés par des grains qui restent cimentés après rupture (empêchant le flambement des chaînes de force à l'intérieur de la bande de cisaillement et entraînant une résistance supplémentaire). Ce phénomène a été montré dans les travaux de Wang and Leung (2008a) via des modélisations par éléments discrets en 2D d'un sable cimenté. Le comportement volumétrique montre une stabilisation à des valeurs supérieures à celles du sable lâche non traité, mais qui restent toujours inférieures à celles des échantillons denses non-traités. Le comportement des sables cimentés présenté dans cette étude montre aussi une dépendance au confinement. Feng and Montoya (2015) ont montré un fort adoucissement qui diminue pour les faibles niveaux de calcification et augmente avec la pression de confinement. L'augmentation de la dilatance dans les échantillons cimentés a été traduit par une augmentation à la pression négative intersticielle dans des essais non-drainés réalisés sur un sable similaire dans la même gamme de cimentation (Montoya and DeJong, 2015) (Figure 2.26b)

2.4.3.4 Paramètres de résistance

L'augmentation de la résistance au cisaillement dans les sols est intimement liée à la cohésion et l'angle de frottement. Différentes travaux de recherche ont étudié l'évolution de ces paramètres de résistance (cohésion et angle de frottement) (Terzis et al., 2016; Montoya and DeJong, 2015; Feng and Montoya, 2015; Cheng et al., 2013; Montoya, 2012; Lin et al., 2015; Cui et al., 2017). Trois tendances ont été observées dans la littérature qui illustrent l'augmentation de la résistance mécanique des sols bio-cimentés : (1) une augmentation de l'angle de frottement maximal et résiduel (Montoya and DeJong, 2015; Feng and Montoya, 2015), (2) une augmentation de l'angle de frottement et de la cohésion (Cheng et al., 2013; Terzis et al., 2016; Cui et al., 2017) et (3) une augmentation uniquement de la cohésion (Lin et al., 2015). Le Tableau 2.1 résume les résultats obtenus dans ces différentes études. Notons que la plupart de ces études n'ont pas exploité la

résistance résiduelle des sols bio-cimentés. Une augmentation de cette résistance a été trouvée dans les travaux de Lin et al. (2015). Cette augmentation est attribuée à une augmentation de l'angle de frottement par Feng and Montoya (2015) et de la cohésion résiduelle par Lin et al. (2015).

Tableau 2.1: Récapitulatif de l'évolution des paramètres de résistance des sables bio-cimentés mis en évidence dans la littérature.

Sable testé		m_c (%)	S_r (%)	C_{max} (kPa)	ϕ_{max}	Références
D_{50} (mm)	C_U					
0.22	1.4	0 - 5.3	100	0 - 59	33 - 41	Feng and Montoya (2015)
0.19	2.1	0 - 8.5		0 - 253	38 - 44	Terzis et al. (2016)
0.22	1.4	0 - 5,.3		/	33 - 43.7	Montoya and DeJong (2015)
0.71	1.17	0 - 1.6		0 - 41	32 - 31	Lin et al. (2015)
0.33	1.43	0 - 2,.6		0 - 58	35 - 32	
0.52	5.08	0 - 12		0 - 450	35.7 - 45	Cui et al. (2017)
0.21	1.5	0 - 9		0 - 140	25 - 27	Cheng et al. (2013)
0.7	1.3	0 - 10		0 - 80	25 - 34	
0.21	1.5	0 - 7.4		0 - 250	25 - 29.5	
0.7	1.3	0 - 7.4		0 - 80	25 - 31	
0.21	1.,5	0 - 4	30	0 - 275	25 - 30.5	
0.7	1.3	0 - 10.3		0 - 115	25 - 40	

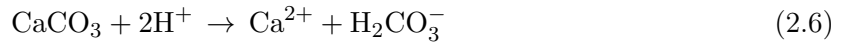
A ce jour, l'influence de la procédure d'injection et des facteurs environnementaux sur les paramètres de résistance n'est pas très claire. En résumé, les valeurs de résistance trouvées dans la littérature (cohésion et angle de frottement au pic) montrent des différences considérables, ces différences sont dues d'une part au processus de traitement qui est différent d'une étude à l'autre, et au sable utilisé qui présente des granulométries différentes. D'après ce tableau, quel que soit la procédure de traitement et les concentrations utilisées, un sable d'une granulométrie étalée conduit à des valeurs maximales de cohésion et minimale d'angle de frottement (Cui et al., 2017; Cheng et al., 2013). Par contre, un sable grossier avec granulométrie uniforme a conduit à des valeurs minimales de cohesion et maximale d'angle de frottement (Cheng et al., 2013). Par ailleurs, un sable fin avec une granulométrie uniforme présente un comportement intermédiaire en terme de cohésion et d'angle de frottement.

2.5 Durabilité de la bio-cimentation

2.5.1 Durabilité chimique

La stabilité chimique de la calcite est fortement affectée par le niveau de pH, la température, l'activité ionique, la présence de CO_2 , ce qui constitue un vrai challenge pour la technique de bio-

cimentation en terme de fiabilité à long terme. Il est bien connu que les eaux pluviales peuvent avoir un pH acide en raison de la grande quantité de gaz combustibles fossiles qui sont libérés dans l'atmosphère. Cela dépend de l'ampleur de l'industrialisation de la zone et de la densité de la population à proximité. De plus, l'activité de certaines espèces vivantes et microorganismes peut produire des produits acides qui peuvent atteindre le sol bio-cimenté par l'infiltration de l'eau de pluie. La réaction chimique de dégradation est donnée dans l'équation 2.6 :



L'effet du pH de la solution sur la solubilité du carbonate de calcium a été étudié dans les travaux de Coto et al. (2012), où la dissolution de la calcite (caractérisée par la masse de Ca^{2+}) semble augmenter avec la diminution de pH et ce pour une température constante (25°C) et une pression constante (100 kPa) (Figure 2.27).

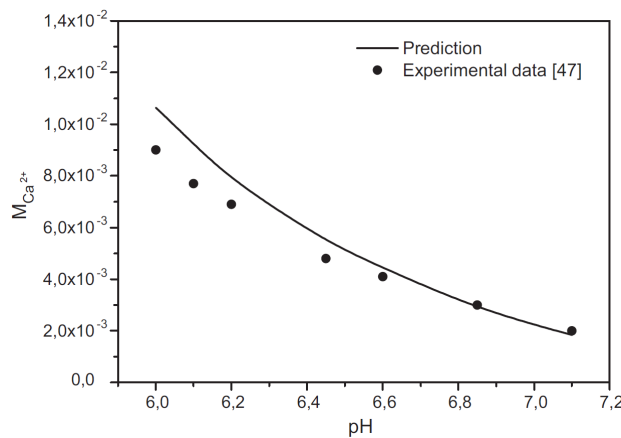


FIGURE 2.27: Influence du pH sur la solubilité de CaCO_3 à une pression d'air (100 kPa) et à une température ambiante de 25°C (Coto et al., 2012).

La saturation partielle de CO_2 a un effet important à cause de la relation directe entre ce facteur et le pH de la solution, ce qui augmente la solubilité du carbonate de calcium dans le milieu. L'effet couplé de la température et de la pression sur la dissolution du carbonate de calcium a été étudié par Coto et al. (2012) qui montrent que la dissolution diminue avec la température et augmente avec la pression (Figure 2.28).

La résistance mécanique des sols biocalcifiés repose directement sur la calcite qui lie les particules et crée une cohésion. Il est donc nécessaire d'évaluer la durabilité chimique de la calcite. Cheng et al. (2013) ont testé la dissolution de la calcite par le rinçage (de haut vers le bas) de colonnes de sable bio-cimenté par une eau à $\text{pH} = 3,5$ similaire à une eau de pluie très acide. Ces colonnes ont été divisées en deux (partie haute et partie basse). Ces parties ont été testées mécaniquement par des essais de compression simple pour évaluer la perte de résistance associée à la dissolution de la calcite. Le volume total de la solution acide de rinçage des colonnes de sable bio-cimenté était de 12 L, ce qui correspond à 5 ans de précipitations (1000 mm/an). La résistance de la

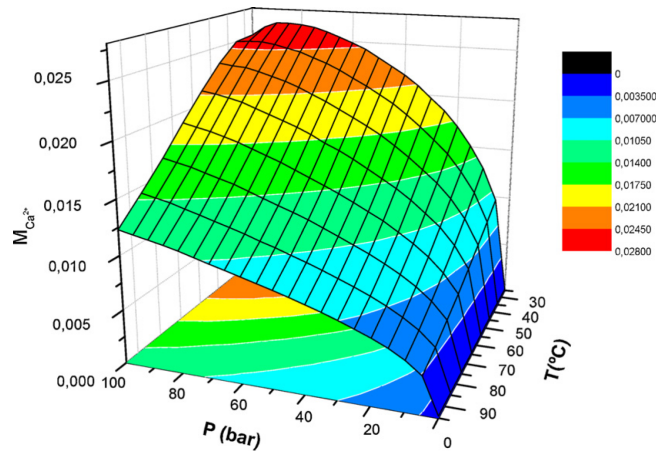


FIGURE 2.28: Influence simultanée de la pression et de la température sur la solubilité du CaCO_3 (Coto et al., 2012).

partie supérieure de la colonne de sable a diminué d'environ 40%, comme le montre la Figure 2.29. Cependant, les valeurs de R_C des échantillons exposés à cette solution agressive montrent qu'aucun dommage évident ne s'est produit dans la partie inférieure de la colonne de sable .

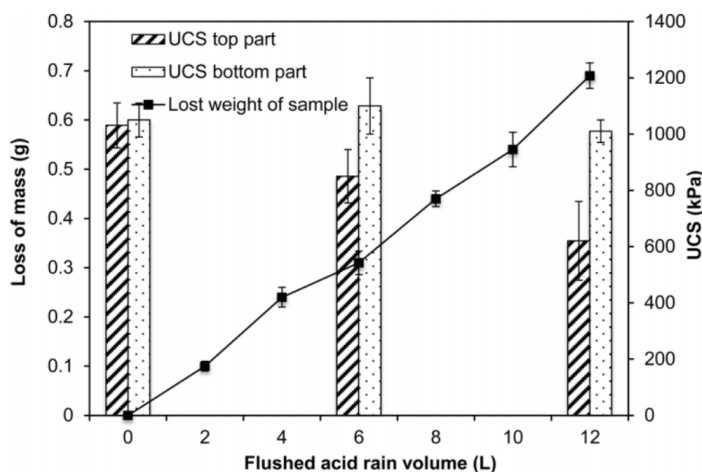


FIGURE 2.29: Résistance à la compression simple (R_C) et masse de calcite dissoute vs le volume de la solution injectée (Cheng et al., 2013).

Dura (2013) a testé des échantillons de sable biocalcifié (entre 12 et 16% de calcite) avec une solution qui contient des composants chimiques similaires à ceux présents dans des pluies acides (pH entre 5 et 6). Les échantillons bio-cimentés ont été rincés par 260 volumes de pore (55L) de solution agressive pendant 10 jours. Cette opération de rinçage a diminué le taux initial de calcite total à l'intérieur de l'échantillon de l'ordre de 4% seulement. Des essais de compression simple sur ces échantillons ont montré une petite diminution de la résistance à la compression simple par la dissolution de la calcite. Cette étude a montré qu'avec un flux de 1m/jour des eaux souterraines acides du même type, la dissolution de la calcite pour une durée de 50 ans ne dépasse pas le 0.01% de la calcite total dans l'échantillon.

2.5.2 Durabilité mécanique

La brutalité de la rupture des ponts de calcite et le comportement global du sable biocalcifié observés dans les études présentées dans les paragraphes précédents a poussé les chercheurs vers l'étude de la durabilité mécanique sous chargement cyclique naturel (les cycles séchage/humidification, gel/dégel ou/et des chargements cycliques mécaniques comme les activités sismiques, le passage des engins sur les routes, le changement de niveau d'eau dans les barrages, etc.), qui peut entraîner un endommagement mécanique de la cohésion formée par les ponts de calcite. Les sols bio-cimentés sont généralement vulnérables à de tels types de chargements, bien que le niveau des dégâts dépend beaucoup de l'amplitude du chargement et la durée de son application.

Chargement triaxial cyclique : La durabilité mécanique du sable biocalcifié a été testée par des chargements triaxiaux cycliques non-drainés dans les travaux de Dura (2013). Dans cette étude une fréquence de l'ordre de 0.2 Hz a été appliquée pendant 72h (52000 cycles) avec une amplitude de chargement variable entre 100 kPa à 1400 kPa. La Figure 2.30 montre pour des chargements faibles (< 100 kPa) que le comportement est presque linéaire. Au-delà de cette amplitude de chargement, la courbe présente une certaine non-linéarité, ce qui peut être dû à la formation de microfissures à l'intérieur des échantillons. La rupture de l'échantillon est soudaine et fragile après un très grand nombre de cycles et sous un chargement très élevé, cela signifie qu'une fissure globale apparaît et que l'échantillon n'est plus résistant.

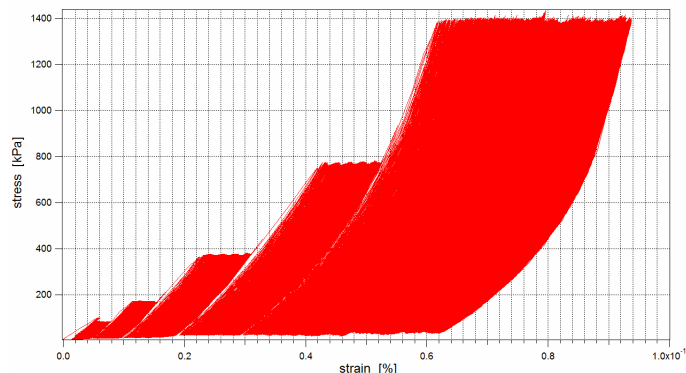


FIGURE 2.30: Chargement cyclique triaxial sur un sable bio-cimenté (Dura, 2013).

Dans la même étude, Dura (2013) a analysé l'évolution du module de cisaillement en fonction de la déformation sous une faible amplitude de chargement (100 kPa), ce qui représente un chargement ordinaire en génie civil (ex : passage de camions). Les résultats de la Figure 2.31 montrent que le module de cisaillement est sensible au chargement cyclique, même dans une faible gamme de chargements. Évidemment, les microfissures se développent dans l'échantillon en détachant la calcite des grains de sable. Il est possible que la dispersion des fissures soit presque uniforme dans tout l'échantillon à cause de la dégradation quasi-linéaire du module de cisaillement. Même si la valeur absolue de la dégradation n'est pas très élevée, elle va sûrement continuer à augmenter pour un plus grand nombre de cycles. Si on considère la durée de vie d'un ouvrage (100 ans ou

plus) et aussi le fait que les camions ou les trains provoquent des vibrations similaires sur une couche de forme bio-cimentée, nous pouvons conclure que la dégradation avec le temps n'est pas un fait trivial.

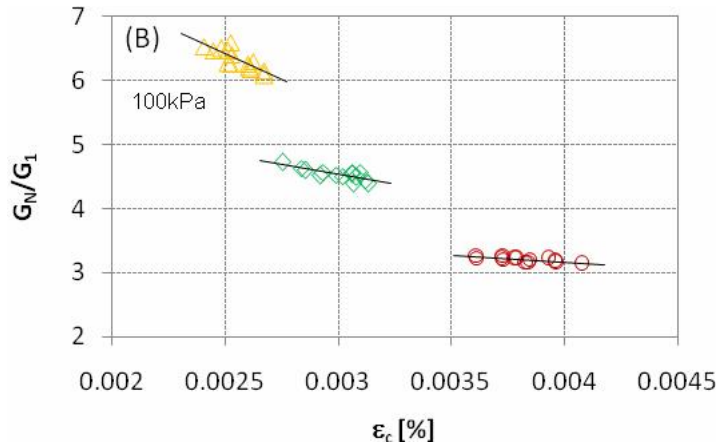


FIGURE 2.31: Dégradation de module de cisaillement de différents échantillons sur un l'amplitude de 100 kPa pour les premiers 700 cycles (Dura, 2013).

Chargement cyclique de gel/dégel : Récemment Cheng et al. (2016) a étudié la durabilité mécanique de 3 types de sable bio-cimenté (sable fin avec une granulométrie serré, sable grossier avec une granulométrie serré et sable avec une granulométrie étalée) après différents cycles (0, 4 et 10 cycles) de gel-dégel (-14 à 25°C).

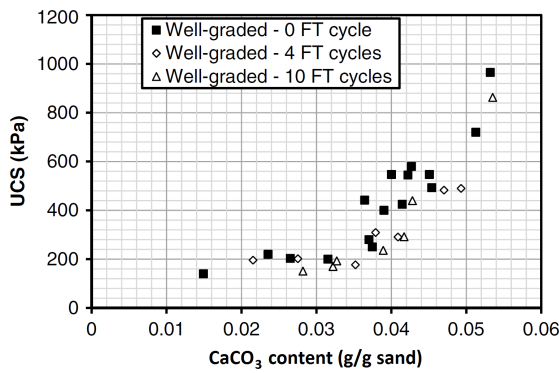


FIGURE 2.32: Dégradation de la résistance à la compression simple d'un sable d'une granulométrie étalée subi à des cycles gel-dégel Cheng et al. (2016).

Ces essais ont été suivis par des essais de résistance à la compression simple (R_C) pour pouvoir explorer la dégradation mécanique due aux cycles de gel-dégel. Généralement les sols qui ont une grande perméabilité et une grande porosité sont les plus résistants aux cycles de gel-dégel. Cependant, le sable de granulométrie étalée et qui contient une faible porosité par rapport aux autres sables a montré une très faible réduction de la résistance mécanique (Figure 2.32). Par contre, dans cette étude, les sables grossiers et fins qui ont des granulométries serrées ont

montré une forte dégradation de la résistance à la compression par rapport à des échantillons intacts (Figure 2.33). Ce phénomène est dû à la résistance des ponts de calcite elle-même dans l'échantillon. En effet, un échantillon de sable d'une granulométrie étalée contient un nombre important de contacts inter-granulaires. Ce nombre élevé de contacts inter-granulaires peut réduire la contrainte à la traction appliquée par l'eau gelée au niveau des contacts.

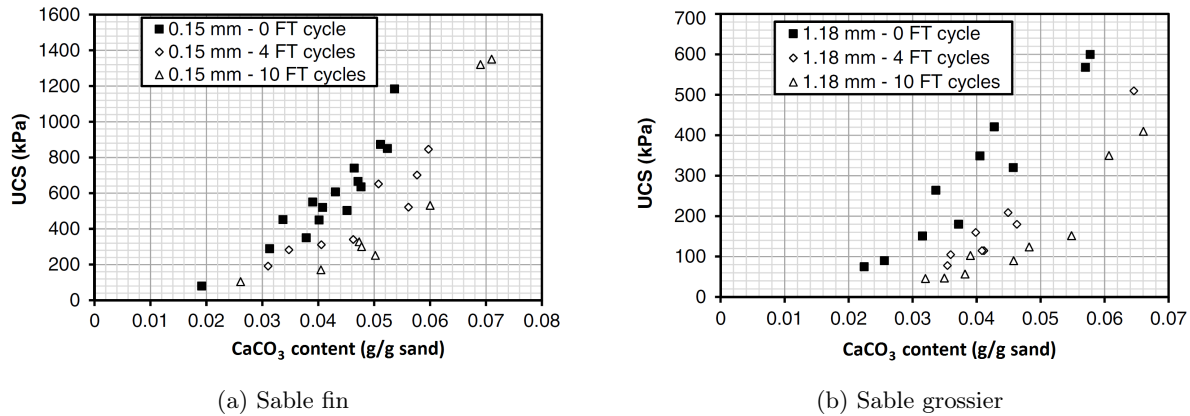


FIGURE 2.33: Dégradation de la résistance à la compression simple des sable d'une granulométrie uniforme subis à des cycles gel-dégel Cheng et al. (2016).

2.6 Stratégie de traitement

Trois stratégies de traitement ont été utilisées dans les études au laboratoire du processus de bio-cimentation (méthode d'injection, méthode de percolation de surface et méthode de pré-mixing). Ces méthodes sont inspirées des méthodes classiques de traitement des sols comme (1) l'injection de coulis, qui consiste à injecter sous une forte pression un mélange visqueux d'un liant hydraulique (Figure 2.34a). (2) le soil-mixing qui consiste à mélanger mécaniquement les sols à traiter par des liants hydrauliques (ciment, chaux, etc.) (Figure 2.34b).



FIGURE 2.34: a) renforcement de sol par l'injection de coulis de ciment, b) réalisation d'une paroi étanche (Canal de Lens - Lille - France).

2.6.1 Méthode d'injection

Cette méthode d'injection est la plus utilisée dans les études antérieures en bio-cimentation, étant donné qu'elle est semblable à la technique des sols injectés, qui est caractérisée par la facilité de contrôle in-situ (contrôle de la vitesse d'injection, direction). En outre, cette méthode est recommandée pour le renforcement des anciennes structures (barrages et digues en terre), qui ne sont pas prêtes pour des techniques intrusives. Une stratégie d'injection a été utilisée dans les premières études sur la bio-cimentation qui consiste à mélanger la solution bactérienne avec la solution calcifiante avant l'injection. Cette méthode a montré une cristallisation de la calcite et la flocculation des bactéries avant injection, ce qui provoque un colmatage important au voisinage du point d'injection (Whiffin et al., 2007). Cette méthode peut être utilisée pour le renforcement des surfaces (ex : couche de forme des chaussées), car elle présente un coût moins élevé par rapport aux autres stratégies d'injection (nombre d'injections minimal). Une méthode d'injection déphasée (solution bactérienne puis solution calcifiante) a été proposée pour éviter les problèmes ci-dessus. Cependant, cette méthode a aussi montré un problème d'uniformité du traitement ; la calcite est distribuée de manière hétérogène dans les sols traités. Cette hétérogénéité du traitement est essentiellement due à (1) la répartition inégale des bactéries en raison de leurs caractéristiques de transport et d'adhérence dans le squelette solide, (2) à la réaction géochimique de la précipitation de la calcite. En effet, la distribution des bactéries dans le sol lors d'un processus d'injection est directement contrôlée par le phénomène d'infiltration, qui peut être influencé par plusieurs facteurs, dont le régime d'écoulement, les caractéristiques de la cellule bactérienne, la distribution granulométrique du sol et sa minéralogie (Harkes et al., 2010). Cette distribution est linéaire, avec une concentration maximale près du point d'injection et minimale proche de la sortie (Ginn et al., 2001; Tobler et al., 2014). Comme mentionné précédemment, l'hétérogénéité de la précipitation de la calcite avec l'opération d'injection n'est pas liée uniquement à la distribution hétérogène des bactéries, mais aussi à la réaction biochimique entre la solution calcifiante (source d'urée et de calcium) et la bactérie. Au cours de l'injection de la solution calcifiante, les bactéries peuvent consommer tous les réactifs (urée et le chlorure de calcium) dans les premiers centimètres près du point d'injection, et ce qui aboutit à une localisation de la précipitation de la calcite (Mujah et al., 2017).

2.6.2 Pré-mixing

L'introduction des bactéries et de la solution calcifiante dans les sols avec cette méthode est réalisée par le malaxage mécanique des deux solutions et le sol à traiter. Cette méthode donne des traitements plus homogènes par rapport à la méthode d'injection (Zhao et al., 2014). Par contre, le malaxage mécanique peut endommager les cellules bactériennes et diminuer l'efficacité du traitement. En outre, cette méthode n'est pas favorable pour plusieurs types de structures notamment les anciennes structures (barrage et digue, fondations des bâtiments, etc.), ou le malaxage mécanique peut provoquer des perturbations locales et des instabilités dans la structure (Mujah et al., 2017).

2.6.3 Percolation de surface

Cette méthode de renforcement consiste à pulvériser la solution bactérienne et la solution calcifiante qui contient des réactifs sur la surface des sols. Les solutions bactérienne et calcifiante vont se diffuser sous l'effet de la gravité dans le sol (Mujah et al., 2017). L'avantage de cette méthode est l'énergie minimale nécessaire pour la réalisation de l'opération de bio-cimentation par rapport aux autres méthodes présentées précédemment. Cette méthode ne permet pas de renforcer des sols dans de grandes profondeurs, notamment les sols dont les faibles perméabilités peuvent gêner la diffusion des bactéries et de la solution calcifiante plus profondément. Cheng and Cord-Ruwisch (2014) ont montré que cette stratégie de traitement a permis de calcifier avec succès, de manière quasi-uniforme, une couche de sable grossier de 2 m. Par contre, cette méthode présente des limitations pour des sables fins (< 3 mm). La précipitation de la calcite ne dépasse pas 1 m avec une grande hétérogénéité (colmatage à la surface). Cette méthode n'est pas adaptée pour les grands ouvrages de dimensions importantes (épaisseurs) et qui sont constitués par des sols fins comme les barrages en terre. Par contre, cette stratégie de traitement peut être une solution très efficace pour le renforcement de la couche de forme dans les projets routiers, pour la suppression de poussières et la stabilisation des sols contre l'érosion externe (Cheng et al., 2016).

2.7 Conclusion

Cette synthèse bibliographique sur la bio-cimentation a montré que l'efficacité de la technique sur l'augmentation et l'amélioration des caractéristiques mécaniques des sols, ce qui a rend prometteuse pour lutter contre des problèmes géotechniques traditionnels, comme l'érosion interne dans les diques et les barrages en terre ou bien la liquéfaction des sols lâches. Cette étude montre aussi que l'efficacité du traitement, d'un point de vue mécanique, dépend de nombreux paramètres à savoir :

- Les propriétés du sol (granulométrie, composition, niveau de saturation, etc.) et les conditions environnementales (température, pH, salinité, etc.).
- Les bactéries/microorganismes (type, concentration).
- La solution calcifiante (composition, concentration).

L'ensemble de ces paramètres vont jouer un rôle important d'une part dans le phénomène de précipitation même (morphologie et cristallographie de la calcite), et d'autre part dans les modifications microstructurales (répartition de la calcite) des sols traités, qui sont-elles-même responsables des modifications des propriétés physiques (perméabilité, diffusivité, etc.) et mécaniques (modules élastiques, paramètres de résistance : cohésion et angle de frottement, dilatance, etc.) observées à l'échelle macroscopique (Figure 2.35).

A ce jour, les liens entre les propriétés microstructurales des sols bio-cimentés et leurs propriétés macroscopiques sont très mal connus. En effet, comme nous avons pu le voir à travers cette

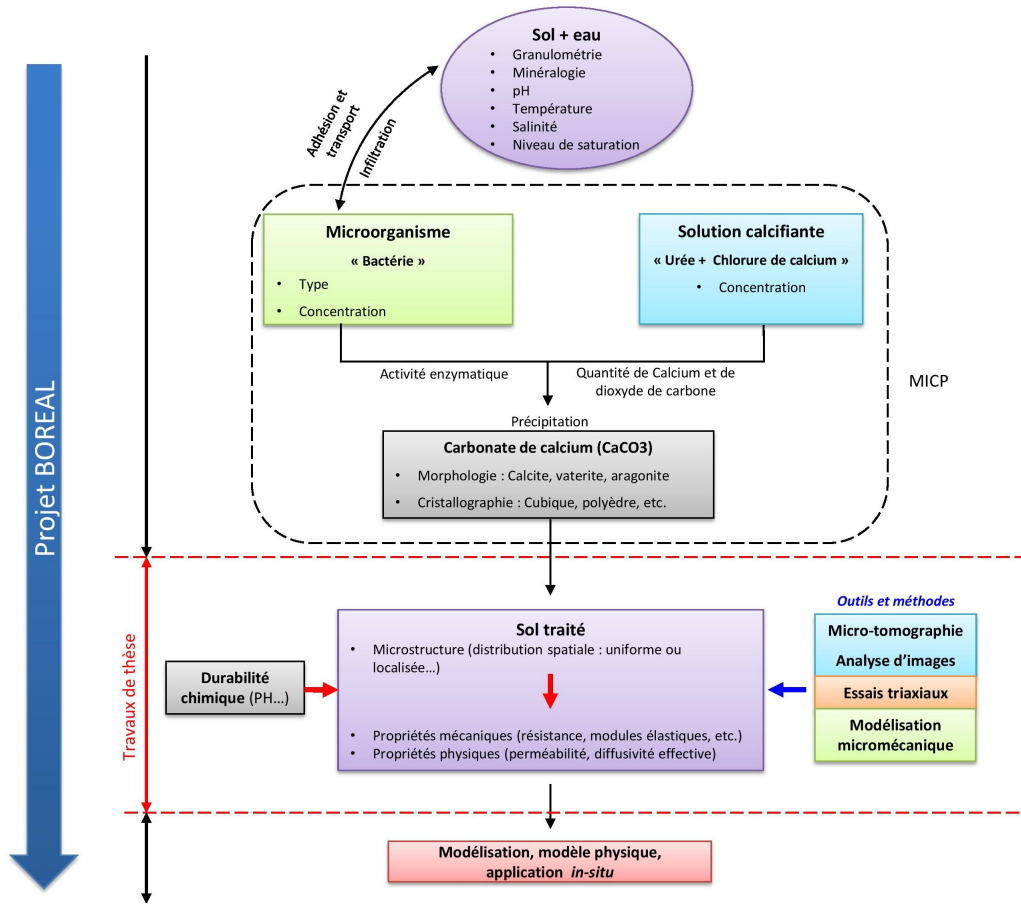


FIGURE 2.35: Schéma de des travaux de thèse et sa position dans le projet BOREAL.

étude bibliographie, la microstructure des sols bio-cimentés a essentiellement été observée par microscopie électronique à balayage. Même si ces images (2D) ont permis de mieux comprendre le processus de biocalcification, elles ne sont malheureusement pas suffisantes notamment en ce qui concerne la répartition de la calcite au sein du réseau poral et pour en déduire l'évolution de paramètres microstructuraux. Ces paramètres microstructuraux pertinents permettant d'évaluer (Approche micromécanique ou méthode d'homogénéisation numériques et/ou analytiques) les propriétés physiques et mécaniques macroscopiques des sols bio-cimentés. Par ailleurs, si il est intéressant d'étudier ces liens lors du processus, il est aussi important de connaître leur évolution au cours du temps, notamment lorsque le sol traité est soumis à un écoulement (durabilité chimique) comme c'est le cas dans les applications qui nous intéressent (renforcement des ouvrages hydrauliques en charge “circulation continue d'eau”).

Le principal objectif de cette thèse, qui s'inscrit dans le cadre du projet BOREAL présenté en introduction, est de lever ces verrous (Figure 2.35). Pour cela une étude expérimentale à différentes échelles a été menée :

- à l'échelle macroscopique, notamment par la réalisation d'essais triaxiaux associés à des mesures de perméabilité sur des échantillons avec différents niveaux de calcification. Le

dispositif triaxial utilisé a aussi été modifié/complété afin d'étudier la durabilité chimique des échantillons.

- A l'échelle microscopique, par la réalisation d'images 3D par tomographie RX à haute résolution d'échantillons de sol biocalcifié. Comme nous le verrons dans les chapitres 3, 4, 5 et 6, après différents traitements, ces images ont permis pour la première fois à notre connaissance de quantifier précisément l'évolution des propriétés microstructurales moyennes (fraction volume de calcite, surface spécifique totale ou de calcite, etc.) et des propriétés associés aux contacts (surface de contact, nombre de coordination, types de contact, etc.).

Les informations microstructurales obtenues à partir des images 3D ont ensuite été utilisées dans des modèles analytiques et numériques (homogénéisation) pour prédire les propriétés physiques (perméabilité et diffusivité) et mécaniques (cohésion, modules élastiques) des sols traités. Enfin, une étude expérimentale de la durabilité chimique a été réalisée pour le but d'explorer la dégradation de la résistance mécanique des échantillons bio-cimentés dégradés chimiquement. Cette étude a été réalisée en couplant des observations MEB et micro-tomographiques pour suivre l'évolution de la microstructure de façon qualitative et quantitative, et des essais triaxiaux instrumentés.

CHAPITRE 3

EVOLUTION OF STRENGTH PROPERTIES OF BIOCEMENTED SAND WITH THE CEMENTATION LEVEL

Sommaire

3.1	Introduction	42
3.2	Material and Method	45
3.2.1	Sample preparation and treatment	45
3.2.2	Experimental procedure	47
3.2.3	Calcite measurements and microstructural observations	48
3.2.4	Permeability measurement	49
3.3	Results and discussion	50
3.3.1	Physical properties	50
3.3.1.1	Calcite amount	50
3.3.1.2	Permeability	50
3.3.2	Mechanical properties	52
3.3.2.1	Biocemented sand behavior	52
3.3.2.2	Evolution of the mechanical properties of the biocemented sand	53
3.3.3	SEM and X-ray observations	56
3.4	Conclusion	58

The content of this chapter is submitted to Canadian Geotechnical Journal.

Abstract

An experimental study has been performed to investigate the biocementation effects on the mechanical strength of treated sand (Fontainebleau sand). The biocementation process has been performed in long plastic columns for high and medium cementation levels and directly in the triaxial cell for low cementation level. High concentration of calcification solution (Calcium Chloride and urea) of 1.4 mol/l has been used in this cementation process with 1 OD₆₀₀ of *Sporosarcina pasteurii* bacteria. Triaxial drained tests with different confining pressures have been performed on the biocemented sand samples presenting a large range of cementation level (from 0 to 11.9 % in mass of calcite). The evolution of the physical properties (permeability and elastic modulus) and the strength parameters (cohesion, maximum and residual friction angles and dilatancy angle) has been determined for the first time for a large range of biocementation levels. The experimental results point out that the strength of the biocemented sand is strongly improved compared to that of initial untreated material. Exponential evolutions of the cohesion and dilatancy angle and quasilinear evolution of the friction angles (maximum and residual) have been observed. Microscopic and micro-tomographic observations of highly cemented subsample show that the calcite has precipitated quasi-uniformly in the porous media with large crystal size (5-15 µm) and that most of these crystals show perfect morphology (polyhedral shapes), which is essentially related to the concentration of the calcification solution used in the biocementation procedure.

3.1 Introduction

In the 20th century, interactions between geotechnical engineering and other fields of science have increased steadily. These interactions were limited to geology and chemistry to solve different soil stability and lack of strength problems (DeJong et al., 2013). Nowadays, biology is a strong partner of geotechnical engineering, especially after the discoveries of different biological processes, which are able to replace the classical reinforcement techniques (generally based on chemical agents such as cement and/or resins). This partnership has paved a way into a new frontier of knowledge called geobiology (Mujah et al., 2017). In this emerging field, different natural and biological processes are under investigation in order to transform them into new techniques of soil reinforcements such as biocementation process, also called Microbially Induced Calcite Precipitation (MICP). MICP is based on precipitation of calcite using bacteria characterized by high enzymatic activity (Urease) and providing to these bacteria a source of urea and calcium. This biological process is able to increase strongly the soil mechanical strength by using microorganism metabolic activities. This technique of soil bio-reinforcement has been suggested by Whiffin (2004) and Mitchell and Santamarina (2005). Since then, numerous research works have been performed to understand and to improve this technique for future field applications. Two factors have been identified as principal parameters controlling the process : (1) type and concentration of bacteria, (2) concentration of the calcification reactants (concentration of calcium ion and dissolved inorganic carbon). Several other environmental parameters such as pH, temperature, availability of nutriments sites and soil/bacteria compatibility also govern the geochemical reac-

tion and overall performances of the biological process (Cheng et al., 2016; Al Qabany and Soga, 2013; Mitchell and Santamarina, 2005; Cheng et al., 2014; Rebata-Landa, 2007; Jiang and Soga, 2016).

A large family of microorganisms is capable of producing urease enzyme, which represents the main factor of the MICP process. Most researches in biological calcification use *Sporosarcina pasteurii* bacteria, because of its high enzymatic activity, adaptability to basic media (pH above 8.5) and high concentration of calcium (greater than 0.75 mol/l) (Ivanov et al., 2015b). The use of greater bacterial concentrations provides faster rates of ureolysis and produces larger and less soluble crystals (Phillips et al., 2013). Generally, an optical density (OD) between 0.8 and 1.2 of *S. pasteurii* bacteria is used in MICP applications with concentrations of calcification solution between 0.1 to 1 mol/l. On the other hand, an equimolar calcification solution would provide better conversion to calcite (Nemati et al., 2005). The use of high concentrations of calcification solution (0.5 to 1 mol/l) can give a significant amount of calcite with large crystals, but with non-homogeneous precipitation inside the soil specimen, which reduces in turn the mechanical efficiency of the process. On the opposite, the use of low concentrations (0.05 to 0.25 mol/l) shows homogenous distribution of calcite within the soil specimens with smaller calcite crystals (Nemati et al., 2005; De Muynck et al., 2010b). Al Qabany and Soga (2013) have shown that low concentration solution and high number of injections resulted in stronger samples for a given total amount of calcite. In practice, the definition of the concentrations and number of injections requires an optimization analysis taking into account the site conditions. Three treatment strategies have been investigated in the literature for the biocementation process (injection method, surface percolation method and premixing method). The stop flow injection method has been mostly used in previous studies, given that this technique is not detrimental for the sensitive structures (old structures) such as earthen dams and dikes. Besides, it is similar to grouting with chemical material for soil improvement, which is easy to control during the tests (controlling the injection velocity and the direction of flow essentially) (Mujah et al., 2017). However, this method has shown some problems of uniformity of treatment, the calcite being non-homogeneously distributed in soils.

Previous studies have employed different experimental devices (unconfined compressive strength tests, triaxial tests, CPT, etc.) to investigate the evolution of the mechanical strength of the biocemented soils. These studies have shown that the mechanical strength and the initial stiffness of biocemented soil increase monotonically with the degree of calcification. This increase is due to : (1) the friction increasing with the precipitation of the calcite on the grain surfaces, (2) cohesion increasing by bonding grains together with the calcite precipitation in the grain contact zones. The unconfined compressive strength (UCS) is the most simple and common test used to evaluate the strength of the biocemented soils (Mujah et al., 2017; Cheng et al., 2013; van Paassen et al., 2009; Al Qabany and Soga, 2013; Zhao et al., 2014; Ivanov et al., 2015b). Most of these studies have shown an exponential evolution of UCS with the amount of calcite. However, this evolution depends not only on the amount of calcite but also on the size and type of crystals

and the precipitation manner (Al Qabany and Soga, 2013; Cheng et al., 2013). UCS tests are not sufficient to evaluate all the strength parameters of the treated soils and to understand their stress-strain behavior. Therefore, drained and undrained triaxial tests have been performed on biocemented sands (Terzis et al., 2016; Montoya and DeJong, 2015; Feng and Montoya, 2015; Cheng et al., 2013; Montoya, 2012; Lin et al., 2015). These different studies have proposed different viewpoints in the evolution of the maximum and residual strength parameters (cohesion and friction angle). Montoya and DeJong (2015) and Feng and Montoya (2015) have tested loose sand up to a maximum calcite content of 5.3%. These studies have shown that the evolution of the maximum strength is controlled principally by the friction angle, a small cohesion being detected simultaneously inside the specimens. Meanwhile, Terzis et al. (2016) and Cheng et al. (2013) have observed an increase in the friction angle (from 38° for untreated sand to 44° for a sand calcified in 8.5% of calcite) and in the cohesion (253 kPa) of the sand compared to the untreated cohesionless state. Lin et al. (2015) have performed triaxial tests on untreated and treated sands (less than 2.6% of calcite). In this study, the friction angle appears almost unchanged by the calcification while the cohesion increases dramatically. Generally, the residual strength of the calcified sand has also shown a slight increase compared to the untreated sand. However, few studies have explored this evolution such as Feng and Montoya (2015) and Lin et al. (2015). In these particular studies, two viewpoints have been introduced to illustrate the slight increase of the residual strength. Feng and Montoya (2015) have shown that the residual friction angle has been improved by the calcification from 32° for untreated sand to 38° for treated sand with 5.3% of calcite. This evolution is probably due to the effect of different parameters such as the persistence of cemented grain agglomerations which can change the effective grain size distribution and effective angularity. The increase of the grains roughness could be also a principal factor in the increase of the residual friction angle. On the contrary, Lin et al. (2015) have shown that the residual friction angle does not change, but that there is residual cohesion that remains inside the specimens. The volumetric behavior in the drained tests shows an evolution of the dilatancy angle with the calcite amount. Correspondingly, in the undrained tests, Lin et al. (2015) observed the development of a negative pore pressure pore inside the specimens during the shear test while it was positive for the untreated sand, which confirms the dilative tendency found in the drained tests (Montoya, 2012). However, no study is available to quantify the evolution of this dilatancy with the calcification level.

The reduction of the hydraulic conductivity has also been estimated and measured by different authors. The biocementation process shows a reduction of the permeability of the treated sand because of the precipitation of the calcite in the porosity of the soils (Van Paassen, 2009; Ivanov et al., 2015a; Al Qabany and Soga, 2013). For small amounts of calcite (about 2% in mass), Al Qabany and Soga (2013) have measured a reduction of 20% in the permeability compared to the untreated sand. Van Paassen (2009) has observed a reduction of 60% of the initial permeability for high cementation level (about 6% of calcite). In fact, the reduction of the permeability in biocemented soils is not only controlled by the reduction of the porosity. The use of high concentrations of the calcification solution show a higher reduction of permeability compared to

the same amount of calcite produced with low concentrations of calcification solution (Al Qabany and Soga, 2013). This difference of permeability reduction can be interpreted as the clogging of pores that appears with higher concentrations because of the localization of the precipitation near the injection point.

The objective of the present paper is to analyze the effect of biocementation on the mechanical behavior of sand, mainly its strength parameters (cohesion, maximum and residual friction angles, dilatancy angle) but also the pre-failure characteristics (elastic modulus). The aim is (1) to explore a wider range of cementation level than that considered in previous researches (from 0 to 11.9%) and (2) to reproduce in the laboratory a cementation protocol that could be close to practitioners recommendations for *in-situ* treatment (minimization of number of injection). The laboratory analysis includes drained triaxial compression tests and permeability measurements performed with confining pressures relevant for the application of the biocementation on dikes and earth dams (from 0 to 100 kPa). SEM and X-ray micro-tomography observations have also been performed on several biocemented sand specimens in order to explore in qualitative way the change of the microstructure, the spatial distribution of calcite crystals and their morphology.

3.2 Material and Method

3.2.1 Sample preparation and treatment

Fontainebleau sand (NE34) has been used in this experimental study of the biocementation process because it is a fine sand ($D_{50} = 210\mu\text{m}$) with narrow particle size distribution (a potential target of the biocementation technique as a mitigation measure for liquefaction problems). It represents optimal sand for the biocementation process in terms of geometric compatibility between the pore and the bacteria cell sizes according to Rebata-Landa (2007). It is composed also by 99% silica, which considered as pure silica sand (no chemical interference with the process). All the physical characteristics are given in Table 3.1.

TABLE 3.1: Fontainebleau sand characteristics.

Sand	Mean diameter D_{50} (mm)	Uniformity coefficient C_U	Minimum void ratio e_{\min}	Maximum void ratio e_{\max}	Weight of sand grains ρ_s (kg/m^3)	Shape
Fontainbleau sand (NE34)	0.21	1.5	0.549	0.886	2650	Sub-rounded

Untreated sand : the untreated sand samples have been prepared using the pluviation technique (Benahmed et al., 2004). The pluviation procedure has been calibrated in order to prepare samples with a density index $Id = 0.8$ (relative density $Dr = 80\%$). The purpose of testing this sand without treatment is to compare their initial results (without treatment) with specimens

calcified at three different levels of calcification (small amount of calcite, i.e. less than 3% of calcite in mass, medium amount of calcite between 6 and 9% of calcite, and high amount of calcite between 9 and 12% of calcite).

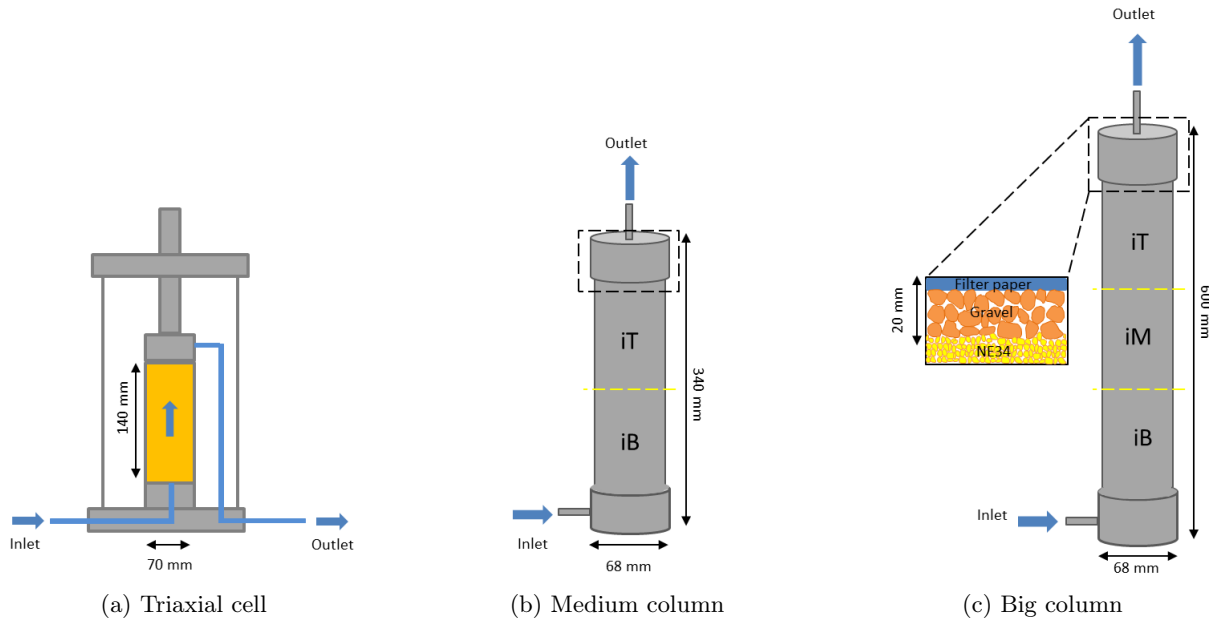


FIGURE 3.1: Treatment schema for the small amount of calcite, b) treatment schema for the medium amount of calcite, c) treatment schema for the higher amount of calcite

Small amount of calcite (less than 3% in mass) : the treated sand in this range of calcite content is very fragile and difficult to handle. For that reason, in this case, the treatment has been performed directly inside the triaxial cell to overcome all the problems of sample damage (Figure 3.1a). Firstly, a sand specimen has been prepared by pluviation technique inside the triaxial mold of 70 mm in diameter with a density index $Id = 0.8$. After preparing the sand specimens, a saturation phase has been performed by injecting 5 pore volumes of commercial water called “Cristaline water”, which has a pH value of about 7.5. Then, bacterial solution has been prepared with the same water which contains 50 mmol/l of NaCl in order to increase the potential attachment of bacteria and an optical density of bacteria (OD) equal to 1 of *Sporosarcina Pasteurii* provided by Soletanche-bachy company under a dried form. One pore volume of this solution has been injected inside the saturated sand sample from the bottom to the top with a flow rate of 0.2 mm/s. An equimolar solution of urea and CaCl₂ (1.4 mol/l) has been prepared with the same commercial water. The injection of this calcification solution has been performed after one hour of bacterial solution injection with a flow rate of 0.14 mm/s. After 10 hours, the specimen is flushed with “Cristaline water” in order to chase all the residues and to prepare the sample for the drained triaxial compression test. This procedure is considered as half a sequence of treatment (Figure 3.2) and leads to small amount of calcite (less than 3% in mass).

Medium amount of calcite (between 6 and 9% in mass) : For this range of calcifica-

tion, the specimens can be handled and resized without any problems. To accelerate the time of sample manufacturing, 4 long columns of around 340 mm in length and 68 mm in diameter have been used to prepare medium calcified sand samples (Figure 3.1b). Small layers of coarse sand (20 mm) and filter paper have been used in the top and the bottom of each column in order to enhance the diffusion of the injected solutions. For this type of columns, the same method of sample preparation and treatment has been used but with 2 injections of bacteria and 3 injections of calcification solution (Figure 3.2) (corresponding thus to 1.5 sequences of treatment). This procedure produces a medium amount of calcite (6-9% in mass).

High amount of calcite (between 9 and 12% in mass) : For this higher range of calcite, 4 long columns of around 600 mm in length and 68 mm in diameter have been used (Figure 3.1c). Two injections of bacteria and 4 injections of calcification solution have been performed in order to get this high amount of calcite (corresponding thus to 2 sequences of treatment) (Figure 3.2). This treatment can give high amount of calcite (9-12% in mass).

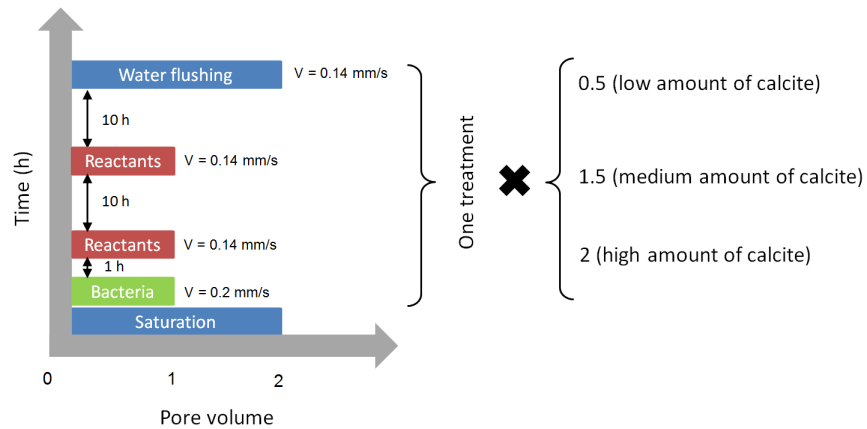


FIGURE 3.2: Schema of the treatment procedure (low, medium and high cementation level), the left figure represents the reference sequence of treatment

3.2.2 Experimental procedure

A sample preparation procedure has been defined in order to obtain triaxial samples with a slenderness approximately equal to 2 (Diameter = 68 mm, Height = 140 mm). After the treatment procedure, each column “*i*” (*i*=8 to 15) has been cut into two or three samples depending on total height of the column. The columns with an overall height of 600 mm have been divided into three triaxial samples. For the column “*i*”, these samples are named “iT” (Top), “iM” (Middle) and “iB” (Bottom) (see Figure 3.1). The 340 mm high columns have been divided into two triaxial samples only (Top and Bottom). Each triaxial sample has a height of 140 mm suitable for standard drained triaxial tests. A total of 23 tests have been performed, 4 samples for the untreated sand, 3 samples for the small amount of calcite, 8 samples for the medium amount of calcite, 8 samples for the highly calcified sand. These samples have been tested at different confining pressures (25, 50, and 100 kPa) covering the range of initial effective stresses encountered in typical applications

(mitigation of liquefaction and internal erosion). Table 3.2 summarizes all the characteristics of the tested samples. The letters T, M, and B stand for Top, Middle and Bottom, respectively, which indicate the positions of the triaxial samples in the columns with respect to the injection point.

TABLE 3.2: Experimental characteristics of the tested samples.

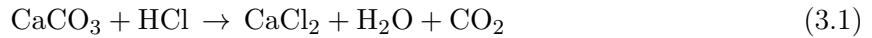
	Column	Triaxial specimen	Height (mm)	Initial porosity (%)	Density index (Id)
Untreated sand	/	1	95	38	0.81
		2	95	38	0.84
		3	94	37.6	0.84
		4	94	37.6	0.84
Low cementation level	/	5	140	38.5	0.78
		6	139	38.3	0.79
		7	138.5	38.2	0.79
Moderately cemented sand	8	8T	142	37	0.88
		8B	142		0.88
	9	9T	140	37	0.88
		9B	140		
	10	10T	139	38	0.81
		10B	142		
	11	11T	123.5	43	0.4
		11B	140		
	12	12T	139	37	0.88
		12M	138.8		
		12B	138		
Highly cemented sand	13	13T	133	38	0.81
		13M	135.5		
		13B	136		
	14	14T	140	37	0.88
		14M	137		
		14B	138		
	15	15T	137	40	
		15M	136		
		15B	138		0.65

After installing the sand sample on the triaxial base inside the membrane, a saturation phase with deaerated water is required for each sample. Before circulating the saturation water, a CO₂ circulation has been performed inside the untreated sample to improve the saturation operation. This CO₂ circulation has not been carried out for the biocalcified samples, to avoid a possible chemical reaction between CO₂ and the precipitated calcite. An initial back pressure of 400 kPa

has been applied for all the specimens to enhance the saturation state of the sample during the test. Compression tests have been performed at a constant axial displacement rate of 1 mm/min for untreated sand, and 0.1 mm/min for biocalcified sand, ensuring a fully drained response for both types of samples.

3.2.3 Calcite measurements and microstructural observations

After each triaxial test, the sample has been extracted and placed in an oven for 24 hours at a maximum temperature of 100°C. These samples have been cut in 4 parts of 2.8 cm in height. From each part 3 subsamples have been extracted in order to determine the calcite amount of the specimen using the Bernard calcimeter (Muller and Gatsner, 1971). This technique of measurements is based on the dissolution of calcite with HCl acid, and the measurement of the released CO₂, which has the same molar quantity as CaCO₃ (Equation 3.1).



The calcite measurements with the Bernard calcimeter have been repeated more than three times for each sub-sample, in order to ensure a good accuracy of the measurement (relative error smaller than 10%) of the deposited calcite within the sand samples. Some subsamples have been observed using Scanning Electron Microscope and a X-ray microtomograph in order to observe the size, distribution and morphology of the precipitated CaCO₃ (Figure 3.3).

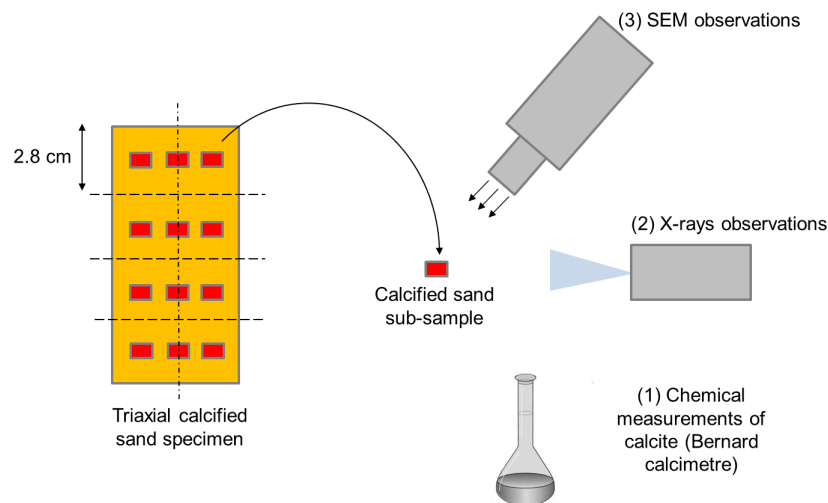


FIGURE 3.3: Schema of the sample dividing and complementary analysis after the triaxial tests

3.2.4 Permeability measurement

The permeability of each triaxial sample has been measured directly in the triaxial cell, using a Mariotte system, based on the measurement of the flow rate through the sample under a constant hydraulic head. These permeability measurements have not been performed on the specimens of small amount of calcite (less than 3%) because of partial clogging inside the triaxial cell and the drainage system, which probably happened during the biocementation process and

which can influence the permeability measurements of these specimens. During the permeability measurement, a confining pressure of 100 kPa is applied to keep a perfect contact between the membrane and the sand sample, and thus avoid lateral circulations of water. These measurements have been repeated more than three times for each sample, in order to ensure a good precision and repeatability.

3.3 Results and discussion

3.3.1 Physical properties

3.3.1.1 Calcite amount

The chemical dosage of calcite shows that the calcification procedure (for low, medium and high calcification levels) leads to repeatable results with small differences from one column to the other (Table 3.3). In all the treatments, heterogeneity along the vertical direction of specimens or columns has been observed (and could not be avoided), the calcification being localized in the first half of the columns as shown in Table 3.3 and Figure 3.4 (see; Appendix A). This heterogeneity is due to the uneven distribution of bacteria and their characteristics of transport and adhesion. Also, the high concentration of reactants has a huge effect on the homogeneity of this process. As a result of this heterogeneity of the treatment, the 600 mm long column exhibited mainly three levels of calcification (bottom : from 10.3 to 11.7%, middle : from 11.4 to 12.4% and top : from 9.1 to 10%) (Table 3.3). The small columns (340 mm) have shown two levels of calcification (bottom : 8.1 to 9.1% and top : 5.9 to 6.6%). Then, in total 7 groups of samples have been defined base on their average calcite content (even though within a sample the calcite distribution is not uniform) : group 1 corresponds to 0% (untreated sand), group 2 : $2.3 \pm 0.1\%$, group 3 : $6.2 \pm 0.3\%$, group 4 : $8.6 \pm 0.5\%$, group 5 : $9.5 \pm 0.5\%$, group 6 : $11 \pm 0.7\%$, and group 7 : $11.9 \pm 0.7\%$. Each group includes more than three specimens for triaxial and permeability measurements. The average calcite profile for each group is presented in Figure 3.4.

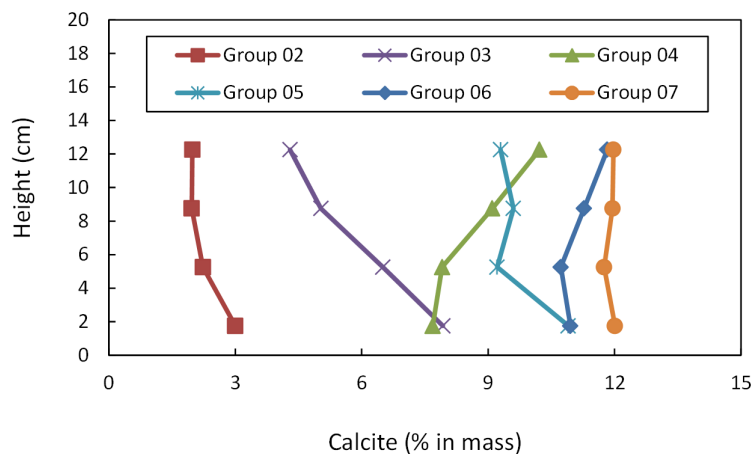


FIGURE 3.4: Average profile of calcite for each group of specimens in each calcification level

TABLE 3.3: Measured permeability and calcite dosage.

	Column	Triaxial specimen	Group	Permeability (m/s) $\times 10^{-5}$	Mass fraction of calcite (%)	Confining pressure (kPa)
Untreated sand	/	1	1	8	0	25
		2				50
		3				75
		4				100
Low cementation level	/	5	2	/	2.3	25
		6		/	2.3	50
		7		/	2.2	100
Moderately cemented sand	8	8T	3	3.68	6.6	100
		8B	4	3.44	8.9	
	9	9T	3	4	6.1	75
		9B	4	3.44	8.6	
	10	10T	3	4.4	6	50
		10B	4	2.8	9.1	
	11	11T	3	5.28	5.9	25
		11B	4	3.76	8.1	
	12	12T	5	2.72	10	0
		12M	7	2.24	11.7	
		12B	6	2.56	11.3	
	13	13T	5	2.96	9.1	25
		13M	7	2.88	11.4	
		13B	6	2.72	10.3	
Highly cemented sand	14	14T	5	2.64	9.9	50
		14M	7	2.8	12.4	
		14B	6	2.8	11.7	
	15	15T	5	2.56	9.8	100
		15M	7	2.88	12.2	
		15B	6	1.61	11.4	

3.3.1.2 Permeability

The permeability has been measured for all the specimens inside the triaxial cell before shearing (Figure 3.5). The error bars represent the minimum and the maximum amount of calcite found in the same specimen. The permeability exhibits a clear quasi-linear decrease with the calcite amount inside the sand specimen. For small amounts of calcite, the permeability has been reduced slightly by 20% compared to the untreated sand. This reduction reaches 75% for the largest amount of calcite tested (12.4%) but the soil can still be considered as highly permeable. The decrease in permeability is mainly due to the reduction in porosity by the calcite precipitation

inside the pore of the sand. Other parameters could influence the permeability of the treated sand such as pore clogging and tortuosity reduction in the porous media (Dadda et al., 2017b). The reduction of the permeability in this study is similar to the one presented by Al Qabany and Soga (2013) and Cheng et al. (2013) but for lower concentrations of reactants (5 to 1.4 times less). However, the highest concentrations considered in Al Qabany and Soga (2013) have shown lower permeability reduction. This difference is due probably to the high injection velocity of reactants in the present study, which allowed a deeper penetration of the calcification solution in the sand columns and avoided an eventual clogging.

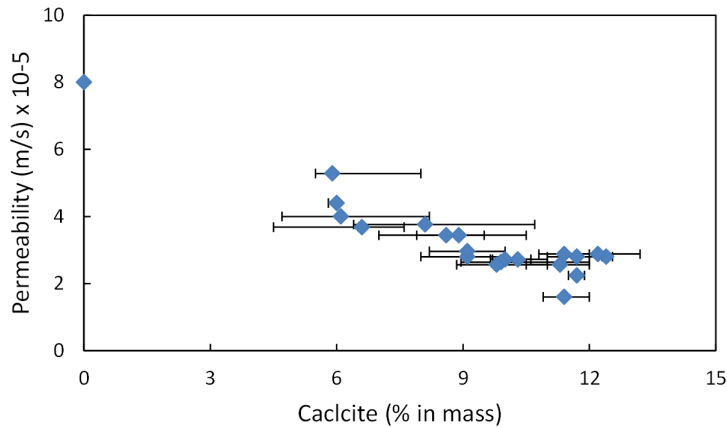


FIGURE 3.5: Permeability of the tested specimens vs the amount of calcite

3.3.2 Mechanical properties

3.3.2.1 Biocemented sand behavior

Triaxial drained tests have been performed on each group of specimens with different confinement pressure (25-50 and 100 kPa) in order to explore the behavior of each level of calcification and its strength parameters such as the friction angle and cohesion.

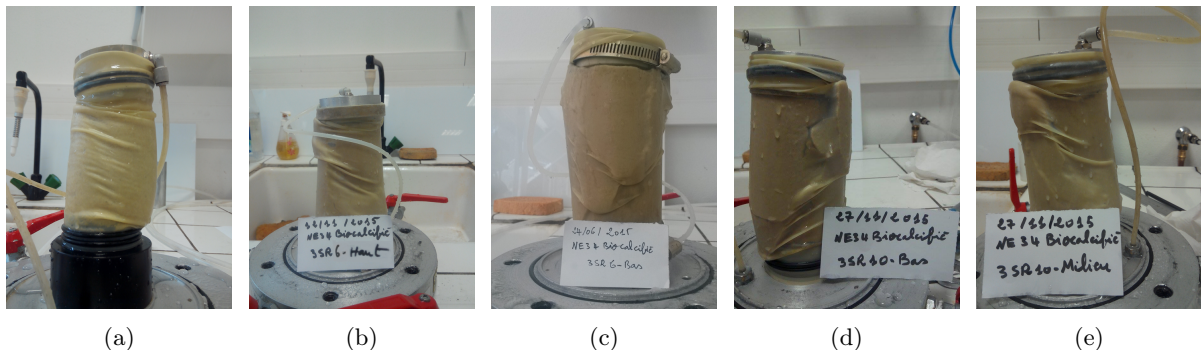
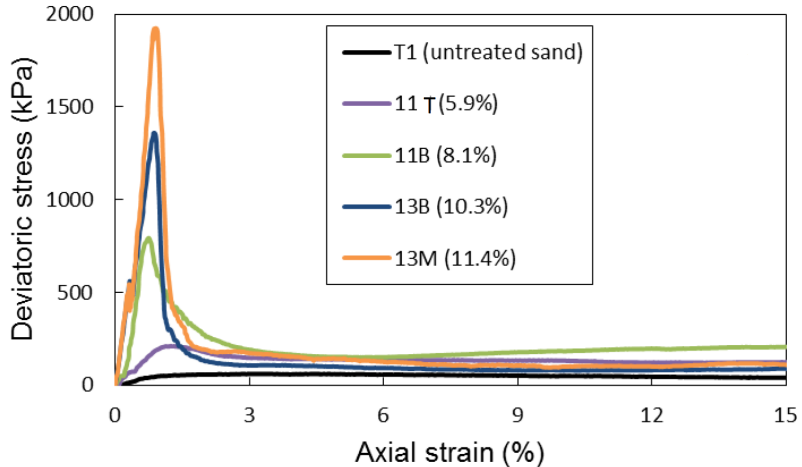


FIGURE 3.6: Triaxial samples after failure a) untreated sand (T1), b) moderately cemented sand (specimen 11T : 5.9%), c) moderately cemented sand (specimen 11B : 8.1%), d) heavily cemented sand (specimen 13B : 10.3%), e) heavily cemented sand (specimen 13M : 11.4%)

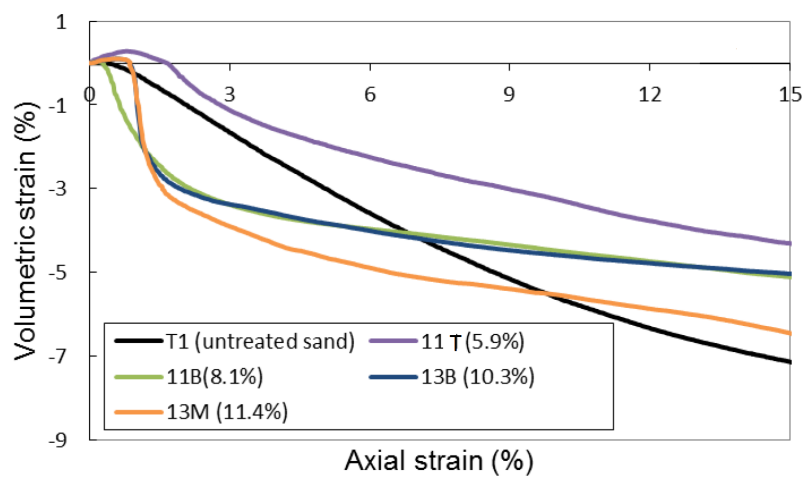
The results of tests corresponding to 5 initial amounts of calcite (untreated, 2 moderately cemented and heavily cemented sand) under the same initial confining pressure (25 kPa) are presented in Figure 3.6 and Figure 3.7. As expected, the highly cemented sample exhibits greater strength and initial stiffness, a more fragile and dilatant behavior after failure compared to the low cemented and untreated sand samples. The strength of these specimens increased monotonically with the amount of calcite (the strength of the highly cemented sand is 30 times larger than that of the untreated sand under a 25 kPa confining pressure). This evolution of the strength is due mainly to the evolution of the cohesion with the calcite precipitation between the grains. In the range of small strains, the highly cemented sample shows a lower deformability with respect to the moderately treated and untreated sand samples. The contribution of biocementation to this behavior is remarkable; deformability is hampered by intact calcite bridges that form an active force network inside the sample as explained in Wang and Leung (2008a). Close to the peak of deviatoric stress, the volumetric behavior changes direction, going from contractancy to dilatancy, due to the high density and the strong cohesion of the cemented sample. After the peak, a shear band appeared in all samples with a clear localization in the highly and moderately cemented samples (Figure 3.6), the rate of expansion increases monotonically with the amount of calcite. The fragile failure of the calcite bridges causes a rapid drop in resistance, which must be compensated by the associated dilatancy. With a small increment of strain after the peak (less than 3%), the sand reaches its residual strength state, slightly higher than that of the untreated sand, which is in agreement with previous results of Feng and Montoya (2015) and Hai et al Lin et al. (2015). The slight difference in the residual strength can be interpreted with two different mechanisms : an additional roughness generated by precipitated calcite on the surface of the grains (as shown in Figure 10 4.4a and 4.4b which represents a SEM observation of treated and untreated sand sample), and the existence of clusters formed by grains which remain cemented after failure (preventing buckling of the forces chains inside the shear band and resulting in additional resistance) as found by Wang and Leung (2008a) for 2D DEM modeling of sand treated with Portland cement. However, the residual volumetric strain has shown lower value compared to the untreated sand.

3.3.2.2 Evolution of the mechanical properties of the biocemented sand

The elastic modulus E which represents the initial slope in the $q-\epsilon_1$ curve has been extracted from all the triaxial tests (Figure 3.8). The error in this curve represents the variation of the calcite amount in each tested specimen. Despite of slight differences in some points, due to the strong heterogeneity of the treatment (Group 3 : 6.2%), the global trend fits with an exponential dependency on the amount of calcite in the highly cemented sand this modulus has exceeded 250 MPa (specimen 15B : 11.4% of calcite). These findings are in agreement with previous results reported by Cheng et al. (2013). The non-linearity of this evolution is probably due to the evolution of the contact surface created by calcite, the densification and the evolution of the coordination number inside the cemented specimens, assumptions confirmed in Dadda et al. (2017a) using quantitative 3D X-ray micro-tomography images analysis on biocemented sand.



(a)



(b)

FIGURE 3.7: Triaxial results of different treated specimens under 25 kPa of confinement, a) mechanical response, b) volumetric response

Using the tests on specimens with the same calcification level (group) but with different confining pressures, the q-p curves (deviatoric vs mean stress) enable to determine the maximum and the ultimate critical state line, which have a theoretical relationship with the peak friction angle (Φ^*) and the cohesion, and critical friction angle (Φ), respectively. The resulting strength parameters for each cementation level are presented in Figure 3.9. The horizontal error bars represent the variation of the calcite amount for each group of samples.

Figure 3.9a shows that the cohesion of the cemented sand evolves non-linearly with the amount of calcite until a value of 215 kPa for cemented specimens with 11.9% of calcite. This non-linearity can be interpreted as the result of the preferential precipitation of calcite at contact between grains. Recently, Dadda et al. (2017a) have proved that the non-linearity of the cohesion evolution is controlled by the evolution of the contact surface area, the coordination number, and the solid fraction increasing inside the specimen. Similar trends have been found by Cheng et al.

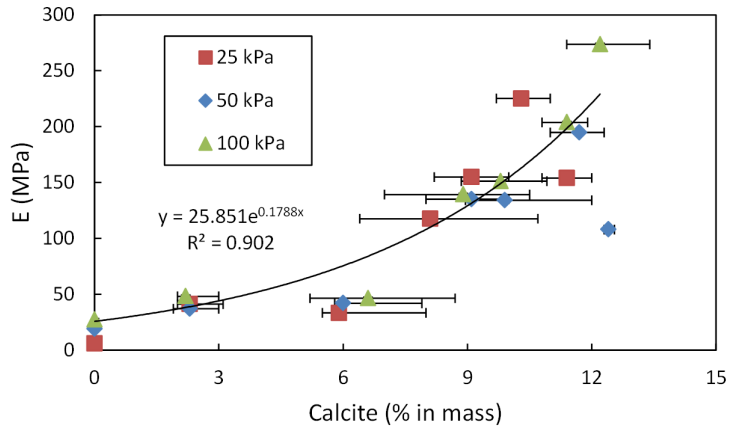


FIGURE 3.8: Evolution of the elastic modulus of different tested biocemented sand under various confining pressure (25, 50 and 100 kPa)

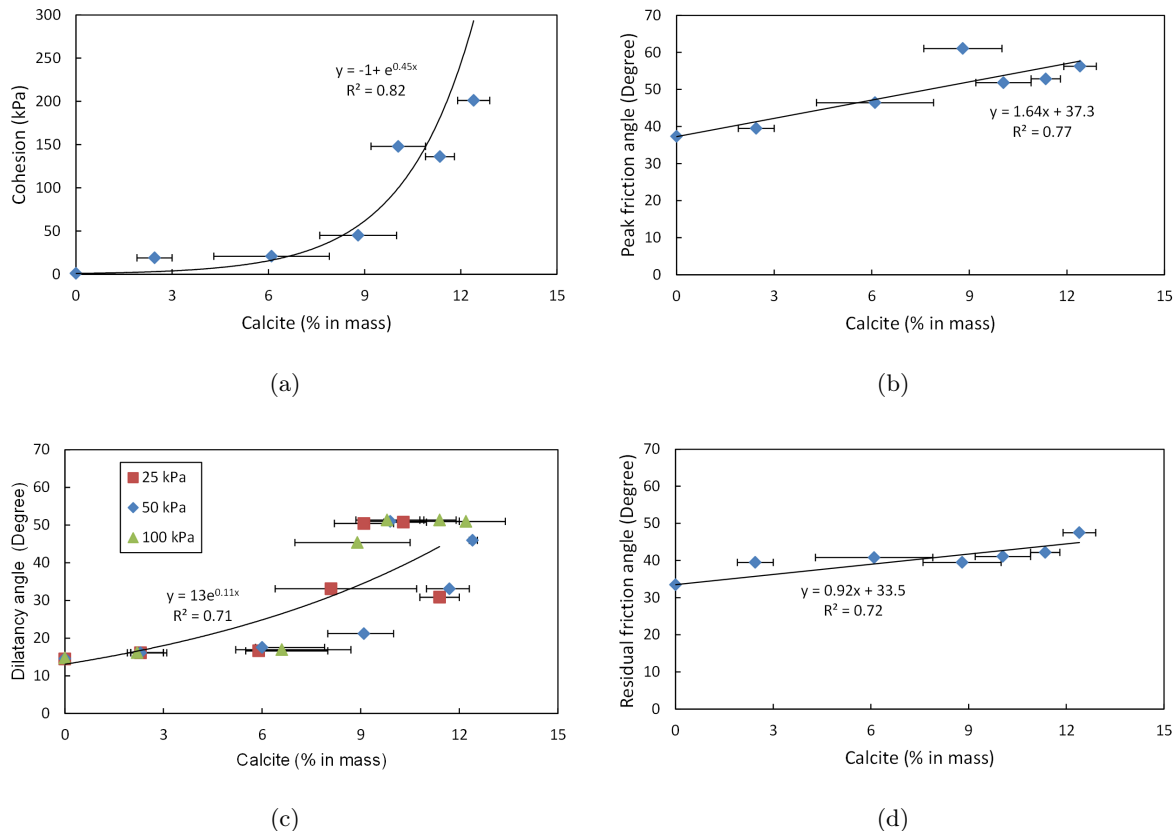


FIGURE 3.9: Evolution of the different mechanical properties with the degree of biocalcification,
a) cohesion , b) peak friction angle, c) dilatancy angle, d) critical friction angle

(2013) for similar sand with smaller amounts of calcite, the fit proposed by the authors being exponential and depending also on the initial saturation state. The results obtained in the present study are slightly lower than the values of cohesion found in Cheng et al. (2013) for saturated specimens. For approximately 10% of calcite in mass the cohesion was around 150 kPa in the

study of cheng et al Cheng et al. (2013), however the trend of the cohesion in the present study shows a value of 100 kPa. This difference could be attributed to the influence of the microstructure and of the injection protocol. In the present study, large crystals have been found as a result of high concentration of reactants, which can endow lower contact surfaces inside the specimen and lower strength of the specimens as shown in the work of Al Qabany and Soga (2013) where larger crystals show lower USC compared to smaller ones.

Regarding frictions angles, Figures 3.9b and d show an overall linear evolution of the friction angles, both peak (Φ^*) and residual (Φ) with the level of cementation. The peak friction angle increases linearly from the initial value of untreated sand (37°) to a final value of 55° in the highly cemented sand (11.9%). The ultimate friction angle is initially equal to 33° in untreated samples ; it increases linearly until a final value of 49° lower than the peak friction angle for the highly cemented sand specimens. The evolution of the maximum and ultimate strength (Φ) can be interpreted as the result of two mechanisms mentioned above : (i) additional roughness generated by calcite distributed on grain surfaces, (ii) persistence of cemented sand grains agglomerates. The effective angularity and particle size distribution as well as the surface roughness can be reduced from the peak to the ultimate strength by the breakage of the persistent agglomerates and the detachment of the calcite crystals from the grain surfaces, which can illustrate the large difference between the peak friction angle (55°) and the ultimate friction angle (49°). Similar trends have been reported by Feng and Montoya (2015) and Cheng et al. (2013) for smaller amounts of calcite. The dilatancy angle Ψ has been computed with the following equation :

$$\sin\Psi = \frac{\partial\epsilon_v/\partial\epsilon_1}{2 - \partial\epsilon_v/\partial\epsilon_1} \quad (3.2)$$

The evolution of the dilatancy angle is presented in Figure 3.9c for all the tested specimens and the different confining pressures. Despite of the noise of the results probably coming from the heterogeneities of the tested specimens, the global trend corresponds to a non-linear evolution with the calcite amount from 15° for untreated sand to 52° for highly cemented specimens with 12.4% of calcite (Figure 3.9c). This evolution is probably controlled by the densification of the sand for the small amounts of calcite and microstructural changes of the solid skeleton in high amounts of calcite (bonded contacts, coordination number, effective particle size distribution and grain morphology).

3.3.3 SEM and X-ray observations

Observations of the biocemented sand samples with SEM and X-ray micro-tomography have been performed after completion of the triaxial tests. These observations can give qualitative information about the calcification (crystals sizes and shape, localization of precipitation, etc.). Figure 3.10 shows the observation of a subsample taken from the highly cemented sand specimen (triaxial specimens 14M : 12.4%). The SEM observation shows a localization of the precipitation between two grains of sand with, on the opposite, small amounts on the surfaces of these grains. This non-homogeneity of the distribution of calcite crystals is due probably to the high concen-

tration of calcification solution which has been used in this work. Figure 3.10d shows crystals attached between two grains forming a calcite bridge with a polyhedral shape and dimensions between 5 and 15 μm . Near this contact zone, a smooth layer of calcite was formed (Figure 3.10d) ; probably a calcite bridge with neighboring grain that got detached during the specimens preparation for the SEM observations. This large size and the perfect morphology of calcite crystals confirm the saturation of the medium with calcium during the biocementation process, which is induced by the high concentration of the calcification solution (calcium source and urea).

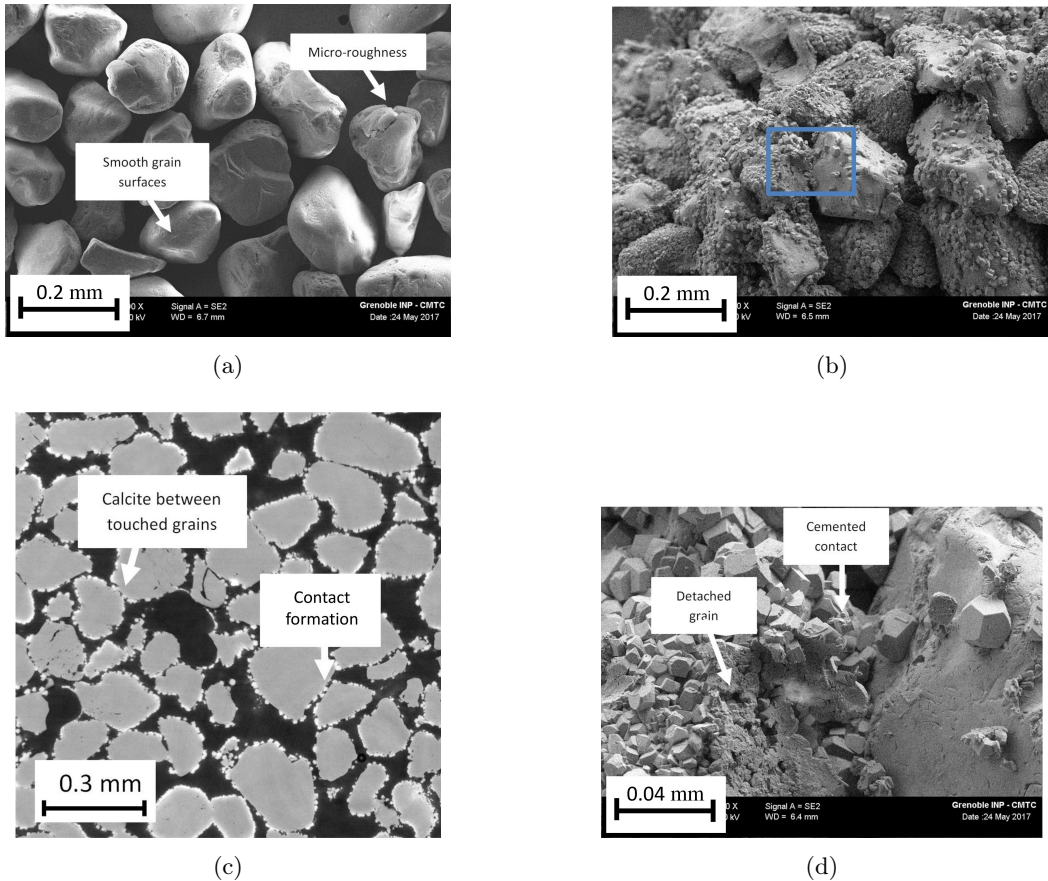


FIGURE 3.10: Microstructural observations of biocemented sand specimens (specimen 14M), a) SEM observation of untreated sand grains (scale = 100 μm) b) SEM observation of cemented agglomeration sand (scale = 100 μm), c) X-ray micro-tomography observation (black : void, grey : sand and white : calcite), d) SEM observation grain to grain contact (scale = 20 μm)

The X-ray tomography 2D image of the same specimen (Figure 3.10c) shows in white the calcite, in grey the sand grains and in black the void. This X-ray tomography observation shows non-uniform precipitation on the grains with small localization in the grain contacts. The width of the precipitated calcite layer is between 5 to 20 μm , which is coherent with the SEM observations. Smaller calcite crystals have been found (2 to 5 μm) in Feng and Montoya (2015), where small concentration of calcification solution (0.37 mol/l) has been used in the calcification process. Although the presented X-ray image is in 2D, this image allows us to see clearly the formation of

two types of contact (1) calcite at the contact between two grains and (2) new bridge of calcite between two grains.

It appears in this image that the grain surfaces have not been totally covered with the calcite precipitation even for a high amount of calcite (12.4%), and significant surface remain uncovered after calcification, which can reinforce the hypothesis of the affinity of bacteria to attach to specific places in the porous media such as : micro-roughness on the grain surfaces and in the grain contacts. The 3D X-ray images can be used to extract different microstructural and physical properties such as (porosity, calcite amount, permeability, etc.) (Dadda et al., 2017b). A first attempt have been recently performed by Dadda et al. (2017a) on 3D images of calcified specimens to extract the contact surfaces created between grains and the coordination number evolution.

3.4 Conclusion

Three protocols of injection have been performed in order to obtain different levels of calcification in plastic columns for the higher and medium cementation levels and directly in the triaxial cell for the smaller cementation level. 7 groups of triaxial specimens with mass fraction of calcite (m_c) from 0 to 11.9% have been considered. The specimens obtained from this calcification operation have been tested in the triaxial cell under different confining pressures in order to determine the evolution of the mechanical strength parameters with the calcite content. The permeability of each specimen has also been measured before each triaxial test. Subsamples along the triaxial specimens have been extracted after each test in order to measure the calcite amount by chemical dosage and to observe the microstructural evolution induced by the precipitation of calcite using SEM and X-rays. The main conclusions of this experimental campaign are :

- The use of high concentration of reactants in the injection protocol results in large crystals (5 to 20 μm) and some heterogeneity along the injection path (precipitation in the bottom of all the columns near the injection point).
- The permeability of the tested specimens shows generally a clear reduction with the calcite amount. For the small amounts of calcite, the permeability is slightly reduced by 20% compared to the untreated sand. This reduction exceeds 75% for the higher amount of calcite (12.4%). This evolution is mainly due to the porosity reduction by the calcite precipitation inside the pores of the sand. Other parameters could also influence the permeability of the treated sand such as pore clogging and tortuosity reduction in the porous media.
- The performed triaxial tests have shown an increase of the strength of the biocemented sand compared to the untreated material. The strength as well as the initial stiffness is increasing monotonically with the amount of calcite. This increase is due to the boost in the contact cohesion, which can hamper the deformation of solid skeleton. The volumetric

behavior changes direction near the peak, going from contractancy to dilatancy and the rate of expansion increases monotonically with the amount of calcite. Regarding the residual strength, the treated sand reaches an ultimate strength state, slightly greater than that of the untreated sand.

- The elastic modulus E shows an exponential relationship with the amount of calcite. An exponential relationship has been found also between the cohesion and the calcite amount inside the specimens (215 kPa for a maximum amount of calcite of 11.9%). These exponential (elastic modulus and cohesion) trends are principally due to the evolution of the contact surface area, the solid fraction and the coordination number inside the treated specimen. Overall linear evolutions of the peak and residual friction angle are observed with the level of cementation. The increase in the ultimate strength of the cemented materials can be interpreted as an additional roughness generated by calcite crystals distributed on grain surfaces, and persistence of cemented sand grains agglomerates. The dilatancy angle increases in a non-linear manner; it can be interpreted as an effect of the densification, the cohesion and modification of the particle size distribution and the angularity by the persistence of cemented sand grains agglomerates.
- SEM observation of biocemented sand sample shows a localization of the precipitation between two grains of sand with small amount distributed on the overall surfaces of the grains. These observations have shown the formation of large calcite crystals with perfect morphology of polyhedral shapes (5 to 15 μm). Tomographic observations of the same specimens show a non-uniform precipitation of the grains with small localization in the grain contacts and uncovered grain surfaces with the precipitated calcite. The width of the precipitated calcite is between 5 to 20 μm which is coherent with the SEM observations. The 2D X-ray images can be used to reconstruct a 3D image in order to determine quantitative informations about the contact characteristics evolution by image processing technique.

CHAPITRE 4

CHARACTERIZATION OF MICROSTRUCTURAL AND PHYSICAL PROPERTIES CHANGES IN BIOCEMENTED SAND USING 3D X-RAY MICROTOMOGRAPHY

Sommaire

4.1	Introduction	62
4.2	Material and Method	64
4.2.1	Biocemented samples preparation	64
4.2.2	Permeability measurement	66
4.2.3	Mass fraction of calcite	66
4.2.4	Microstructural and physical properties computed on 3D images	67
4.2.4.1	Image acquisition and treatment	67
4.2.4.2	Computed microstructural properties	68
4.2.4.3	Physical properties	71
4.3	Results and discussion	74
4.3.1	Microstructural and physical properties from 3D X-ray microtomography	74
4.3.1.1	Initial porosity and mass fraction of calcite	74
4.3.2	Correlation lengths	75
4.3.2.1	Total specific surface area (<i>SSA</i>) and specific area of calcite (<i>SSA_c</i>) :	75
4.3.3	Permeability and effective diffusion	77
4.4	Comparison with analytical estimates and numerical values	79
4.4.1	Models	79
4.4.2	Correlation lengths and total specific surface area (<i>SSA</i>)	80
4.4.3	Permeability and effective diffusion	81
4.5	Conclusions	81

The content of this chapter has been published in Acta Geotechnica in september 2017.

Abstract

An experimental study has been performed to investigate the effect of the biocalcification process on the microstructural and the physical properties of biocemented Fontainebleau sand samples. The microstructural properties (porosity, volume fraction of calcite, total specific surface area, specific surface area of calcite, etc.) and the physical properties (permeability, effective diffusion) of the biocemented samples were computed for the first time from 3D images with a high resolution images obtained by X-ray synchrotron microtomography. The evolution of all these properties with respect to the volume fraction of calcite are analyzed and compared with success to experimental data, when it is possible. In general, our results point out that all the properties are strongly affected by the biocalcification process. Finally, all these numerical results from 3D images and experimental data were compared to numerical values or analytical estimates computed on idealized microstructures constituted of periodic overlapping and random non-overlapping arrangements of coated spheres. These comparisons show that these simple microstructures are sufficient to capture and to predict the main evolution of both microstructural and physical properties of biocemented sands for the whole range of volume fraction of calcite investigated.

4.1 Introduction

Several soil reinforcement techniques were developed in the last 50 years, with the huge development that has occurred in the industry such as ; chemical grouts, mechanical compactations, rigid inclusions, jet grouting, etc. These techniques show limitations for specific cases (great depth situations, old and sensitive structures); it is considered also as money and time consuming techniques, and harmful technologies for the environment (DeJong et al., 2010a). In the recent years, the application of biological processes in geotechnical engineering has received more attention. Different biological processes have been recommended to overcome all the drawbacks of the classical techniques of soil improvements, such as bio-gas processes, bio-film formation and bio cementation (DeJong et al., 2014b). The Microbiologically Induced Calcite Precipitation (MICP) technique represents one of the most promising techniques of biocementation based on the precipitation of calcite by biochemical reactions. These reactions are governed by a strong ureasic activity of bacteria such as *Sporosarcina pasteurii*, which can decompose the urea ($(\text{NH}_2)_2\text{CO}$) into ammonium (NH_4^+) and carbonate (CO_3^{2-}). This chemical component can participate in the composition of the final product (calcite : CaCO_3) (Equation 4.1). This phenomenon can be reproduced within soils, by the injection of the ureasic bacteria and chemical reactants (Urea + calcium source).



This phenomenon plays a considerable role in increasing the mechanical strength of the treated soils, by bounding soil grains together with the precipitation of the calcite. Different studies have been performed to explore the increase of the mechanical strength of the soils treated by MICP

(Al Qabany et al., 2011a; Feng and Montoya, 2015; Filet et al., 2012; Martinez et al., 2013; Montoya et al., 2013; van Paassen et al., 2010; Chu et al., 2014; Morales et al., 2015). These studies show a significant increase in shear strength of bio-mediated soils, where the calcite precipitates preferentially at the inter-granular contacts (Al Qabany et al., 2011a; Girinsky, 2009), which increase the amount of the cohesive contact surface between grains, thus the cohesion and the strength of the soil. On the other hand, the precipitation of calcite decreases the porosity of the soil specimen, and changes its microstructural properties (pore structure and geometry, specific surface area) depending on the procedure of injection, which influences the deposition manner of calcite in pores. These changes lead to a slight decrease in the physical properties (permeability, effective diffusion) for a small amount of calcite, depending mainly on the quantity of injected bacteria and chemical reactants (Martinez et al., 2013; Whiffin et al., 2007).

Increasing the shear strength of a soil is highly desirable in geotechnical engineering. However, the permeability reduction could be an advantage or drawback depending on its application. For example, decreasing the permeability in order to control the infiltration of water into soil slope can minimize the risk of landslide. However, its reduction may not be favorable for controlling failure induced by earthquake in liquefiable soils (Montoya, 2012). Several applications of this process have proven their worth in geotechnical engineering, such as the reinforcement of dams against seepage-internal erosion, where the MICP process improves the critical shear stress and reduces the erodibility of sand-clay mixtures with wide gap, by cementing grains with each other, without a significant decrease in permeability (Jiang et al., 2014). Liquefiable soils could be reinforced with the biocementation ; in Montoya (2012) Montoya proved that the biocementation increases the cyclic strength and stiffness of sand and provides significant improvement against liquefaction.

The evolution of the physical and mechanical properties is related directly to the changes of the microstructure of the biocemented sand. However, a clear relation between the change of the microstructure and these properties is not yet established. Several investigations have been performed in different works using different techniques of observations at the microscale (transmission light optical microscopy, scanning electron microscopy, and energy dispersive x-ray spectroscopy), in order to explore in a qualitative manner the spatial distribution of calcite, as well as the calcium carbonate morphology. These studies show that the calcite appears in different morphological nature around individual microbes or their aggregates, and deposits preferentially in particle-particle contacts with thin layer on the grain surface. This illustrates the affinity of bacteria to deposit in these regions of porous media (Martinez and DeJong, 2009; DeJong et al., 2010b, 2006; Girinsky, 2009; Ng, 2013). Al Qabany et al. (2011a) show that the protocol of injection, in particular the urea-calcium chloride concentrations, has an influence on the distribution, the shape and the size of calcite crystals. Lower concentration gives small calcite crystals with uniform distribution all around the grains. These results were confirmed by Terzis et al. (2016) showing that crystals are found to precipitate in two forms : smaller single particles distributed uniformly on the surface of grains for small concentrations of reactants, and single mesocrystals

which have bigger size for large concentrations of reactants.

The exploration in a quantitative way of the treated soils microstructure is necessary to understand the evolution of the mechanical and physical properties of the biocemented soils. Different alternative techniques exist to explore these properties in a porous media. The rapid developments of imaging and computer technology make the X-ray microtomographic observations expanding fast in the geomaterials field. The use of this technique permits to visualize in a quantitative and precise manner the microstructure of scanned objects, which gives more rigorous and reliable results for the properties inferred from the 3D images. Few works have been addressed using X-ray microtomography to study the microstructure of biocemented sand such as Tagliaferri et al. (2011), where they perform *in-situ* microtomography by driving triaxial test on biocemented sand. In this work the chosen resolution of $15 \mu\text{m}$ is not sufficient to capture the shape and the distribution of the calcite at the pore scale.

In the present work, different sand specimens with various calcification levels have been observed in the European Synchrotron Radiation Facility (ESRF) at a very high resolution in order (1) to observe the distribution of the calcite at the pore scale and (2) to characterize the evolution of the microstructural (volume fraction of calcite, specific surface area, etc.) and physical properties (permeability tensor, effective diffusion tensor) of biocemented sand as a function of the cementation level. The numerical results computed on Representative Elementary Volumes extracted from the 3D images are compared with experimental data, analytical models (self-consistent estimates) and numerical values obtained on simple periodic arrangements of coated spheres. The paper is organized as follows. The section 4.2 is devoted to the material and methods : sample preparation, permeability and calcite mass fraction measurements, 3D images acquisition and treatment, computed microstructural and physical properties. In section 4.3, the properties computed from the 3D images are presented, discussed and compared with experimental data and analytical estimates.

4.2 Material and Method

4.2.1 Biocemented samples preparation

Two solutions have been prepared for the biocementation process : (1) bacterial solution which contains one optical density (1 OD_{600}) of *S. pasteurii* provided under a dried form by Soletanche Bachy (Soletanche Bachy Entreprise, Rueil-Malmaison, France) with 3 g of Sodium Chloride (NaCl) dissolved in one litter of commercial water, in order to increase potential attachment of bacteria to soil grains ; (2) Reactants solution (calcifying solution) which contains 1.4 moles of urea and the same amount of calcium chloride. Fontainebleau sand (NE34) was used in this experimental investigation of the biocementation procedure. The characteristics of this sand are listed in Table 5.1.

TABLE 4.1: Fontainebleau sand characteristics.

Sand	Mean diameter $D_{50}(mm)$	Uniformity coefficient C_U	Minimum void ratio e_{min}	Maximum void ratio e_{max}	Weight of sand grains $\rho_s(kg/m^3)$	Shape
Fontainbleau sand (NE34)	0.21	1.5	0.549	0.886	2650	Sub-rounded

Eight sand columns with the same diameter of 68 mm and different heights (4 columns have a height of 600 mm and 4 columns of 300 mm) were prepared with a pluviation technique in the plastic tubes of the injection system, showed in Figure 4.1. These columns were prepared with a relative density of 80% ; between two filter papers and small layers of 20 mm of coarse sand, in order to homogenize the water flow injection. A saturation phase of each column was adopted before starting the treatment injections. After this phase, an injection of one pore volume of the bacterial solution was performed from the bottom to the top with a flow rate of 0.2 mm/s. After one hour, two injections of calcifying solution of one pore volume were carried out with a flow rate of 0.14 mm/s and with a time offset of 10 hours between these two injections. After the second treatment, two pore volumes of flushing water were injected inside columns with a flow rate of 0.14 mm/s, in order to expel all the process residues. This injection procedure usually leads to columns with a mass fraction of calcite of about 5 to 6%. This injection was repeated twice on eight columns in order to reach higher mass fractions of calcite, typically between 10 to 12%.

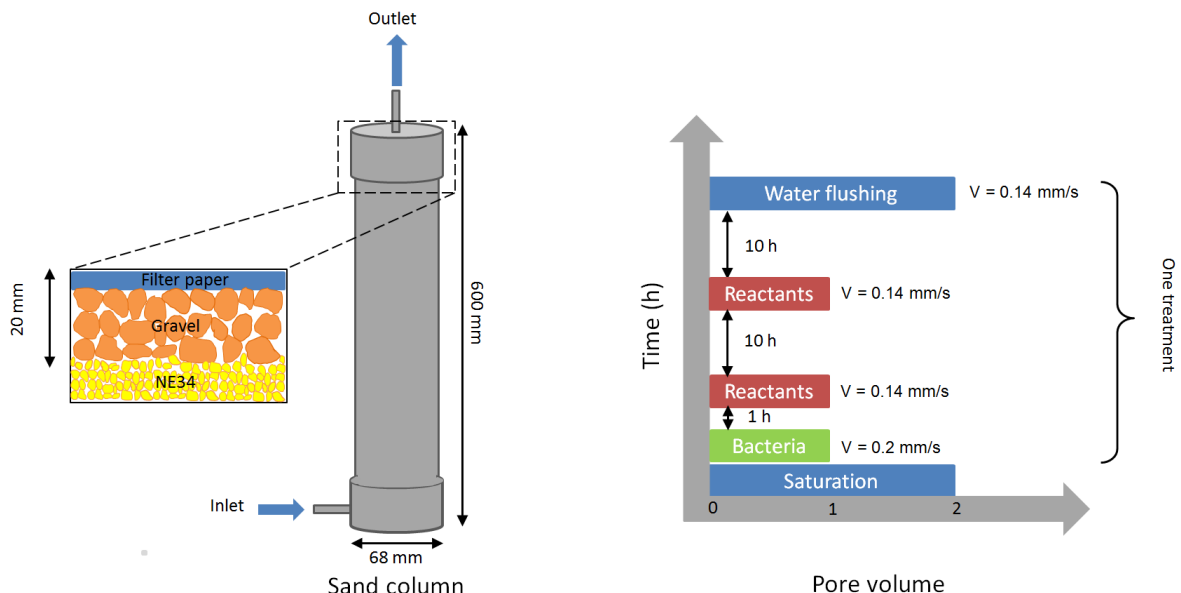


FIGURE 4.1: Injection protocol for biocementation process.

After the treatment procedure, each column “i” ($i=8$ to 15) was cut in two or three samples depending on its total height. The columns with an overall height of 600 mm were divided into three triaxial samples. For the column “i”, these samples are named “iT” (Top), “iM” (Middle) and “iB” (Bottom) (see Figure 4.2). The columns of height 300 mm were divided into two triaxial samples only (Top and Bottom). Each triaxial sample has a height of 140 mm suitable for standard drained triaxial tests. After the triaxial test, sub-samples with a volume of around 500mm^3 were taken at the top and the bottom of each triaxial sample, and are denoted “iT”, “iT”, “iMT”, “iMB”, “iBT” and “iBB”. These sub-samples were used in order to measure the mass fraction of calcite along the column using the Bernard calcimeter. Unfortunately, these volumes are too big to be used for the X-ray observation. Therefore, sub-samples with a volume of around 10mm^3 were taken at the same position as the previous ones to characterize the distribution of the calcite at the pore scale by X-ray microtomography.

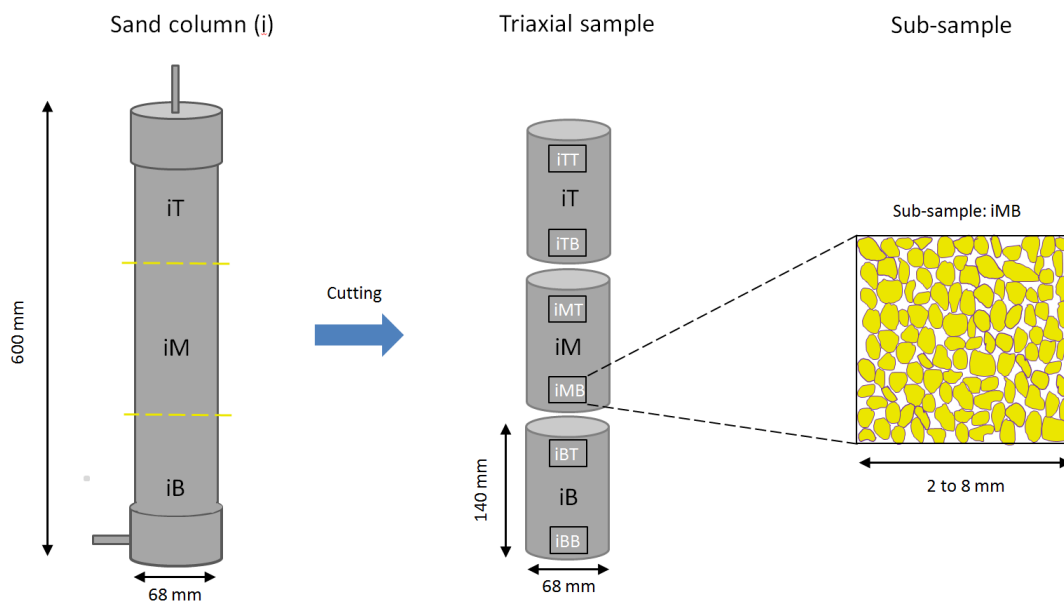


FIGURE 4.2: Injection protocol for biocementation process.

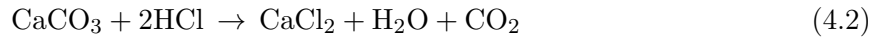
4.2.2 Permeability measurement

The permeability for each triaxial sample was measured in a triaxial cell, using a Mariotte system, based on the measurement of the flow rate through the sample under a constant hydraulic head. During the permeability measurement, a confining pressure of 100 kPa is applied to stick the membrane on the sand sample and to avoid lateral circulations of water between the membrane and the sand sample. These measurements have been repeated more than three times for each sample, in order to ensure a good precision and reproducibility.

4.2.3 Mass fraction of calcite

The mass fraction of calcite of each sub-sample was measured using the Bernard calcimeter (Afnor, 1996). It is based on the dissolution of the calcite with HCl acid, and the measurement

of the released CO₂, which has the same molar quantity as CaCO₃ (Eq 4.2).



The calcite measurements with the Bernard calcimeter were repeated more than three times for each sub-sample, in order to ensure a good accuracy of the measurement (less than 10%) of the deposited calcite within the sand samples.

4.2.4 Microstructural and physical properties computed on 3D images

4.2.4.1 Image acquisition and treatment

3D images of some biocemented sand sub-samples (see Table 4.2) were performed using X-ray synchrotron microtomography on the ID19 beamline at the ESRF in Grenoble. To obtain such 3D images, the sub-sample is fixed between the parallel beam line and the detector (FReLoN CCD), which is characterized by fast data saving and a low noise. A resolution of (0.65 μm³/voxel was chosen in order to visualize precisely the calcite crystals, which have a typical size of 15 micrometers (see SEM images in Figure 4.3). The field of view is (3250 x 3250 x 2000 voxels), i.e (2.11 x 2.11 x 1.3 mm³) to obtain 3D images large enough to be representative of the material.

TABLE 4.2: List of the scanned sub-samples with its associated properties.

Column	Initial porosity (%)	Triaxial specimen	Sub-sample	Calcite (% in mass)
8	37	8T	8TB	14.3
		8B	8BT	12.6
9	37	9B	9BB	5.7
10	38	10T	10TT	13.5
		10B	10BT	6.9
11	43	11T	11TT	3.9
			11TB	8.8
		11B	11BT	12.7
12	36	12M	12MB	5
13	36	13T	13TT	7
			13TB	15.2
		13M	13MT	13.4
			13MB	16.9
		13B	13BT	12.7

The transmitted rays were recorded for 1800 projections. Later, these images were collected to reconstruct numerically the internal microstructure of the sample using a filter back projection algorithm. Due to weak difference in absorption between the calcite and the sand, a phase retrieval approach was used (Paganin et al., 2002). The obtained 3D images represent a 3D map that is proportional to the density of each phase within the scanned sample.

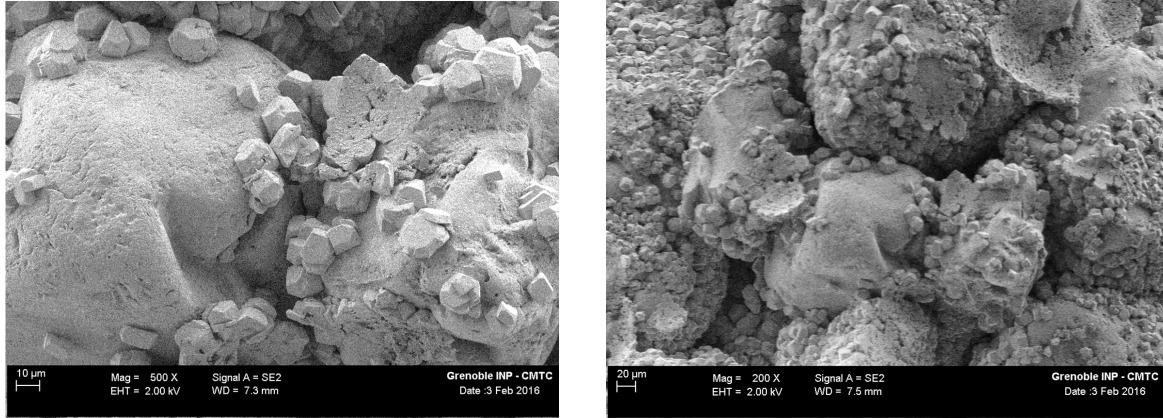


FIGURE 4.3: SEM observation of the biocemented sand (subsample 13MB).

Figure 4.4 shows some 2D views of three sub-samples after reconstruction. We can distinguish the three phases : air (dark phase), sand grain (grey phase) and calcite (light grey phase). The chosen approach allows increasing the contrast between both phases with a slight brightness of calcite, which is coating sand grains (Figure 4.4). In the case of pure absorption images, it would not have been possible to distinguish between calcite and sand, because of the similar absorption coefficients of the two phases which is related to their densities ($\rho_s = 2650 \text{ kg/m}^3$, $\rho_c = 2710 \text{ kg/m}^3$).

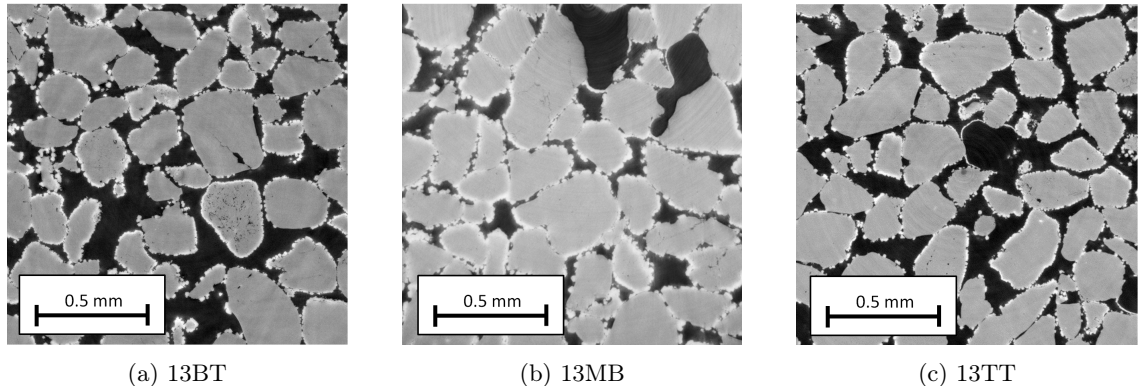


FIGURE 4.4: X-ray micro-tomography images of biocemented sand subsamples (column 2).

In order to compute some microstructural quantities, the 3D images in grey levels must be treated to separate the three phases (pore, sand and calcite) (Schlüter et al., 2014). The typical grey level histogram of an image is presented on Figure 4.5. It shows that the pore and the sand phases can be easily separated by a simple thresholding (Otsu, 1979). By contrast, the separation of the calcite and the sand phases is not straightforward, because of the similar density of these two constituents. In the present work, the separation of these two phases has been performed by using the first threshold (between sand and pore) and assuming that the grey level histogram of the sand phase follows a Gaussian distribution to define the second threshold by symmetry (between sand and calcite) following the method proposed by Otsu (1979). By visual observations, the partial

volume effect has not a significant effect because of the high quality of the obtained images and the large contrast between the solid (calcite and sand) and the void. After the treatment of all the slices (2D images), the 3D image of each sample is obtained (Figure 4.5).

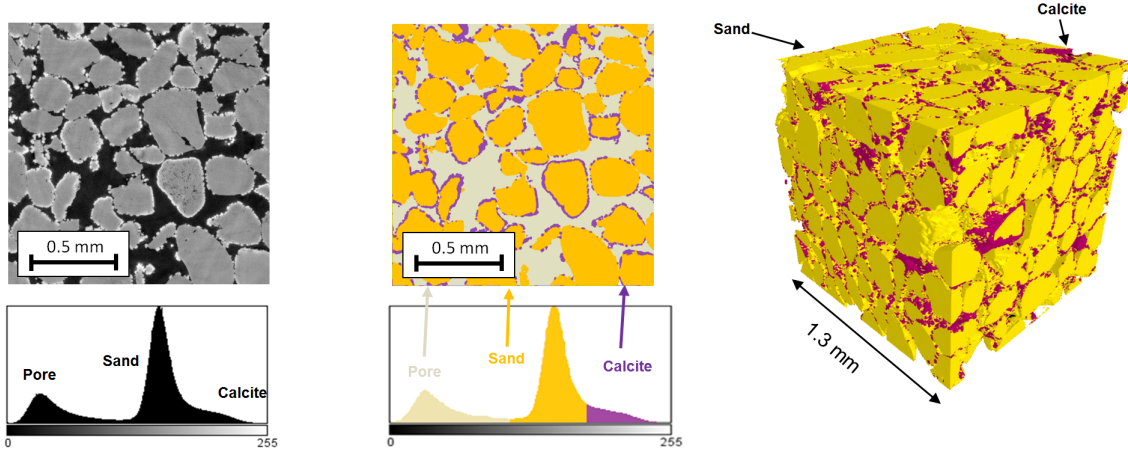


FIGURE 4.5: Image treatments applied on 2D images and the corresponding 3D volume.

4.2.4.2 Computed microstructural properties

Microstructural properties, such as the porosity (ϕ), the volume fraction of calcite (f_c), the correlation length (l_h), the overall specific surface area (SSA) and the specific surface area of calcite (SSA_c) can be computed on 3D volumes extracted from the total segmented 3D images. These volumes must be large enough to be representative of the material. For that purpose, here after, two methods have been used (Kanit et al., 2003) :

- The Representative Elementary Volume (REV) is estimated by performing a systematic analysis of the volume size influence on the computed properties. The REV is given by the size of the volume for which the fluctuations of the effective property become limited. For that purpose, each microstructural property was computed on volumes of size ($l \times l \times l$ mm³), where l varies from 0.1 mm to 1.3 mm. In the following, this method is referred as the “REV approach”.
- The effective property under consideration is computed by taking the average of the apparent properties of a large number of non-overlapping sub-volumes of the same size (Kanit et al., 2003; du Roscoat et al., 2007). In the present case, sub-volumes of 400³ voxel (of about one sand grain) distributed over the total volume have been chosen for the computation of the effective properties from the 3D images. This choice was done after testing different configurations of different sizes and numbers of sub-volumes in order to find the most effective configuration (from the points of view of accuracy and computation time). In the following, this method is referred as a “statistical approach”.

As already mentioned five microstructural properties have been computed on the 3D images of biocemented samples :

Porosity (ϕ) and volume fraction of calcite (f_c) : These two quantities are computed by a simple counting of voxels of each phase within the 3D images. The mass fraction of calcite (m_c) can be easily deduced from these two quantities, assuming that the density of the sand and the calcite are $\rho_s = 2650 \text{ kg/m}^3$, $\rho_c = 2710 \text{ kg/m}^3$, respectively.

Correlation lengths (l_h) : For each image, we can compute the following two-points correlation function for the air phase : $S_2(r) = < I(x)I(x+r) >$ where r is a vector, $I(x)$ is the characteristic function of the air phase ($I(x) = 1$ if x lies in the air phase and 0 otherwise) and the angular brackets denote the volume average. In general $S_2(r=0)=\phi$ where ϕ is the porosity ; $S_2(r)$ decreases with increasing r and tends towards an asymptote defined by $S_2(r=l_h)=\phi^2$, where the norm of l_h is defined as the correlation length. This correlation length can be computed for any direction of the vector r within the 3D space. These correlation lengths are often used to characterize the typical size of the heterogeneities within the microstructure, and to quantify its anisotropy (du Roscoat et al., 2007; Calonne et al., 2014; Torquato, 2013).

Total specific surface area (SSA) and specific area of calcite (SSA_c) : Several numerical methods have been proposed in the literature to compute the specific surface area from 3D binary images (the stereological approach, the marching cubes approach, and the voxel projection method (Flin et al., 2011)). In this work, the stereological approach is used. This method is based on the averaging of the number of interface points per unit length computed in the 3 directions of the 3D image (Flin et al., 2011). This method has been used to compute :

- The total specific surface area (SSA) defined as $SSA = (S_g + S_c)/V$, where S_g and S_c are the surface area of the grain and the calcite in contact with the voids (of the air or fluid) respectively, and $V = L^3$ is the volume under consideration (Figure 4.6).
- The specific surface of calcite (SSA_c) defined as $SSA_c = S_c/V$. This specific surface area of calcite, characterizes the surface of calcite in contact with voids. This area will play an important role in the durability of the biocementation process.

In order to evaluate the influence of the biocementation process on the microstructural properties, the porosity, the correlation lengths and the total specific surface area (SSA) were also computed on the same 3D images without calcite, i.e. by replacing the calcite voxels by pore voxels within the 3D images.

The Figure 4.7a presents the typical evolution of the two points correlation function $S_2(x)$ along x for one image of the sub-sample “13MB” with and without calcite. This figure shows that the

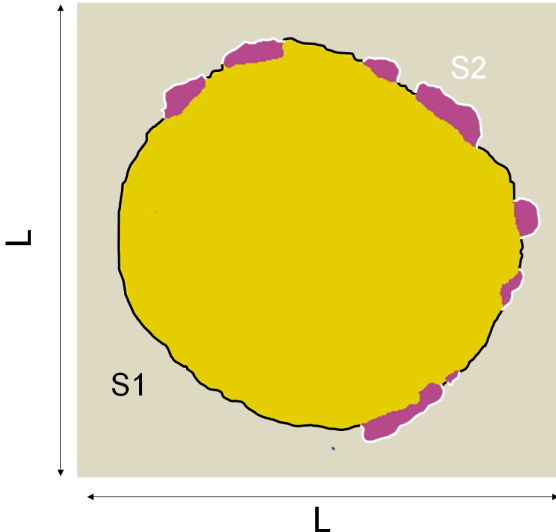


FIGURE 4.6: Total specific surface area : $SSA = (S_g + S_c)/V$; Specific surface of calcite : $SSA_c = S_c/V$.

correlation length l_h is the order of $75 \mu\text{m}$ without calcite. This correlation length characterizes the size of the “heterogeneity” within the sample along x. This correlation length slightly increases with the biocementation process, due to the deposition of the calcite over sand grains. This correlation length has been computed for various angles within the three main planes (x,y), (y,z) and (x,z). The obtained results (red marks Figure 4.7b and Figure 4.7c) were then fitted by an ellipsoid in order to determine the three principal correlation lengths with and without calcite. In the present case, l_{hmax}/l_{hmin} is close to 1 (1.2 without calcite and 1.46 with calcite).

This result, as well as Figure 4.7b and Figure 4.7c, shows that the microstructure of the sand sample before and after treatment is almost isotropic. Similar results have been obtained on all the observed sub-samples whatever the volume fraction of calcite. Figure 4.8 presents the microstructural properties (volume fraction of calcite, porosity, SSA and SSA_c) computed on the sub-sample “13MB” using both the REV and statistical approaches. The numerical results obtained using the “REV approach” (Figure 4.8a,c,e,g) show that all the computed properties tend towards a constant value when the volume size is larger than $(1 \times 1 \times 1 \text{mm}^3)$, i.e. larger than around $(10 \times 10 \times 10)_h^3$ (1000 heterogeneities). Figures 4.8 (b,d,f,h) present the evolution of the computed properties with respect to the number of sub-volumes. In this figure, “M” the relative error, defined as $(M_{SA} - M_{RA})/M_{RA}$, where the subscripts SA and RA refer to the value computed following the statistical approach and REV approach respectively, is also reported for each microstructural property. The value M_{RA} is the computed value on a volume of $(1 \times 1 \times 1 \text{mm}^3)$. We can observe that in general, this relative error between the two approaches is smaller than 5% when the number of sub volumes is greater than 16. Similar results have been obtained on all the sub-samples.

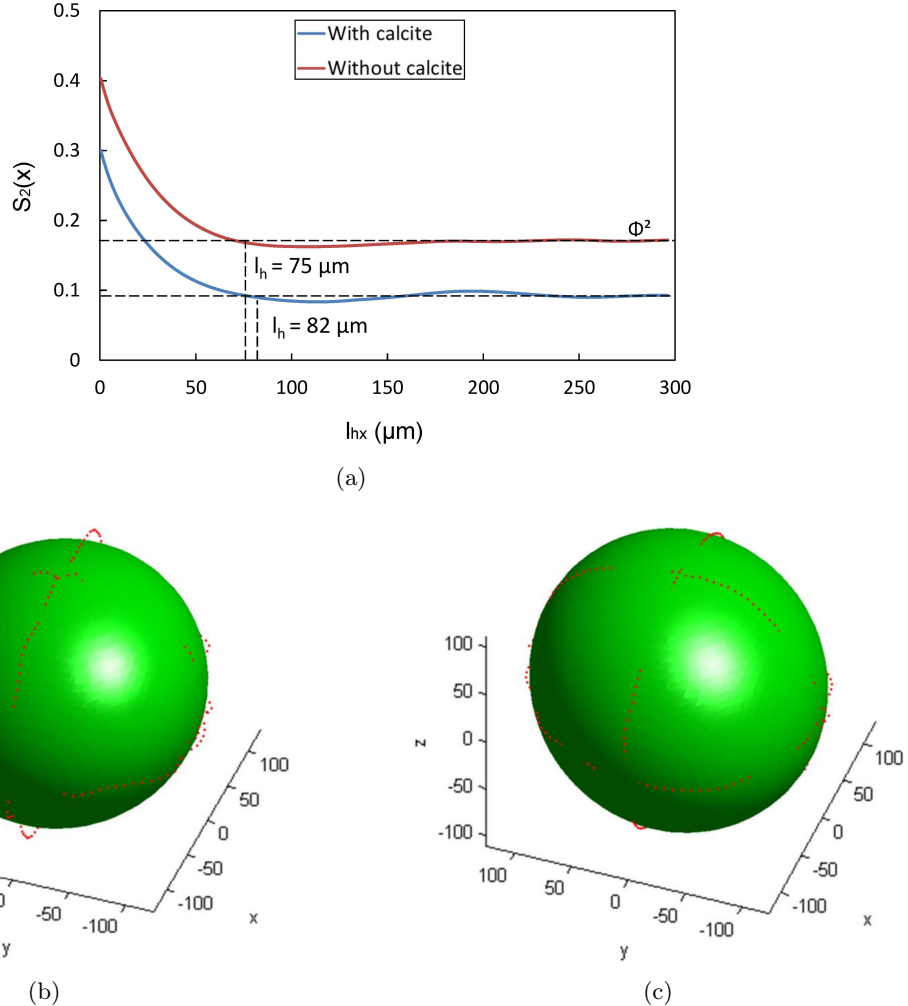


FIGURE 4.7: Two-points correlation function $S_2(x)$ for the air phase computed on a 2D image of the sub-sample “13MB”. Correlation lengths computed on the total 3D volume of the sub-sample “13MB” within the three main planes (x,y), (y,z) and (x,z) (b) without calcite, (c) with calcite. The green surface was adjusted on the numerical values (red mark).

4.2.4.3 Physical properties

The permeability tensor (\mathbf{K}) and the effective diffusion tensor (\mathbf{D}) of the biocemented samples have been computed by solving on 3D images specific boundary value problems arising from the periodic homogenization process (Boutin and Geindreau, 2010; Auriault et al., 2010). The knowledge of these two effective physical properties is important in order to describe the transfer through the soil during and after the process, or to study the stability of the reinforcement. These two tensors have been computed on binarized 3D images by using the Geodict software and following the statistical approach only, which is more efficient (short computation time, less memory resources are needed). For a better accuracy, even if 16 subvolumes could have been sufficient (according to the section 4.2.4.2), the computations have been performed on a maximum of 27 sub-volumes. Figures 4.9a and b show the components of the permeability tensor and the dimensionless effective diffusion tensor (D/D_m) where D_m is the molecular diffusion coefficient)

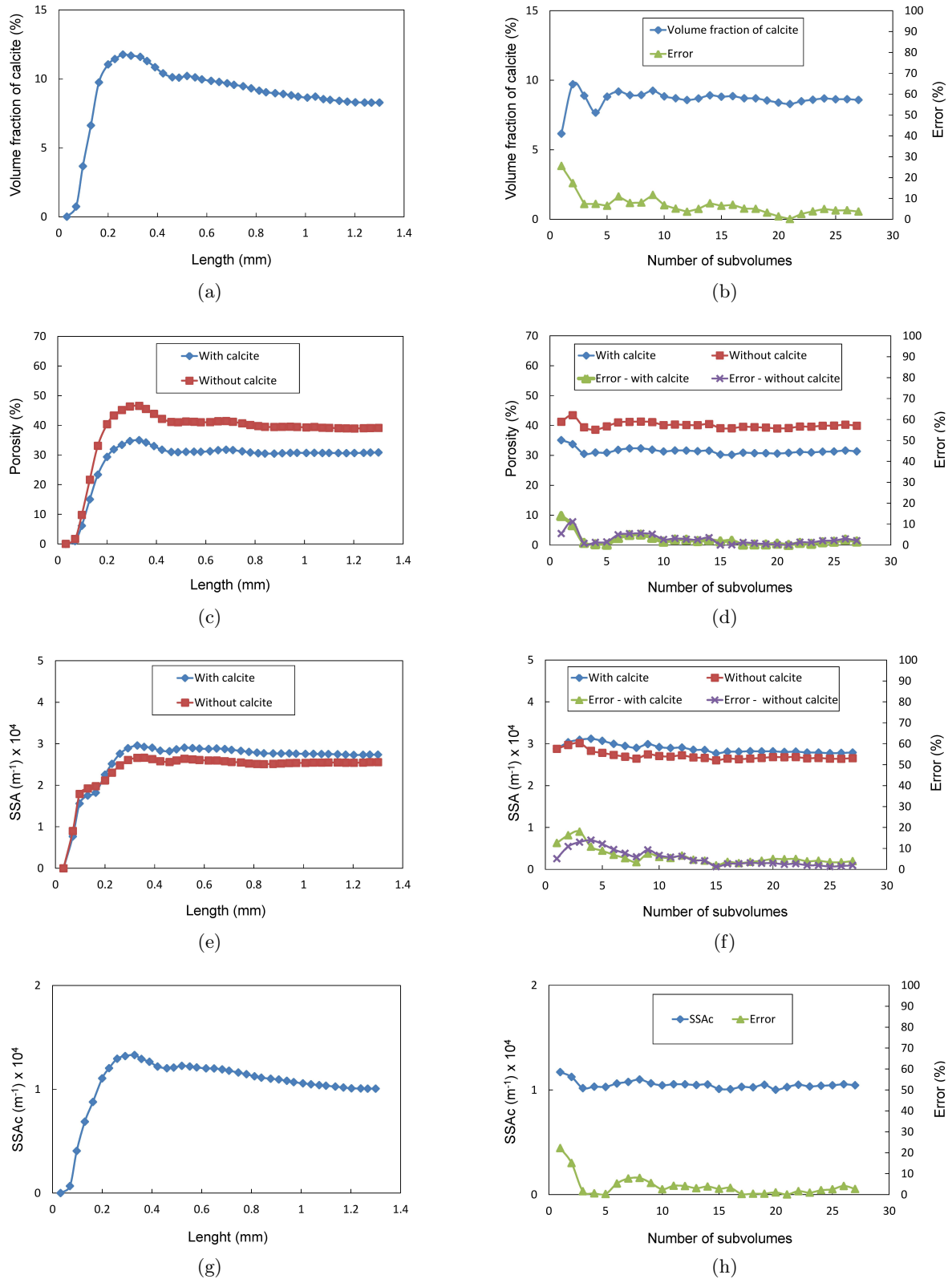


FIGURE 4.8: Microstructural properties computed on the sub-sample "13MB" by using the REV approach (a,c,e,g) and the statistical approach (b,d,f,h).

of the sub-sample 13MB mentioned previously. The sample appears to be isotropic (Figures 4.9a and b) because :

- The off-diagonal terms are negligible compared to the 3 diagonal ones.
- The 3 diagonal components of the permeability and diffusion tensor are almost identical, and consequently these two properties can be considered as isotropic.

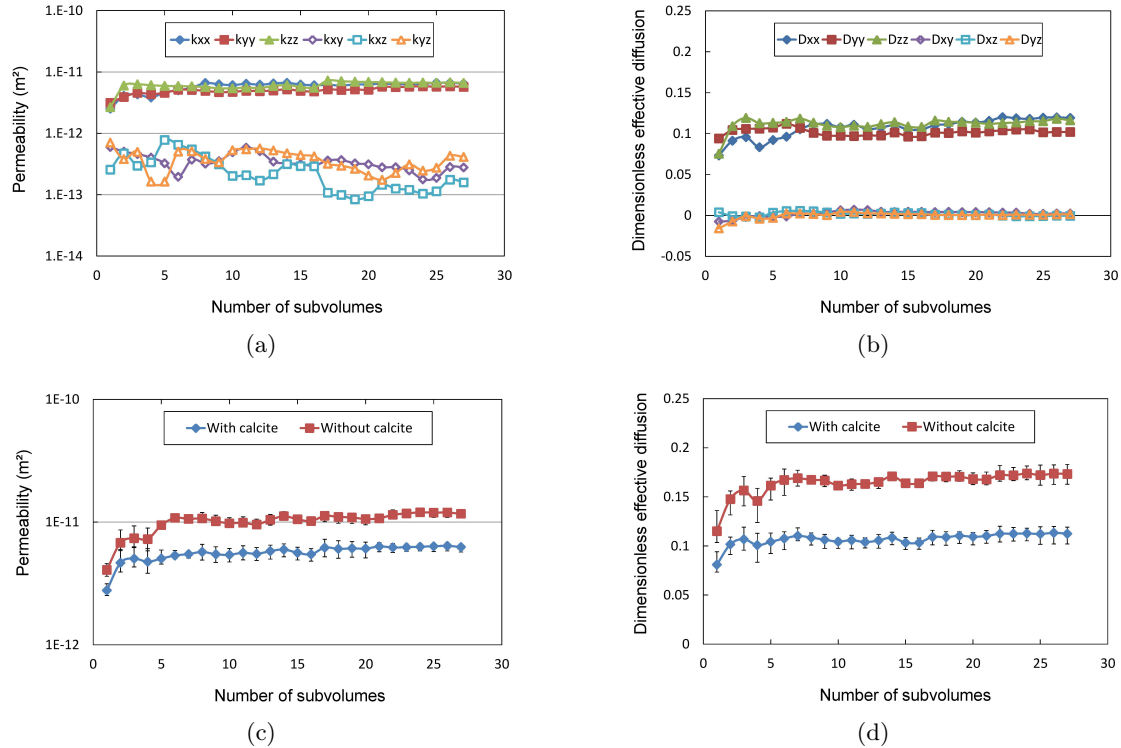


FIGURE 4.9: Evolution of the physical properties computed on the 3D images of the sub-sample “13MB” versus the number of subvolumes under consideration : (a) and (b) permeability components, (c) and (d) dimensionless effective diffusion components.

This result is consistent with the isotropy of the microstructure observed using the correlation lengths. The values of the properties under consideration stabilize after a small number of sub-volumes greater than 10 sub-volumes. According to these results, in the following the effective value of each property (permeability, effective diffusion) is taken as the mean of the 3 diagonal components computed on 27 sub-volumes. The same comments apply for the properties computed on images where the calcite has been replaced by voids (labelled “without calcite” in Figures 4.9c and d) and are valid for all the sub-samples under consideration in this work.

4.3 Results and discussion

In what follows, all the results computed on the 3D images correspond to the value obtained by using the statistical approach considering 27 sub-volumes of 400^3 voxels.

4.3.1 Microstructural and physical properties from 3D X-ray microtomography

4.3.1.1 Initial porosity and mass fraction of calcite

Porosity : The initial porosity of the sand columns has been measured during the preparation of the columns ; the corresponding values are presented in Table 4.2 for each sand column. The experimental values of the initial porosity measured on the entire column can be compared with the ones computed on 3D images of the sub-samples extracted from the same column (Figure 4.10a). The Figure 4.10a shows a good agreement between both the experimental and numerical values. The observed differences can be mainly explained by the difference of scales of the considered samples : the total porosity of columns corresponds to a volume of $2 \times 10^3 \text{ mm}^3$, whereas for 3D images, the volume of the subsamples is of about 2 mm^3 , which represents a local measurement of the porosity.

Mass fraction of calcite : The measurements of the mass fraction of calcite show a non-uniform distribution of the amount of the deposited calcite along the sand columns (Table 4.2), which can be due to several parameters : injection velocity, bacteria and ingredients concentration. In general, this distribution is characterized by a maximum of calcification in the middle of the columns as shown in Table 4.2, and in Figure 4.4, which presents 2D images obtained by X-ray microtomography from the same column (2) at different positions (Bottom, Middle, and Top). Figure 4.10b presents a comparison between the mass fractions of calcite deduced from the 3D images with the ones measured using Bernard calcimeter. This figure shows a good agreement between both experimental numerical values. Once again, the observed differences can be mainly explained by the difference in volume size of the samples used for 3D imaging (2 mm^3) and in Bernard calcimeter (500 mm^3). Despite these differences, this comparison validates the image treatment proposed in section 4.2.4.1, and more precisely the proposed methodology for the separation between the two overlapped phases, which is based on the assumption of a Gaussian distribution of the grey level for the sand phase

4.3.2 Correlation lengths

The mean correlation length, defined as the mean of the principal values of the ellipsoid fitted on numerical values (see section 4.2.4.2) has been computed on the 3D images of all the sub-samples under consideration. In absence of calcite, we found that this mean correlation length associated to the grain sand and pores is about $85 \pm 8 \mu\text{m}$. The Figure 4.11 show the evolution of the ratio between mean correlation lengths before and after the MICP treatment with respect the

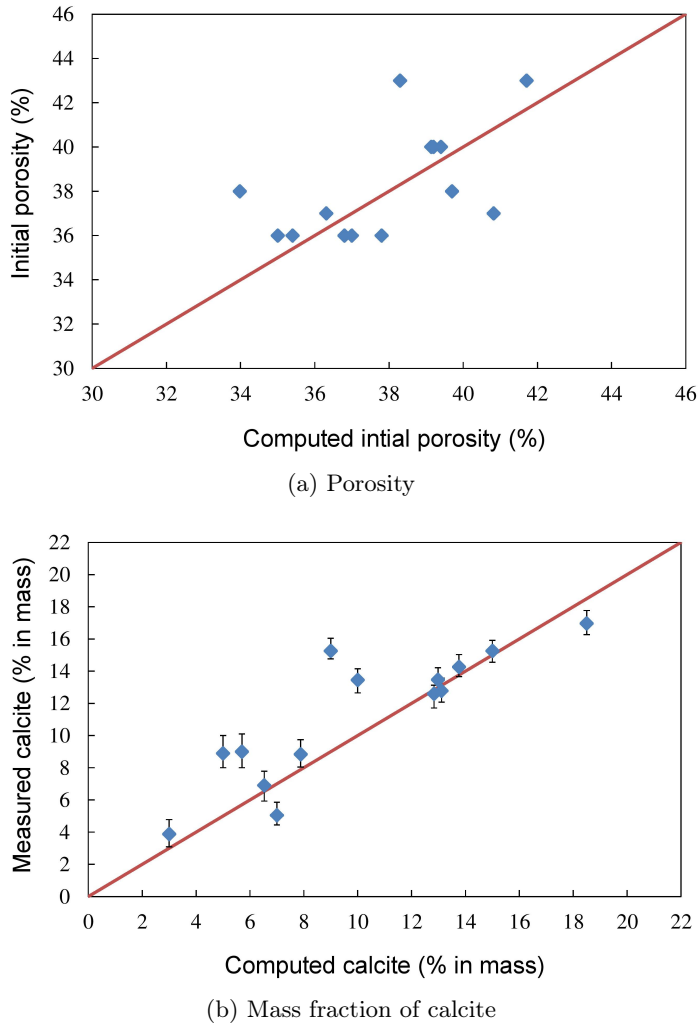
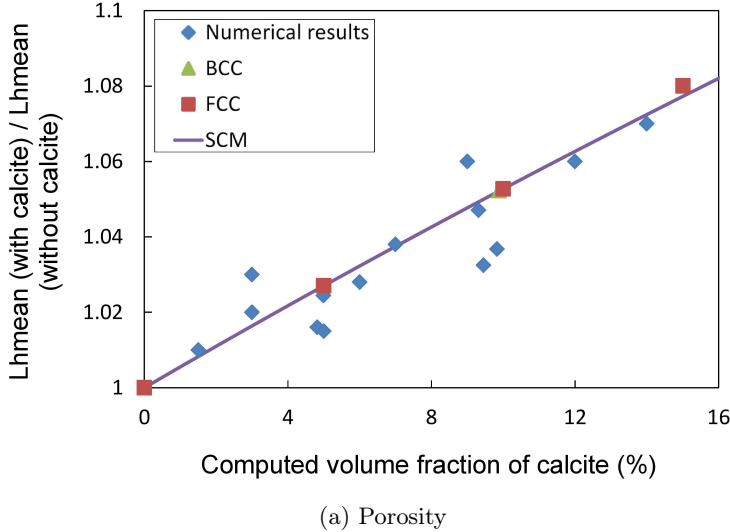


FIGURE 4.10: Experimental versus the numerical results computed on 3D images : (a) initial porosity, (b) mass fraction of calcite. The vertical error bar represents the minimum and the maximum of 4 measurements.

computed volume fraction of calcite (f_c). As already observed on Figure 4.7, this ratio increases almost linearly with increasing the volume fraction of calcite and indicates, in first approximation, that the mean thickness of the calcite layer which covers the “heterogeneities” is the order 6 to 7 microns in average when $f_c=15\%$. This thickness represents typically one layer of calcite crystals, as shown in 4.3.

4.3.2.1 Total specific surface area (SSA) and specific area of calcite (SSA_c) :

Total specific surface area (SSA) : The evolution of the total specific surface (SSA) area is not significant with the increase of the quantity of the deposited calcite. Figure 4.12 shows the evolution of the ratio of the SSA with and without calcite versus the volume fraction of calcite. This figure shows that this ratio, which ranges between 0.8 and 1.15, slightly increases when $f_c < 10\%$ approximately and then decreases. The slight increase can be interpreted as the development of a rough layer created by the precipitation of calcite on the grain surface,



(a) Porosity

FIGURE 4.11: Evolution of the ratio of the mean correlation lengths with and without calcite versus the volume fraction of calcite.

without modification of the number of contacts between grains. For $f_c > 10\%$, the rough surface created by the deposition of calcite on the grain surfaces is balanced by the disappearance of surfaces induced by the creation of new contacts between grains, leading to a decrease of the SSA .

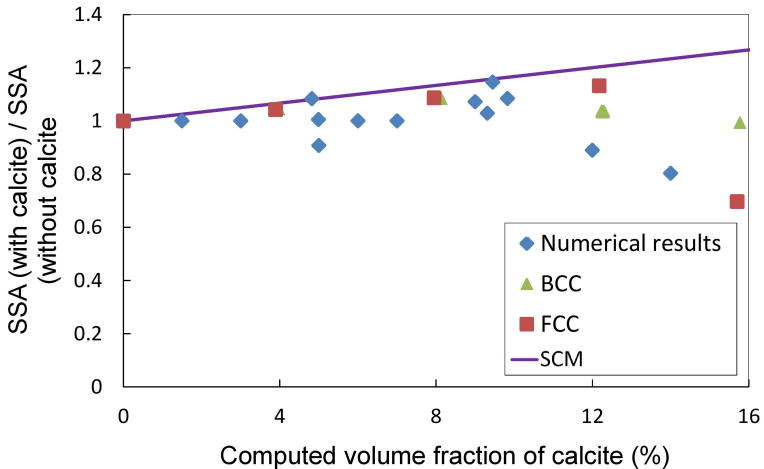


FIGURE 4.12: Evolution of the ratio of the SSA with and without calcite versus the volume fraction of calcite computed on 3D images. Comparison with analytical estimate (SMC) and numerical values (BCC, FCC).

Specific area of calcite (SSA_c) : Figure 4.13 presents the evolution of the ratio between the specific surface area of calcite SSA_c) and the total specific surface area (SSA) of the cemented sand versus the volume fraction of calcite. According to the definition of $SSAc$ and SSA (see section 4.2.4.2), this ratio is written : $SSAc/SSA = (S_c/S_g)/(1 + (S_c/S_g)$, where S_c and S_g are the surface area of the grain and the calcite in contact with the voids. This ratio, which

characterizes the percentage of the initial surface of sand covered by the calcite, is equal to 0 when $S_c = 0$ (no calcite), to 0.5 when $S_c = S_g$ and 1 when $S_g = 0$, i.e sand grains are totally covered with calcite. The figure shows that when $f_c < 6\%$ approximately, this ratio increases almost linearly with increasing the volume fraction of calcite and then seems to reach a constant value around 0.4 to 0.5, i.e the calcite covers between 40 and 50% of the sand surface. As already mentioned, the injection procedure is repeated twice to get columns with a high mass fraction of calcite. The above results seem to show that during the second injection procedure, the bacteria are preferably attached on the calcite crystals already precipitated during the first injection procedure.

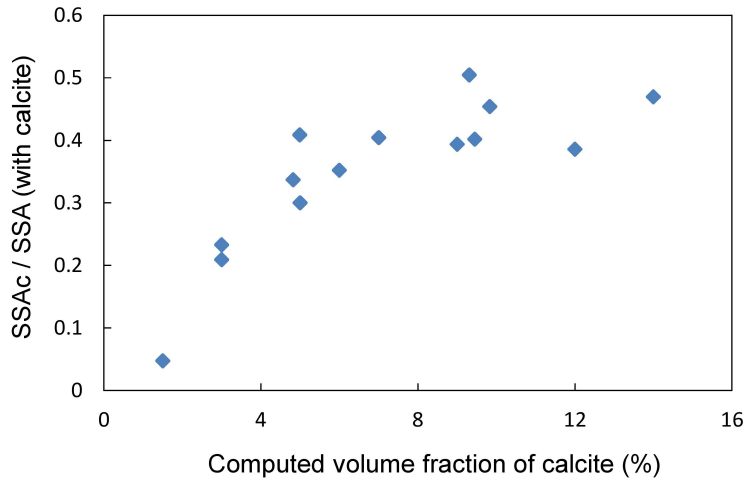


FIGURE 4.13: Evolution of the ratio SSAC/SSA versus the volume fraction of calcite computed on 3D images.

4.3.3 Permeability and effective diffusion

Permeability : Figure 4.14 shows the evolution of the permeability ratio of the same sub-sample with and without calcite versus the volume fraction of calcite. A non-linear decrease of permeability of the cemented sand was found with the increase of the cementation level (Figure 4.14). This reduction, which is about 70% for a volume fraction of calcite of 14%, is mainly due to the reduction of the porosity of the porous media, and the change of the microstructural properties (SSA, tortuosity) with the calcite deposition. Figure 4.14 shows also a good agreement between the permeability computed on the 3D images of sub-samples and the ones measured on triaxial samples. The slight differences observed can be mainly explained by the difference in volume size of the sample used for 3D imaging and for triaxial tests, i.e. the heterogeneity in cementation of the sand columns and potential clogging localized in the porous structure generated by the calcite precipitation within the pores.

Effective diffusion : The evolution of the effective diffusion ratio of the same sub-sample with and without calcite versus the volume fraction of calcite is presented on Figure 4.15. This ratio

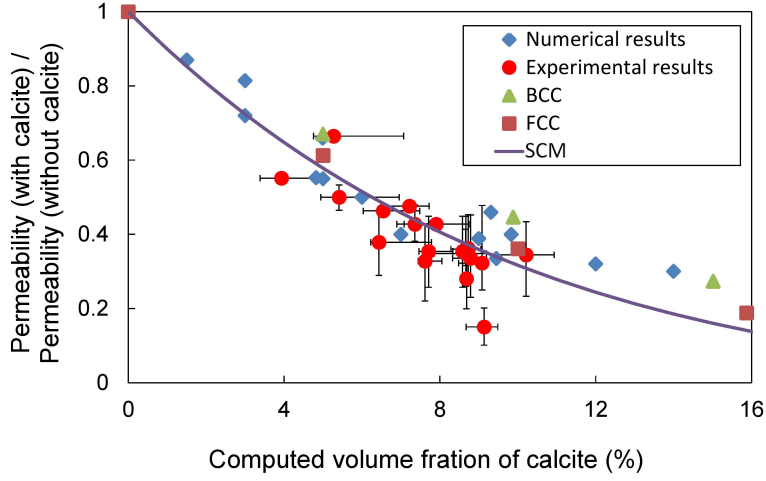


FIGURE 4.14: Evolution of the permeability ratio of the same sub-sample with and without calcite versus the volume fraction of calcite computed from 3D images. Comparison with experimental values, analytical estimate (SCM) and numerical values (BCC, FCC). The vertical and horizontal bars represent the minimum and the maximum values of three different measurements.

decreases almost linearly when increasing the volume fraction of calcite, i.e. when decreasing the porosity. For a volume fraction of 14%, the effective diffusion is reduced by around 50%.

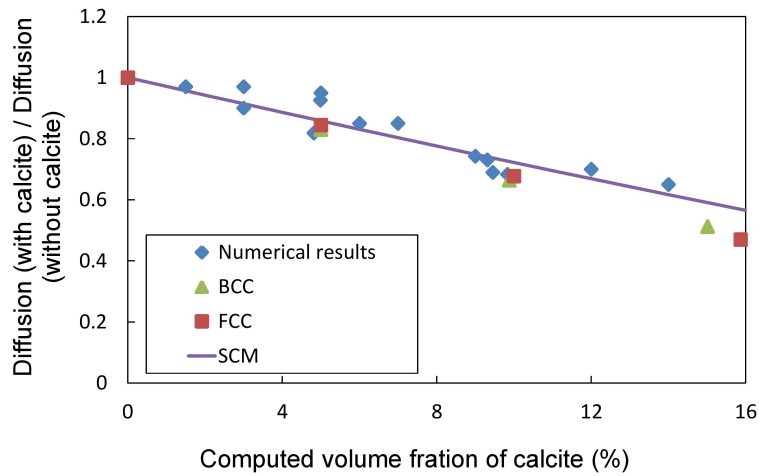


FIGURE 4.15: Evolution of the effective diffusion ratio of the same sub-sample with and without calcite versus the volume fraction of calcite computed from 3D images. Comparison with analytical estimate (SCM) and numerical values (BCC, FCC).

4.4 Comparison with analytical estimates and numerical values

4.4.1 Models

The prediction of the physical and the microstructural properties from basic morphological information on the porous media is available nowadays. The periodic homogenization method (HPM) represents one of the most important approaches, to go from the microscopic to the macroscopic description of the material (Boutin and Geindreau, 2010; Auriault et al., 2010). It requires a minimum of information on the porous structure, for instance in the case of a granular material, on the shape, size and arrangement of grains. The self-consistent method (SCM) represents an alternative approach, which does not require detailed information on the morphology of the microstructure and thus enables to obtain analytical estimates. In the following, we proposed to compare our numerical and experimental results obtained on biocemented soils (see section 4.3.1) with numerical results and analytical estimates obtained for simple arrangements of coated spheres with calcite. More precisely, our results are compared :

- with numerical values computed using the HPM method (Boutin and Geindreau, 2010) on two periodic arrangements Body Centered Cubic (BCC) and Face Centered Cubic (FCC) of overlapping coated spheres of same radius. The representation of the calcite deposition in the sand sample is simulated by the growth of a uniform layer on the spheres in both BCC and FCC microstructures (Figures 4.16a and b).

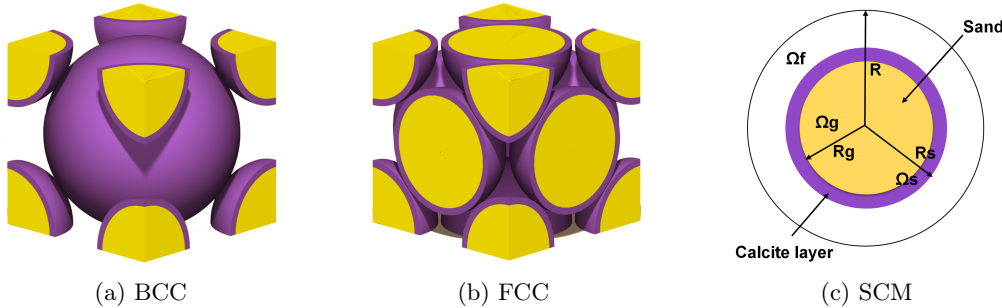


FIGURE 4.16: Periodic lattices of coated shperes with calcite : a) body-centred cubic arrangement (BBC), b) face-centred cubic arrangement (FCC), c) bi-compisite sphere constituted by a coated grain Ω_s (sand (Ω_g) + calcite) surrounded by a spherical shell Ω_f full of fluid.

- with analytical estimates derived by the SCM method. In that case, the microstructure is seen as a random assemblage of non-overlapping coated spheres surrounded by a fluid shell (bi-composite spherical pattern) (Figure 4.16c). The analytical estimates for the permeability and the effective diffusion can be easily deduced from the ones presented in Boutin and Geindreau (Boutin and Geindreau, 2010). The permeability estimate is written :

$$k = \frac{R^3}{2} \left[-1 + \frac{2 + 3\beta^5}{\beta(3 + 2\beta^5)} \right] \quad (4.3)$$

where $k(f_c)$ is the intrinsic permeability (m^2), $\beta = R_s/R$ where R and R_s are the radius of the bi-composite sphere and the solid phase respectively. This factor can be expressed as a function of the current porosity (ϕ) by $\beta = \sqrt[3]{1 - \phi}$ with $\phi = \phi_0 - f_c$, where ϕ_0 and f_c are the initial porosity and the volume fraction of calcite respectively. The effective diffusion estimate reads :

$$D = D_m \left(\frac{2\phi}{3 - \phi} \right) \quad (4.4)$$

where D_m is the molecular diffusion coefficient.

4.4.2 Correlation lengths and total specific surface area (SSA)

On Figure 4.11, for each microstructure, the ratio between the radius of the grain with and without the calcite layer with respect to the volume fraction of calcite is reported. This figure shows a good agreement between numerical values of the correlation lengths ratio computed on 3D images and this ratio whatever the volume fraction of calcite. This result confirms our previous comments about the thickness of the calcite layer, which covers the sand grain.

For each microstructure, the total specific surface area (SSA) can be analytically estimated. These analytical estimates are based on the calculation of surface area of the spheres for each structure taking into account the evolution of the contacts surfaces as a function of the growth of the calcite layer. The initial porosity of all the microstructures is supposed to be about 37%, as the experimental one. The evolution of the SSA with respect to the volume fraction of calcite for the three microstructures under consideration is presented on Figure 4.12. For $f_c < 10\%$ approximately, this figure shows a good agreement between all the results from 3D images and simple arrangements of coated spheres. For $f_c > 10\%$ approximately, the SSA of the bi-composite spheres still increases with increasing the volume fraction of calcite, which is not consistent with numerical values computed on 3D images. By contrast, Figure 4.12 shows that the SSA of both BCC and FCC arrangements of coated spheres decreases when the volume fraction is typically larger than 8 and 12% respectively. Indeed, when this volume fraction is reached, the spheres start to overlap and new contacts appear, and consequently the SSA decreases. All these results confirm that the particular evolution of the SSA with respect to the volume fraction of calcite is strongly linked to the creation of new contacts within the microstructure.

Finally, let us remark that these simple microstructures suppose that $SSA_c/SSA = 1$ for the whole range of considered porosities, which is not consistent with our numerical results presented on Figure 4.13.

4.4.3 Permeability and effective diffusion

The evolution of the permeability and the effective diffusion with respect to the volume fraction of calcite for the three microstructures under consideration are presented on Figures 4.14 and 4.15 respectively. These figures show a good agreement between all the results for the whole range of volume fraction of calcite under consideration. As expected, the volume fraction of calcite is, at the first order, the most important microstructural parameter responsible for the permeability (or effective diffusion) decay measured experimentally.

4.5 Conclusions

In the present paper, biocemented sand columns with different levels of calcification ($0 < f_c < 14\%$) have been achieved in order to quantify the influence of the precipitated calcite on microstructural (volume fraction of calcite, porosity, correlation lengths, total specific surface area, specific area of calcite) and physical properties (permeability, effective diffusion). All these properties were computed on 3D images at high resolution of sub-samples using synchrotron X-ray tomography and compared with experimental data, when it was possible. All the comparisons have shown a good agreement between numerical and experimental data, despite the differences in volume size of the used samples (for 3D imaging, Bernard calcimeter, permeability). This good correlation between these data also proves the validity of the proposed method to treat the 3D images and to separate the three different phases (sand, calcite, pore). All these numerical and experimental results show that :

- the biocementation process creates a thin layer of calcite over the sand grains. In average, the thickness of this layer is the order of 6 to 7 microns, i.e. the order of one layer of calcite crystals ;
- at low volume fraction of calcite (typically $f_c < 10\%$), the total specific surface area (SSA) slightly increases when increasing the volume fraction, due to the formation of rough surfaces with the precipitation of the calcite on the grain surface. By contrast, for volume fraction of calcite larger than 10%, our results show that the SSA slightly decreases, due to the creation of new contacts between grains.
- the specific surface area of the calcite (SSA_c) increases when increasing the volume fraction of calcite and does not exceed 45% of the total surface of the sand grain when $f_c > 10\%$. This asymptotic value seems to show that the calcite precipitates in preferential locations (contact between grains...).
- the permeability and the effective diffusion, before and after treatment, are isotropic and decrease with an increase of the volume fraction of calcite. For $f_c = 14\%$, these decreases of the permeability and the effective diffusion are about 70% and 40% respectively.

Finally, all these numerical results from 3D images and experimental data have been compared to numerical values or analytical estimates computed on idealized microstructures constituted of periodic overlapping (BCC and FCC) and random non-overlapping (SCM) arrangements of coated spheres. These comparisons show that these simple microstructures are sufficient to capture and to predict the main evolution of the microstructural and physical properties of biocemented sands for the whole range of volume fraction of calcite investigated.

CHAPITRE 5

CHARACTERIZATION OF CONTACT PROPERTIES IN BIOCEMENTED SAND USING 3D X-RAY MICROTOMOGRAPHY

Sommaire

5.1	Introduction	84
5.2	Material and Method	86
5.2.1	Samples and image acquisition	86
5.2.2	Image treatments	86
5.2.2.1	Identification of three phases (pore, sand, calcite)	87
5.2.2.2	Grains separation and labeling	87
5.2.2.3	Identification of each contact and labeling	89
5.2.3	Computed contact properties	89
5.2.3.1	Coordination number	89
5.2.3.2	Contact surface area	89
5.2.3.3	Identification of contact types	91
5.2.3.4	Contact orientation	93
5.3	Results and discussion	94
5.3.1	Coordination number	94
5.3.2	Contact surface area	94
5.3.3	Contacts orientation	96
5.3.4	Contact types and distribution	98
5.3.5	Precipitation pattern and modeling	99
5.4	Conclusion	103

The content of this chapter is submitted to Granular Matter.

Abstract

The mechanical efficiency of the biocementation process is directly related to the microstructural properties of the biocemented sand, such as, the volume fraction of calcite, its distribution within the pore space (localized at the contact between grains, over the grain surfaces) and the contacts properties; coordination number, contact surface area, contacts orientation, types of contact... In the present work, all these micromechanical properties are computed, for the first time, from 3D images obtained by X-ray tomography of biocemented samples. The evolution of all these properties with respect to the volume fraction of calcite are analyzed and compared between each other (from untreated sand to highly cemented sand). Whatever the volume fraction of calcite, it is shown that the precipitation of the calcite is localized at the contacts between grains. These results are confirmed by comparing our numerical results with analytical estimates assuming that the granular media is made of periodic simple cubic (SC) arrangements of grains and by considering two extreme cases of precipitation : (1) the calcite is localized at the contact, (2) the grains are covered by a uniform layer of calcite. In overall, the obtained results show that a small percentage of calcite is sufficient to get a large amount of cohesive contacts.

5.1 Introduction

Strong interactions between the geotechnical engineering and the biology these recent years have resulted in the discoveries of different natural processes, which can be transformed to soil reinforcement techniques such as : the biocementation by using catalytic microorganisms, and the bioclogging for water filtrations, which can be performed by pore-filling material generated by microbial process (Al Qabany and Soga, 2013; Umar et al., 2016). The Microbial Induced Calcite Precipitation (MICP) is considered as one of the most promising techniques of biocementation. Hence, several research works have been performed on order to evaluate the efficiency of this technique for different geotechnical problems ; in the lab by performing standard geotechnical tests (Montoya et al., 2013; Martinez et al., 2013; Jiang and Soga, 2016; Al Qabany and Soga, 2013; Feng and Montoya, 2015; Cheng et al., 2013; Whiffin et al., 2007; Jiang and Soga, 2016) and in-situ by achieving large-scale tests (DeJong et al., 2010a; van Paassen et al., 2010). These studies have shown that this technique strongly enhances the mechanical properties of the soil and slightly decreases the transfer properties such as permeability (Dadda et al., 2017b). Most of these studies (Al Qabany and Soga, 2013; Cheng et al., 2013) also point out that the mechanical efficiency of this process is directly related to the microstructural properties changes of the sand induced by the biocementation process (precipitation pattern of calcite inside the sand specimen and size of calcite crystals). Two precipitation scenarios have been discussed in previous works :

- The localized precipitation : In that case the calcite precipitates preferentially in the grain contacts zone, and increases the cohesion of the soil significantly, with a slight modification of the friction angle. The part of calcite which forms a bridge between two grains is called the effective part (active calcite). This configuration or precipitation pattern is the most

common one which has been observed by using scanning electron microscope (DeJong et al., 2010b; Tobler et al., 2011; Rong et al., 2013; Sel et al., 2015). This affinity of precipitating in particle to particle contacts has been described by DeJong et al. (2010b) using two parameters : the biological behavior and filtering process. During the biocementation process, the bacteria prefers to get attached in the grain contact zones, because of the weak shear stress of fluid flow and the availability of nutriments in these specific places (biological behavior). The other amount of bacteria is suspended in pore fluid and the calcification occurs in this place. Thus, small crystals are suspended and are then forced by the injection process to be attached near the region of intergranular contacts (filtering process). Controlling the amount of effective calcite is possible in reinforced soils by controlling the soil saturation during the biocementation process. Cheng et al. (2013) have shown that lower saturation states have provided more resistant specimen compared with higher saturated specimens due to the localization of the calcite in the small meniscus of water (intergranular contacts).

- Uniform precipitation : The calcite is deposited uniformly on the soil grains and increases slightly the intergranular contact surface area which causes a slight increase of cohesion and friction angle. In that case, a large amount of the calcite is considered as passive because it is not contributing in the cohesion evolution, but it is contributing in an indirect way to the mechanical strength, by roughening the grain surfaces and increasing the friction angle of the treated soil. The surface roughness is an important parameter in the angle friction evolution but not the only one, other parameters interact between each other such as the effective particle size distribution after cementation, the effective angularity, and the coordination number, etc.

Concerning the size of calcite crystals, Al Qabany and Soga (2013) have recently shown that this parameter has a slight influence on the unconfined compression strength. More precisely, they have shown that smaller calcite crystals obtained by low concentration of reactant give slightly higher mechanical resistance compared to a biocemented sand, which contains larger calcite crystal obtained by high chemical reactant concentrations.

Clearly, the mechanical efficiency of the biocementation process is directly related to the microstructural properties of the biocemented sand, such as, the calcite volume fraction and its distribution within the pore space (at the contact between grains, at the surfaces of the grains), the coordination number, the contact surface area, the contact orientation, etc. Nowadays, X-ray micro-tomography represents one of the most efficient techniques to explore the 3D microstructural properties of a porous media in qualitative and quantitative way. The accuracy of the results depends to the resolution and the contrast of the objects in the 3D images. Different studies have been performed to follow the contact characteristics during triaxial test (Druckrey et al., 2016; Ando, 2013). Ando (2013) has performed triaxial tests with X-ray micro-tomography observations on sand and have extracted the evolution of the contact parameters for different triaxial stress levels by separating in two different ways the grains in the 3D images, and by computing the

evolution of the contacts surface area and the coordination number. In this work, the resolution was not sufficient to capture the punctual contact between two grains and the contact surface area have been quantified by direct counting of voxels, which can result in some errors. Tagliaferri et al. (2011) have performed in-situ triaxial test on biocemented sand coupled with X-ray micro-tomography observations. In this work the chosen resolution of $15 \mu\text{m}^3/\text{voxel}$ was not sufficient to capture the shape and the distribution of the calcite at the pore scale. Recently, 3D images of some biocemented samples were performed using X-ray synchrotron micro-tomography on the ID19 beamline at the ESRF in Grenoble (Dadda et al., 2017b). A resolution of $(0.65\mu\text{m}^3)/\text{voxel}$ was chosen in order to visualize precisely the calcite crystals, which have a typical size of 15 micrometers. After thresholding, the trinarized images were used to compute mean microstructural properties (porosity, volume fraction of calcite, specific surface area...) and to quantify their impact on some transport properties (permeability, effective diffusion tensor...) according to the level of biocementation.

In the present work, we propose to determine and to quantify the evolution of the contact properties (contact surfaces, coordination number, contacts orientation, type of contact, etc.) of biocemented sand as function of the cementation level using 3D images obtained by X-ray micro-tomography. The numerical results computed on Representative Elementary Volumes extracted from the 3D images are then compared with numerical values obtained on simple periodic arrangements (SC) of sand grains, assuming that the precipitation is localized at the contacts between grains or uniform. The present paper is organized as follows. The section 5.2 is devoted to the material and methods : 3D images treatment, computed contact properties (coordination number, contact surface area, contact orientation and type of contact). In section 5.3, the properties computed from the 3D images are presented, discussed and compared with analytical estimates on simple microstructures (SC), with a uniform or a localized precipitation.

5.2 Material and Method

5.2.1 Samples and image acquisition

Different biocemented sub-samples have been extracted from triaxial specimens of biocemented sand (Table 5.1). These triaxial specimens have been prepared using Fontainebleau sand (NE34) with an initial porosity ranging from 37% to 40% under different protocol of injections, leading to different biocementation levels (see Dadda et al, 2017, for more details). The mean diameter of sand grain is $D_{50} = 0.21\text{mm}$ with a uniformity coefficient $C_U=1.5$. In the present work, six sub-samples with an amount of calcite ranging from 0 to 17% in mass are considered. As already mentioned, 3D images of these biocemented samples were performed using X-ray synchrotron micro-tomography with a resolution of $(0.65\mu\text{m}^3)/\text{voxel}$ in the ID19 beamline at the ESRF (Grenoble, France). The field of view is $(3250 \times 3250 \times 2000 \text{ voxels})$, i.e $(2.11 \times 2.11 \times 1.3 \text{ mm}^3)$ to obtain 3D images large enough to be representative of the material.

TABLE 5.1: Characteristics of the scanned sub-samples (Dadda et al., 2017b).

Sub-sample	2T	12MB	13TT	11BB	13BT	13MB
Volume fraction of calcite f_c (%)	1.9	3.2	4.7	6.2	8.8	14.9
Mass fraction of calcite m_c (%)	3	5	7	9	12.7	16.9
Initial porosity ϕ_0	38	36	36	43	36	36

5.2.2 Image treatments

To compute the microstructural properties linked to the contact, the 3D images must be treated in order to (1) identify the three phases (pores, sand and calcite), (2) separate and label the grains, which constitute the (sand + calcite) phase, and (3) to identify and label the contacts between grains.

5.2.2.1 Identification of three phases (pore, sand, calcite)

After reconstruction, 3D images in grey levels represent a 3D map that is proportional to the density of each phase within the scanned sample. In order to compute microstructural quantities, the 3D images in grey levels (Figure 5.1 - A1) have been treated to separate the three phases (pore, sand and calcite). In the present case, the pore and the solid (sand+calcite) phases were easily separated by a simple thresholding (Otsu, 1979). By contrast, the separation of the calcite and the sand phases was not straightforward, because of the similar density of these two constituents (for the sand $\rho_s = 2650 \text{ kg/m}^3$, for the calcite $\rho_c = 2710 \text{ kg/m}^3$). To overcome this problem, a method based on the grey level distribution was proposed (see Dadda et al. (2017b) for more details). The Figure 5.1 - A3 shows a 2D image of the sample “12MB” after treatment, where we can distinguish the three phases : pore in light grey, sand in orange, calcite in purple.

5.2.2.2 Grains separation and labeling

The second step of this image processing consists in the separation of the grains, which constitute the (sand+ calcite) phase. This operation has been performed on binarized 3D images of biocemented sand, i.e. assuming that the sand and the calcite phases have the same grey level (Figure 5.1 - A2), using the software Visilog®. Particle separation is obtained using a 3D watershed algorithm. The particle labeling was then achieved with Matlab® by detecting the grains in the 3D images. The key parameter of this watershedding is the tolerated intensity variation to group the markers of the objects in 3D. Indeed, this parameter controls directly the final number of grains. In the biocemented sand, the surfaces of grains are rough, which can lead to an over separation of the grains if this parameter is too small. In the present work, several attempts have been performed on the 3D images in order determine the optimal value leading to realistic grain separation. An optimal value of 8 was found. For example, the image A5 (Figure 5.1) corresponds to the image A2 where the grains (sand+calcite) are now separated and labeled by using different color levels. The contact between two grains is characterized by a voxel clouds with a width of one voxel. Finally, let us remark, for each biocemented sub-sample, a similar 3D image

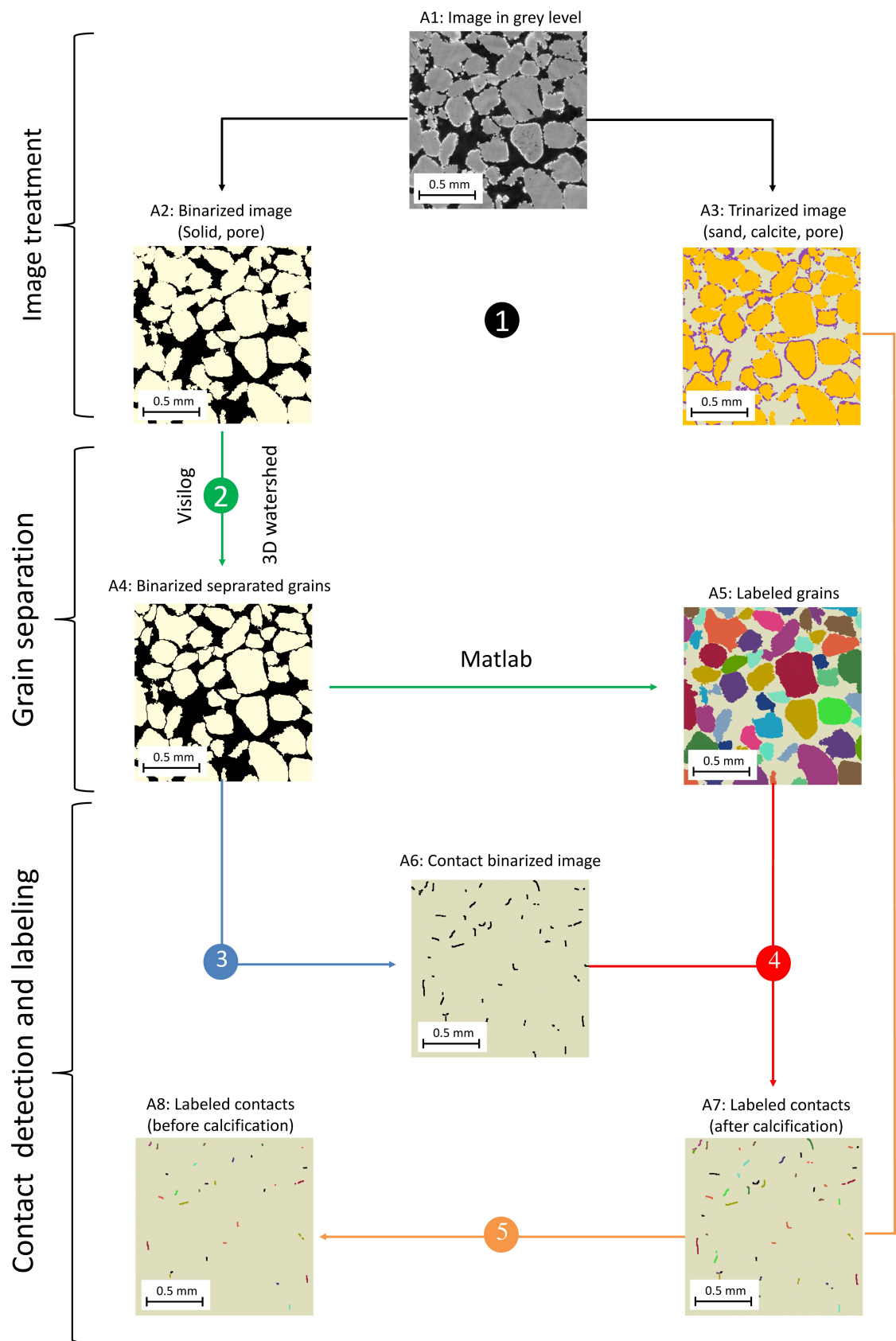


FIGURE 5.1: Different steps of the image treatment (subsample "13BT").

containing the sand grains only can be obtained by removing the calcite phase identified on the 3D image A3 from the image A5. This image is considered as the initial state of the sand before calcification for each sub-sample.

5.2.2.3 Identification of each contact and labeling

In order to identify and label each contact, a dedicated routine has been developed in Matlab®. All the contacts surfaces (Figure 5.1 - image A6) are computed by subtracting the image A2 and the image A4 (Figure 5.1). Then, the Matlab routine allows labeling all the contacts between grains by following a method similar to the one developed by Ando (2013). This method consists in scanning the 26 neighbor voxels of each voxel of the contact surfaces (image A6), and in determining the minimum and the maximum color level of these neighbor voxels in the labeled grains image (image A5). All the voxels with the same minimum and maximum color levels are then supposed to constitute one surface of contact between the two grains labeled with the minimum and the maximum color levels respectively. If the maximum and the minimum color levels are equal, which can occur due some artifacts induced by the grains separation process (voxel of a contact surface inside a grain for example), the voxel is deleted. The image A7 (Figure 5.1) corresponds the image A6 after the labeling of all the contacts. As previously, the 3D image of the labeled contacts without calcite (Figure 5.1 - A8) is then obtained by removing the calcite phase identified on the image A3 from the image A7.

5.2.3 Computed contact properties

5.2.3.1 Coordination number

From both images A5 and A7 (Figure 5.1), a list of all the labeled grains with their corresponding contacts can be constructed. From this list, the coordination number (Z_i) of each grain 'i' can be easily computed. Figure 5.2c shows the distribution of the coordination number (the number of contacts per grain) computed on the 3D image of size (1.3 x 1.3 x 1.3 mm³), which contains around 700 grains (Figure 5.2a), without and with calcite, i.e before and after biocementation. According to these results, we can observe that many grains present 1 to 4 contacts with the others only, which is unrealistic. These grains correspond to the ones located close to the edges of the image. In order to avoid this "edge effects", all these grains (around 300), in black on Figure 5.2b, have not been taken into account in the following analysis. Figure 5.2d presents the new distribution of the coordination number within the sample. This distribution has a classical Gaussian shape. From this distribution, for each sample, we can compute the mean coordination number (\bar{Z}) and the total number of contact (n_t), before (noted with a subscript 'b') and after (noted with a subscript 'a') the biocalcification. For the sample "12MB" presented on Figure 5.2, we have typically : $n_{tb}=798$, $\bar{Z}_b=7.7$ and $n_{ta}=809$, $\bar{Z}_a=7.8$.

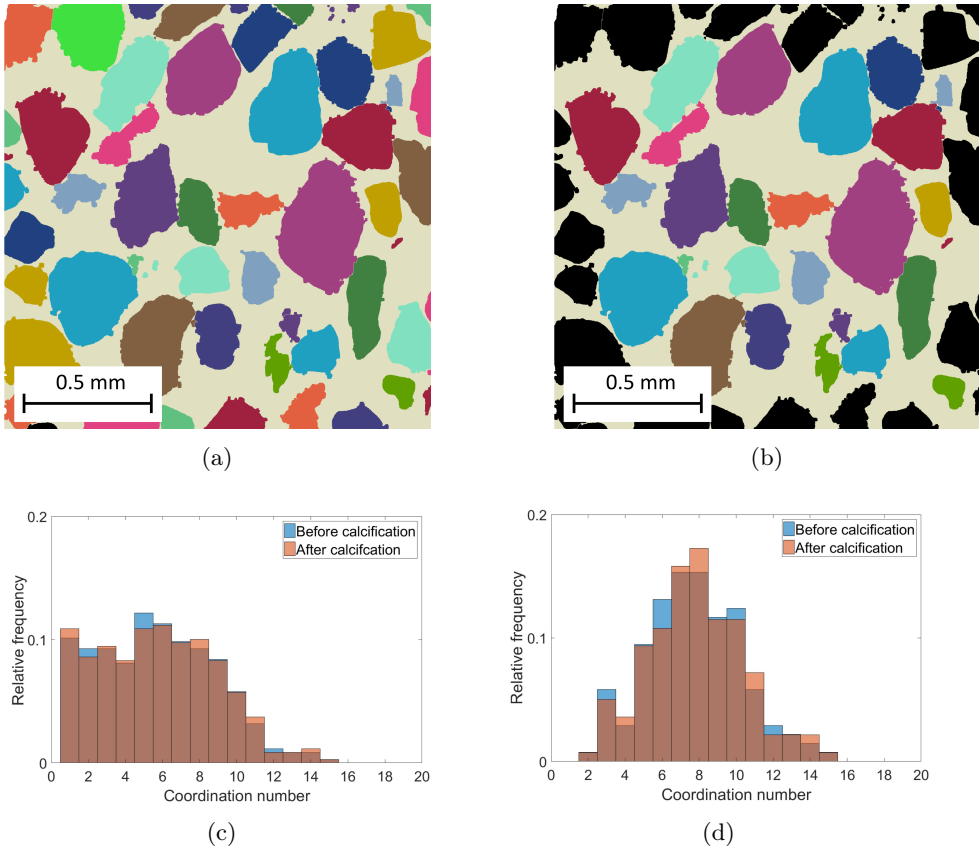


FIGURE 5.2: Distribution of the coordination numbers (c) within the image (a) before and after biocementation, Distribution of the coordination numbers (d) within the image (b) before and after biocementation, without edge effects (subsample “12MB”).

5.2.3.2 Contact surface area

A cloud of voxels with a complex 3D shape (inclined rough surface) represents each contact surface between two grains (Figures 5.3b and 5.3c). A direct computation of the voxels number can be used as a first estimation of the contact surface area. However, this method usually underestimates the real value. For that reason, different methods (marching cube, voxel-based area estimation, Crofton method, etc.) have been proposed in order to compute the surface area of a cloud of voxels (Liu et al., 2010; Legland et al., 2011). In this work, all the contact surface areas have been estimated by using the Matlab function “geometric measures in 2D/3D images” developed by Legland et al. (2011). The surface area is measured using a discretization of the Crofton formula. For regular 3D objects (cubes, spheres and plane surfaces), a discretization along the three main orthogonal directions is sufficient to get a good accuracy of the surface area. When the surface is irregular with a complex shape, it has been shown that 13 directions of discretization are sufficient to estimate the surface area with accuracy (Legland et al., 2011). In order to evaluate the errors induced by the method, we have computed the surface area of well known surfaces. The surfaces under consideration are planar square surfaces of different sizes (the number of voxels varies between 100 and 10000, i.e. the area ranges between $50\mu\text{m}^2$ and

$5000\mu\text{m}^2$), and inclined with an angle of 45° with respect to both planes (XY) and (XZ). An error has been found ranging from 3% for the smaller surfaces to 15% for the larger ones.

For example, Figure 5.3d presents the distribution of the contact surface area for the sub-sample “12MB”, before and after biocalcification. From these results, we can compute the total contact surface area S_t within the sample and the mean contact surface area of each contact defined as $\bar{S}=S_t/n_t$. The total cohesive (or calcite) contact surface area, noted S_{tc} is obtained by subtracting to the contact surface area after calcification S_{ta} the one before calcification S_{tb} : $S_{tc} = S_{ta} - S_{tb}$. The mean cohesive (calcite) contact surface area (\bar{S}_c) per contact is given by : $\bar{S}_c=S_{tc}/n_{ta}$. For the subsample “12MB”, we have typically : $S_{tb}=4.3\times 10^5 \mu\text{m}^2$, $S_{ta}=10^6 \mu\text{m}^2$, $S_{tc}=5.7\times 10^5 \mu\text{m}^2$, $\bar{S}_b=S_{tb}/n_{tb}=564\mu\text{m}^2$, $\bar{S}_a=S_{ta}/n_{ta}=1237\mu\text{m}^2$, $\bar{S}_c=S_{tc}/n_{ta}=705\mu\text{m}^2$. In the present case, the mean contact surface area after biocementation (with calcite) is more than 2 times larger than the one before biocementation (without calcite).

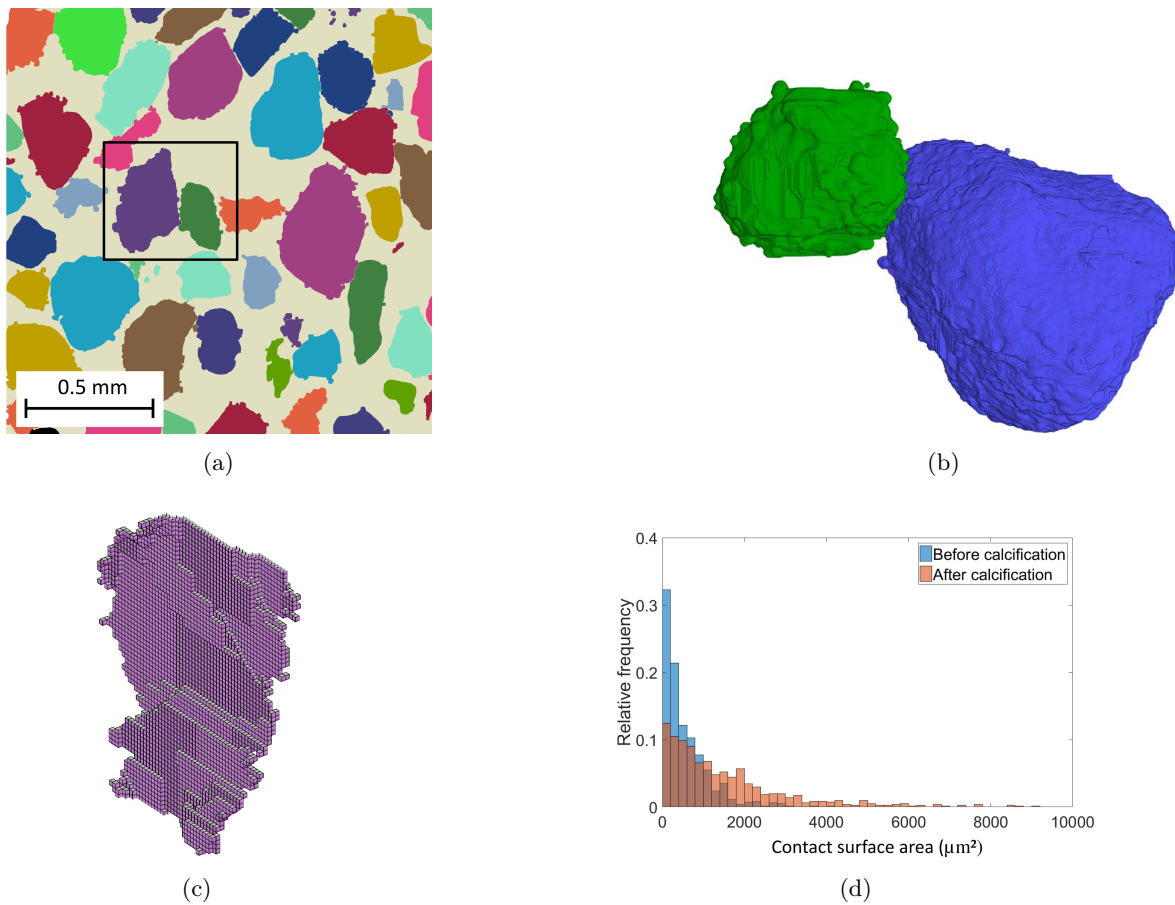


FIGURE 5.3: Geometry of the grain to grain contacts : (a) 2D labeled grains image, (b) example of two grains in contact, (c) contact surface between the two grains in contact, (d) distribution of the contact surface area before and after calcification (subsample “12MB”).

5.2.3.3 Identification of contact types

The type of contact in soil micromechanics is a very important parameter to understand and to predict the macro-mechanical behavior of soils. Generally, in untreated saturated sand, the contacts between two grains of silica are 'frictional'. After cementation, we can distinguish three different types of contact : (1) 'frictional' contacts (silica only) as in untreated sand, (2) 'mixed' contacts and (3) 'cemented' contacts (Figure 5.4). "Mixed" contacts are 'frictional' contacts which became 'cohesive' due to the biocalcification process, as illustrated in Figure 5.4. 'Cemented' contacts are new contacts created by a bridge of calcite between two grains (Figure 5.5). A Matlab® routine has been developed in order to determine these different type of contact in each sample, by scanning the constituent (calcite and/or sand) of each contact surface using images A3 and A7 (Figures 5.1 and 5.4).

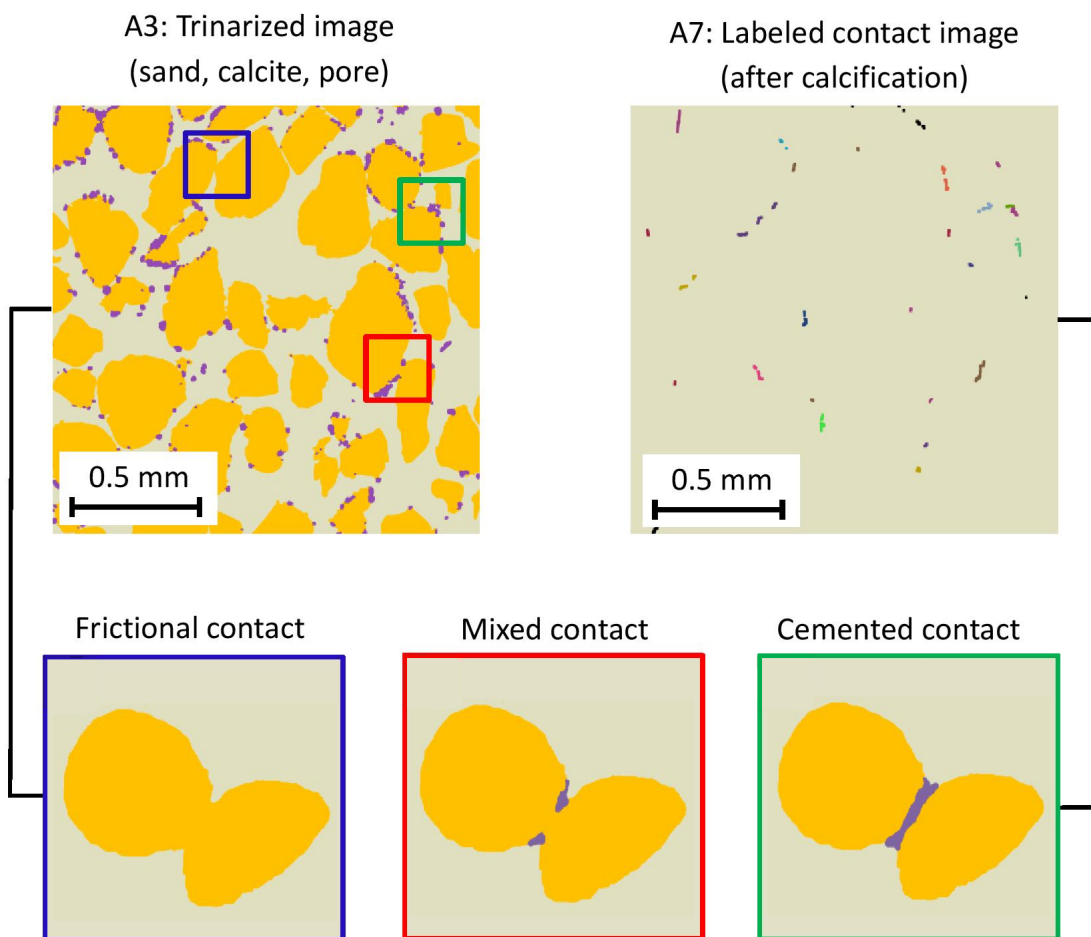


FIGURE 5.4: Definition of the different types of contact.

5.2.3.4 Contact orientation

A cloud of voxels characterizes each contact between two grains. In order to determine the orientation of each contact, this cloud of voxels has been fitted (mean square method) by the equation of a plane in 3D. The normal of this plane, which represents the contact orientation, is then com-

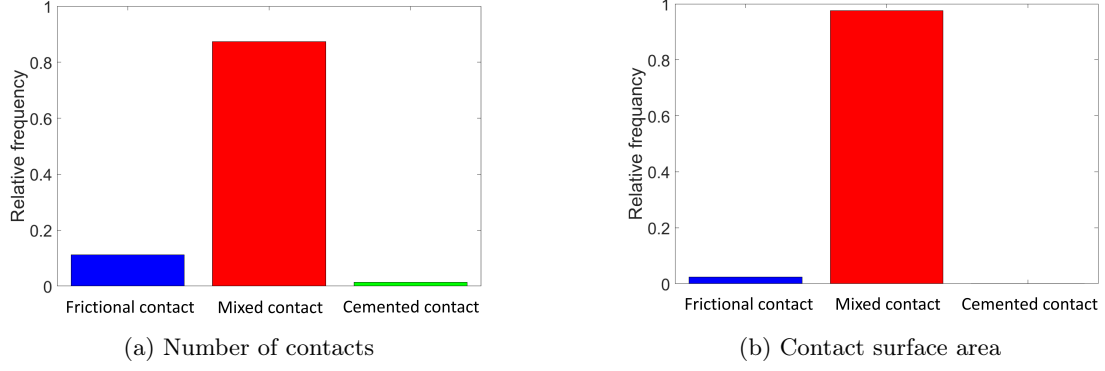


FIGURE 5.5: Distribution of the different types of contact. (a) number of contacts, (b) contact surface area. (subsample “12MB”).

puted. In the following, \mathbf{p}_i is the unit vector associated to the contact ‘i’. These orientations have been computed for the contacts within the sample before and after biocalcification. In a fixed orthonormal coordinate system, the vector \mathbf{p}_i can be defined by its polar angle θ $[0, 2\pi]$, and its azimuthal angle ϕ $[0, \pi]$. Figure 5.6 presents the polar orientation of all the contacts with the sample “12MB”, before and after biocalcification. Different colors are used to distinguish the orientation of the ‘frictional’ contacts (in blue), the ‘mixed’ contacts (in red) and the ‘cemented’ contacts (in green). In the present case, we can observe that the contacts within the sample, before and after biocalcification, are not oriented in a privileged direction, and almost all the “frictional” contacts before biocalcification became ‘mixed’ contact after biocalcification. This later result is consistent with the one presented in Figure 5.5.

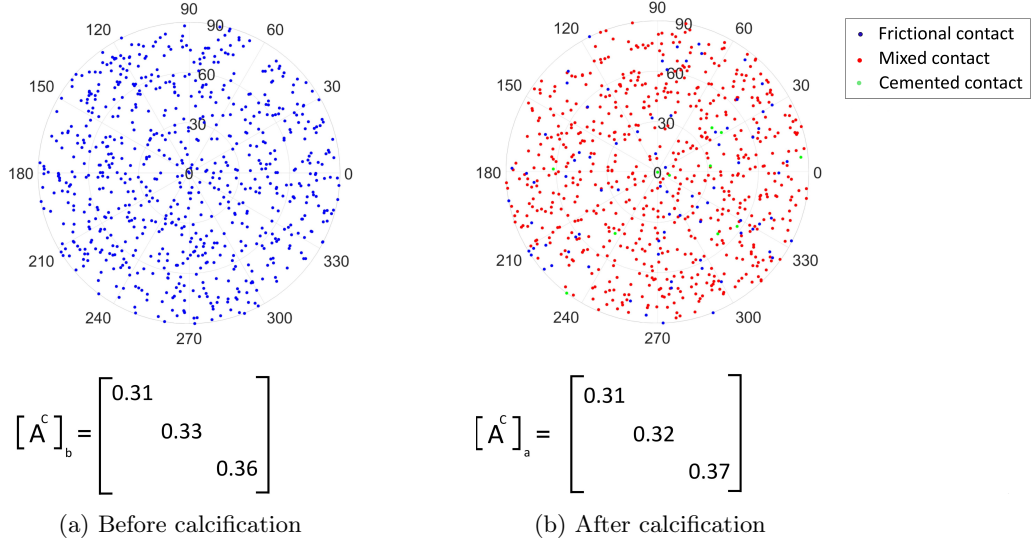


FIGURE 5.6: Contact orientation before (a) and after (b) biocalcification (subsample “12MB”).

Using these results, we can also compute the fabric tensor (\mathbf{A}^c) associated to the contacts orientation, and defined as : $[\mathbf{A}^c] = \sum_N \mathbf{p}_i \otimes \mathbf{p}_i$ where N ($=n_{ta}$, or n_{tb}) is the total of contacts under consideration. Figure 5.6 presents the matrix associated to (\mathbf{A}^c) in the principal axis. We can

observe that the diagonal values are close to 0.33, which confirms that the contact orientation within the sub-sample '12MB' before and after biocalcification is isotropic.

5.3 Results and discussion

5.3.1 Coordination number

Figure 5.7b presents the distribution of the coordination number within the 6 samples under consideration, before and after biocalcification. This figure shows that whatever the volume of calcite, the distribution has a Gaussian shape. When the volume fraction of calcite increases, the distribution after biocalcification slightly moves to the right, i.e. the number of contacts per grain slightly increases due to the calcification process. This result is confirmed by Figure 5.8 which presents the evolution of the ratio (\bar{Z}_a/\bar{Z}_b) of the mean coordination number after and before biocalcification with respect to the volume fraction of calcite. Let us remark that the initial mean coordination number \bar{Z}_b of all the specimen is about 7.1 to 8.5 depending on the initial porosity ϕ_0 which varies between 37 to 40% (see Table 5.1). This ratio (\bar{Z}_a/\bar{Z}_b) is almost constant and equal to 1 when the volume fraction of calcite is lower than 3.2%, and then increases non-linearly until 1.08 for a volume fraction of calcite equal to 14.9%. As expected, due to the calcification process, new contacts or calcite bridges between grains are created. Even if this increase of the mean coordination number is moderate, it can affect significantly the macroscopic behavior of the sample, such as the shear strength.

5.3.2 Contact surface area

Figure 5.7c shows the distribution of contact surface areas before and after calcification for the six specimens. Before biocalcification, as expected, the contact surface areas are small. For all the samples, these contact surface areas typically range between 0 and $3000 \mu\text{m}^2$, and more than 50% of these contact surfaces are smaller than $600 \mu\text{m}^2$, which represents less than 0.4% of the typical outer surface of a grain ($S_{D50}=14 \times 10^4 \mu\text{m}^2$ with $D_{50}=210 \mu\text{m}$). These small values of contact surface area before calcification are due to the nature of contacts between grains in 3D which are almost punctual. After biocalcification, Figure 5.7c clearly shows that the distribution of contact surface areas change progressively as function of the volume fraction of calcite. Indeed, the small surfaces are progressively transformed into large surfaces. The distribution of the contact surface areas becomes almost uniform for a volume fraction of calcite larger than 6.2% and the contact surface areas typically range between 0 and $10000 \mu\text{m}^2$.

From these distributions, we can compute the total surface area of contact, but also the mean contact surface area before calcification (\bar{S}_b), after calcification (\bar{S}_b), and the mean cohesive (calcite) contact surface area (\bar{S}_c) as defined in section section 5.2.3.2. Figure 5.9 presents the evolution of the ratios (\bar{S}_a/\bar{S}_b) and (\bar{S}_c/\bar{S}_a) with respect to the volume fraction of calcite. The ratio (\bar{S}_a/\bar{S}_b) increases almost linearly with respect the volume fraction of calcite. For a volume fraction of calcite of 14.9%, this ratio is of the order of 6. The ratio (\bar{S}_c/\bar{S}_a) increases non-linearly

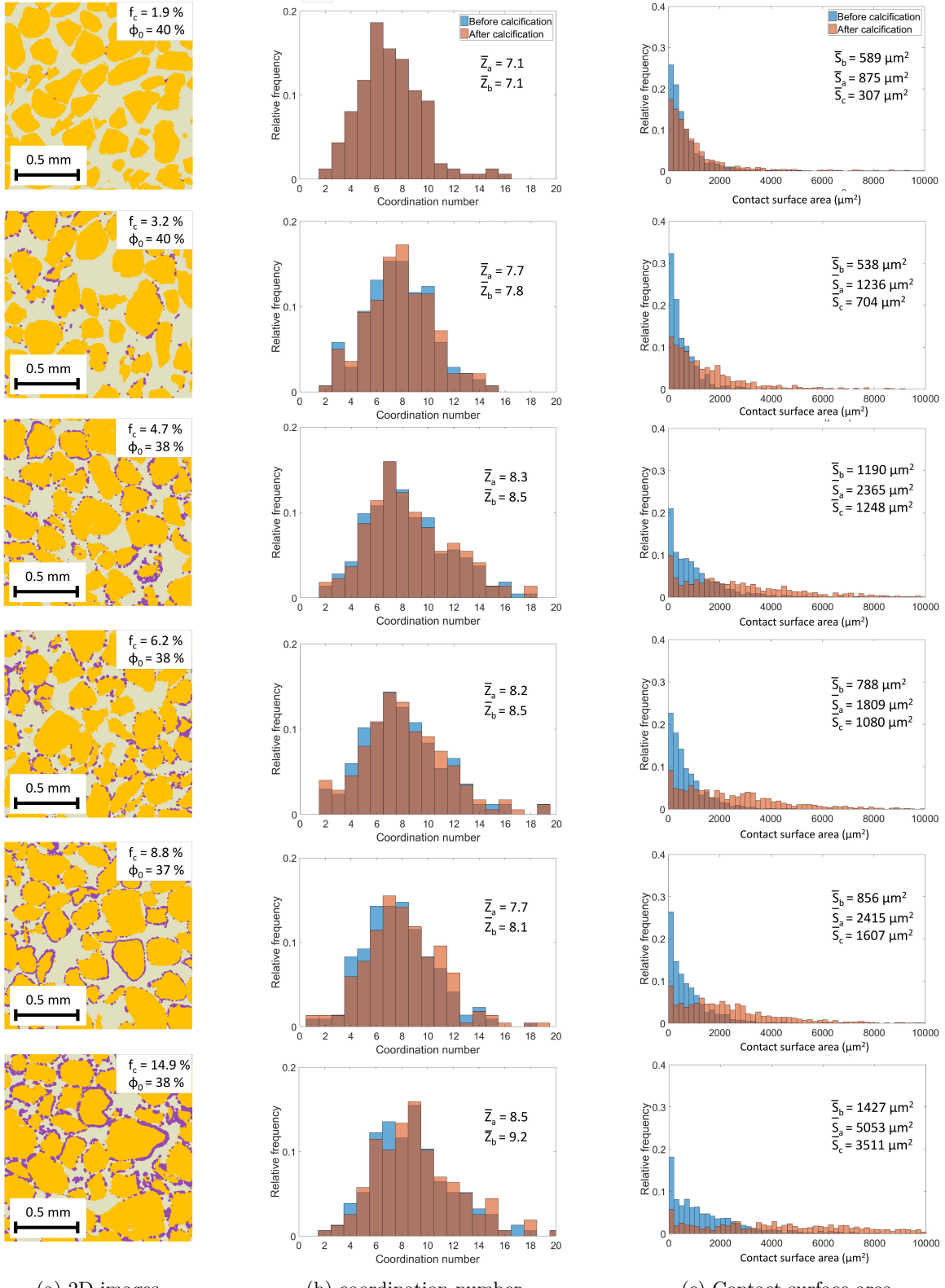


FIGURE 5.7: (a) 2D trinarized images, (b) Distribution of the coordination number within the six samples, (c) Distribution of the contact surface areas within the six samples, before and after biocalcification.

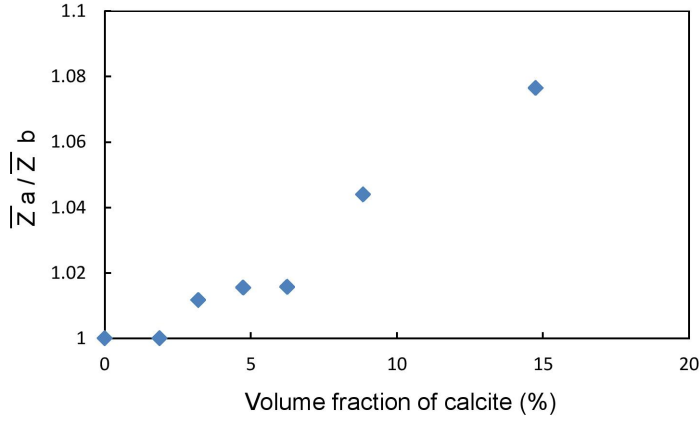


FIGURE 5.8: Evolution of the ratio \bar{Z}_a/\bar{Z}_b of the mean coordination number after and before biocalcification with respect to the volume fraction of calcite.

with respect to the volume fraction of calcite. This evolution shows that for a volume fraction of calcite larger than few percents (around 3%), more than 60% of the contact surface areas after biocalcification are cohesive.

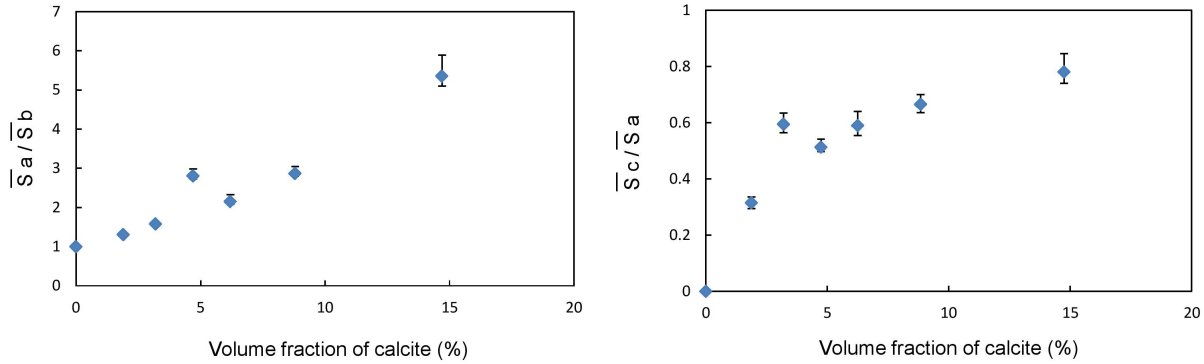


FIGURE 5.9: Evolution of the ratios (\bar{S}_a/\bar{S}_b) and (\bar{S}_c/\bar{S}_a) with respect to the volume fraction of calcite.

5.3.3 Contacts orientation

Figure 5.10 presents the orientation of the contacts within the six samples under consideration, before and after biocalcification. In the polar representation, different colors are used to distinguish the orientation of the 'frictionnal' contacts (in blue), the 'mixed' contacts (in red) and the 'cemented' contacts (in green). The components of the fabric tensor (A^c) are also given. This figure shows that whatever the volume fraction of calcite, the orientation of the contacts is isotropic before calcification and remains isotropic after biocalcification. This latter result seems to prove that preferential direction of the flows (injection of the bacterial solution, reactants etc.) during the biocementation process does not induce any anisotropy. In the present case, after these injections, there is no flow through the sample. This biocementation process can be qualified as 'static'. In practice, if the biocementation process is applied to a dam, there is usually a

continuous flow through the soil. The biocementation process is 'dynamic', and in that case may lead to an anisotropic orientation of the cemented contacts. Finally, Figure 5.10 also shows that almost all the contacts which are initially frictional contacts become mixed contacts when the volume fraction of calcite is larger than few percents. This point is discussed more in details in the following section.

5.3.4 Contact types and distribution

Figure 5.11 presents the distribution of the different types (frictional, mixed, cemented) of contact in terms of number of contacts (Figure 5.11b) and contact surface area (Figure 5.11c) for the six samples under consideration. Figure 5.11b shows that, for a volume fraction of calcite of 1.9% (3% of calcite in mass), around 85% of the contacts are still 'frictional' contacts and 15% are now 'mixed' contacts. Even if the biocementation level is low, these 'mixed' contacts represent almost half of the total contact surface area within the sample. For a biocementation level around 3%, we can observe (Figure 5.11b) that the number of 'frictional' of contacts rapidly decreases and becomes lower than 8%. Most of the contacts (around 90%) are now mixed contacts and very few (around 2%) 'cemented' contacts are created. Figure 5.11c shows that the 'mixed' contacts represent around 98% of the total contact surface area. By increasing the level of biocementation, the number of 'frictional' of contacts still decreases and is equal to zero for the highest volume fraction of calcite, $f_c=14.9\%$. The number of 'mixed' contacts remains the most important one, even if the number of 'cemented' contacts slightly increases. These remarks are also valid for the distributions in terms of contact surface area.

Figures 5.12a and 5.12b summarize the evolution of these distributions with respect to the volume fraction of calcite. As already underlined, the transition between samples with a majority of 'frictional' or 'mixed' contacts occurs for a volume fraction of calcite around 3%. This transition seems to be linked to the biocementation process, and more precisely to the injection protocol of both the bacterial solution (BS) and the calcification solution (CS) (see Dadda et al. (2017b) for more details). The typical protocol corresponding to the different levels of biocalcification is presented on Figure 5.12c. This figure shows that :

- After one injection of the bacterial solution, one injection of the calcification solution leads to a small amount of calcite (around 2%) and thus most of the contacts within the sample remain "frictional". After the second injection of the calcification solution, most of the contacts become mixed contacts, even if the volume fraction of calcite is quite small, typically the order of 3% to 4%. This second injection of the calcification solution is required in order to activate all the injected bacteria. The large number of mixed contacts created suggests that the bacteria are located in these zones, i.e. where the shear stresses induced by the flow are very small. Less than 10% of the contacts remain frictional. They are probably located in the vicinity of large pores, where high shear stresses do not allow bacteria attachment. Finally, let us remark that after this second injection of the calcification solu-

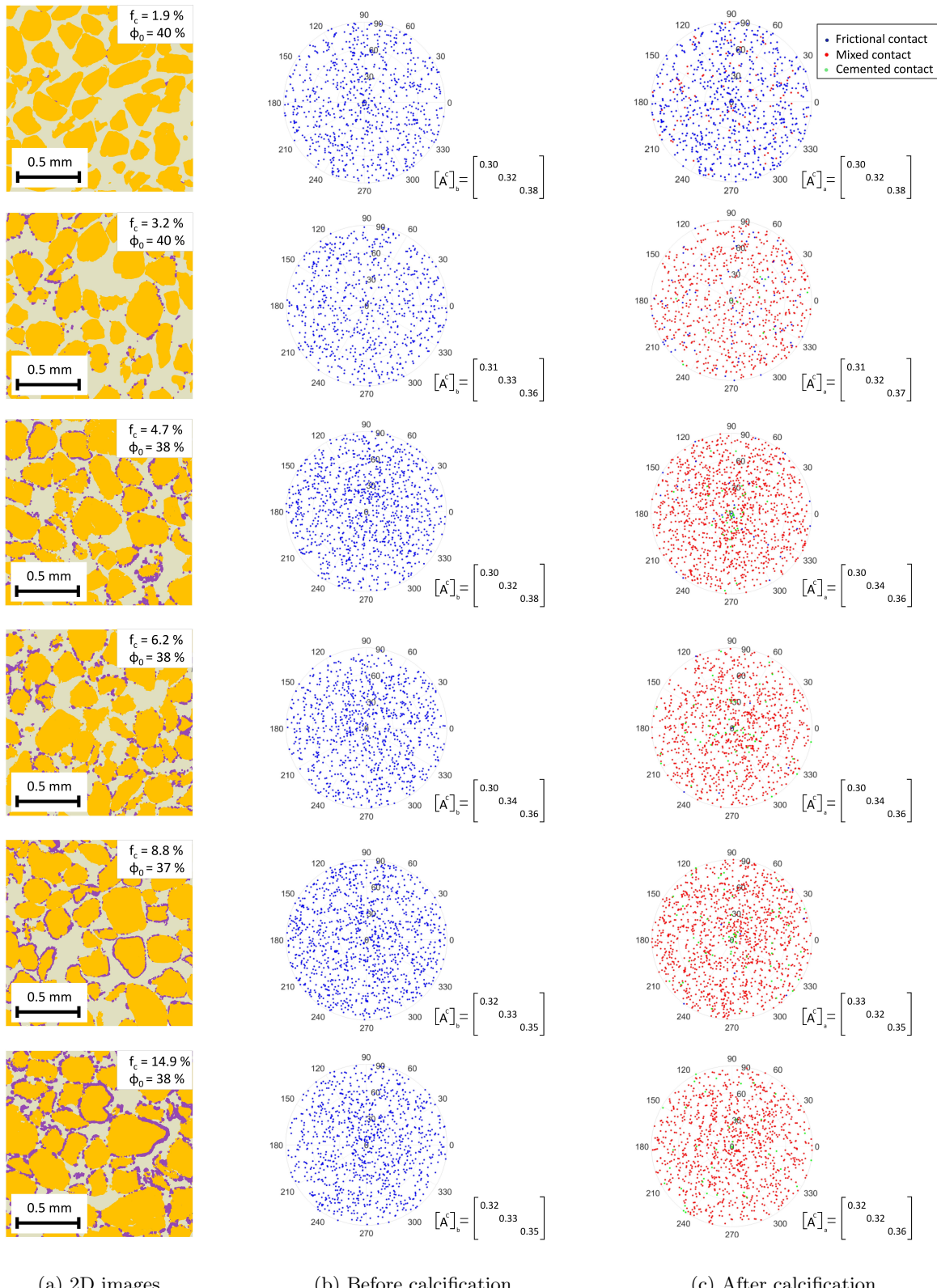


FIGURE 5.10: Orientation of the contacts within the six samples under consideration, (a) 2D trinarianized images, (b) before and (c) after biocalcification.

tion, the mean cohesive contact surface area represents around 60% of the mean contact surface area after calcification (see Figure 5.9).

- After the second injection of the bacterial solution and the third and fourth injection of the calcification solution, the distribution of the different types of contact in terms of number or in terms of surface area remains almost the same. As expected, since the volume fraction increases, 'frictional' contacts disappear progressively, and the number of 'cemented' contacts slightly increases and represents less than 10% of the total number of contacts. This latter remark suggest that the new bacteria injected are once again attached in the zone of the initial contacts between grains, where the shear stresses are small and where grain surfaces present a high roughness created by the calcite crystals precipitated after the first injection. This is confirmed by the increase of the mean cohesive contact surface area which reaches around 80% of the mean contact surface area after calcification (see Figure 5.9).

5.3.5 Precipitation pattern and modeling

As already discussed in the introduction, several studies have shown by simple qualitative observations (SEM, tomography, etc.) that the precipitation of calcite occurs mainly at the contacts between grains, but also on the surface of grains (DeJong et al., 2010b; Tobler et al., 2011; Rong et al., 2013; Sel et al., 2015). According to these observations, the calcite precipitation can be seen as localized or uniform. In this section, we propose to use our results computed on 3D images in order to identify and quantify which calcite precipitation process dominates. For that purpose, in the following we focus our attention on two microstructural properties :

- the ratio (\bar{S}_c/\bar{S}_a) , i.e. the ratio of the mean cohesive contact surface area (S_c) to the mean contact surface area (S_a) after biocalcification (Figure 5.15).
- the ratio (SSA_c/SSA) , i.e. the ratio between specific surface area of calcite (SSA_c) and the total specific surface area of the medium (SSA) (Dadda et al., 2017b). The total specific surface area (SSA) is defined as $SSA = (S_g + S_c)/V$, where S_g and S_c are the surface area of the grain and the calcite in contact with the voids (of the air or fluid) respectively, and $V=L^3$ is the volume under consideration (Figure 5.13). The specific surface of calcite (SSA_c) defined as $SSA_c=S_c/V$. This specific surface area of calcite, characterizes the surface of calcite in contact with voids. According to the definition of SSA_c and SSA , we have : $SSA_c/SSA = (S_c/S_g)/(1+(S_c/S_g))$. This ratio, which characterizes the percentage of the initial surface of sand covered by the calcite, is equal to 0 when $S_c=0$ (no calcite), to 0.5 when $S_c=S_g$, and 1 when $S_g=0$, i.e sand grains are totally covered with calcite.

Figure 5.13 shows the evolution of these two ratios (\bar{S}_c/\bar{S}_a) and (SSA_c/SSA) with respect to the volume fraction of calcite. As already underlined, the ratio (\bar{S}_c/\bar{S}_a) increases non-linearly with

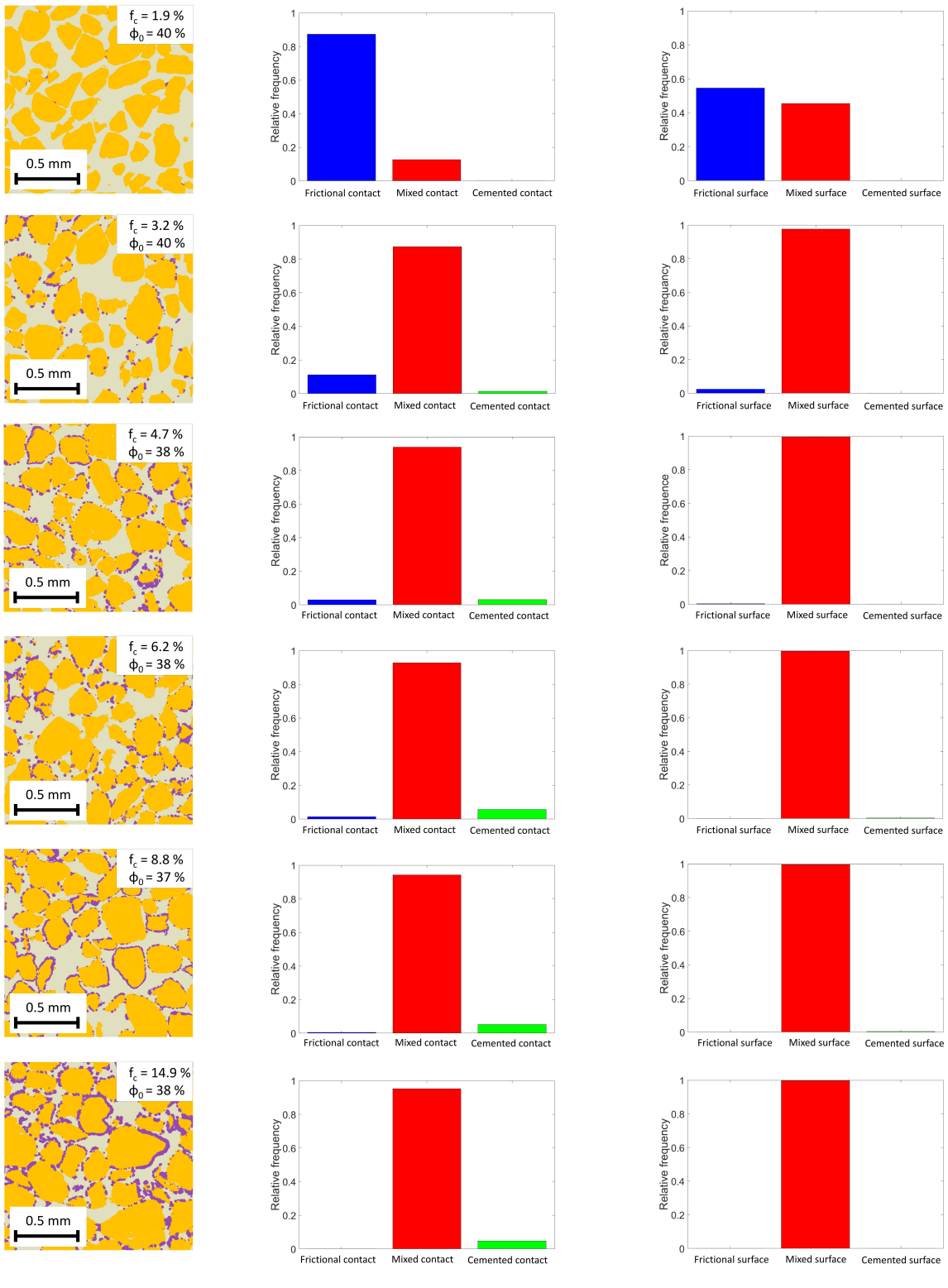
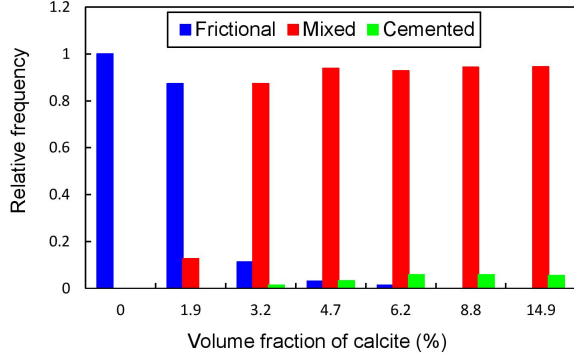
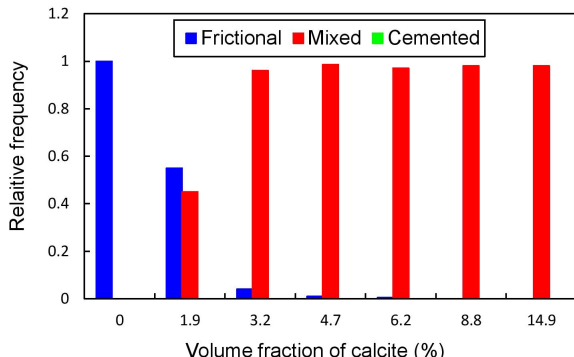


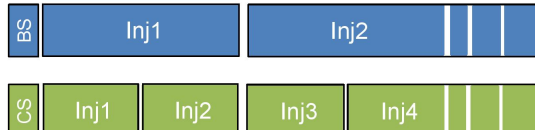
FIGURE 5.11: Distribution of the different types of contact, in each sample after biocementation, in terms of (b) number of contacts, (c) contacts surface area.



(a) Number of contacts



(b) Contact surface area



(c) Injection protocol

FIGURE 5.12: Evolution of the distribution of the different types of contact with respect the volume fraction of calcite, in terms of (a) number of contacts, (b) contact surface area. (c) Typical protocol for the biocementation process : number of injections of bacterial solution (BS) and calcification solution (CS).

respect to the volume fraction of calcite and is equal to 80% for $f_c=14.9\%$. The ratio (SSA_c/SSA) also increases non-linearly with respect to the volume fraction of calcite and tends towards an asymptotic value 0.45 (less than 45% of the sand initial surface covered by the calcite) for $f_c=14.9\%$. The evolution of these two ratios proves that the second injection of bacteria (Figures 5.12a) does not increase the surface of the grain already cover by the calcite, but mainly increases the size of the contacts. It confirms that in general the calcite precipitated in the zone of contact.

In order to validate these results, they are now compared with analytical estimates assuming that the granular media is made of periodic simple cubic (SC) arrangements of grains. The initial porosity is fixed to 40% and the diameter of grain is equal to D_{50} . Two extreme cases of precipitation are considered (Figures 5.14) : in the first case, we suppose that the calcite is localized at the contact and assumes a cylindrical shape (Figures 5.14a). In the second case, the

grains are supposed to be covered by a uniform layer of calcite (Figures 5.14b). Let us remark that in both cases (1) the coordination number is equal to 6, which is smaller to the one measured on 3D images, which ranges between 7.7 to 9.2, and (2) the creation of 'cemented' contacts is neglected.

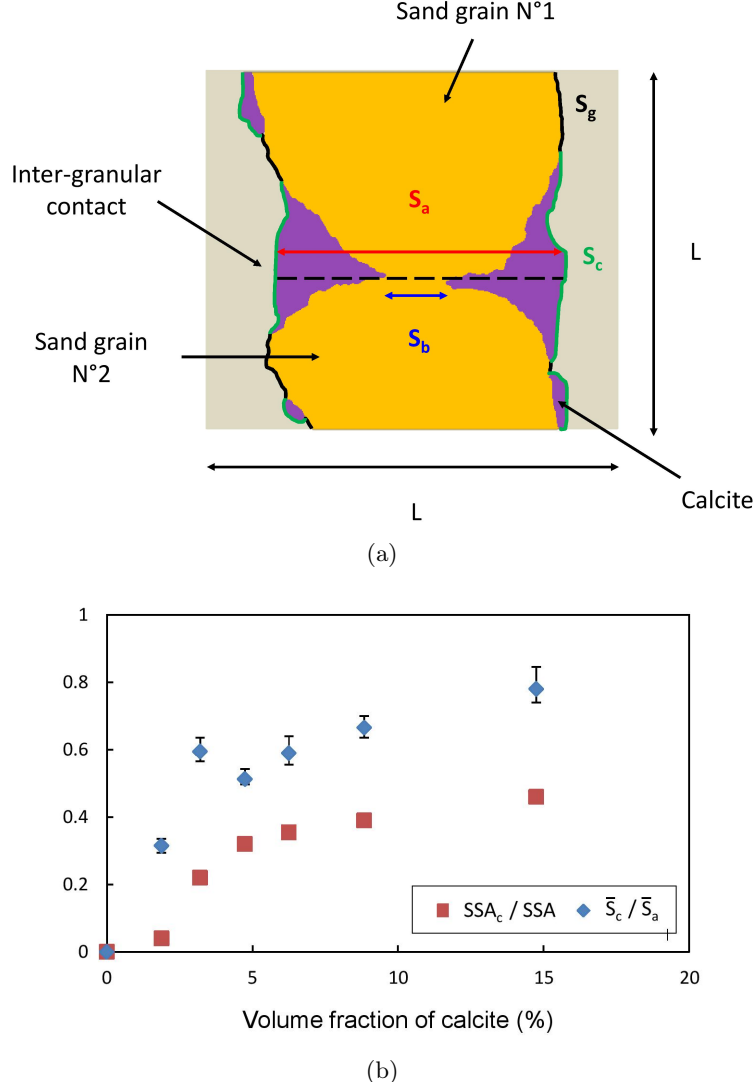


FIGURE 5.13: (a) distribution of the calcite at the grain scale, (b) evolution of the ratio between the mean cohesive contact surface area and the mean contact surface area after calcification (\bar{S}_c / \bar{S}_a), and the ratio between the specific surface area of calcite and the total specific surface area (SSA_c / SSA) with the volume fraction of calcite

Figures 5.15 shows the evolution of the ratios (\bar{S}_c / \bar{S}_a) and (SSA_c / SSA) computed on 3D images with respect to the volume fraction of calcite, in comparison with the ones derived analytically from the above simple microstructures. The numerical values of (\bar{S}_c / \bar{S}_a) lies between the two modelings (Figures 5.15a). By contrast, Figures 5.15b shows that the numerical values of (SSA_c / SSA) are in good agreement with the analytical estimates when the calcite is localized at the contacts. This comparison between our numerical results obtained on 3D images and ana-

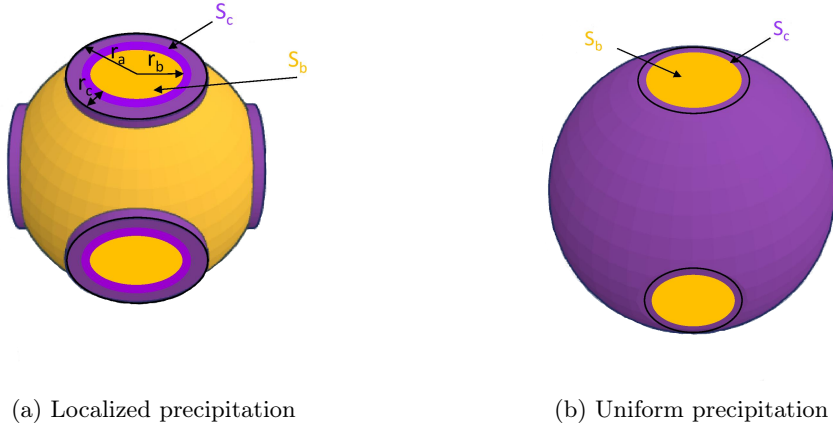


FIGURE 5.14: Granular media is made of periodic simple cubic (SC) arrangements of grains. (a) the calcite is localized at the contact, (b) the calcification is uniform at the grain surface.

lytical estimates confirm that the calcite is in general mainly localized at the contact between grains. Let us remark that this precipitation at the inter-granular contacts can be enhanced by performing the biocementation in non-saturated conditions (Cheng et al., 2013).

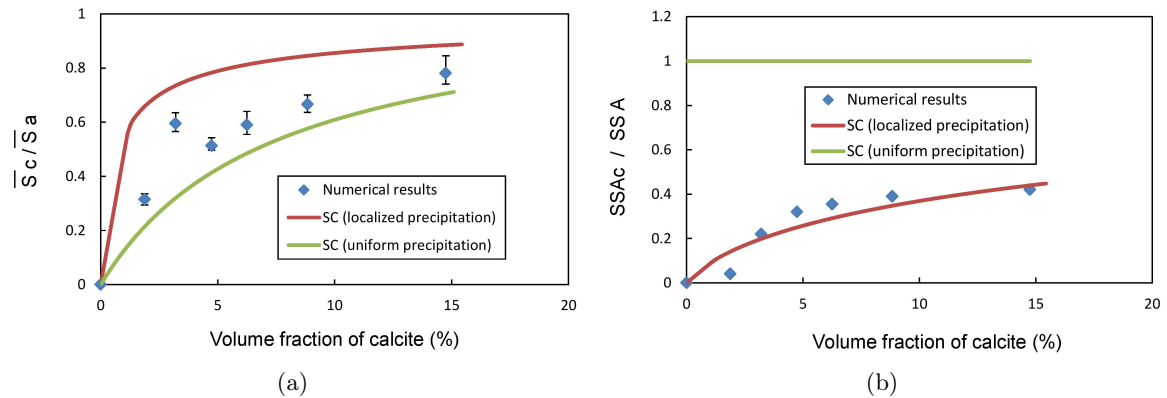


FIGURE 5.15: Comparison between the analytical estimates and the numerical results from 3D image. (a) Evolution of the ratio (\bar{S}_c/\bar{S}_a), (b) Evolution of the ratio (SSA_c/SSA) with respect to the volume fraction of calcite.

5.4 Conclusion

As underlined in the introduction, the mechanical efficiency of the biocementation process is directly related to the microstructural properties of the biocemented sand, such as, the calcite volume fraction and its distribution within the pore space (localized at the contact between grains, uniform over the grain surface), the coordination number, the contact surface area, the contact orientation. In the present work, the evolution of the contact properties (contact surfaces, coordination number, contacts orientation, type of contact, etc.) of biocemented sand have been determined as function of the cementation level ($0 < f_c < 15\%$) by using 3D images obtained by

from micro-tomography observations. The obtained results point out that :

- The coordination number, due to the creation of new contacts (cemented contacts), slightly increases when increasing the volume fraction of calcite. This increase is about 8% for a volume fraction of calcite of 14.9%.
- The distribution of contact surface areas changes progressively with the volume fraction of calcite (f_c). The ratio (\bar{S}_a/\bar{S}_b) between the mean contact surface areas after calcification (\bar{S}_a) and before calcification (\bar{S}_b) increases almost linearly with respect to the volume fraction of calcite, and is the order of 6 for $f_c=14.9\%$. By contrast, the ratio (\bar{S}_c/\bar{S}_a) (where \bar{S}_c is the mean cohesive contact surface area) increases non-linearly with the volume fraction of calcite, and is of the order of 60% for $f_c \simeq 3\%$.
- The orientation of contacts within the samples are isotropic before and after calcification. This result must be put in regards to the biocementation process, which is static in the present case. There is no flow through the samples after the injection of both the bacterial and calcification solutions. Probably, these observations are no more valid when a continuous flow is present during the process.
- Three types of contact ('frictional', 'mixed' and 'cemented' contacts) can be considered after biocalcification. For a volume fraction of calcite lower than 3%, most of the contacts remain 'frictional'. Beyond this value, most of the contacts (in terms of number and surface area) are 'mixed' contacts. Whatever the value of f_c , the number of new contacts ('cemented' contacts) created by the biocementation process remains quite small (less than 10% for $f_c=14.9\%$) and the corresponding contact surface area is almost negligible. This evolution of the contacts, in terms of type, seems to be also related to the injection protocol of both the bacterial and calcification solutions.
- The precipitation of the calcite mainly occurs at the contacts between grains. Indeed, we have shown that the ratio (\bar{S}_c/\bar{S}_a) , increases non-linearly and tends towards 80% for $f_c=14.9\%$, whereas the ratio (SSA_c/SSA) , i.e. the ratio between specific surface area of calcite (SSA_c) and the total specific surface area of the medium (SSA), does not exceed 45% for $f_c=14.9\%$. These results show that the contact surface area still increases with increasing the volume fraction of calcite, whereas less than half of the surface of the grain is covered with the calcite. These results are confirmed by comparing our numerical results with analytical estimates assuming that the granular media is made of periodic simple cubic (SC) arrangements of grains and by considering two extreme cases of precipitation : (1) the calcite is localized at the contact, (2) the grains are covered by a uniform layer of calcite.

For a given practical application (mitigation of liquefaction or internal erosion), the objective in terms of overall mechanical behaviour (whether stiffness or strength under static or dynamic

loading) does not necessarily require that 100 of contacts become cohesive (and therefore a calcite amount that is even smaller than the value mentioned above). All the computed microstructural properties (coordination number, contact surface, cohesive surface, etc.) will be used in the future as input parameters in micromechanical models (DEM simulations..) in order to link these microstructural properties to the macroscopic effective properties (Young modulus and shear modulus) and strength properties (cohesion and friction angle).

CHAPITRE 6

RELATIONSHIP BETWEEN THE MICROSTRUCTURAL PARAMETERS AND THE MACROSCOPIC PROPERTIES OF BIOCEMENTED SAND

Sommaire

6.1	Introduction	108
6.2	Material and Method	111
6.2.1	Image acquisition and processing	111
6.2.2	Effectives properties estimates	112
6.2.2.1	Effective Elastic properties	112
6.2.2.2	Cohesion estimation	116
6.3	Results and discussion	116
6.3.1	Elastic properties	116
6.3.2	Cohesion	117
6.4	Conclusion	119

Abstract

Microstructural properties of biocemented sand, such as the contact surface area, the coordination number, the volume fraction of each phase, computed on 3D X-ray micro-tomography images are used as an input in current analytical models to estimate the elastic properties (Young's and shear modulus) and the strength properties (Coulomb cohesion). For the elastic properties, the analytical estimates (contact cement theory model "CCT") are compared to classical bounds, self-consistent estimate and numerical results obtained by direct computation (FEM computation) on the same 3D images. Concerning the Coulomb cohesion, the analytical model initially developed by Richefeu et al. (2006) to estimate the cohesion due to suction in unsaturated soils is modified to evaluate the macroscopic Coulomb cohesion of biocemented sands. Such analytical model is calibrated on experimental data obtained from triaxial tests performed on the same biocemented sand. In overall, the presented results point out the important role of some microstructural parameters, notably those related to the contact, on such effective parameters.

6.1 Introduction

The effective macroscopic properties, such as elasticity or strength of biocemented sands strongly depend on the microstructure (volume fraction of calcite, calcite morphology, size, distribution at the pore scale, contact number, contact surface area, etc), which is controlled principally by the treatment conditions : concentrations of bacteria, calcification solution, and the *in-situ* conditions : water content, particle size and distribution, temperature, etc. (Al Qabany et al., 2011a; Cheng et al., 2013, 2016; Al Qabany et al., 2011b).

In order to characterize such effective elastic properties, the shear wave velocity has been measured through cemented sand samples with different level of biocalcification has been measured (Al Qabany et al., 2011b; Montoya, 2012; Montoya and DeJong, 2015; Sharma et al., 2011). The obtained results show a linear relationship between the shear wave velocity and the calcite amount. Al Qabany et al. (2011b) found an increase of the shear velocity V_S from 180 m/s for untreated sand to 700 m/s in cemented sand with 5% of calcite in mass, which corresponds to a shear modulus ranging from around 100 to 800 MPa. As expected, these results clearly show that the biocalcification process affects the evolution of the elastic properties such as the shear modulus. The full measurements of the elastic properties of biocemented sand with accuracy are not straightforward (difficulty of the device implementation). To the best of our knowledge, such results are still missing in the literature.

Many experimental studies have been conducted in order to determine the evolution of the strength properties (cohesion, friction angle, etc.) induced by the biocementation process. Cheng et al. (2013) have shown that the cohesion increases non-linearly (exponential) with respect to the mass fraction of calcite. They typically found a cohesion of 140 kPa for fine sand with 9% of calcite in mass. The biocalcification process also modifies the friction angle. Depending on the

experimental conditions, the friction angle slightly or rapidly increases : for example, the peak friction angle increases from 0 to 30% according to the biocalcification level (Cheng et al., 2013; Feng and Montoya, 2015; Terzis et al., 2016; Montoya and DeJong, 2015; Cui et al., 2017). This evolution is due to the increase of the inter-granular friction by the deposition of calcite on their surfaces, and to the changes in the effective particle size distribution and the angularity of the biocemented sand (Shen et al., 2016; Wang and Leung, 2008b).

As already mentioned, all these results measured at the macroscopic scale strongly depend on the microstructure modifications at the pore scale induced by the biocalcification process. The main objective of the present work is to better understand the link between these microstructural changes and the evolution of the effective properties. We will focus our attention on the effective elastic properties and the Coulomb cohesion.

The study of the relationship between the microstructure on the overall elastic properties of heterogeneous materials is a long-standing problem. The prediction of the effective elastic properties from some microstructural information can be done following at least three different ways :

- In the literature, several theoretical formulae such as rigorous bounds, exact expansions and self-consistent estimations, have been proposed to make accurate effective properties estimations of heterogeneous materials. In the isotropic case, these bounds and estimates mainly depend on the volume fraction of the different phases (pores, solid phase, etc.) and the elastic properties of the different constituents (grain, calcite, etc.). They can provide accurate estimations of the effective elastic properties of porous materials, however they usually fail in the case of granular media, when the contact surface areas become small (Hashin and Shtrikman, 1963; Hill, 1965; Torquato, 1991; Bouhlel et al., 2010).
- In the case of granular materials, different analytical models have been developed (Chang et al., 1990; Dvorkin et al., 1994; Richefeu et al., 2006; Xue-Hui et al., 2014) taking into account the volume fraction of the different phases but also some information coming from the contacts between grains, such as the coordination number, the mean contact surface area. Chang et al. (1990) have developed an analytical model to estimate the shear modulus of cemented granular materials based on classical law developed basically to estimate this property in cohesionless granular material. This model is based on an incremental relationship, which links the stress to the strain and the stiffness tensor (C_{ijkl}). In this relationship, the fourth rank stiffness tensor (C_{ijkl}) is expressed as the volumetric average of the contact stiffness in a defined spheres packing. In the work of Chang et al. (1990), the sand is modeled as an isotropic random packing of identical spheres linked between each other with springs, which have normal and tangential stiffnesses, which represent the adhesion due to the cement in addition to the friction at the particle-particle contacts. The shear modulus can be estimated using this model which takes into account the contact adhesion and friction, the confining pressure, the particle size, the void ratio and the coordination number.

Dvorkin et al. (1994) have developed also an analytical model based on the estimation of the normal and tangential stiffness between two grains bonded with a cylinder of cement. These stiffnesses, which depend on the geometrical and physical properties of the medium, can be then used as a constitutive law in numerical computation or mean-field approximations, such as the Digby's model (Digby, 1981). This latter model allows to estimate the effective bulk modulus of spherical particles packing according to the microstructural properties (coordination number, grain size, contact surface area, porosity) and the intrinsic properties of grains and cement. This model has been used successfully in order to estimate the elastic properties of different cemented granular material such as epoxy-cemented sand, frozen glass beads and injected sand (Dvorkin and Nur, 1996; Benhamida et al., 2005). Recently, Xue-Hui et al. (2014) have extended the laws developed in Dvorkin et al. (1994) by adding the effect of the contact thickness, which appears as an important parameter in the case of the cementation by soil mixing, where the cement can form a significant thickness between the grains. It is not the case in the biocementation process with bacterial injection, where almost all the contacts have no thickness after cementation ; the grains are already in contacts before the biocementation by soft injection of reactants and bacteria.

- The effective elastic properties can be also estimated by performing numerical simulations on 3D images of the material obtained by X-ray micro-tomography. This method has been used successfully to estimate the elastic properties of different cohesive porous materials such as snow, ceramic, metals and sandstone rocks (Wautier et al., 2015; Arns et al., 2002; Saadatfar et al., 2005; Kajetan, 2017). This method is based generally on the meshing of 3D voxelized image and then by solving specific boundary value problem arising from the homogenization process (Wautier et al., 2015; Kanit et al., 2006). Youssef et al. (2005) have presented three main methods of meshing of 3D voxelized structure : (1) cubic elements, (2) beams or wall elements and (3) tetrahedral elements. The tetrahedral elements meshing method have shown the most appropriate method to keep the maximum microstructural information. This meshing method has been used also by Wautier et al. (2015) to estimate the elastic properties of the snow samples.

By contrast, few works have been addressed to estimate analytically the cohesion using the microstructural properties (coordination number, solid fraction, contact strength, etc.) such as the model developed by Richefeu et al. (2006), to estimate the cohesion due to suction in unsaturated soils. Different DEM models have been also developed to predict the behavior of cohesive and cohesless soils (Wang and Leung, 2008b; Shen et al., 2016; Jiang et al., 2011; Utili and Nova, 2008). Jiang et al. (2011) have studied the evolution of the cohesion, the peak and residual friction angle in cemented sand by performing 2D DEM simulations. Some recent works start investigating deeper microstructural information (type of contacts and its distributions) on the evolution of the strength parameters (Shen et al., 2016; Bono et al., 2015). Wang and Leung (2008b) have shown by performing 2D DEM simulations on cemented sand that the cementation endows a supplementary increase of the residual strength due to the preexisting grains clusters

which remain cemented after the peak strength. Bono et al. (2015) and Shen et al. (2016) have confirmed such results by doing 3D DEM simulations and have shown in addition that the specimens which have the larger gap of bond strength had the weaker peak strength and higher residual strength and volumetric strain. However, none of these numerical studies was performed using realistic microstructural information (mean contact surface, contact surface distribution, coordination number, etc.), which can be computed from 3D x-ray micro- tomography images (Dadda et al., 2017a).

The objective of this paper is to use the real microstructural properties of biocemented sand (such as contact surface area, the coordination number, the volume fraction of each phase...) computed on 3D x-ray micro- tomography images as an input in current analytical models to estimate the elastic properties (Young's and shear modulus) and the strength properties (Coulomb cohesion). The analytical estimates of the elastic properties are then compared to numerical results obtained by direct computation (FEM computation) on the same 3D images. Concerning the Coulomb cohesion, the analytical model initially developed by Richefeu et al. (2006) to estimate the cohesion due to suction in unsaturated soils is modified to estimate the macroscopic Coulomb cohesion of biocemented sands. These analytical results are then compared to experimental results obtained from triaxial tests performed on the same biocemented sand. This paper is organized as follows. The section 6.2 is devoted to the material and methods : (1) the 3D images acquisition and treatment, (2) presentation of the analytical models and numerical simulations performed to estimate the elastic properties and/or the cohesion. In section 6.3, the obtained results are presented and discussed according to previous results available in the literature.

6.2 Material and Method

6.2.1 Image acquisition and processing

X-ray synchrotron micro-tomography observations in ESRF (Grenoble/France) have been performed on different biocemented sand with cementation levels between 1.9 and 14.9% of calcite in volume (Table 6.1). These observations have been achieved with a resolution of $0.65\mu\text{m}/\text{pixel}$ in order to visualize the calcite crystals which has small size (15 to $20\mu\text{m}$). Each 3D image in grey level (Figure 6.1a) has been then treated in order to separate the phases (sand grains, calcite and pores) (Figure 6.1b) and also to separate each grains and thus to identify the contacts between grains (Figure 6.1c) (for more details see chapter 5). The treated 3D images have been then used to extract the evolution of the mean micromechanical properties (porosity, volume fraction of calcite, specific surface areas, etc.) and also properties linked to the contact between grains : coordination number, contact surface area, contact orientations. Some of these microstructural quantities are summarized in Table 6.1 for each sample.

TABLE 6.1: Characteristics of the observed sub-samples.

Sub-sample	2T	12MB	13TT	11BB	13BT	13MB
Volume fraction of calcite f_c (%)	1.9	3.2	4.7	6.2	8.8	14.9
Mass fraction of calcite m_c (%)	3	5	7	9	12.7	16.9
Computed initial porosity ϕ_0	40	38	38	38	37	38
Solid fraction (f_s)	0.62	0.63	0.65	0.66	0.69	0.75
Mean cohesive contact surface \bar{S}_c (μm^2)	314	745	1040	897	1332	4160
Mean contact diameter $2a$ (μm)	10.3	15.4	18.2	16.9	20.6	36.4
Mean coordination number (\bar{Z}_a)	7.1	7.8	8.5	8.8	8.7	9.2
Normal stiffness (S_n)	0.041	0.071	0.084	0.078	0.095	0.12
Shear stiffness (S_t)	0.11	0.18	0.21	0.20	0.24	0.32

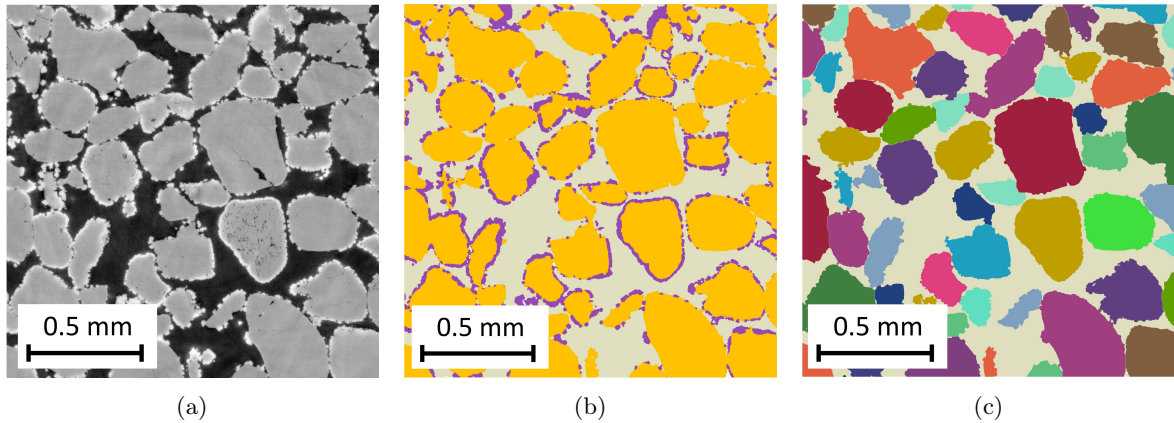


FIGURE 6.1: a) 3D images in grey levels, b) 3D trinarized image which contains grains (orange), calcite (purple) and pores, c) 3D images which contains separated grains (subsample “13BT”).

6.2.2 Effectives properties estimates

6.2.2.1 Effective Elastic properties

6.2.2.1.1 Contact cement theory (CCT)

In this work, the contact cement theory (CCT) is used to estimate the elastic properties of the biocemented sand by using microstructural properties computed from the 3D images and physical properties available in the literature. In this model, the normal and the tangential stiffnesses (S_n and S_t) are computed by solving the problem of two elastic grains bonded with a thin cement layer (Figure 6.2). The cement layer bonding the two particles is considered as elastic cylindrical foundation with radius (a) and height (h). By reducing the grain-cement interaction problems to linear integral equations, the normal and tangential stiffness is linked successfully to the microstructural and physical properties of the material by simple integrations (Dvorkin et al., 1994; Dvorkin and Nur, 1996). The original theory developed by Dvorkin et al. (1994) requires some computation effort in order to estimate the normal and tangential stiffnesses (S_n and S_t).

These computations have been performed by Dvorkin and Nur (1996) to reduce this model to analytical formulas as presented in the appendix of Dvorkin and Nur (1996). The relationships show that S_n and S_t depend on the contact surface area (or radius), the size of the grain and the elastic properties of the cement and the grains. Based on the work of Digby (Digby, 1981), Dvorkin and Nur (1996) have proposed the following expressions for the effective bulk modulus K_{eff} and shear modulus G_{eff} respectively :

$$K_{\text{eff}} = \frac{\bar{Z}_a(1 - \phi_0)}{6} M_c S_n \quad (6.1)$$

$$G_{\text{eff}} = \frac{3}{5} K_{\text{eff}} + \frac{3\bar{Z}_a(1 - \phi_0)}{20} G_c S_t \quad (6.2)$$

where \bar{Z}_a is the mean coordination number (after calcification), ϕ_0 is the initial porosity, M_c is the compressional wave modulus of the cement material, which can be written as follow :

$$M_c = \frac{E_c(1 - \nu_c)}{(1 + \nu_c)(1 - 2\nu_c)} \quad (6.3)$$

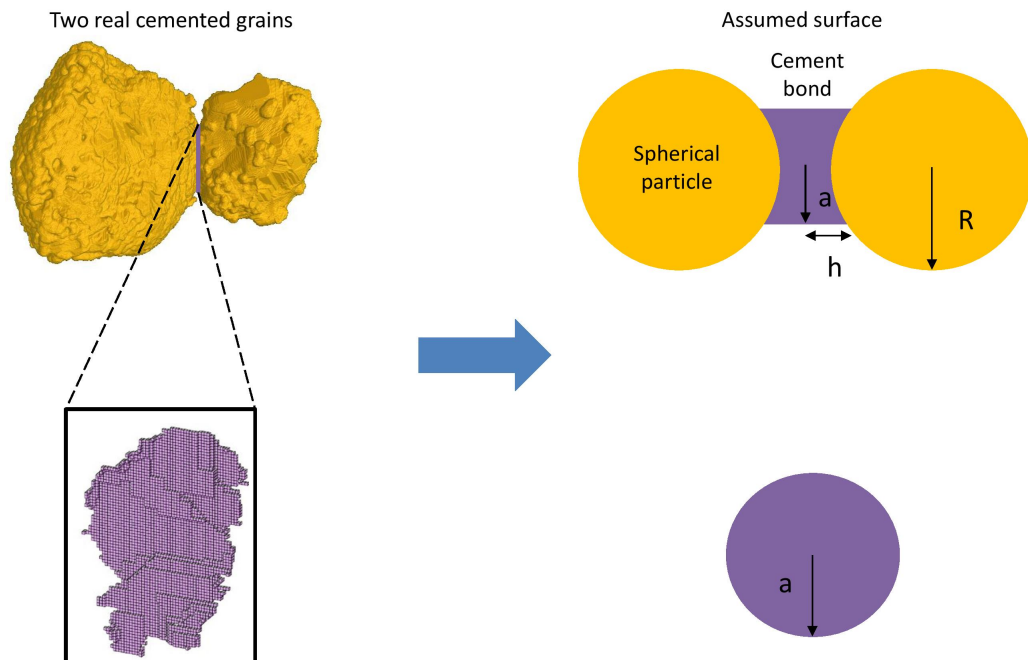


FIGURE 6.2: Contact between 2 grains deduced from 3D images and idealized contact used in the contact cement theory.

where E_c , ν_c and G_c are the Young's modulus, the Poisson's ratio and shear modulus of the cement phase, respectively.

In the following, the effective elastic moduli K_{eff} and G_{eff} of our samples have been estimated (i) using the microstructural properties computed on the 3D images presented in Table 6.1 and assuming that the contact surface have a circular shape, (ii) assuming that the particle diameter is equal to the mean particle diameter of the sand grains ($D_{50}=210\mu\text{m}$) (Fontainebleau sand) and (iii) assuming that the elastic properties of the quartz sand and the calcite are similar and equal to $G_s=G_c=32\text{GPa}$ and $\nu_s=\nu_c=0.25$. This latter hypothesis is consistent with previous results in the literature (Ayoub et al., 2011; James and Lord, 1992).

6.2.2.1.2 Self-consistent method (SCM)

The self-consistent method (SCM) (Auriault et al., 2010), involves considering each heterogeneity, i.e. an inclusion with a given shape and with given elastic properties, to be embedded in an infinite elastic matrix whose properties are the effective properties of the material being considered. The solution of the elasticity equations for the isolated inclusion (pore or particles) then yields an implicit equation which may be solved for the effective moduli. If we assume that the inclusions are spheres and the porous medium is macroscopically isotropic, from the results of Hill (1965) it can be shown that the effective bulk modulus K^{SCM} and the effective shear modulus G^{SCM} of the porous medium are written :

$$G^{\text{SCM}} = \frac{3}{16} \left[-K_s(2 + f_s) - G_s((7/3) - 5f_s) + \sqrt{\Delta} \right] \quad (6.4)$$

$$K^{\text{SCM}} = \frac{4G^{\text{SCM}}K_s f_s}{3((1 - f_s)K_s + 4G^{\text{SCM}})} \quad (6.5)$$

where Δ is a parameter which depends to the solid fraction of the material and its elastic properties :

$$\Delta = (K_s(2 + f_s) + G_s(7/3 - 5f_s))^2 - 32G_sK_s(1 - 2f_s) \quad (6.6)$$

Consequently, we have :

$$E^{\text{SCM}} = \frac{9K^{\text{SCM}}G^{\text{SCM}}}{3K^{\text{SCM}} + G^{\text{SCM}}} \quad (6.7)$$

$$\nu^{\text{SCM}} = \frac{3K^{\text{SCM}} - 2G^{\text{SCM}}}{6K^{\text{SCM}} + 2G^{\text{SCM}}}. \quad (6.8)$$

In all these analytical bounds and estimates, the solid fraction of the material is given by : $f_s = 1 - \phi_0 + f_c$; where ϕ_0 and f_c are the initial porosity and volume fraction of calcite respectively (see Table 6.1).

6.2.2.1.3 Numerical homogenization from 3D images

The effective elastic properties have been also determined by solving numerically the specific boundary value problems arising from homogenization process on Representative Elementary

Volume (REV) extracted from the 3D images. For that purpose, the methodology proposed by Wautier et al. (2015) has been followed (Figure 6.3).

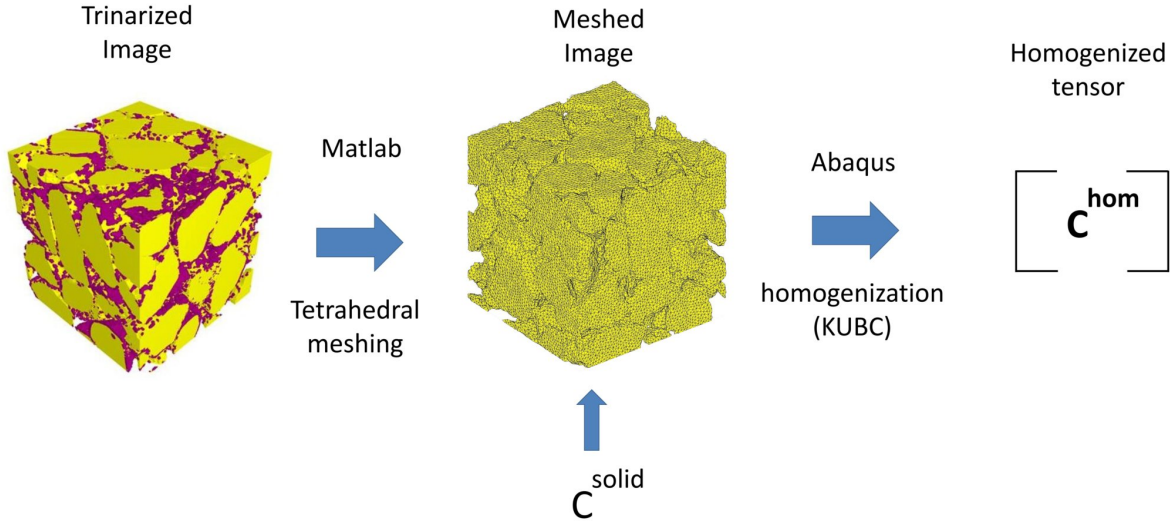


FIGURE 6.3: Computation schema of the elastic properties of the biocemented sand specimens.

This method consists in first meshing the 3D voxelized images corresponding to the REV. In the present case, cubic 3D images with side length of 0.9 mm (1400 voxels) (which represents 10x10x10 times the correlation length) of each specimen has been meshed with 2.5 million of tetrahedral elements (Figure 6.3). The Iso2mesh Matlab® toolbox has been used for the meshing step with the meshing option of the Computational Geometry Algorithms Library (CGAL). The meshed volume has been then exported to Abaqus® to solve classical elasticity boundary value problems (Wautier et al., 2015), with kinematically uniform boundary conditions, i.e. with a macroscopic homogenous strain imposed on the boundary of the 3D meshed volume. This boundary value problem is written :

$$\left\{ \begin{array}{ll} \operatorname{div} \boldsymbol{\sigma} = 0 & \text{for } \mathbf{x} \in V \\ \mathbf{u} = \mathbf{E} \cdot \mathbf{x} & \text{for } \mathbf{x} \in \partial V \\ \boldsymbol{\varepsilon} = \frac{1}{2} (\boldsymbol{\nabla} \mathbf{u} + {}^t \boldsymbol{\nabla} \mathbf{u}) & \text{for } \mathbf{x} \in V \\ \boldsymbol{\sigma} = \frac{E_s(\mathbf{x})}{1 + \nu_s} \left(\boldsymbol{\varepsilon} + \frac{\nu_s}{1 - 2\nu_s} \operatorname{Tr}(\boldsymbol{\varepsilon}) \mathbf{1} \right) & \text{for } \mathbf{x} \in V_s \end{array} \right. , \quad (6.9)$$

where V stands for the domain occupied by the whole snow sample and ∂V its boundary. V_s stands for the domain occupied by solid skeleton. The macroscopic stress tensor $\boldsymbol{\Sigma}$ is deduced from the knowledge of its microscopic counterpart thanks to the volume averaging

$$\boldsymbol{\Sigma} = \frac{1}{|V|} \int_V \boldsymbol{\sigma} dV = \langle \boldsymbol{\sigma} \rangle \quad (6.10)$$

As a result, for a given macroscopic strain loading \mathbf{E} , the macroscopic stress response $\boldsymbol{\Sigma}$ is recovered and we have $\mathbf{E} = (\mathbf{C}^{\text{hom}})^{-1} : \boldsymbol{\Sigma}$, where \mathbf{C}^{hom} is the homogenized stiffness tensor (Wautier et al., 2015). This tensor can be obtained by performing only six simulations on Representative

Elementary Volumes extracted from 3D images. In the following, the above boundary value problem has been solved assuming that $G_s=32\text{GPa}$ and $\nu_s=0.25$.

The computed results of all the 3D images show that the homogenized stiffness tensor is almost isotropic. For example, the 2BT subsample has shown very similar results in the 3D space directions (Young modulus : $E_1 = 29 \text{ GPa}$, $E_2 = 29 \text{ GPa}$, and $E_3 = 25 \text{ GPa}$). This result is consistent to the ones obtained concerning the microstructure and other physical properties (Effective diffusion tensor, permeability) (Dadda et al., 2017b). According to this result, the computed effective elastic properties reduce to the Young's modulus and shear modulus.

6.2.2.2 Cohesion estimation

The estimation of the Coulomb cohesion of the biocemented granular material from the microscopic properties has not been addressed in the literature with analytical models. However, a cohesion estimate has been developed for unsaturated soil which has small cohesion due to capillarity forces between grains (Richefeu et al., 2006). Generally, the Coulomb cohesion (c) of a cohesive sand is directly related to the tensile strength (σ_t) and the internal friction coefficient (μ) by $c=\mu\sigma_t$. Richefeu et al. (2006) have developed an expression of the tensile strength of cohesive material using the volume averaging technique taking into account the capillary force (suction). In order to represent our material, we proposed to replace the capillary force by the bonding force induced by the contact cementation. This inter-particle force can be defined by :

$$f_n = \bar{S}_c \cdot \sigma_{ten} \quad (6.11)$$

Where \bar{S}_c is the cohesive contact surface area of the cemented bond and σ_{ten} is its tensile strength, as introduced in Santamarina (2003)

Generally, in the granular material the tensile strength depends on the intrinsic strength of the cement material and its adhesion with the grain surface. Assuming that we have a monodisperse grain assembly and introducing the expression of the cementation force in the expression developed by Richefeu et al. (2006), the Coulomb cohesion due to the cementation in granular media is written :

$$c = \frac{f_s \bar{Z}_a \bar{S}_c \sigma_{ten}}{\pi D_{50}^2} \quad (6.12)$$

where D_{50} represents the mean diameter of grains, f_s the solid fraction inside the specimen after calcification, \bar{Z}_a the mean coordination number and \bar{S}_c the mean cohesive contact surface formed by the calcite. In this expression the internal friction coefficient μ is considered equal to (2/3) and the parameter (σ_{ten}), which represents the inter-particle tensile strength, is adjusted to reflect the experiments.

6.3 Results and discussion

6.3.1 Elastic properties

The evolution of the effective dimensionless Young and shear moduli, as well as the effective Poisson ratio ν_{eff} of the biocemented sand obtained with the three methods (CCT model, SCM estimations and numerical homogenization) are presented on the Figure 6.4. In this figure, we have also reported classical bounds (Voigt and Reuss, Hashin and Hashin and Shtrikman) and self-consistent estimate (SCM) Auriault et al. (2010). Voigt (V) and Reuss (R) bounds are written :

$$G^R = 0 < G_{\text{eff}} \leq G^V = f_s G_s \quad (6.13)$$

$$E^R = 0 < E_{\text{eff}} \leq E^V = f_s E_s \quad (6.14)$$

Hashin and Strickman bounds are defined as :

$$G^{HS-} = 0 < G_{\text{eff}} \leq \frac{f_s G_s (9K_s + G_s)}{(9K_s + G_s) + 6(1 - f_s)(K_s + 2G_s)} = G^{HS+} \quad (6.15)$$

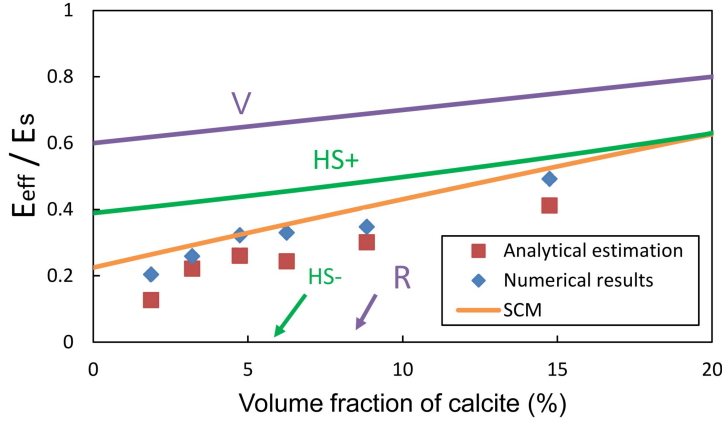
$$K^{HS+} = \frac{4f_s G_s K_s}{4G_s + 3(1 - f_s)K_s} \quad (6.16)$$

and thus, we have :

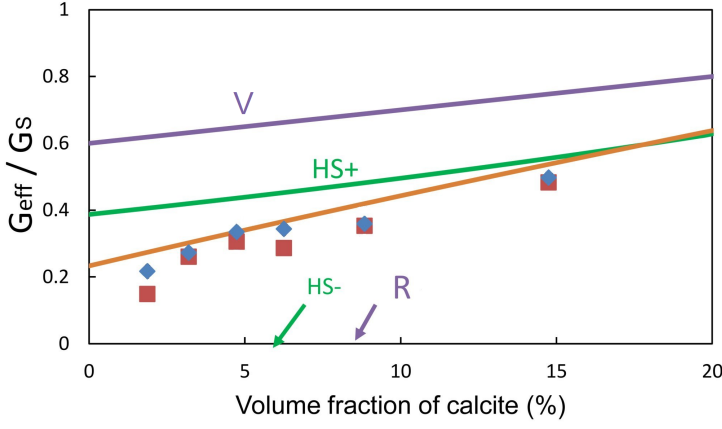
$$E^{HS-} = 0 < E_{\text{eff}} \leq \frac{9K^{HS+} G^{HS+}}{3K^{HS+} + G^{HS+}} = E^{HS+} \quad (6.17)$$

The Figures 6.4a and 6.4b show a good agreement between the results given by the CCT model and the numerical results for both effective modulus. As expected, in both case, the Young's and the shear moduli increase with increasing the volume fraction of calcite. This increase is nonlinear for low volume fraction of calcite ($f_c < 3.2\%$) and then is almost linear for larger volume fraction of calcite, which is consistent with experimental measurements (Al Qabany et al., 2011b; Duraisamy and Airey, 2015). This non-linear increase is due to the non-linear increase of the contact surface area between grains induced by the biocalcification process. Figure 6.4 also shows that both analytical and numerical estimates lie between the bounds and are in good agreement with the self consistent estimate when the volume fraction of calcite is larger than 3%. In the self consistent model, the material is viewed as a simple matrix with spherical voids. This simple microstructure is not able to reflect the mechanical behavior of our granular materials, especially when the contact surface area are small, i.e for low volume fraction of calcite. In overall, these comparison between different modellings underline the important role of the contact properties on the effective elastic modulus when the volume fraction of calcite is small.

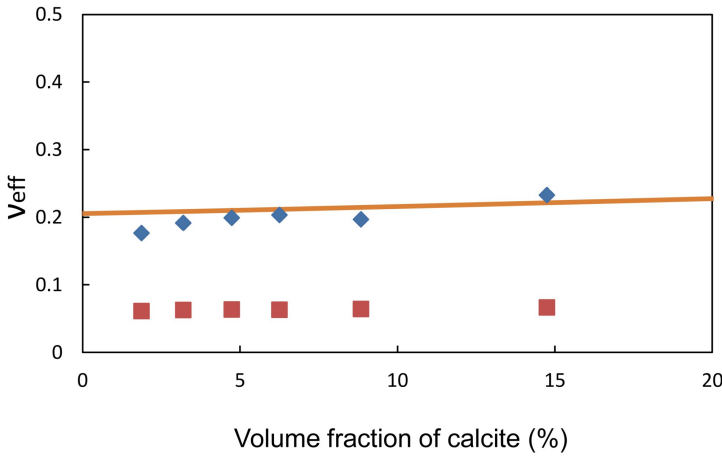
Finally, the Figure 6.4c shows that the effective Poisson's ratio deduced from the evolution of the Young and the shear moduli, is almost constant on the whole rang of calcite volume fraction. It is of the order of 0.2-0.25 for the numerical results and of 0.06 for the CCT model. These differences result from the slight differences in terms of shear and Young's moduli that we can observe on Figures 6.4a and 6.4b. Finally, let us remark that the numerical values are in good agreement with the Self Consistent Estimate (SCM).



(a)



(b)



(c)

FIGURE 6.4: Evolution of the dimensionless estimated elastic properties of the biocemented sand (a) Young's modulus (b) Shear modulus, and (c) the evolution of Poisson's ratio.

6.3.2 Cohesion

The microstructural parameters of each sample presented in Table 6.1 have been used to estimate the cohesion using the relation (Eq 6.12). The parameter (σ_{ten}) is considered as a model parameter

(tensile strength) and has been calibrated (Figures 6.5) in order to reflect our experimental results (chapter 3), where the cohesion has been measured by drained triaxial tests on the same biocemented sand. The calibrated value of the intrinsic tensile strength (σ_{ten}) is 2.75 MPa. Montoya and Feng (2015) have shown through surface energy measurements that the particle-bond-particle exhibits more likely calcite bond failure than calcite detachment from the grain surface. As a consequence, the tensile strength of the two bonded grains is comparable to the tensile strength of the limestone rocks which are composed basically by calcium carbonates (CaCO_3) (Baykasoglu et al., 2008). This calibration value confirms in another way that the adhesion between the calcite and the sand grains is stronger than the adhesion between the calcite crystals. Generally, the evolution of the cohesion in the biocemented sand shows an exponential trend with the calcite amount. This exponential relationship is controlled mainly by the cohesive contact surface area, the coordination number and the solid fraction as shown in the equation 6.12.

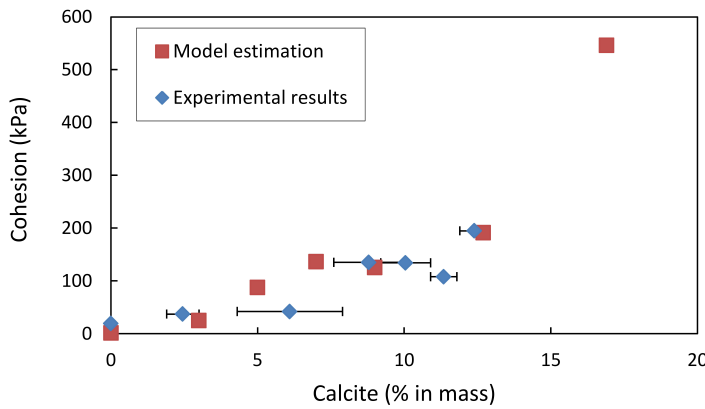


FIGURE 6.5: Estimation of the cohesion evolution compared with experimental results.

6.4 Conclusion

In the present paper, the real microstructural properties of biocemented sand, such as contact surface area, coordination number, volume fraction of each phase computed on 3D x-ray microtomography images have been used as an input in current analytical models to estimate the evolution of the elastic properties (Young's and shear modulus) and the strength properties (Coulomb cohesion) with the calcite content.

Concerning the effective elastic properties, the CCT model proposed by Dvorkin et al. (1994) has been used to estimate the effective moduli and Poisson's ratio. These estimates have been also compared to numerical results obtained by FEM simulations on 3D images, classical bounds and self-consistent estimate. Our results point out a good agreement between the numerical results and the CCT model on the whole range of volume fraction of calcite. Both results shows that both modulus increase non-linearly for low volume fraction of calcite ($f_c < 3.2\%$) and then increase linearly for larger volume fraction of calcite. This non-linear increase is due to the non-linear

increase of the cohesive contact surface area between grains induced by the biocalcification process. Moreover, we have shown that the self-consistent estimate is also in good agreement with both numerical and analytical results when $f_c > 3.2\%$.

Concerning the Coulomb cohesion, the analytical model initially developed by Richefeu et al. (2006) to estimate the cohesion due to suction in unsaturated soils is modified to estimate the macroscopic Coulomb cohesion of biocemented sands. The tensile strength (σ_{ten}) involved in this model has been adjusted on experimental results obtained from triaxial tests performed on the same biocemented sand. The obtained value is consistent with the one measured on limestone rocks which are composed basically of calcium carbonates.

All these results point out the important role of some microstructural parameters, notably those related to the contacts, on the effective parameters.

CHAPITRE 7

MECHANICAL AND MICROSTRUCTURAL CHANGES OF BIOCEMENTED SAND SUBJECTED TO AGGRESSIVE SOLUTION : CHEMICAL DURABILITY

Sommaire

7.1	Introduction	122
7.2	Material and Method	125
7.2.1	Specimens and chemical solution preparations	125
7.2.2	Dissolution device and protocol	126
7.2.3	Calcite dosage and microstructural observations	127
7.3	Results and discussion	128
7.3.1	Chemical durability of biocemented sand	128
7.3.2	Mechanical response	130
7.3.3	Microstructural observations	132
7.3.3.1	SEM observations	132
7.3.3.2	Microstructural properties	132
7.3.3.3	Contact properties	135
7.3.4	Calcification versus dissolution	140
7.4	Conclusions	141

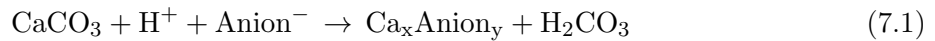
Abstract

An experimental study has been performed to investigate the effects of an aggressive solution on the mechanical strength of biocemented Fontainebleau sand. The tests have been performed on small triaxial samples extracted from a large scale model test. An aggressive chemical solution composed of hydrogen chloride and Tris buffer with an initial pH of 6.6 has been injected in the triaxial apparatus in different amounts. The changes of the physical and mechanical properties of the sample have been studied afterwards. Triaxial drained tests with constant confining pressures have been performed on the chemically treated samples in order to determine the remaining strength of the samples. The experimental results point out that the strength of the treated specimens decreases dramatically compared to that of the initial untreated specimens (a 50% strength reduction has been found for 10% of total calcite dissolution). Several SEM microscope and X-ray micro-tomography observations have been performed in order to identify the changes in the microstructure due to the chemical dissolution. Generally, these microstructural observations have shown a uniform calcite dissolution at the pore scale (no preferential locations). The calcite crystal structures have been damaged randomly by the chemical solution. A reduction of the densities and sizes of these crystals have been found from the SEM microscope and X-ray micro-tomography observations. The contact surface area created by the calcite deposition between the grains has shown clear reduction with the dissolution, which causes the degradation of the mechanical strength. However, the coordination number and the specific surface area of calcite inside the observed samples do not show any evolution during these dissolution tests. Generally the evolution of the properties computed from the 3D images after the dissolution process was almost the same as the computed 3D images of sand during biocementation process.

7.1 Introduction

Biocementation is a rather recent biotechnology that is used to improve the physical and mechanical properties of weak soils. It utilizes bacteria that have the ability to decompose urea, which in combination with calcium soluble salts, facilitate the production of calcite. The calcite is randomly dispersed and it precipitates on and between the soil particles, which can improve the mechanical properties of the soil (Al Qabany et al., 2011a; Feng and Montoya, 2015; Filet et al., 2012; Martinez et al., 2013; Montoya et al., 2013; van Paassen et al., 2010; Morales et al., 2015). The deposition of calcite reduces the porosity and clogs the pores of the soil, which can reduce dramatically the permeability and for high calcification level may produce almost impermeable layers (Jiang et al., 2014). This technique can be used in many engineering fields, such as water retention structures, petroleum industry, construction, slope protection and erosion control (Han et al., 2016; Jiang and Soga, 2016; Jiang et al., 2016; DeJong et al., 2010a, 2013). A main advantage compared to other methods, such as chemical grouting, is the low impact on environment and the low cost of materials. The most common inputs are ureolytic bacteria and solution of urea plus calcium chloride. The outcome of the reactions is ammonium chloride that serves as a nutrient for plants and is soluble and harmless in low concentration (Patnaik, 2003).

In engineering applications, one should consider the lifespan of the structures. It is therefore necessary to assess the durability of the cementation in order to plan future interventions. Usually the water that circulates in nature rarely presents a neutral pH. While alkaline waters will not have a negative effect on the calcite (biocement), the acid waters may dissolve the calcite and reduce the mechanical properties of the soil. Therefore, it is crucial to assess this phenomenon and to explore its influences on the mechanical strength of reinforced soils. The biocemented soil is most of the time affected by superficial or underground waters. It is well known that rainwaters may have an acidic pH due to the large amounts of fossil fuel gases that are released in the atmosphere. This depends on the magnitude of the industrialization of the area and the density of population nearby. Also the activity of living macro and microorganisms may produce acid sub-products that will probably reach the biocemented soil through rainwater. This acidic rainwater may influence on the long term the calcite crystals. The reaction of acid and calcite produces a calcium salt and the weak carbonate acid, which quickly dissolves into water and carbon dioxide as presented in the following equations :



The pH effect on the solubility of calcium carbonate has been studied in Coto et al. (2012), where the calcite dissolution rate appears as increasing with decreasing pH in the medium for ambient temperature (25°C) and constant pressure (100 kPa). The partial saturation of CO_2 has an important effect also, because of the direct relationship between this factor and the pH of the solution, which increases the solubility of the calcium carbonate in the medium. The coupled effect of temperature and pressure on the dissolution of calcium carbonate has been studied also in Coto et al. (2012). The dissolution has been increased in this study by decreasing the temperature and increasing the pressure. However, the dissolution due to an acidic solution (low pH) is still the most significant one. In nature, the acid rainwaters can slowly dissolve the calcite and reduce the cohesion and the bearing capacity of the cemented soil. This reduction may lead to failure of the structures nearby. It is therefore necessary to assess the chemical durability of biocementation. Cheng et al. (2013) tested internal erosion resistance and residual strength of biocemented sand samples after exposure to artificial acid rainwater from the top to the bottom. Changes in the specimen masses and unconfined compressive strength (UCS) at the top and bottom of the biocemented sand columns have been monitored. The artificial acid rain with pH = 3.5 continuously dissolved the calcite within the biocemented samples, resulting in a loss of weight. The total flushing of acid rain through the sand column was 12 L, corresponding to 5 years of rainfall (1000 mm/year). The UCS results of the dissolved samples reflected that no obvious damage occurred at the bottom part of the sand column (9 - 18 cm). However, the strength of the top part (near the injection point) of the sand column decreased proportionally to the acid rain. With 6 liters of rain, the UCS changed from 1.1 MPa to 0.8 MPa and with 12 liters it changed from 1 MPa to 0.6 MPa. The mass loss was almost linear and exhibited the calcite removal from the specimen. Dura (2013) has used biocalcified sand samples with calcite

contents between 12 and 16% in mass to study the effect of chemical dissolution on the mechanical properties. A solution that contains chemical components similar to acid rain (pH between 5 and 6) has been used in this study. The bio-cemented samples have been rinsed with 260 pore volumes (55 L) of the aggressive solution during 10 days. This rinsing operation decreased only the total initial calcite amount by 4%. UCS tests have shown a small decrease (less than 10%) in the strength of these samples induced by the dissolution of calcite. Dura (2013) has shown that with a flux of 1 m/day of acidic groundwater, calcite dissolution does not exceed 0.01% of the initial calcite over a period of 50 years, which represents negligible risk in the lifespan of a reinforced structure. However, environmental parameters can change from a structure to another (the acidity of water circulating inside the structure, temperature of the region, depth, speed of circulation, etc.) which can influence significantly the chemical dissolution of the calcite and decrease the lifespan of the structure. The microstructural properties of biocalcified soils (morphology of precipitated calcite, specific surface area of calcite, crystal structures and size, etc.) may also play a role in the chemical reaction of dissolution. The dissolution manner of calcite crystals inside the cemented sand is also a key factor for this study; localized calcite dissolution in the inter-particle contacts can reduce dramatically the strength of the soil and the lifespan of the structure. However, dissolution of the calcite precipitated on the grain surfaces will not cause significant decreases of the strength of the biocemented soil. For that propose, the chemical dissolution deserve to be studied at the microscale by using qualitative and quantitative tools such as : SEM and micro-tomography (Dadda et al., 2017a). Minto et al. (2017) have studied the porosity and permeability evolution during biocementation and dissolution of calcite inside sand specimens by using x-ray micro-tomography. However, the resolution of the scans in this study was not sufficient to capture the evolution of the contact properties. For that propose, future studies must be added to answer all these questions in order to be able to estimate the feasibility of the treatment for a specific structure, in a specific region and treated by a specific protocol.

The objective of the present paper is to analyze the changes in the mechanical and microstructural properties of biocemented sand subjected to aggressive solution. Triaxial sand specimens with a calcite content of about 6% in mass have been extracted from a large scale model test on biocemented Fontainebleau sand. These specimens have been subjected to aggressive solution in different proportions and compared to undissolved ones, in order to detect the strength changes due to the degradation of the calcite. The dissolution process has been followed by chemical measurements (pH and conductivity) in order to estimate continuously the dissolution of calcite. Small subsamples have been extracted from dissolved and undissolved triaxial samples in order to explore qualitatively and quantitatively the evolution of the microstructural properties using scanning electron microscope (SEM) and x-ray micro-tomography observations. This paper is organized as follow : section 7.2 presents the extraction and the preparation of the specimens, details the preparation of the aggressive solution and the experimental device developed in this work for the chemical dissolution of the biocemented sand, and shows the image processing methodology used in order to compute the microstructural properties of the sand from the 3D images obtained from x-ray micro-tomography. Finally section 7.3 discusses the obtained results

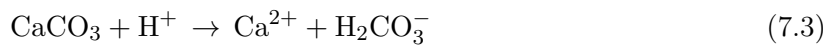
at both the micro and macro scales (mechanical and microstructural properties).

7.2 Material and Method

7.2.1 Specimens and chemical solution preparations

Sample preparation : Several blocks with almost the same cementation level of 6% of calcite in mass have been extracted from a large scale test of biocementation of Fontainebleau sand (NE34). The sand has been poured in several layers and compacted with a small vibratory roller in order to obtain a uniform porosity of about 40%. Two solutions have been used in this biocementation test : (1) the bacterial solution (1 g/L of bacteria + 3g/L of NaCl) and (2) the calcification solution (0.6 mol/L of Urea and CaCl₂). From these blocks, five specimens have been cut manually (avoiding as far as possible any disturbance created by vibrations) in order to be tested for mechanical strength in the triaxial apparatus after the chemical dissolution. The specimens are cylindrical and of small size (diameter d=35mm and height h=70mm approximately) in order to avoid a possible heterogeneity of the dissolution usually observed in large specimens.

Chemical solution preparation : In order to check the chemical durability of the biocemented sand, each specimen has been subjected to a slightly acid chemical solution and then tested for the remaining mechanical strength in the triaxial apparatus. Generally, the calcite dissolves in an acidic environment and releases carbon dioxide. The speed of dissolution depends mostly on the pH of the environment. Other factors affect the dissolution process such as the temperature or other chemical components diluted in water. Whiffin et al. (2007) observed that the calcite dissolution rate (in log scale) is proportional to the pH of the solution for 5 > pH > 1. For pH > 5, the reaction is steady and slow. For that purpose, a chemical solution which has a pH greater than 5 is appropriate to obtain slow and stable dissolution rate of calcite. In the present work, a solution of pH of 6.6 has been chosen which contains 1 litre of distilled water with 0.195 mol/L of HCl and 0.2 mol/L of Tris (Trishydroxyméthylaminométhane), which can play the role of a buffer solution that prevents high changes in pH. The dissolution capacity of this solution has been estimated by using PHREEQC software for reaction equilibrium computation (Equation 7.3).



This capacity depends on the contact time between the calcite and the aggressive solution ; this time can be translated into the flow speed of the solution inside the specimen. A maximum amount of calcite of about 0.6 mmol/l (equivalent to 0.6 g/l of calcite) can be dissolved by this solution, which represents the total saturation of the solution with the calcite. The pH of the solution changes when it passes through the calcified specimen, this pH has been used as an indicator of the dissolution inside the specimens. The outlet value of pH can be changed from 6.6 as an initial value to 7 as final values (total saturation of the solution with the calcite). Figure 7.1 represents different amounts of dissolved calcite as a function of the pH of the aggressive solution in equilibrium, which had initially a pH equal to 6.6. This computation has been performed

in PHREEQC software (reaction equilibrium computation). This figure shows a quasi-linear relationship between the output pH and dissolved calcite. These computations have been used in order to choose the amount solution injected inside the calcified sand specimens in order to get a precise dissolution level.

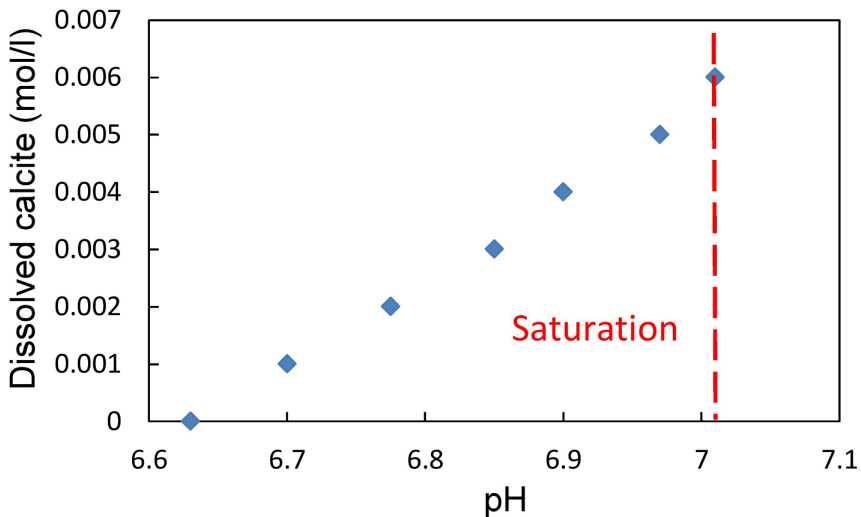


FIGURE 7.1: Dissolved calcite depending on output pH.

7.2.2 Dissolution device and protocol

A dissolution device has been developed in this work. The main role of this device is to perform the chemical dissolution of the biocemented specimens directly inside the triaxial apparatus (in order to avoid the disturbance expected during the installation in the triaxial apparatus of an already dissolved specimen) simultaneously achieving the chemical measurements (pH and conductivity) (Figure 7.2). The dissolution test has been performed by injecting the chemical solution stored in a tank by a peristatic pump from the bottom to the top of the triaxial cell.

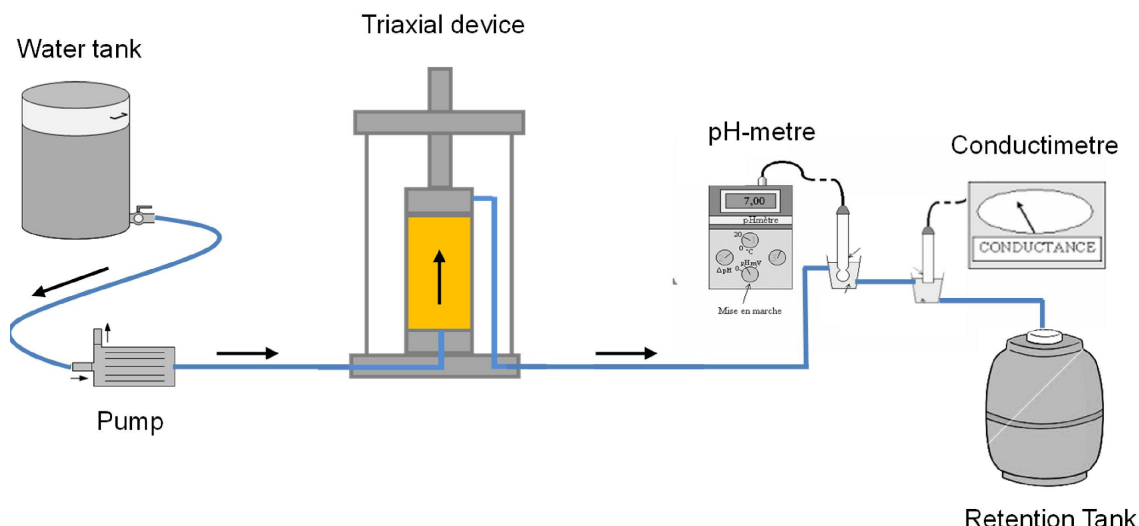


FIGURE 7.2: Schematic representation of the dissolution device.

The output solution goes through a pH meter and a conductivity meter for an evaluation of the dissolved calcite. The speed of injection is first adjusted until the initial output pH is at least 6.8. In order to obtain this output pH, a low speed of injection has been maintained, about $5.4\text{cm}^3/\text{min}$, throughout the dissolution phase. Different volumes of chemical solution have been used, resulting into different dissolution levels. Table 7.1 summarizes the characteristics of the different tests (initial mass fraction of calcite in the specimen, injected volume, etc.).

TABLE 7.1: Characteristics of the performed tests.

Specimen	Initial calcite content content (% in mass)	Total injected volume (L)	Confinement pressure (kPa)
S_0	6.3	0	50
S_1	5.7	1.2	
S_2	5.6	2.4	
S_{3a}	6.2	6	
S_{3b}	5.8	6	

The first sample (S_0) has been tested mechanically without dissolution in order to get a reference value for the strength of these biocemented samples. Two specimens (S_{3a} and S_{3b}) have been flushed with 6 litres in order to confirm the repeatability of the dissolution process. Two other specimens (S_1 and S_2) have been flushed with smaller amounts (2.6 and 1.2 L) in order to draw the evolution of the strength of these specimens at different stages of dissolution. After the injection, drained triaxial compression tests are performed with a constant confinement pressure of 50 kPa.

7.2.3 Calcite dosage and microstructural observations

Calcite content : The calcite content has been measured for all the specimens after the triaxial compression test. The specimens have been cut in 5 slices 1.4 cm in height and 3 elementary samples have been taken from each slice (Figure 7.3). The calcite content of each elementary sample has been determined using the Bernard calcimeter by putting the sample in a glass vessel that is linked to a gas volume measurement tube. Then, the calcite in the sample is dissolved using HCl and CO₂ is released. Based on the ideal gas law, the number of moles of the gas is determined; it is equal to the moles of calcite.

Microstructural observations : The microstructure of the biocemented sand is of high importance for a precise understanding of the reasons why the strength parameters increase compared to the untreated sand. The calcite crystals formation depends highly on several factors such as the amount of bacteria, the concentration of reactants and the saturation level of the medium. In this study, it was necessary to observe the evolution of the calcite crystals for different stages of the dissolution process. For that purpose, an undissolved subsample considered as reference and 3 dissolved subsamples have been scanned by SEM and X-ray micro-tomography. The x-ray

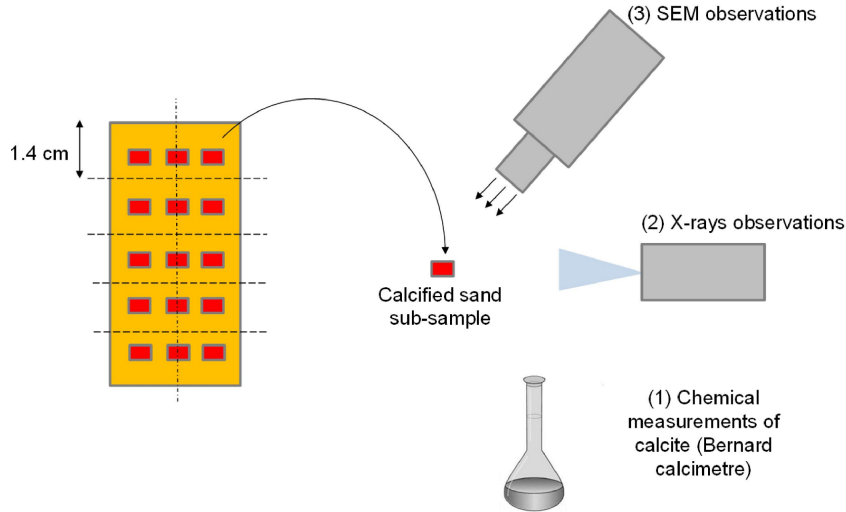


FIGURE 7.3: Schema of the sample dividing and complementary analysis after the triaxial tests.

micro-tomography observations correspond to cubic volumes of 1.2 mm in dimensions (thus including more than 300 particles with an average diameter of 0.21 mm) with a resolution of 0.6 $\mu\text{m}/\text{pixel}$. The obtained 3D images have been treated with the same method used in (Dadda et al., 2017b) assuming the existence of a Gaussian distribution for the grey levels of each of the phases (pore, sand and calcite). The analysis of these images provides the different mean microstructural properties such as calcite content, porosity and specific surface areas of both the whole medium and the calcite phase using the numerical procedures developed in the chapter 5. More advanced microstructural properties (such as : contact properties and orientations) have been also investigated based on these 3D images by the separation of the grains in 3D and computing the evolution of the coordination number, the contact surfaces and the type of the contact ('frictional', 'mixed' and 'cemented') (for more details see chapter 5). The determination of all these properties enable to understand the phenomenon in quantitative manner by exploring the dissolution spatial distribution and the zones of calcite which have been mostly attacked by the aggressive solution (active calcite "intergranular calcite" or passive calcite "grain surfaces calcite").

7.3 Results and discussion

7.3.1 Chemical durability of biocemented sand

In this experimental work, the calcite content has been measured before and after dissolution in all the tested samples. Before dissolution, all the samples have shown similar profiles of calcite near 6.5% of calcite in mass. The initial profiles of these samples is similar to the one of the undissolved sample " S_0 " (Figure 7.4a). In the dissolution tests, the specimens " S_1 " and " S_2 " have been flushed with different volumes of the aggressive solution (1.2 and 2.4 L respectively) in order to get different dissolution levels, these amounts of aggressive solution can dissolve theoretically 10 and 20% of the total amount of calcite, respectively. Two other tests have been performed on

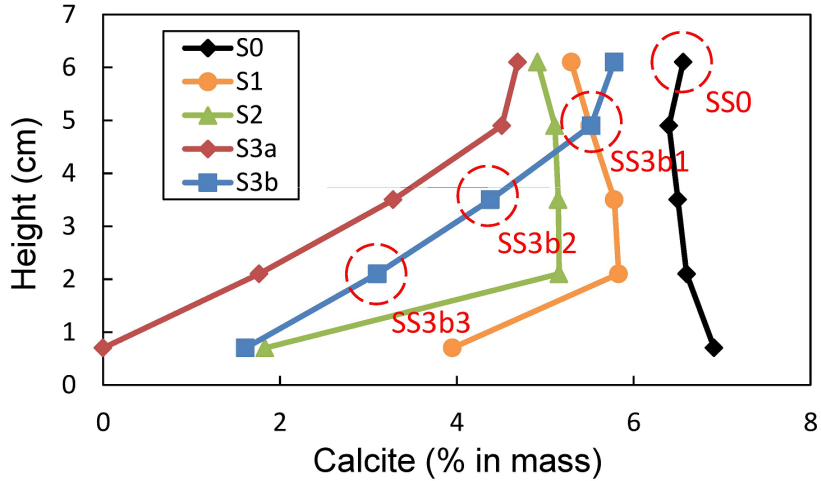
almost the same initial calcification level (S_{3a} and S_{3b}). In these tests, the samples have been flushed with the same volume of the aggressive solution (6L) in order to check the repeatability of the dissolution in terms of calcite profile and chemical measurements (pH and conductivity). This amount of the aggressive solution (6L) is able to dissolve theoretically 50% of the total calcite in these specimens (based on the numerical results in Figure 7.1). Generally, the calcite profiles of all the dissolved specimens have shown very strong heterogeneity compared to the initial profile (before dissolution), which is due to the dissolution localization near the injection point (bottom part). From the Figure 7.4b the aggressive solution didn't reach the saturation with calcium ions (pH output < 7) thanks to the Tris who keep small variation of pH during the dissolution process and retards a little the dissolution, but apparently not sufficiently to cause a homogeneous dissolution. The only way to obtain a more homogenous profile of calcite is to increase the injection speed. However, it was not possible in the current study because of the low permeability of the specimens (in the range of 10^{-5}m/s). Any attempt to do this would increase the pressure of the injection and would cause local failure in the specimen.

In order to obtain a more homogeneous specimen after dissolution, a new injection procedure has been tested and applied on an additional specimen. The injection was performed in both directions (upwards and downwards) by alternating between them every hour. The obtained profile was still not satisfying with a larger dissolution at both ends, while the middle of the specimen remains almost intact.

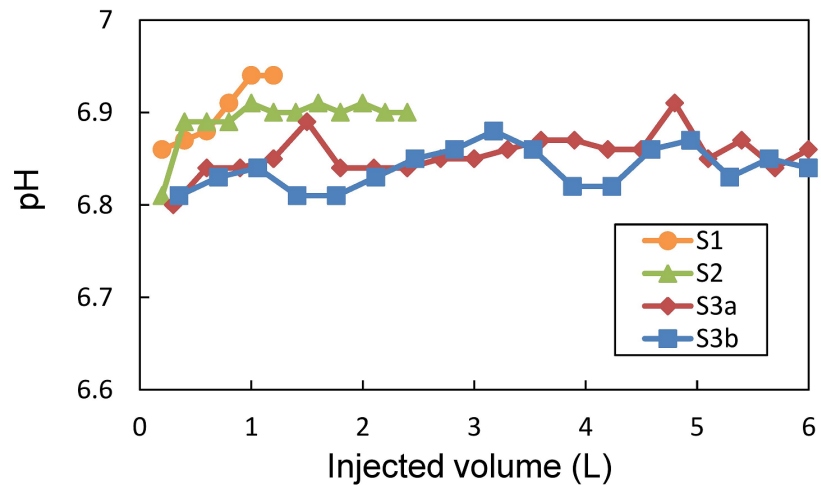
7.3.2 Mechanical response

A total of five tests have been performed in this work, the first sample have been tested mechanically without dissolution, the other four samples have been flushed with different amount of aggressive solution in order to get different degree of calcite degradation as mentioned in the previous paragraphs. These samples have been tested under the same confining pressures (50 kPa) covering the range of horizontal effective stresses encountered in practical application of the biocementation for the reinforcement of earth dams and dikes. The compression tests have been performed at a constant axial displacement rate of 0.1 mm/min, which ensures a fully drained response for the biocemented sand.

The undissolved specimen (S_0) shows a maximum deviatoric stress of about 900 kPa under 50 kPa of confinement pressure. This specimen shows a typical behaviour of cemented sand (fragile failure and dilatancy) (Figure 7.5). The strength of this sample is higher than a specimen with the same calcite amount but calcified with a different protocol of injection (higher concentration of the calcification solution which provides larger calcite crystals) (chapter 3). This result confirms the conclusion found in the work of Al Qabany et al. (2011a), where specimens treated with lower concentrations of calcification solutions have shown smaller calcite crystals and higher compression strength. This fact can be related to the higher cohesion of smaller calcite agglomerations compared to larger calcite crystals.



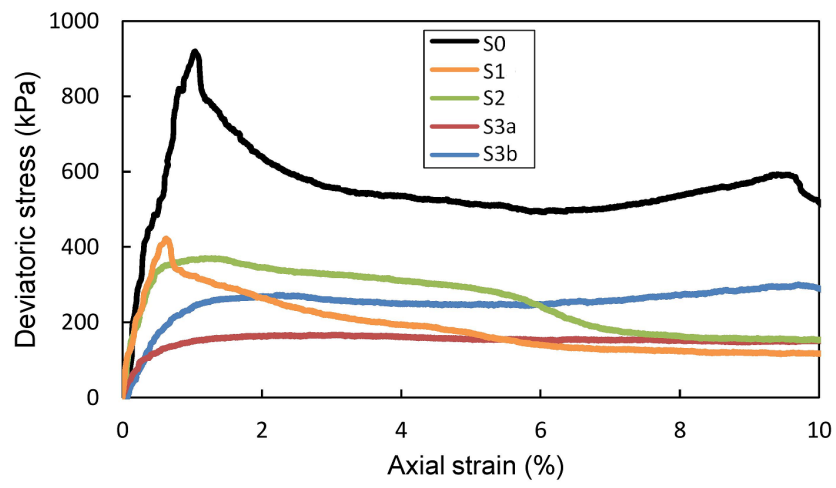
(a)



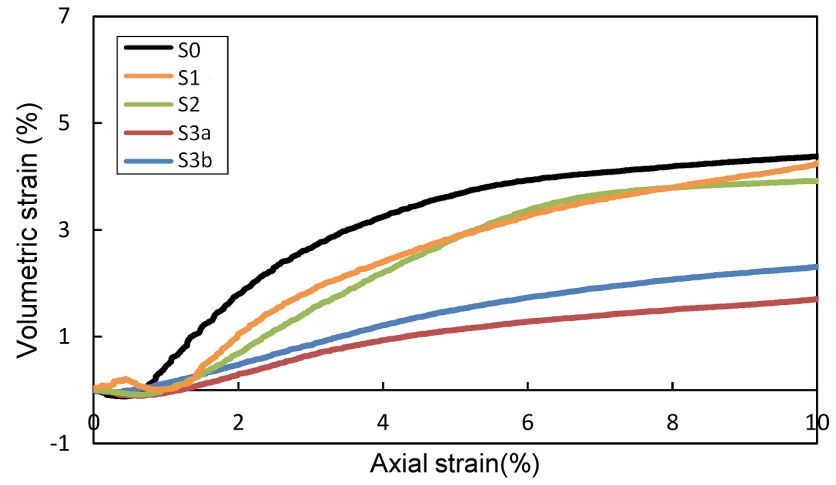
(b)

FIGURE 7.4: a) calcite profile of all the tested specimens before and after dissolution, b) pH variation of output water.

Despite the high heterogeneity of the dissolved specimens (Figure 7.5a), the results of the triaxial tests can be analysed to a certain extent. The dissolved specimens show lower peak deviatoric stress and lower dilatancy with the disappearance of the fragile behaviour (Figure 7.5). The behaviour and the strength of the flushed specimens is controlled basically by the weak (bottom) part which contains a smaller amount of calcite (Figure 7.5a). The decrease of the peak strength follows monotonically the volume injected inside the specimen (Figure 7.7) : the decrease of strength is significant for small injected volumes (less than 2 litres) but more gentle (even quasilinear) for larger injected volume. The maximum deviatoric stress tends asymptotically towards the strength of the untreated sand (120 kPa) (clean Fontainebleau sand) under the same confining pressure (50 kPa) (chapter 3). Since the strength in these dissolved samples is controlled by the weaker part which has smaller height compared to the standards, the decrease of the strength of homogeneous samples should be more severe than what has been found in



(a)



(b)

FIGURE 7.5: Triaxial results of different dissolved and undissolved specimens under 50 kPa of confinement, a) mechanical response, b) volumetric response.

these results ((Figure 7.6)).

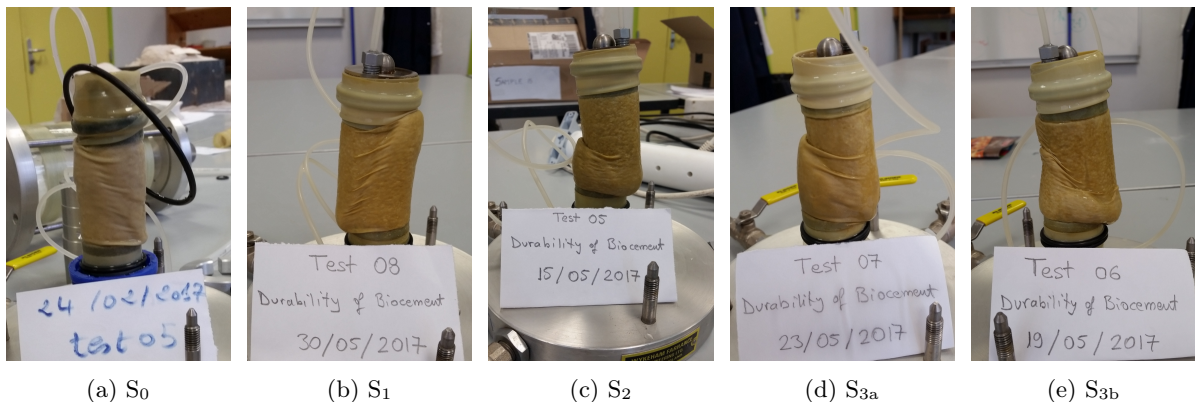


FIGURE 7.6: Triaxial samples after failure.

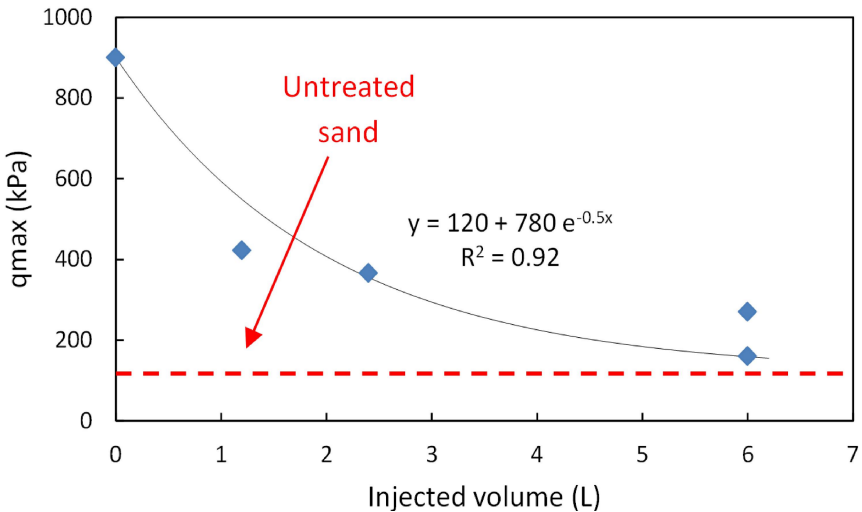


FIGURE 7.7: Peak deviatoric stress vs volume of injected solution.

7.3.3 Microstructural observations

During the calcite dosage of the specimen “S_{3b}”, small subsamples (SS_{3b1}, SS_{3b2}, SS_{3b3}) have been extracted from each layer in order to perform SEM and x-ray micro-tomography. One subsample (SS₀) has also been extracted from the undissolved sample “S₀” in order to analyse the evolution of the microstructure from intact calcified sample to dissolved samples. The positions of these scanned sub-samples are shown in Figure 7.4a.

7.3.3.1 SEM observations

Figure 7.8 presents SEM images at different scales of the four sub-samples. Through these images, it is possible to observe the difference in the calcite content in terms of both the crystals density and their structural integrity. In the undissolved subsample (SS₀) (Figure 7.8), a high density of crystals covers almost all the grain surfaces and forms calcite bridges in the vicinity of contacts. The zoom shows that the crystal surfaces are flat and regular. The well-formed calcite crystals confirm the saturation of the medium with calcium ions Ca²⁺ during the calcification process. In the dissolved specimens (SS_{3b1}, SS_{3b2}, SS_{3b3}) the number of calcite crystals decreases and the surfaces of the grains become visible. The size of the calcite crystals appears also reduced. Indeed, the size of the calcite crystals is about 10 μm for the undissolved subsample and less than 4 μm for the dissolved subsamples. Probably in many cases, the acid solution managed to detach the crystals from the grains and in the other cases to damage their surface. This damage forms different patterns which all increase the specific surface area of the calcite thus leading to a faster dissolution. This is probably one of the factors that cause a concentrated dissolution close to the injection point.

7.3.3.2 Microstructural properties

The porosity (ϕ) and volume fraction calcite (f_c) have been computed by counting the number of voxels of each phase (sand, calcite and void) in a 3D image. The total specific surface area

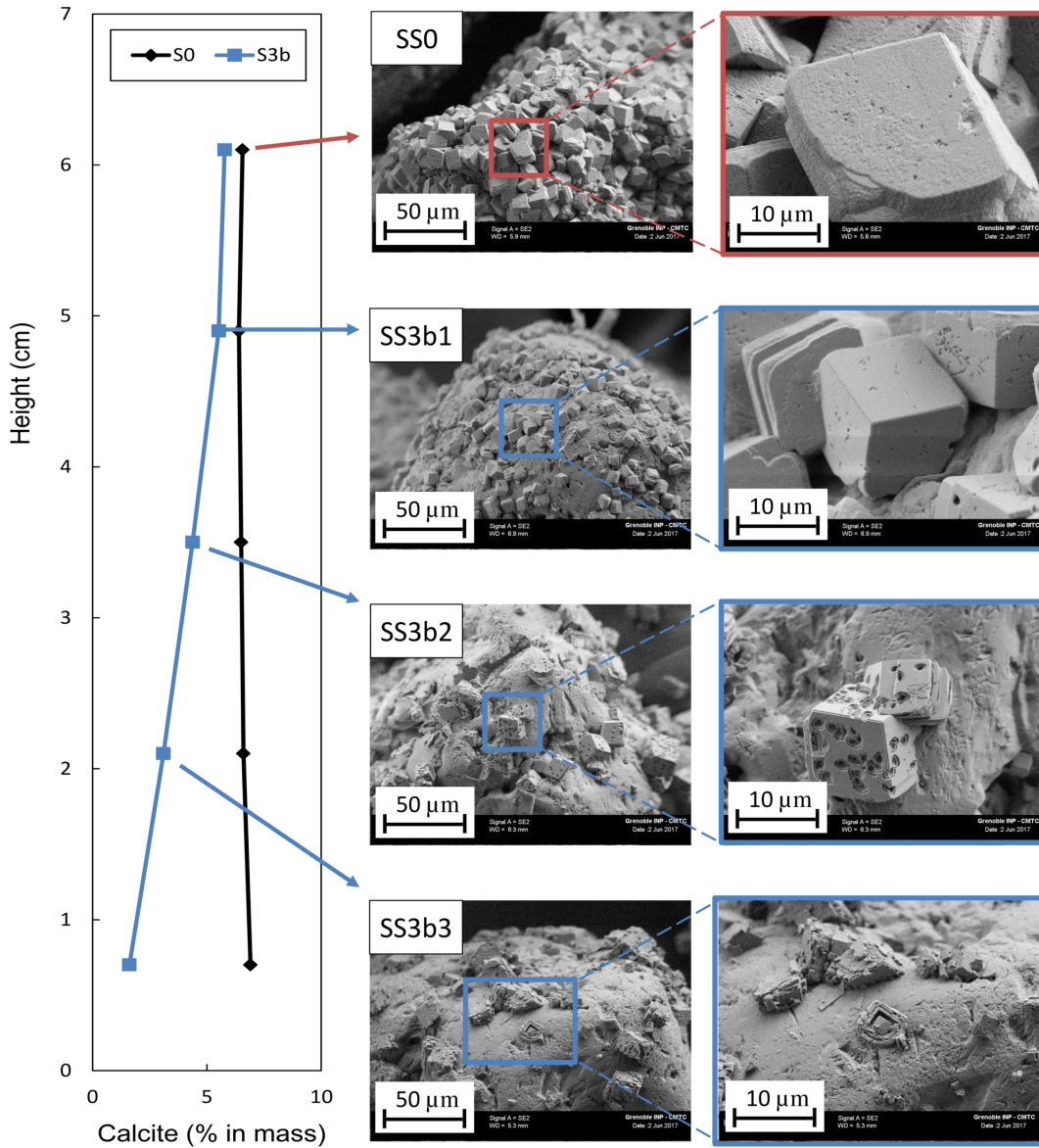


FIGURE 7.8: SEM observation of different undissolved (SS_0) and dissolved specimens (SS_{3b1} , SS_{3b2} and SS_{3b3}).

with calcite SSA and the specific surface area of calcite SSA_c have been computed using line intercept method (Dadda et al., 2017b). In order to check that the 3D images are large enough to be representative, these quantities have been computed on 3D volumes with increasing size extracted from the 3D images. Figure 7.9 shows that all these average microstructural properties reach a constant value when the volume size is about 1 mm^3 . The corresponding values for each property is summarized in the Table 7.2.

Porosity and volume fraction of calcite : The initial porosity ϕ_0 , i.e. the porosity without calcite, of our samples can be easily deduced from the final porosity ϕ and the volume fraction of calcite f_c computed from the 3D images. Table 7.2 and Figure 7.10a show that the initial porosity ϕ_0 of all the specimens is close to 40%. These values are in agreement with the experimental

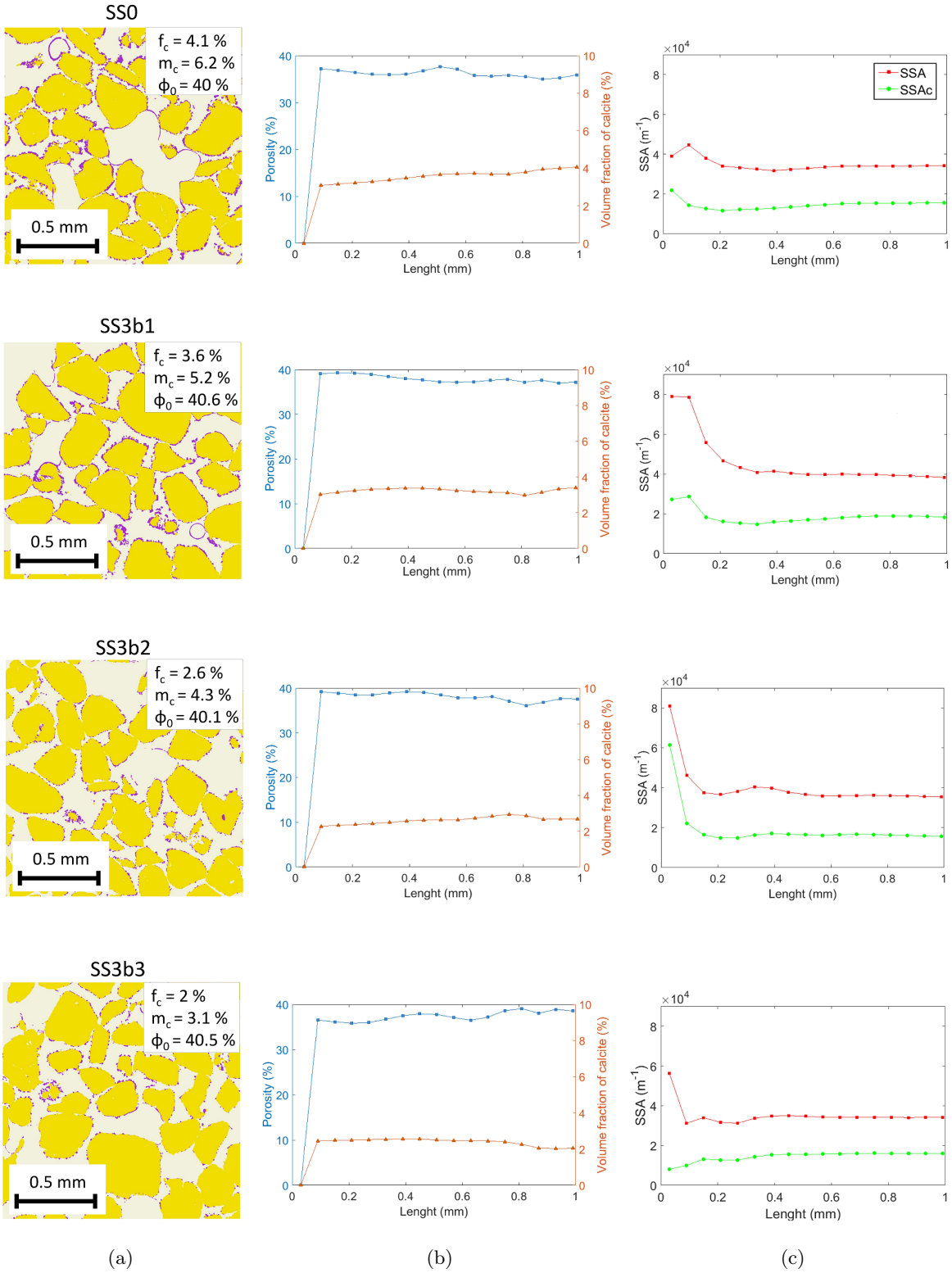


FIGURE 7.9: Microstructural properties of the four scanned subsamples (SS₀, SS_{3b1}, SS_{3b2} and SS_{3b3}), a) 2D treated images, b) final porosity and volume fraction of calcite, c) the specific surface area with and without calcite and the specific surface area of calcite.

values of the initial porosity within the large-scale model ($\phi_0 = 40\%$). Similarly, the Figure 7.12a shows that the volume fraction of calcite computed from the 3D images are in good agreement

TABLE 7.2: Computed microstructural properties of the subsamples.

Subsample	SS_0	SS_{3b1}	SS_{3b2}	SS_{3b3}
Initial porosity ϕ_0 (%)	40	40.6	40.1	40.5
Mass fraction of calcite m_c (%)	6.2	5.2	4.3	3.1
Volume fraction of calcite f_c (%)	4.1	3.6	2.6	2
SSA (m^{-1})	34239	38228	35518	34171
SSA_c (m^{-1})	15564	18015	15692	15950
\bar{Z}_b	8.4	7.6	8.4	8.1
\bar{Z}_a	9.1	8.3	9.2	8.5
\bar{S}_b (μm^2)	1450	1010	1115	895
\bar{S}_a (μm^2)	2529	1436	1590	1114
\bar{S}_c (μm^2)	1170	572	535	290

with the experimental values measured by using the Bernard calcimeter, which confirms the validity of the image treatment process.

Specific Surface Areas : Table 7.2 shows that both the total specific surface area SSA and the specific surface area of the calcite SSA_c of the dissolved specimen slightly decreases with decreasing the volume fraction of calcite. However, the Figure 7.10c shows that the ratio (SSA_c/SSA) is almost constant and equal to 0.5 whatever the level of dissolution. According to the definition of both specific surface areas (Dadda et al., 2017b), this ratio characterizes the percentage of the initial surface of sand covered by the calcite. It is equal to 0 when there is no calcite, 0.5 when half of the grains surface is covered with calcite and 1 when sand grains are totally covered with calcite. This latter result shows that despite the decrease of the volume fraction of calcite, the distribution of the calcite over the grain is not modified. It seems to prove that the dissolution of the calcite by the chemical solution mainly results in a decrease of the thickness of the calcite layer which covers the grains, as shown by the SEM observations (Figure 7.8).

7.3.3.3 Contact properties

The 3D images have further been used to determine different contact properties such as the coordination number, the contact surface area, the type and the orientation of the contacts following the methodology presented in chapter 5.

7.3.3.3.1 Coordination number and contact surface area

Coordination number : The Figure 7.11b presents the distribution of the coordination number in each subsample with and without calcite. From these distribution, one can easily compute the mean coordination number of each subsample with and without calcite, noted \bar{Z}_a and \bar{Z}_b respectively. The obtained values presented in Table 7.2 show that the coordination number of a given specimen is larger when the calcite is present, which is consistent with previous observations

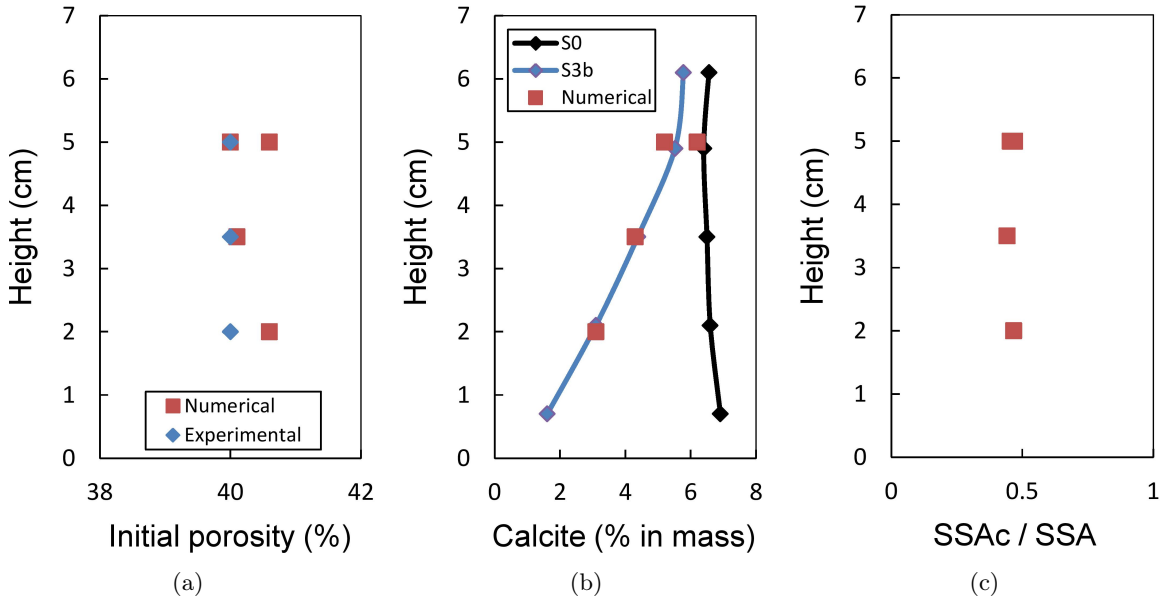


FIGURE 7.10: Microstructural properties of the four scanned subsamples (SS_0 , SS_{3b1} , SS_{3b2} and SS_{3b3}), a) measured and computed initial porosity, b) measured and computed mass fraction of calcite, c) ratio between the specific surface area of calcite (SSA_c) and the total specific surface area with calcite (SSA_a).

(chapter 5). The Figure 7.12 shows that the ratio \bar{Z}_a/\bar{Z}_b slightly decreases at the bottom of the specimen SS_{3b} (from 1.1 to 1.05), where the volume fraction of calcite is the lowest due to the dissolution process.

Contact surface area : The Figure 7.11c presents the distribution of the contact surface area in each sub-sample with and without calcite, from which we can compute the mean contact surface areas \bar{S}_a and \bar{S}_b respectively. The mean cohesive contact surface area is given by : $\bar{S}_c = \bar{S}_a - \bar{S}_b$. The obtained values presented in Table 7.2 show that the mean contact surface area generally increases with increasing the volume fraction of calcite, which is consistent with previous observations (chapter 5). As previously, due to the dissolution process, the ratio \bar{S}_c/\bar{S}_a decreases at the bottom of the specimen SS_{3b} (from 0.45 to 0.25), where the volume fraction calcite is the lowest.

7.3.3.3.2 Distribution of contact and surfaces types

Three types of contact can be distinguished after biocalcification (chapter 5) : (1) 'frictional' contacts (silica only) as in untreated sand, (2) 'mixed' contacts and (3) 'cemented' contacts (Figure 4-c). 'Mixed' contacts are 'frictional' contacts which became 'cohesive' due to the biocalcification process. 'Cemented' contacts are new contacts created by a bridge of calcite between two grains.

Figure 7.13 presents the distribution of the different types ('frictional', 'mixed', 'cemented') of contact in terms of number of contact (Figure 7.13b) and contact surface area (Figure 7.13c)

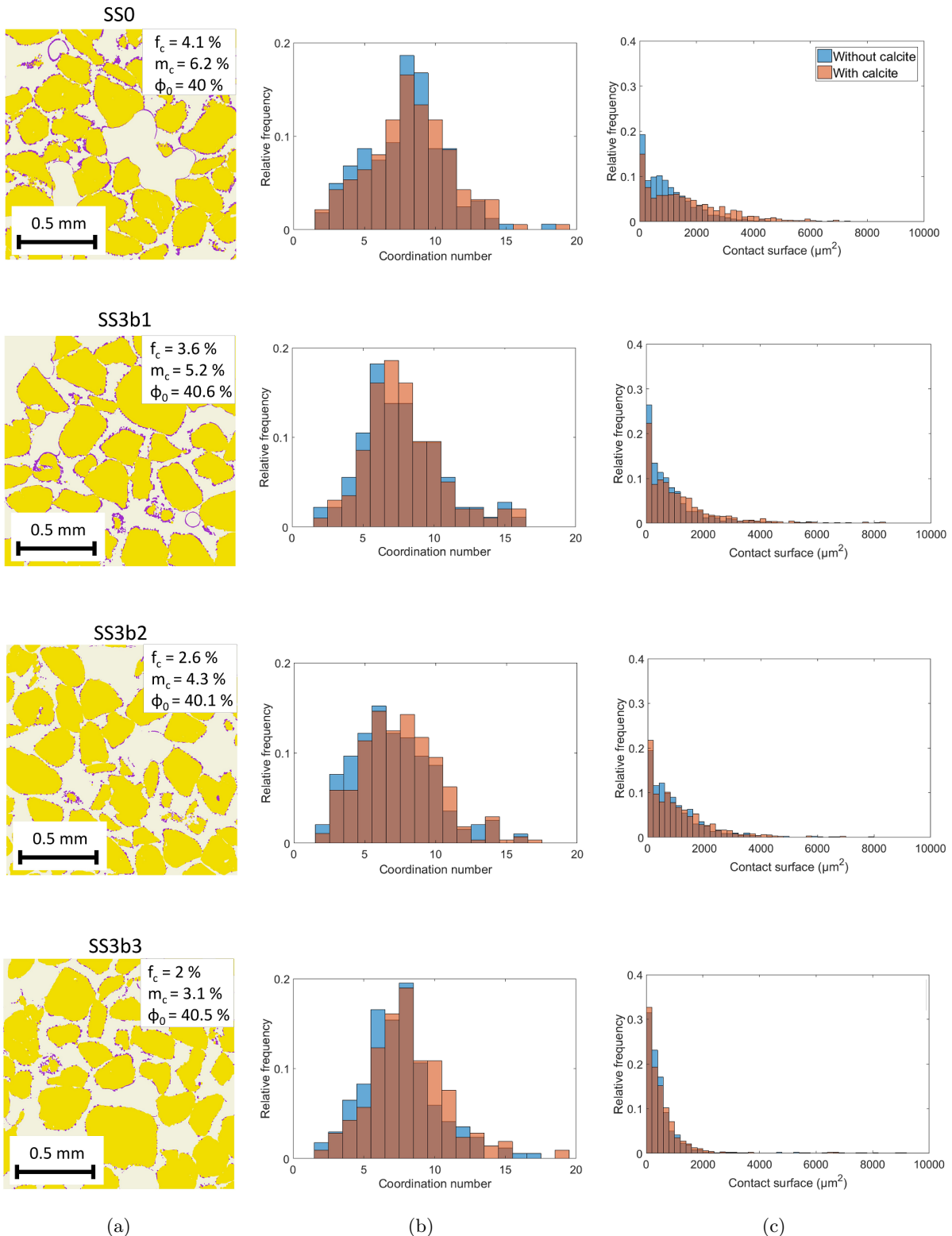


FIGURE 7.11: Contact properties of the four scanned subsamples (SS₀, SS_{3b1}, SS_{3b2} and SS_{3b3}),
a) 2D treated images, b) coordination number distribution with and without calcite c) contact
surface area with and without calcite.

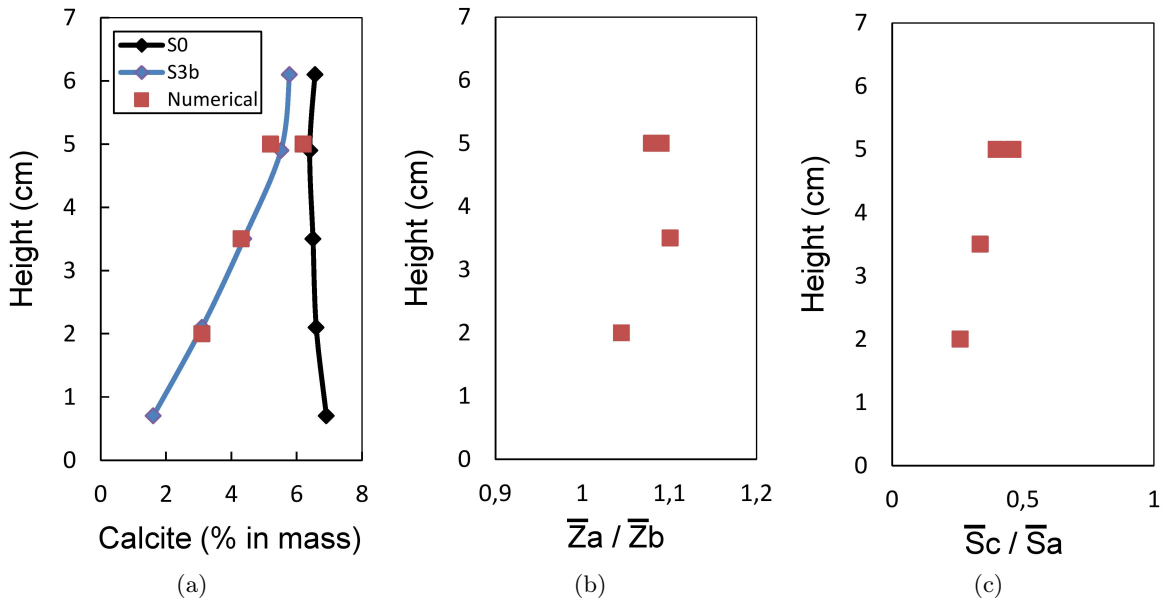


FIGURE 7.12: Contact properties of the four scanned subsamples (SS₀, SS_{3b1}, SS_{3b2} and SS_{3b3}), a) measured and computed mass fraction of calcite, b) coordination number, c) contact surface.

for the 4 samples under consideration. As already observed in chapter 5, even if the volume fraction of calcite is small, most of the contacts in each sub-sample are 'mixed'. In the undissolved specimen (SS₀) (Figure 7.13b), the 'mixed' contacts represent more than 80% of the total number of contacts, with only a small percentage of 'cemented' and 'frictional' contacts. Moreover, the contact surfaces of the 'cemented' and 'frictional' contacts are very small compared to the 'mixed' ones (Figure 7.13c). With the dissolution, the Figure 7.13b shows that the number of 'frictional' contacts slightly increases, whereas the number of 'mixed' contact slightly decreases. In the meantime, the percentage of 'cemented' contacts does not change significantly. Similar trends can be observed concerning the contact surface area of each type of contact. All these results seem to point out that the small 'mixed' contacts are more sensitive to the dissolution process.

7.3.3.3.3 Contact orientation

The orientation of the contacts has been computed by fitting plans on the cloud of voxels constituting the contacts in 3D and determining the two orientation angles (azimuth ψ and zenith angle θ). The fabric tensor can subsequently be computed from the distribution of the vectors normal to the contact surface in order to quantify the degree of anisotropy of the contact network (for more details see chapter 5). The orientation of the different types of contact within each sub-sample, as well as the corresponding fabric tensor is presented on the Figure 7.14. These quantities have been computed on the 3D images with and without calcite. As already underlined in chapter 5, the orientation of the contacts within the sample without calcite are almost isotropic and remains isotropic when the calcite is present. This latter remark is valid for both undissolved and dissolved sub-samples. These results seem to prove that the flow direction of the aggressive solution did not create any anisotropy in the cemented contacts.

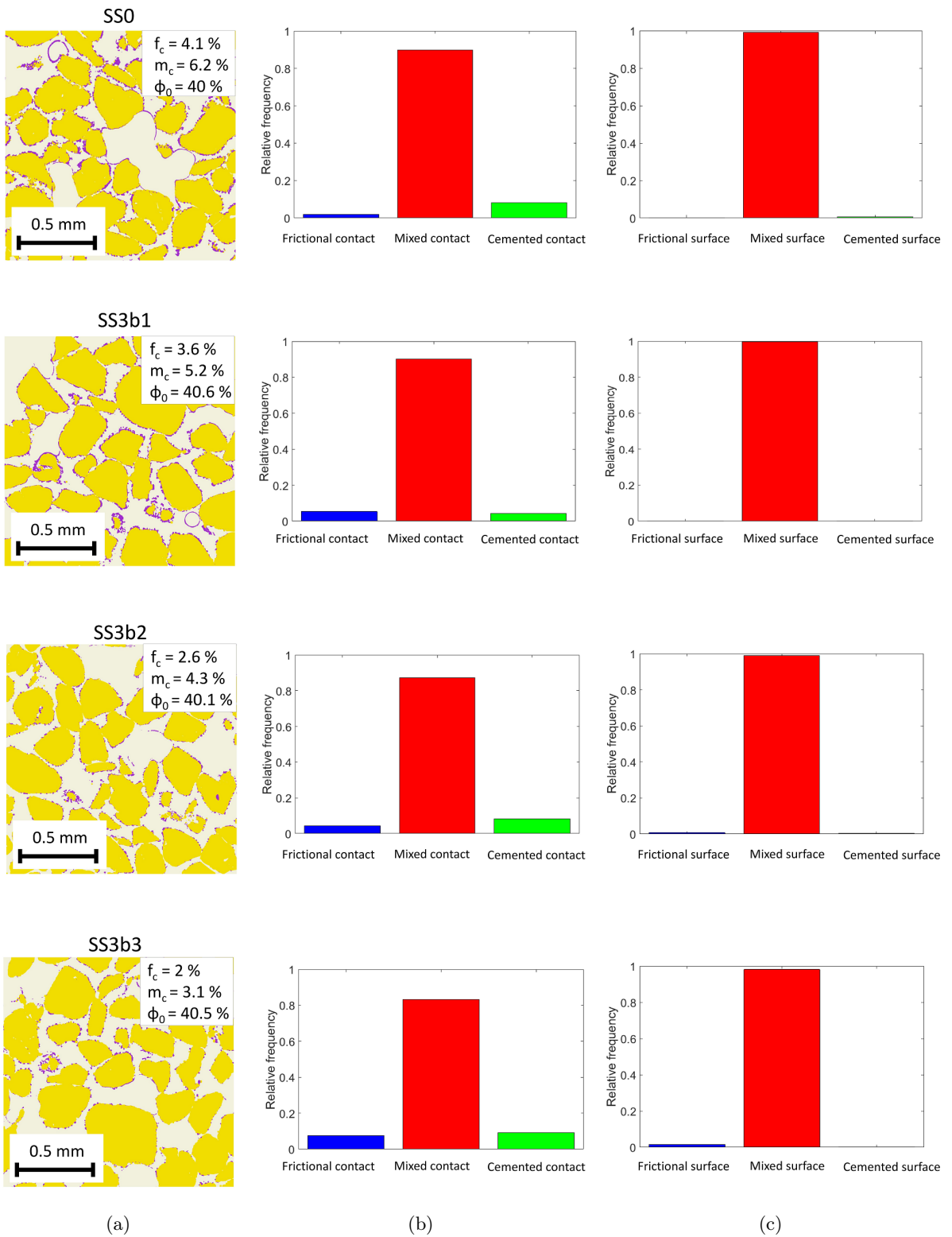


FIGURE 7.13: Contact properties of the four scanned subsamples (SS₀, SS_{3b1}, SS_{3b2} and SS_{3b3}),
a) 2D treated images, b) type of contact distribution, c) type of contact surface distribution.

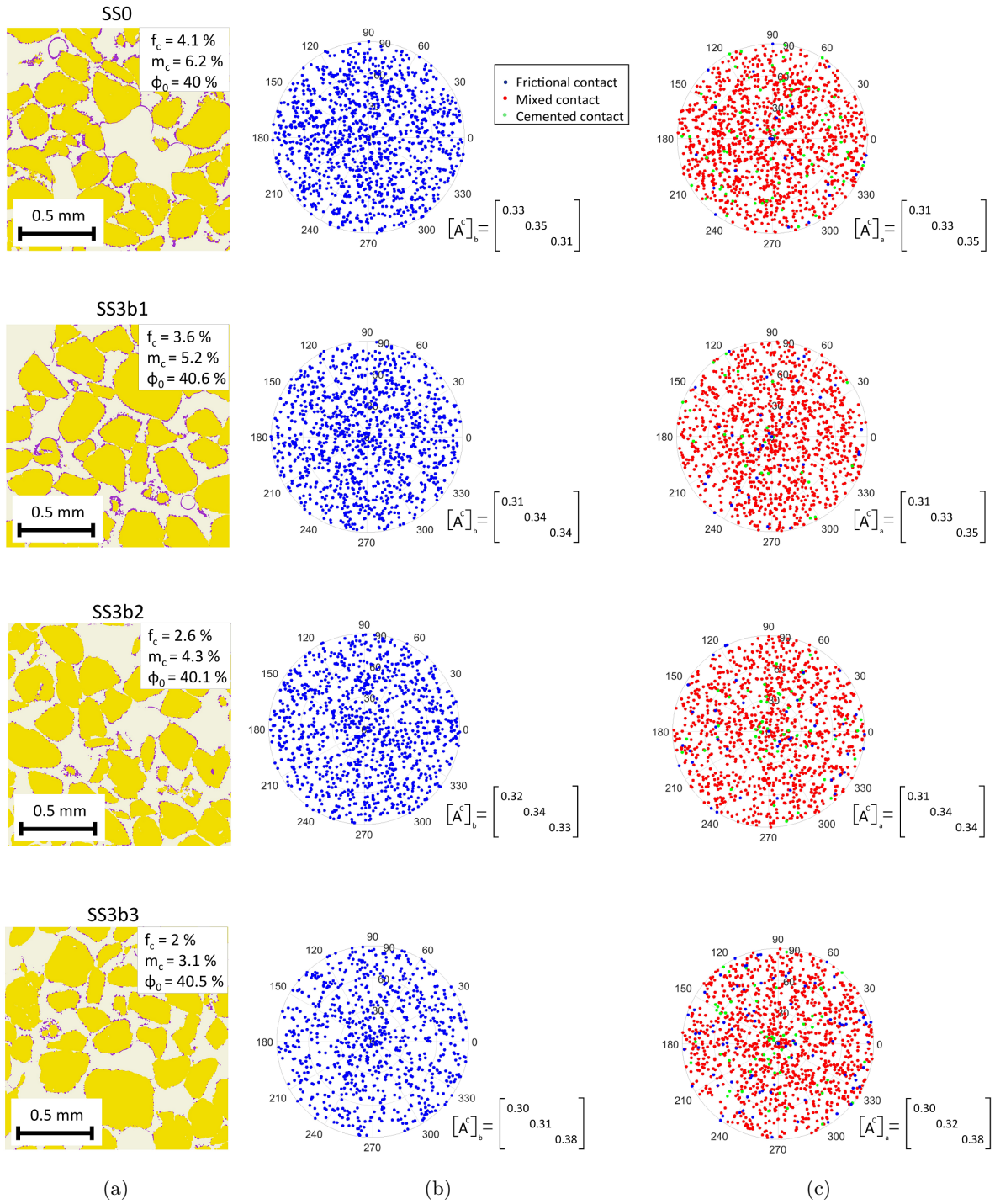


FIGURE 7.14: Orientation of the different types of contact within the subsamples (SS0, SS3b1, SS3b2 and SS3b3), Contact properties of the four scanned subsamples (SS0, SS3b1, SS3b2 and SS3b3), a) 2D treated images, b) contact distribution before calcification c) contact distribution after calcification .

7.3.4 Calcification versus dissolution

To understand more the evolution of the microstructural properties of the dissolved biocemented sand specimens, the results obtained from these specimens (contact surface area, specific surface

area and the coordination number) have been compared to previous results obtained from biocemented specimens with different calcification levels (chapter 5). This comparison permits to understand if there is a hysteresis between the calcification (or precipitation) and the dissolution processes and to explore the dissolution manner of the calcite.

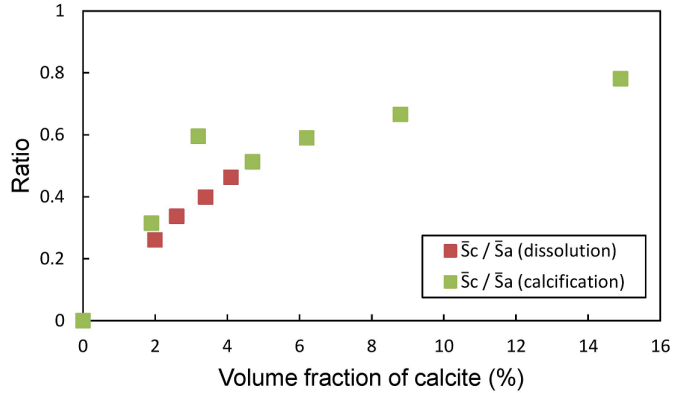
Figure 7.15 presents a comparison of computed microstructural properties (SSA_c/SSA , \bar{S}_c/\bar{S}_a , \bar{Z}_a/\bar{Z}_b) from calcified and dissolved specimens. The evolutions of the ratios \bar{S}_c/\bar{S}_a (Figure 7.15a) show a good agreement between the mean contact surface areas (cohesive, total) obtained during calcification and dissolution. However, the covered sand surface with calcite characterized by the ratio SSA_c/SSA appears to be slightly different. This can be illustrated by the smaller crystals of calcite ($10\mu m$) in this study compared to the previous study (15 to $20\mu m$). As already underlined, the evolution of this covered surface in the dissolution specimens is almost stable, and doesn't decrease when the volume fraction of calcite decreases, as observed in specimens during the calcification. This can be linked to two factors :

- the aggressive solution attacks the calcite everywhere and decreases the thickness of the calcite layers (on the grain surfaces and between the grains). This phenomenon can be seen in the evolution of the calcite layers from the x-ray micro-tomography images and from the SEM images, where the size of the calcite crystals has been reduced from $10\mu m$ (undissolved subsample “ SS_0 ”) to less than $4\mu m$ (dissolved subsample “ SS_{3b3} ”) (Figure 7.8) ;
- the degraded calcite surface has been roughened compared to the initial surface with the passage of the aggressive solution. This fact can be seen clearly from SEM images where the degradation of the calcite crystals starts with micro-damages, which increase the effective surface of calcite (Figure 7.8 and 7.14a). The surface seems rougher than the computed one in the x-ray micro-tomography. Indeed, these micro-damages (rough surfaces) cannot be detected totally with the X-ray micro-tomography observation due to the chosen resolution which is higher or the same order of magnitude of these micro-damages.

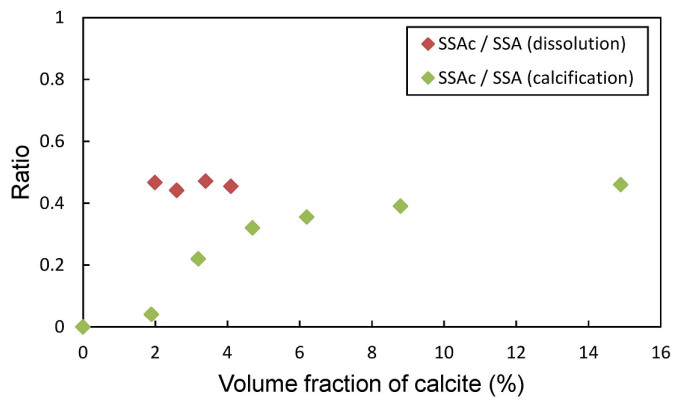
Finally, Figure 7.15c presents the ratio \bar{Z}_a/\bar{Z}_b for both calcified and dissolved specimens. The mean coordination number in the subsamples studied in this work is higher compared the ones obtained in previous work. However, the evolution of this parameter is almost the same. From this comparison, it seems that there is no hysteresis in the biocementation and the dissolution ways ; this means that the mechanical properties of the specimens which have the same calcification levels after calcification or after dissolution should be similar.

7.4 Conclusions

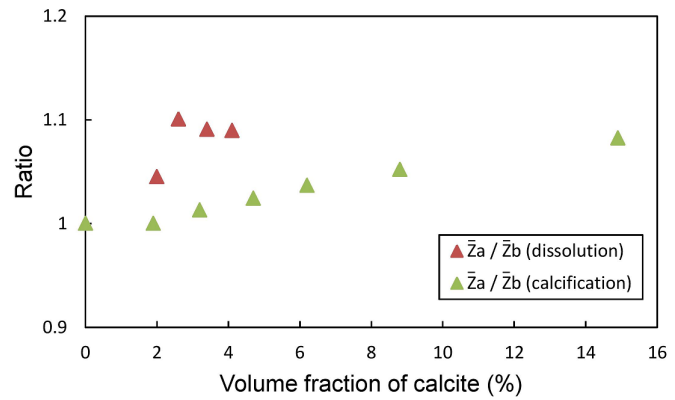
In this work, blocks of biocemented sand have been taken from a large scale physical model and triaxial specimens have been extracted from them. An aggressive solution has been used to study the influence of calcite dissolution on the mechanical and microstructural properties of the



(a)



(b)



(c)

FIGURE 7.15: Microstructural properties computed on 3D images of calcified and dissolved specimens, a) mean cohesive contact surface area (\bar{S}_c / \bar{S}_a), b) Calcite specific surface area (SSA_c / SSA) and c) coordination number evolution (\bar{Z}_a / \bar{Z}_b).

specimens. This solution is composed basically with HCL and Tris, and has an initial pH of 6.6. Undissolved and dissolved specimens with different degree of dissolution which have initially the same amount of calcite (around 6.5% in mass) have been tested under triaxial compression tests. Four small sub-samples have been then extracted from such undissolved and dissolved triaxial specimen in order to perform SEM and X-ray micro-tomography images. After treatment, these

images have been used to compute mean microstructural properties and discrete ones linked to the contacts between grains. The obtained results point out that :

- The calcite dissolution is non-homogenous within each sample. The bottom part (near the injection point) of the specimens is more attacked than the top part. This result clearly shows that the characteristic time associated to the dissolution process is much smaller than the one associated to the flow, which is of the order of 700s in our experiments. At the bottom of the sample, the dissolution process is also increased due to the increase of the surface area of the calcite in contact with the chemical solution. Indeed, as observed with the SEM, when the dissolution starts, the calcite crystals are damaged and thus their surface in contact with the chemical solution increases. When the chemical solution arrives at the top of the sample, it is already saturated with Ca^{2+} ions, which reduces its capacity of dissolution.
- The strength of the dissolved specimens is controlled directly by the weaker part (bottom part of the specimen). This strength decreases non-linearly with increasing the level of dissolution, and then tends towards the strength of the untreated sand. For a dissolution of about 12% of the total amount of calcite, the strength is typically reduced by 55% (from 900 kPa to 400 kPa).
- At the sand grain scale, the dissolution process reduces the size of the calcite crystals and creates random damage on their surface. SEM observations have shown that the size of the calcite crystals is typically of the order of $10\mu\text{m}$ in undissolved specimen and of the order of $4\mu\text{m}$ in dissolved specimens. According the SEM and x-ray tomography images, the chemical dissolution process mainly induces a decrease of the thickness of the calcite layer which covers the sand grains, at the same time leading to a decrease of the coordination number, the mean contact surface area and the number of 'mixed' contacts. Such trends observed during the dissolution process are consistent with previous results obtained during the calcification process (chapter 5).

CHAPITRE 8

CONCLUSIONS AND PERSPECTIVES

8.1 Conclusions

The work presented in this document is a part of the BOREAL research project and focusses on the microstructural changes of biocemented sand and their influence on the macroscopic mechanical properties, either during the biocementation itself or after chemical dissolution of the calcite (durability). For that purpose, this work started with performing biocementation on sand columns in order to prepare triaxial specimens of biocemented sand in order to simultaneously (1) verify the feasibility of biocementation in the lab, (2) estimate its capacity to increase the strength of sand by performing triaxial drained tests under different confining pressure in order to estimate the cohesion and the friction angle evolutions (3) estimate the reduction of permeability in these biocemented triaxial samples by using a Mariotte measurement system. After the triaxial tests, small subsamples of biocemented sand with different calcite content have been extracted and observed using x-ray synchrotron micro-tomography (ESRF) under very high resolution ($0.65\mu\text{m}/\text{pixel}$). Image processing methods using different softwares (Matlab, Visilog, VGStudio, etc.) have been developed in this work and used later in order to treat the obtained images, and quantify the microstructural changes for increasing cementation levels. These microstructural changes have been measured by computing mean microstructural properties (calcite amount, porosity, specific surface area and specific surface area of calcite) and contact properties (contact surface area, coordination number, type of contacts, orientation of contacts, etc.). The evolution of the microstructural properties (specific surface area, contact surface area, specific surface area of calcite) and physical properties (permeability) have been compared to experimental and numerical results in order to confirm and to understand these evolutions. These informations extracted from the 3D images (coordination number, solid fraction, cohesive contact surface area) have been used also in simple micromechanical models which can estimate the mechanical parameters such as the cohesion and the elastic properties of the biocemented sand. Finally, the chemical dissolution and durability of the calcite has been investigated by flushing the biocemented sand specimens by an aggressive solution inside the triaxial device. Microstructural

observations (SEM and x-ray-micro-tomography) have been performed for different dissolved biocemented sand samples in order to analyse the evolution of its microstructure. The above microstructural properties have been computed from the 3D micro-tomography images by using the same tools developed in the previous part, in order to follow the evolution of the microstructural parameters during the dissolution (coordination number, cohesive contact surface area).

The main conclusions of this study are listed in the following points :

Mechanical strength and permeability (Chapter 3)

- The biocementation has been successfully reproduced in the lab in many sand columns ; however this biocementation shows some heterogeneities in the higher cementation levels (higher cementation near the injection point and lower close to the outlet).
- Clear evolution of the strength of the biocemented sand has been found to depend directly on the amount of calcite inside the sample. This evolution results in a non-linear increase of the cohesion and a quasi-linear variation of the friction angle. The dilatancy and the initial stiffness of the material follow the same non-linear trend with the precipitated calcite amount. The residual strength has also shown small evolution compared to the non-treated sand (quasi-linear evolution of the residual friction angle has been observed).
- A clear reduction of the permeability has been found in the biocemented sand samples but it does not exceed one order of magnitude. For the small amounts of calcite (corresponding to the objectives of treatment of actual hydraulic works), the permeability is slightly reduced by 20% compared to the untreated sand. This reduction reaches 75% for the higher amount of calcite (12.4%). This evolution is mainly due to the porosity reduction associated to the calcite precipitation inside the pores of the sand. Other parameters could also influence the permeability of the treated sand such as pore clogging and tortuosity reduction in the porous media.

Microstructure (Chapters 4 and 5)

- The scanned 3D subsamples have shown that, at low volume fraction of calcite (typically $f_c < 10\%$), the total specific surface area (SSA) slightly increases when increasing the volume fraction, due to the formation of rough surfaces with the precipitation of the calcite on the grain surface. By contrast, for volume fraction of calcite larger than 10%, our results show that the SSA slightly decreases, due the creation of new contacts between grains.
- The specific surface area of the calcite (SSAc) increases when increasing the volume fraction of calcite but does not exceed 45% of the total surface of the sand grain when $f_c > 10\%$. This asymptotic value seems to show that the calcite precipitates in preferential locations (contact between grains...).

- A quasi-linear evolution of the coordination number and of the cohesive contact surface area has been found from the 3D images. The coordination number only increased by 8% in the specimen which contains 14.9% of calcite in mass (this rather low increase is probably related to the initial already dense arrangement of grains). In the meantime, for the same specimen, the contact surface has been multiplied by 6 compared to its initial value, explaining therefore the simultaneous large increase of strength.
- The orientation of the cemented contacts within the samples has been found isotropic before and after calcification. This result must be put in regards to the biocementation process, which has been performed in so-called static conditions in the present case : there is no continuous flow through the samples after the injection of both the bacterial and calcification solutions. Probably, these observations will be modified when a continuous flow is present during the process.
- Three types of contact (frictional, mixed and cemented contacts) can be considered after biocalcification. For a volume fraction of calcite lower than 3%, most of the contacts remain frictional. Beyond this value, most of the contacts (both in terms of number and surface area) are mixed contacts. Whatever the value of f_c , the number of new contacts (cemented contacts) created by the biocementation process remains quite small (less than 10% for $f_c = 14.9\%$) and the corresponding contact surface area is almost negligible. This evolution of the contacts, in terms of type, seems to be also related to the injection protocol of both the bacterial and calcification solutions. The initial density of the sand can influence also these results (low densities of sand could give smaller cohesive total surface given that the precipitation is localized in the inter-granular contacts).
- A comparison of the evolution of the mean contact surface area and the specific surface area with simple cubic arrangement with two extreme scenario of precipitation (uniformly precipitated and localized in the contact) has been performed. This comparison has confirmed that the calcite in the biocementation process has precipitated preferentially in the contact zones.

Relation between the microstructure and the effective properties (Chapters 4 and 6)

- The measured and computed permeability and specific surface area have been compared to idealized microstructures corresponding to either periodic overlapping (BCC and FCC) and random non-overlapping (SCM) arrangements of coated spheres. These comparisons show that these simple microstructures are sufficient to capture and to predict the main evolution of the microstructural and physical properties of biocemented sands for the whole range of volume fraction of calcite investigated (that covers a priori the range of potential

application of the biocementation technique to hydraulic works).

- The effective elastic properties estimated from the 3D images by a direct numerical computation on the images and by an analytical estimation which used the computed microstructural properties have shown a good agreement in the whole range of volume fraction. Both results show that Young's and shear moduli increase non-linearly for low volume fraction of calcite ($f_c < 3.2\%$) and then vary almost linearly for larger volume fractions of calcite. This non-linear increase is due to the non-linear increase of the cohesion contact surface area between grains induced by the biocementation process.
- The analytical estimation of the cohesion has shown that the cohesion is controlled mainly by four parameters (cohesive contact surface area, coordination number, final solid fraction and tensile strength σ_{ten} of the contact). The tensile strength involved in this model has been adjusted on the triaxial test results obtained on the same biocemented sand. The calibrated value is consistent with the one measure on limestone rocks which are composed basically by calcium carbonate.

Durability of biocemented sand (Chapter 7)

- The experimental tests of calcite dissolution inside the triaxial device have shown a strong non-homogeneity within each sample. The bottom part (near the injection point) of the specimens undergoes a stronger dissolution than the top part. At the bottom of the sample, the dissolution process is also increased due to the increase of the surface area of the calcite in contact with the chemical solution. Indeed, as observed with the SEM, when the dissolution starts, the calcite crystals are damaged and thus their surface in contact with the chemical solution increases. When the chemical solution arrives at the top of the sample, it is already saturated with Ca^{2+} ions, which reduces its capacity of dissolution.
- The strength of the dissolved specimens is controlled directly by the weaker part (bottom part of the specimen). This strength decreases non-linearly when increasing the level of dissolution, and then tends towards the strength of the untreated sand. For dissolution of about 12% of the total amount of calcite, the strength is typically reduced by 55% (from 900 kPa to 400 kPa).
- At the sand grain scale, the dissolution process reduces the size of the calcite crystals and creates random damage on their surface. SEM observations have shown that the size of the calcite crystals is typically of the order of $10 \mu\text{m}$ in undissolved specimens and $4 \mu\text{m}$ in dissolved specimens. According to the SEM and x-ray tomography images, the chemical dissolution process mainly induces a decrease of the thickness of the calcite layer that covers the sand grains, which at the same time leads to a decrease of the coordination number, the mean contact surface area and the number of 'mixed' contacts. Such trends observed

during the dissolution process are consistent with previous results obtained during the calcification process.

8.2 Perspectives

From this study, we can summarize the aspects which should be studied and clarified in future works in the following points :

- The image processing tools developed in this work can be used in future studies in order to :
 - (1) optimize the biocementation process by changing the experimental parameters (concentration of bacteria and reactants, injection velocity direction, soil density and saturation, etc.) and the environmental parameters (temperature, salinity, pH, etc.), (2) explore the influence of a continuous water circulation during the biocementation process (situation that would be met in practical applications on existing dams and dikes) on the microstructural properties and the spatial distribution of the calcite by performing a continuous X-ray micro-tomography observations so-called *in-situ* on an injection micro-system and (3) analyse, in the case of other cementation processes (portland cement, epoxy, etc ...), the microstructural properties of reinforced soil samples extracted from already treated dams and dikes or investigate the evolution of these microstructural properties with time.
- The data obtained from the 3D images such as the contact surface area distribution and contact types should be investigated in advanced numerical modeling such as Discrete Element Modelling (DEM) and FEM modeling in order to determine the influence of these properties on the macroscopic properties and global response. These simulations can show and explore the influence of these microstructural properties on the peak friction angle and the residual friction angle which can be influenced by the different distribution of cohesive surfaces. The same specimens can be used in numerical simulations in order to analyses the reinforced sand response under other conditions (cyclic response, undrained tests, etc.).
- The durability aspects have to be studied deeply, especially at the microscopic scale by investigating a larger interval of cementation and performing *in – situ* dissolution tests (continuous micro-tomography observation) in order to follow the evolution of the same specimen under the aggressive chemical solution, and if it is possible establishing a clear relation between the microstructural properties and strength of the dissolved specimens.

ANNEXE A _____

_____ ESSAIS TRAXIAUX ET MESURE DE CALCITE

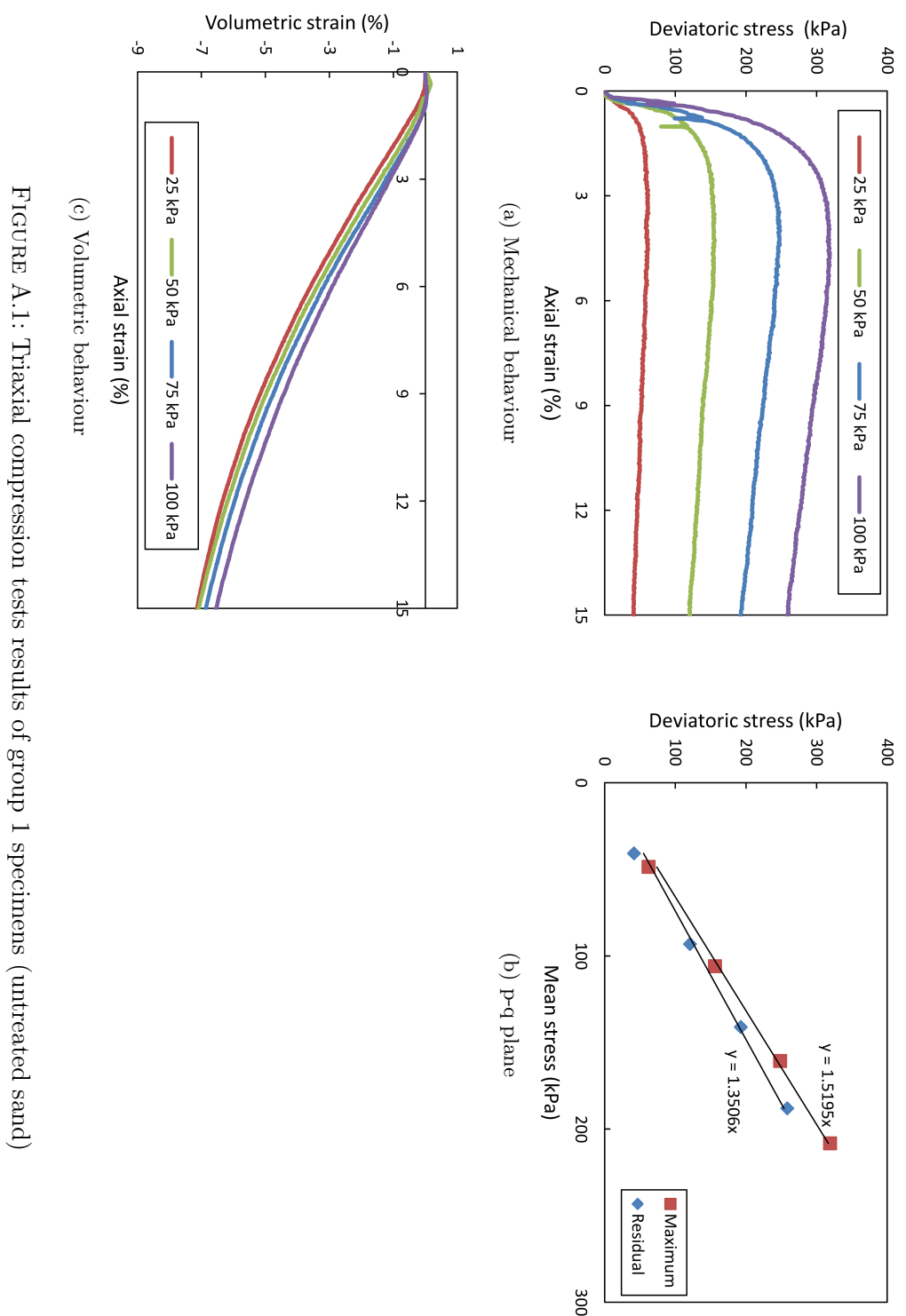


FIGURE A.1: Triaxial compression tests results of group 1 specimens (untreated sand)

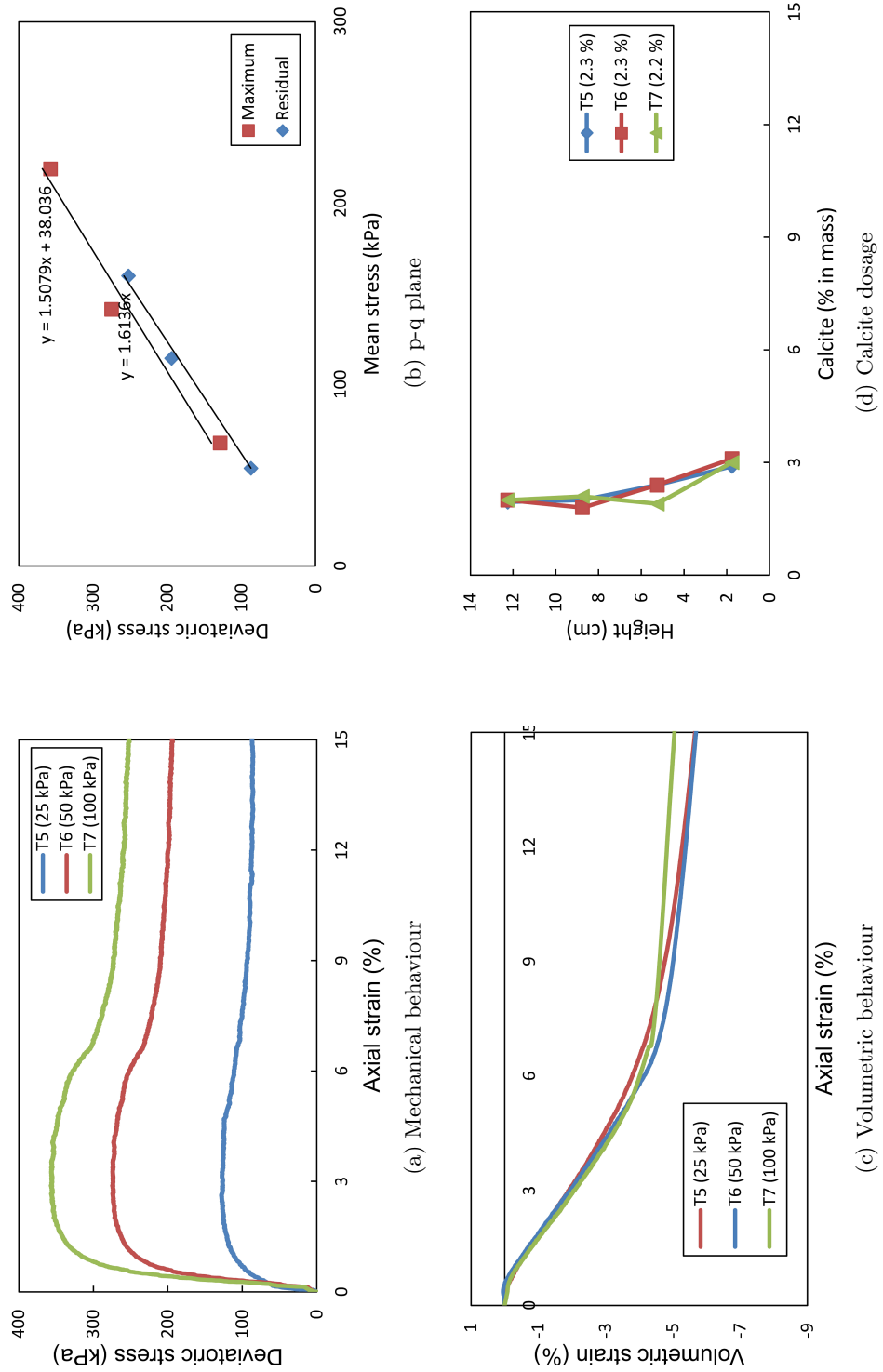


FIGURE A.2: Triaxial compression tests results of group 2 specimens

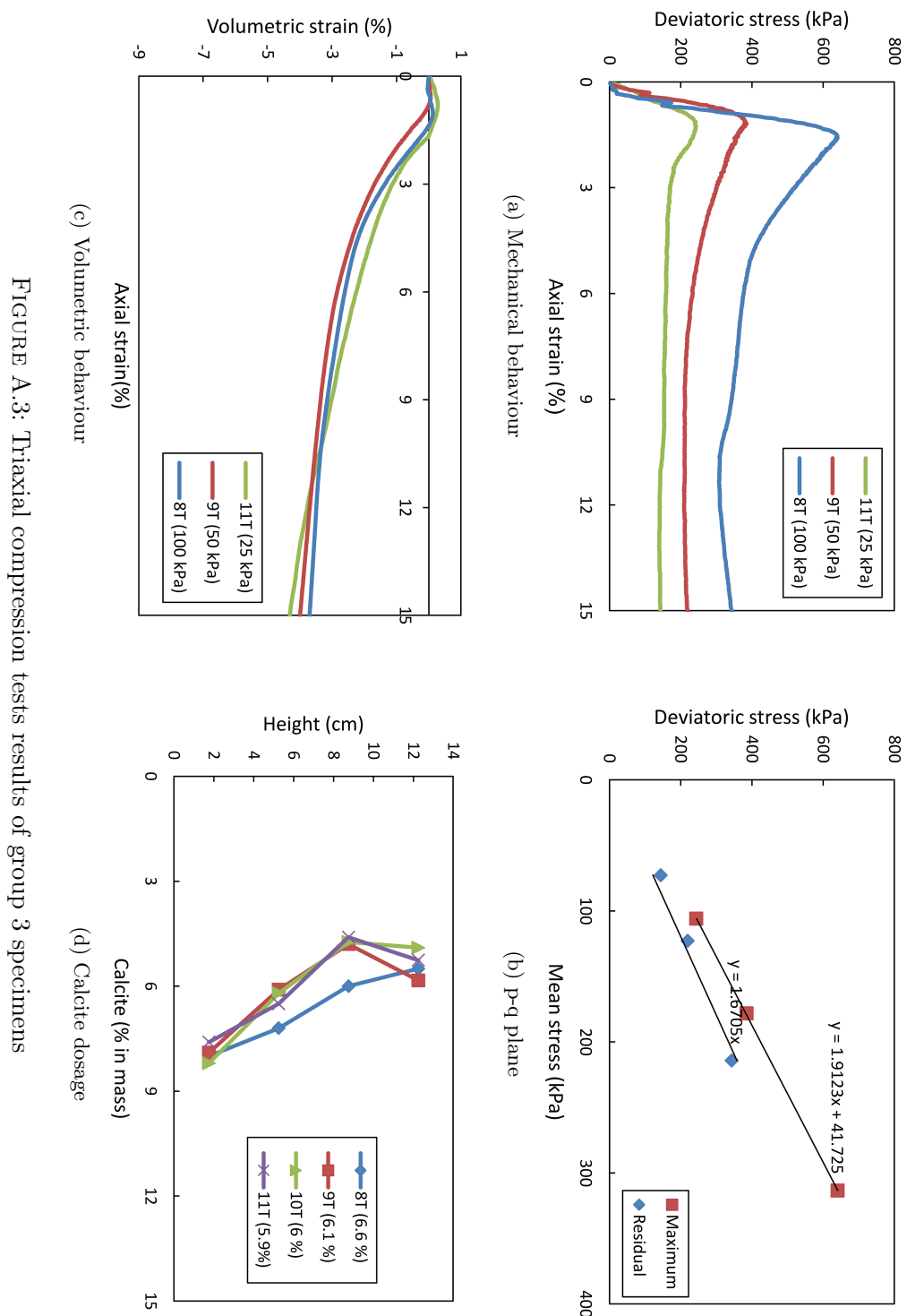


FIGURE A.3: Triaxial compression tests results of group 3 specimens

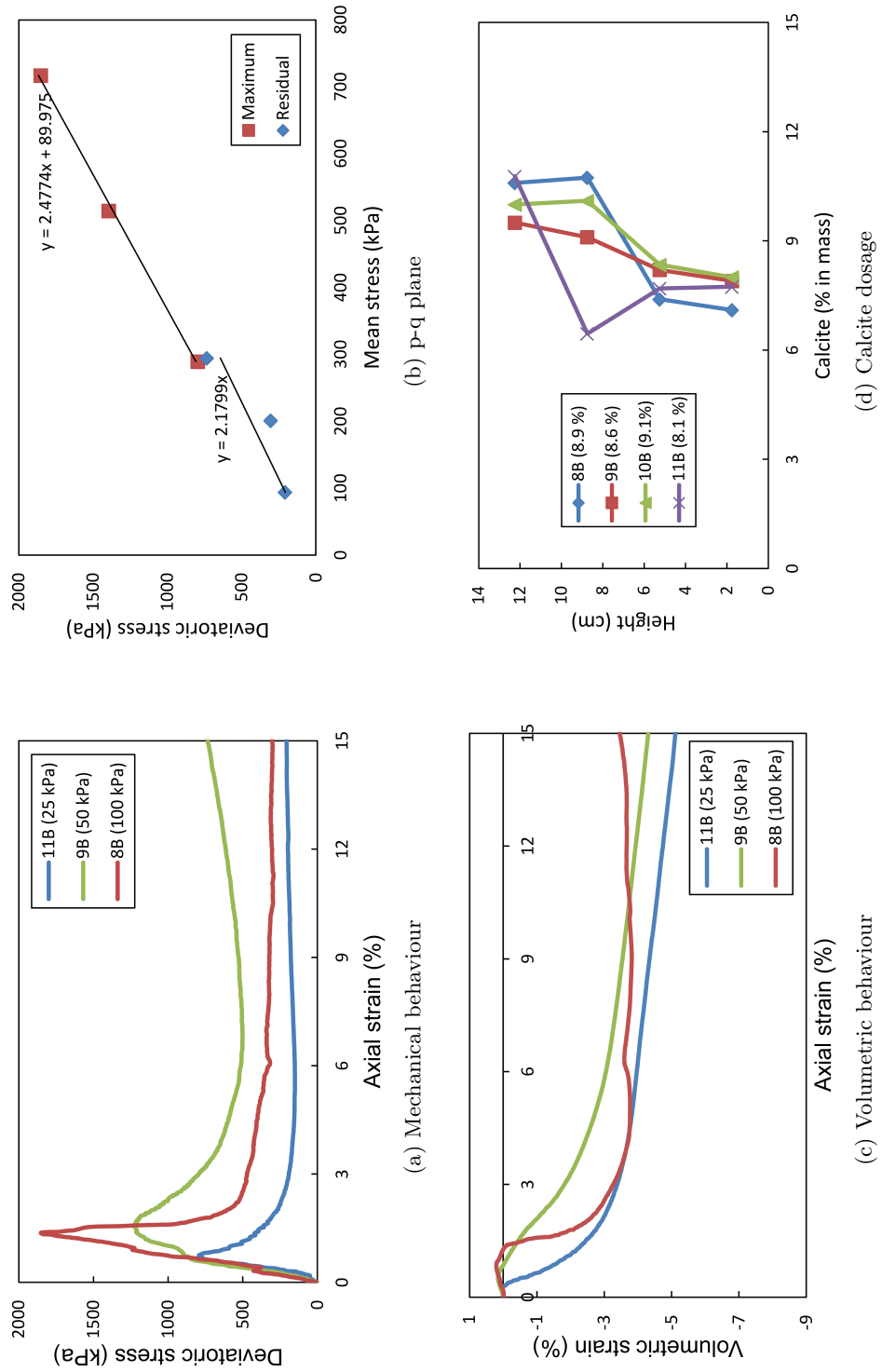


FIGURE A.4: Triaxial compression tests results of group 4 specimens

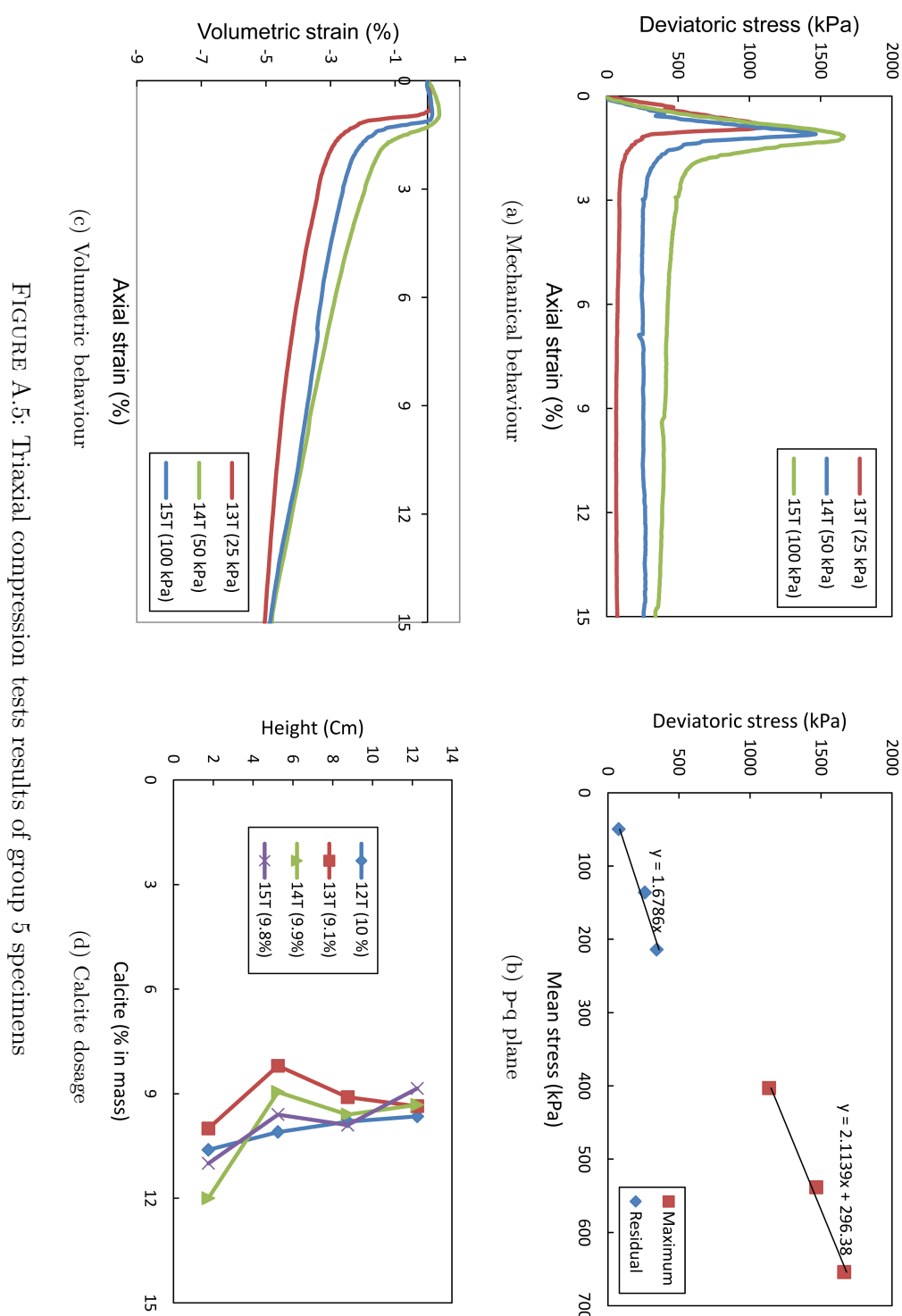


FIGURE A.5: Triaxial compression tests results of group 5 specimens

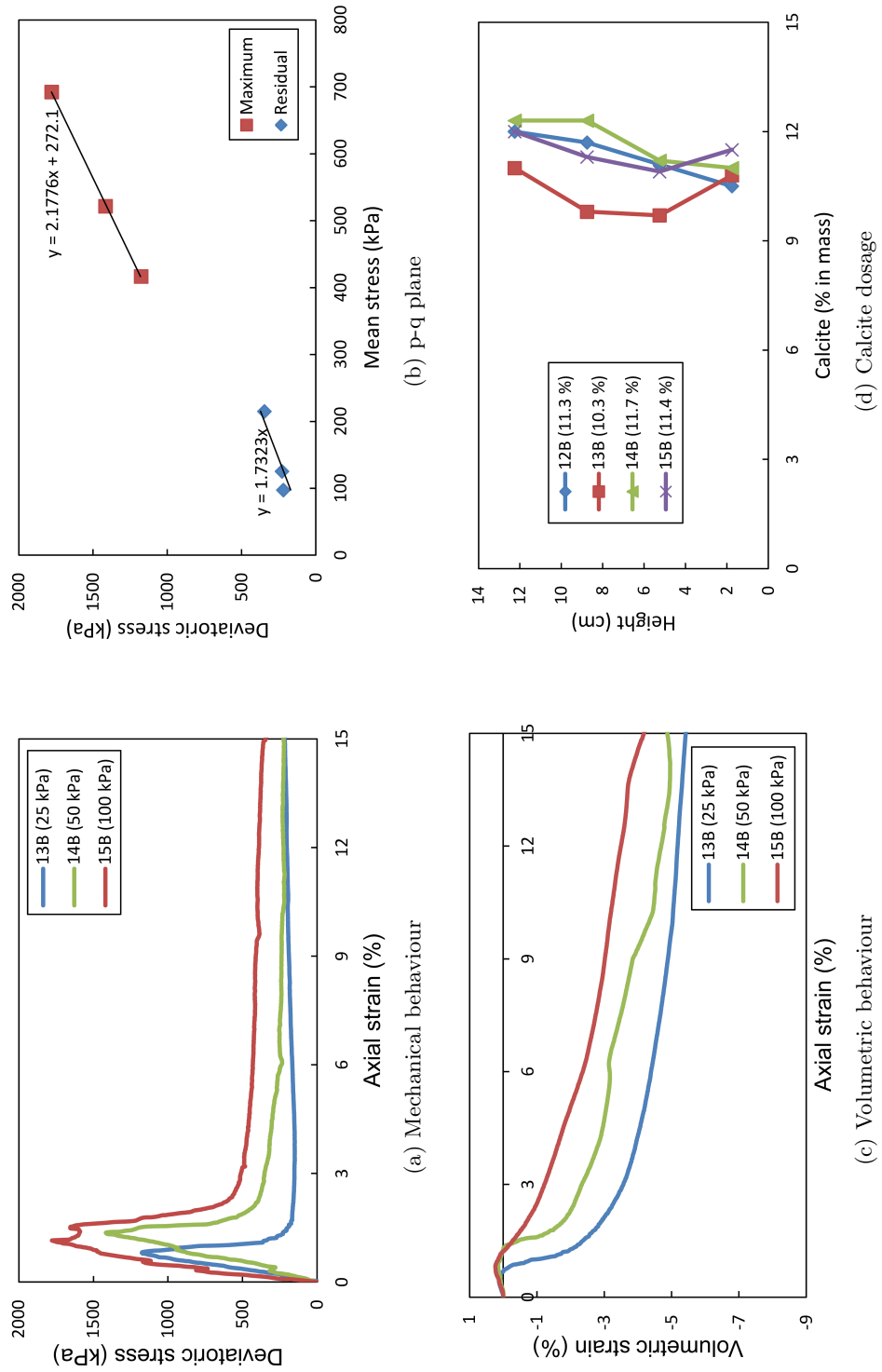


FIGURE A.6: Triaxial compression tests results of group 6 specimens

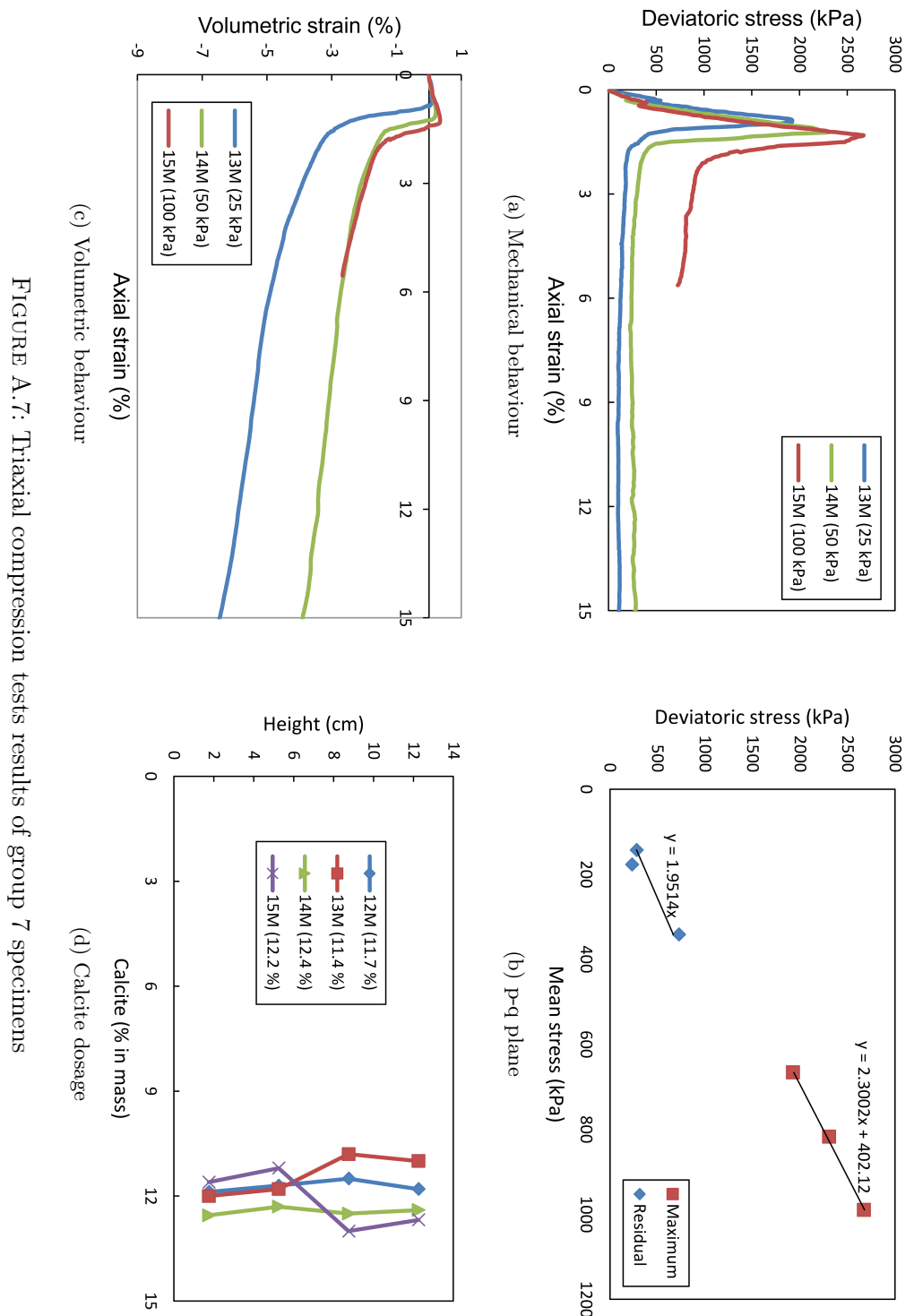


FIGURE A.7: Triaxial compression tests results of group 7 specimens

BIBLIOGRAPHIE

- Abdulla, A. A. and Kiousis, P. D. (1997). Behavior of cemented sands i. testing. *International Journal for Numerical and Analytical Methods in Geomechanics*, 21(8) :533–547.
- Achal, V., Mukherjee, A., Basu, P., and Reddy, M. S. (2009). Lactose mother liquor as an alternative nutrient source for microbial concrete production by *sporosarcina pasteurii*. *Journal of industrial microbiology & biotechnology*, 36(3) :433–438.
- Achal, V. and Pan, X. (2011). Characterization of urease and carbonic anhydrase producing bacteria and their role in calcite precipitation. *Current microbiology*, 62(3) :894–902.
- Afnor, N. (1996). P94-048. *Sols : Reconnaissance et essais-Détermination de la teneur en carbonate-Méthode du calcimètre*.
- Ajorloo, A., Mroueh, H., and Lancelot, L. (2012). Experimental investigation of cement treated sand behavior under triaxial test. *Geotechnical and Geological Engineering*, 30(1) :129–143.
- Al Qabany, A. and Soga, K. (2013). Effect of chemical treatment used in micp on engineering properties of cemented soils. *Géotechnique*, 63(4) :331.
- Al Qabany, A., Soga, K., and Santamarina, C. (2011a). Factors affecting efficiency of microbially induced calcite precipitation. *Journal of Geotechnical and Geoenvironmental Engineering*, 138(8) :992–1001.
- Al Qabany, A. A., Mortensen, B., Martinez, B., Soga, K., and DeJong, J. (2011b). Microbial carbonate precipitation : correlation of s-wave velocity with calcite precipitation. In *Geo-Frontiers 2011 : Advances in Geotechnical Engineering*, pages 3993–4001.
- Al-Thawadi, S. M. (2011). Ureolytic bacteria and calcium carbonate formation as a mechanism of strength enhancement of sand. *J. Adv. Sci. Eng. Res*, 1(1) :98–114.
- Ando, E. (2013). *Experimental investigation of microstructural changes in deforming granular media using x-ray tomography*. PhD thesis, Université Grenoble Alpes.

- Arns, C. H., Knackstedt, M. A., Pinczewski, W. V., and Garboczi, E. J. (2002). Computation of linear elastic properties from microtomographic images : Methodology and agreement between theory and experiment. *Geophysics*, 67(5) :1396–1405.
- Auriault, J.-L., Boutin, C., and Geindreau, C. (2010). *Homogenization of coupled phenomena in heterogenous media*, volume 149. John Wiley & Sons.
- Ayoub, A., Zaoui, A., and Berghout, A. (2011). High-pressure structural phase transitions and mechanical properties of calcite rock. *Computational Materials Science*, 50(3) :852–857.
- Bang, S. S., Galinat, J. K., and Ramakrishnan, V. (2001). Calcite precipitation induced by polyurethane-immobilized bacillus pasteurii. *Enzyme and microbial technology*, 28(4) :404–409.
- Baykasoglu, A., Güllü, H., Çanakçı, H., and Özbakir, L. (2008). Prediction of compressive and tensile strength of limestone via genetic programming. *Expert Systems with Applications*, 35(1) :111–123.
- Benahmed, N., Canou, J., and Dupla, J.-C. (2004). Structure initiale et propriétés de liquéfaction statique d'un sable. *Comptes rendus mécanique*, 332(11) :887–894.
- Benhamida, A., Bouchelaghem, F., and Dumontet, H. (2005). Effective properties of a cemented or an injected granular material. *International journal for numerical and analytical methods in geomechanics*, 29(2) :187–208.
- Bono, J., McDowell, G., and Wanatowski, D. (2015). Investigating the micro mechanics of cemented sand using dem. *International Journal for Numerical and Analytical Methods in Geomechanics*, 39(6) :655–675.
- Bouhlel, M., Jamei, M., and Geindreau, C. (2010). Microstructural effects on the overall poroelastic properties of saturated porous media. *Modelling and Simulation in Materials Science and Engineering*, 18(4) :045009.
- Boutin, C. and Geindreau, C. (2010). Periodic homogenization and consistent estimates of transport parameters through sphere and polyhedron packings in the whole porosity range. *Physical review E*, 82(3) :036313.
- Burbank, M. B., Weaver, T. J., Green, T. L., Williams, B. C., and Crawford, R. L. (2011). Precipitation of calcite by indigenous microorganisms to strengthen liquefiable soils. *Geomicrobiology Journal*, 28(4) :301–312.
- Calonne, N., Flin, F., Geindreau, C., Lesaffre, B., and Rolland du Roscoat, S. (2014). Study of a temperature gradient metamorphism of snow from 3-d images : time evolution of microstructures, physical properties and their associated anisotropy. *The Cryosphere*, 8(6) :2255–2274.

- Castanier, S., Le Metayer-Levrel, G., and Perthuisot, J.-P. (2000). Bacterial roles in the precipitation of carbonate minerals. In *Microbial sediments*, pages 32–39. Springer.
- Chang, C., Misra, A., and Sundaram, S. (1990). Micromechanical modelling of cemented sands under low amplitude oscillations.
- Cheng, L. and Cord-Ruwisch, R. (2014). Upscaling effects of soil improvement by microbially induced calcite precipitation by surface percolation. *Geomicrobiology Journal*, 31(5) :396–406.
- Cheng, L., Cord-Ruwisch, R., and Shahin, M. A. (2013). Cementation of sand soil by microbially induced calcite precipitation at various degrees of saturation. *Canadian Geotechnical Journal*, 50(1) :81–90.
- Cheng, L., Shahin, M., Cord-Ruwisch, R., Addis, M., Hartanto, T., Elms, C., et al. (2014). Soil stabilisation by microbial-induced calcite precipitation (micp) : Investigation into some physical and environmental aspects. In *7th International Congress on Environmental Geotechnics : iceg2014*, page 1105. Engineers Australia.
- Cheng, L., Shahin, M. A., and Mujah, D. (2016). Influence of key environmental conditions on microbially induced cementation for soil stabilization. *Journal of Geotechnical and Geoenvironmental Engineering*, 143(1) :04016083.
- Chu, J., Ivanov, V., Naeimi, M., Stabnikov, V., and Liu, H.-L. (2014). Optimization of calcium-based bioclogging and biocementation of sand. *Acta Geotechnica*, 9(2) :277–285.
- Coto, B., Martos, C., Peña, J. L., Rodríguez, R., and Pastor, G. (2012). Effects in the solubility of caco₃ : experimental study and model description. *Fluid Phase Equilibria*, 324 :1–7.
- Cui, M.-J., Zheng, J.-J., Zhang, R.-J., Lai, H.-J., and Zhang, J. (2017). Influence of cementation level on the strength behaviour of bio-cemented sand. *Acta Geotechnica*, pages 1–16.
- Dadda, A., Emeriault, F., and Geindreau, C. (2017a). Relation between microstructural properties and strength parameters of biocemented sands. 6th International Young Geotechnical Engineers Conference (iYGEC).
- Dadda, A., Geindreau, C., Emeriault, F., du Roscoat, S. R., Garandet, A., Sapin, L., and Filet, A. E. (2017b). Characterization of microstructural and physical properties changes in biocemented sand using 3d x-ray microtomography. *Acta Geotechnica*, 12(5) :955–970.
- Dano, C. (2001). *Comportement mécanique des sols injectés*. PhD thesis, Ecole Centrale de Nantes.
- De Muynck, W., De Belie, N., and Verstraete, W. (2010a). Microbial carbonate precipitation in construction materials : a review. *Ecological Engineering*, 36(2) :118–136.

- De Muynck, W., Verbeken, K., De Belie, N., and Verstraete, W. (2010b). Influence of urea and calcium dosage on the effectiveness of bacterially induced carbonate precipitation on limestone. *Ecological Engineering*, 36(2) :99–111.
- DeJong, J., Martinez, B., Ginn, T., Hunt, C., Major, D., and Tanyu, B. (2014a). Development of a scaled repeated five-spot treatment model for examining microbial induced calcite precipitation feasibility in field applications.
- DeJong, J., Proto, C., Kuo, M., and Gomez, M. (2014b). Bacteria, biofilms, and invertebrates : the next generation of geotechnical engineers ? In *Geo-Congress 2014 : Geo-characterization and Modeling for Sustainability*, pages 3959–3968.
- DeJong, J., Soga, K., Kavazanjian, E., Burns, S., Van Paassen, L., Al Qabany, A., Aydilek, A., Bang, S., Burbank, M., Caslake, L. F., et al. (2013). Biogeochemical processes and geotechnical applications : progress, opportunities and challenges. *Geotechnique*, 63(4) :287.
- DeJong, J. T., Fritzges, M. B., and Nüsslein, K. (2006). Microbially induced cementation to control sand response to undrained shear. *Journal of Geotechnical and Geoenvironmental Engineering*, 132(11) :1381–1392.
- DeJong, J. T., Mortensen, B. M., Martinez, B. C., and Nelson, D. C. (2010a). Bio-mediated soil improvement. *Ecological Engineering*, 36(2) :197–210.
- DeJong, J. T., Soga, K., Banwart, S. A., Whalley, W. R., Ginn, T. R., Nelson, D. C., Mortensen, B. M., Martinez, B. C., and Barkouki, T. (2010b). Soil engineering in vivo : harnessing natural biogeochemical systems for sustainable, multi-functional engineering solutions. *Journal of the Royal society Interface*, page rsif20100270.
- Dekuyer, A., Cheng, L., Shahin, M. A., and Cord-Ruwisch, R. (2012). Calcium carbonate induced precipitation for soil improvement by urea hydrolysing bacteria. In *World Congress on Advances in Civil, Environmental and Materials Research*, pages 2785–2793.
- Dhami, N. K., Reddy, M. S., and Mukherjee, A. (2014). Synergistic role of bacterial urease and carbonic anhydrase in carbonate mineralization. *Applied biochemistry and biotechnology*, 172(5) :2552–2561.
- Dick, J., De Windt, W., De Graef, B., Saveyn, H., Van der Meeren, P., De Belie, N., and Verstraete, W. (2006). Bio-deposition of a calcium carbonate layer on degraded limestone by bacillus species. *Biodegradation*, 17(4) :357–367.
- Digby, P. (1981). The effective elastic moduli of porous granular rocks. *Journal of Applied Mechanics*, 48(4) :803–808.
- Dilrukshi, R. and Kawasaki, S. (2016). Effective use of plant-derived urease in the field of geoenvironmental. *Geotechnical Engineering. J Civil Environ Eng*, 6(207) :2.

- Druckrey, A. M., Alshibli, K. A., and Al-Raoush, R. I. (2016). 3d characterization of sand particle-to-particle contact and morphology. *Computers and Geotechnics*, 74 :26–35.
- du Roscoat, S. R., Decain, M., Thibault, X., Geindreau, C., and Bloch, J.-F. (2007). Estimation of microstructural properties from synchrotron x-ray microtomography and determination of the rev in paper materials. *Acta Materialia*, 55(8) :2841–2850.
- Dupraz, S., Ménez, B., Gouze, P., Leprovost, R., Bénézeth, P., Pokrovsky, O. S., and Guyot, F. (2009). Experimental approach of co₂ biomineralization in deep saline aquifers. *Chemical Geology*, 265(1) :54–62.
- Dura, H. (2013). Durability of biogrout. Technical report, Delft University of Technology, Department of Geoengineering.
- Duraisamy, Y. (2016). Strength and stiffness improvement of bio-cemented sydney sand.
- Duraisamy, Y. and Airey, D. (2015). Small strain modulus of bio-cemented sand. In *Deformation Characteristics of Geomaterials : Proceedings of the 6th International Symposium on Deformation Characteristics of Geomaterials, IS-Buenos Aires 2015, 15-18 November 2015, Buenos Aires, Argentina*, volume 6, page 283. IOS Press.
- Dvorkin, J. and Nur, A. (1996). Elasticity of high-porosity sandstones : Theory for two north sea data sets. *Geophysics*, 61(5) :1363–1370.
- Dvorkin, J., Nur, A., and Yin, H. (1994). Effective properties of cemented granular materials. *Mechanics of materials*, 18(4) :351–366.
- Feng, K. and Montoya, B. (2015). Influence of confinement and cementation level on the behavior of microbial-induced calcite precipitated sands under monotonic drained loading. *Journal of Geotechnical and Geoenvironmental Engineering*, 142(1) :04015057.
- Ferris, F., Phoenix, V., Fujita, Y., and Smith, R. (2004). Kinetics of calcite precipitation induced by ureolytic bacteria at 10 to 20 °C in artificial groundwater. *Geochimica et Cosmochimica Acta*, 68(8) :1701–1710.
- Filet, A. E., Gadret, J.-P., Loygue, M., and Borel, S. (2012). Biocalcic and its applications for the consolidation of sands. In *Grouting and deep mixing 2012*, pages 1767–1780.
- Flin, F., Lesaffre, B., Dufour, A., Gillibert, L., Hasan, A., Rolland du Roscoat, S., Cabanes, S., and Pugliese, P. (2011). On the computations of specific surface area and specific grain contact area from snow 3d images. *Physics and Chemistry of Ice*, pages 321–328.
- Folk, R. L. (1974). The natural history of crystalline calcium carbonate : effect of magnesium content and salinity. *Journal of Sedimentary Research*, 44(1).

- Ginn, T., Murphy, E., Chilakapati, A., and Seeboonruang, U. (2001). Stochastic-convective transport with nonlinear reaction and mixing : application to intermediate-scale experiments in aerobic biodegradation in saturated porous media. *Journal of contaminant hydrology*, 48(1) :121–149.
- Girinsky, O. (2009). *Pré-industrialisation d'un procédé de consolidation de sol par biocalcification in situ*. PhD thesis, Université d'Angers.
- Gomez, M. G., Anderson, C. M., Graddy, C. M., DeJong, J. T., Nelson, D. C., and Ginn, T. R. (2016). Large-scale comparison of bioaugmentation and biostimulation approaches for biocementation of sands. *Journal of Geotechnical and Geoenvironmental Engineering*, 143(5) :04016124.
- Gray, D. H. and Sotir, R. B. (1996). *Biotechnical and soil bioengineering slope stabilization : a practical guide for erosion control*. John Wiley & Sons.
- Han, Z., Cheng, X., and Ma, Q. (2016). An experimental study on dynamic response for micp strengthening liquefiable sands. *Earthquake Engineering and Engineering Vibration*, 15(4) :673–679.
- Harkes, M. P., Van Paassen, L. A., Booster, J. L., Whiffin, V. S., and van Loosdrecht, M. C. (2010). Fixation and distribution of bacterial activity in sand to induce carbonate precipitation for ground reinforcement. *Ecological Engineering*, 36(2) :112–117.
- Hashin, Z. and Shtrikman, S. (1963). A variational approach to the theory of the elastic behaviour of multiphase materials. *Journal of the Mechanics and Physics of Solids*, 11(2) :127–140.
- Hill, R. (1965). A self-consistent mechanics of composite materials. *Journal of the Mechanics and Physics of Solids*, 13(4) :213–222.
- Ivanov, V., Chu, J., and Stabnikov, V. (2015a). Basics of construction microbial biotechnology. In *Biotechnologies and biomimetics for civil engineering*, pages 21–56. Springer.
- Ivanov, V., Chu, J., Stabnikov, V., and Li, B. (2015b). Strengthening of soft marine clay using bioencapsulation. *Marine Georesources & Geotechnology*, 33(4) :320–324.
- Ivanov, V. and Stabnikov, V. (2017). Biocementation and biocements. In *Construction Biotechnology*, pages 109–138. Springer.
- Iwatsuki, T., Satake, H., Metcalfe, R., Yoshida, H., and Hama, K. (2002). Isotopic and morphological features of fracture calcite from granitic rocks of the tono area, japan : a promising palaeohydrogeological tool. *Applied geochemistry*, 17(9) :1241–1257.
- James, A. M. and Lord, M. P. (1992). *Macmillan's chemical and physical data*. Macmillan.

- Jiang, M., Yan, H., Zhu, H., and Utili, S. (2011). Modeling shear behavior and strain localization in cemented sands by two-dimensional distinct element method analyses. *Computers and Geotechnics*, 38(1) :14–29.
- Jiang, N.-J. and Soga, K. (2016). The applicability of microbially induced calcite precipitation (micp) for internal erosion control in gravel–sand mixtures. *Géotechnique*, 67(1) :42–55.
- Jiang, N.-J., Soga, K., and Dawoud, O. (2014). Experimental study of the mitigation of soil internal erosion by microbially induced calcite precipitation. In *Geo-Congress 2014 : Geo-characterization and Modeling for Sustainability*, pages 1586–1595.
- Jiang, N.-J., Soga, K., and Kuo, M. (2016). Microbially induced carbonate precipitation for seepage-induced internal erosion control in sand–clay mixtures. *Journal of Geotechnical and Geoenvironmental Engineering*, 143(3) :04016100.
- John, V. M. (2003). On the sustainability of concrete. *Industry and Environment*, 26(2) :62–63.
- Kadhim, F. J. and Zheng, J.-J. (2017). Influences of calcium sources and type of sand on microbial induced carbonate precipitation. *International Journal of Advances in Engineering & Technology*, 10(1) :20.
- Kajetan, W. (2017). *Couplage entre transport, comportement mécanique et dégradation par dissolution de réservoirs de roche*. PhD thesis, Université de Montpellier.
- Kanit, T., Forest, S., Galliet, I., Mounoury, V., and Jeulin, D. (2003). Determination of the size of the representative volume element for random composites : statistical and numerical approach. *International Journal of solids and structures*, 40(13) :3647–3679.
- Kanit, T., N’Guyen, F., Forest, S., Jeulin, D., Reed, M., and Singleton, S. (2006). Apparent and effective physical properties of heterogeneous materials : representativity of samples of two materials from food industry. *Computer Methods in Applied Mechanics and Engineering*, 195(33) :3960–3982.
- Karol, R. H. (2003). *Chemical grouting and soil stabilization, revised and expanded*, volume 12. Crc Press.
- Legland, D., Kiêu, K., and Devaux, M.-F. (2011). Computation of minkowski measures on 2d and 3d binary images. *Image Analysis & Stereology*, 26(2) :83–92.
- Li, D., Liu, X., and Liu, X. (2015). Experimental study on artificial cemented sand prepared with ordinary portland cement with different contents. *Materials*, 8(7) :3960–3974.
- Lin, H., Suleiman, M. T., Brown, D. G., and Kavazanjian Jr, E. (2015). Mechanical behavior of sands treated by microbially induced carbonate precipitation. *Journal of Geotechnical and Geoenvironmental Engineering*, 142(2) :04015066.

- Liu, Y.-S., Yi, J., Zhang, H., Zheng, G.-Q., and Paul, J.-C. (2010). Surface area estimation of digitized 3d objects using quasi-monte carlo methods. *Pattern Recognition*, 43(11) :3900–3909.
- Maier, R. M., Pepper, I. L., and Gerba, C. P. (2009). *Environmental microbiology*, volume 397. Academic press.
- Martinez, B., DeJong, J., Ginn, T., Montoya, B., Barkouki, T., Hunt, C., Tanyu, B., and Major, D. (2013). Experimental optimization of microbial-induced carbonate precipitation for soil improvement. *Journal of Geotechnical and Geoenvironmental Engineering*, 139(4) :587–598.
- Martinez, B. C. and DeJong, J. T. (2009). Bio-mediated soil improvement : load transfer mechanisms at the micro-and macro-scales. In *Advances in Ground Improvement : Research to Practice in the United States and China*, pages 242–251.
- Minto, J. M., Hingerl, F. F., Benson, S. M., and Lunn, R. J. (2017). X-ray ct and multiphase flow characterization of a ?bio-grouted ?sandstone core : The effect of dissolution on seal longevity. *International Journal of Greenhouse Gas Control*, 64 :152–162.
- Mitchell, A. C. and Ferris, F. G. (2006). The influence of bacillus pasteurii on the nucleation and growth of calcium carbonate. *Geomicrobiology Journal*, 23(3-4) :213–226.
- Mitchell, J. K. and Santamarina, J. C. (2005). Biological considerations in geotechnical engineering. *Journal of geotechnical and geoenvironmental engineering*, 131(10) :1222–1233.
- Mobley, H., Island, M. D., and Hausinger, R. P. (1995). Molecular biology of microbial ureases. *Microbiological reviews*, 59(3) :451–480.
- Montoya, B. and DeJong, J. (2015). Stress-strain behavior of sands cemented by microbially induced calcite precipitation. *Journal of Geotechnical and Geoenvironmental Engineering*, 141(6) :04015019.
- Montoya, B., DeJong, J., and Boulanger, R. (2013). Dynamic response of liquefiable sand improved by microbial-induced calcite precipitation. *Géotechnique*, 63(4) :302.
- Montoya, B. and Feng, K. (2015). Deformation of microbial induced calcite bonded sands : a micro-scale investigation. In *International Symposium on Deformation Characteristics of Geomaterials*.
- Montoya, B. M. (2012). *Bio-mediated soil improvement and the effect of cementation on the behavior, improvement, and performance of sand*. University of California, Davis.
- Morales, L., Romero, E., Jommi, C., Garzón, E., and Giménez, A. (2015). Feasibility of a soft biological improvement of natural soils used in compacted linear earth construction. *Acta Geotechnica*, 10(1) :157–171.

- Mujah, D., Shahin, M. A., and Cheng, L. (2017). State-of-the-art review of biocementation by microbially induced calcite precipitation (micp) for soil stabilization. *Geomicrobiology Journal*, 34(6) :524–537.
- Muller, G. and Gatsner, M. (1971). Neues jahrbuch flur mineralogy monatshefte. *Chemical analysis*, 10 :466–469.
- Nemati, M., Greene, E., and Voordouw, G. (2005). Permeability profile modification using bacterially formed calcium carbonate : comparison with enzymic option. *Process Biochemistry*, 40(2) :925–933.
- Ng, W. S. (2013). *Improvements in engineering properties of tropical residual soil by Microbially-Induced Calcite Precipitation*. PhD thesis, UTAR.
- Ng, W.-S., Lee, M.-L., and Hii, S.-L. (2012). An overview of the factors affecting microbial-induced calcite precipitation and its potential application in soil improvement. *World Academy of Science, Engineering and Technology*, 62 :723–729.
- Otsu, N. (1979). A threshold selection method from gray-level histograms. *IEEE transactions on systems, man, and cybernetics*, 9(1) :62–66.
- Pacheco-Torgal, F. and Labrincha, J. (2013). Biotech cementitious materials : some aspects of an innovative approach for concrete with enhanced durability. *Construction and Building Materials*, 40 :1136–1141.
- Paganin, D., Mayo, S., Gureyev, T. E., Miller, P. R., and Wilkins, S. W. (2002). Simultaneous phase and amplitude extraction from a single defocused image of a homogeneous object. *Journal of microscopy*, 206(1) :33–40.
- Patnaik, P. (2003). *Handbook of inorganic chemicals*, volume 529. McGraw-Hill New York.
- Phillips, A. J., Gerlach, R., Lauchnor, E., Mitchell, A. C., Cunningham, A. B., and Spanler, L. (2013). Engineered applications of ureolytic biomimetic mineralization : a review. *Biofouling*, 29(6) :715–733.
- Rebata-Landa, V. (2007). *Microbial activity in sediments : effects on soil behavior*. Georgia Institute of Technology.
- Richefeu, V., El Youssoufi, M. S., and Radjai, F. (2006). Shear strength properties of wet granular materials. *Physical Review E*, 73(5) :051304.
- Rong, H., Qian, C., and Li, L. (2013). Influence of number of injections on mechanical properties of sandstone cemented with microbe cement. *Advances in Cement Research*, 25(6) :307–313.
- Saadatfar, M., Arns, C. H., Knackstedt, M. A., and Senden, T. (2005). Mechanical and transport properties of polymeric foams derived from 3d images. *Colloids and Surfaces A : Physicochemical and Engineering Aspects*, 263(1) :284–289.

- Santamarina, J. C. (2003). Soil behavior at the microscale : particle forces. In *Soil behavior and soft ground construction*, pages 25–56.
- Schlüter, S., Sheppard, A., Brown, K., and Wildenschild, D. (2014). Image processing of multiphase images obtained via x-ray microtomography : a review. *Water Resources Research*, 50(4) :3615–3639.
- Schnaid, F., Prietto, P. D., and Consoli, N. C. (2001). Characterization of cemented sand in triaxial compression. *Journal of Geotechnical and Geoenvironmental Engineering*, 127(10) :857–868.
- Sel, I., Ozhan, H. B., Cibik, R., and Buyukcangaz, E. (2015). Bacteria-induced cementation process in loose sand medium. *Marine Georesources & Geotechnology*, 33(5) :403–407.
- Sharma, R., Baxter, C., and Jander, M. (2011). Relationship between shear wave velocity and stresses at failure for weakly cemented sands during drained triaxial compression. *Soils and foundations*, 51(4) :761–771.
- Shen, Z., Jiang, M., and Thornton, C. (2016). Dem simulation of bonded granular material. part i : Contact model and application to cemented sand. *Computers and Geotechnics*, 75 :192–209.
- Stabnikov, V., Jian, C., Ivanov, V., and Li, Y. (2013). Halotolerant, alkaliphilic urease-producing bacteria from different climate zones and their application for biocementation of sand. *World Journal of Microbiology and Biotechnology*, 29(8) :1453–1460.
- Stevik, T. K., Aa, K., Ausland, G., and Hanssen, J. F. (2004). Retention and removal of pathogenic bacteria in wastewater percolating through porous media : a review. *Water research*, 38(6) :1355–1367.
- Stocks-Fischer, S., Galinat, J. K., and Bang, S. S. (1999). Microbiological precipitation of caco 3. *Soil Biology and Biochemistry*, 31(11) :1563–1571.
- Tagliaferri, F., Waller, J., Andò, E., Hall, S. A., Viggiani, G., Bésuelle, P., and DeJong, J. T. (2011). Observing strain localisation processes in bio-cemented sand using x-ray imaging. *Granular Matter*, 13(3) :247–250.
- Terzis, D., Bernier-Latmani, R., and Laloui, L. (2016). Fabric characteristics and mechanical response of bio-improved sand to various treatment conditions. *Géotechnique Letters*, 6(1) :50–57.
- Thomas O'Donnell, S. and Kavazanjian Jr, E. (2015). Stiffness and dilatancy improvements in uncemented sands treated through micp. *Journal of Geotechnical and Geoenvironmental Engineering*, 141(11) :02815004.
- Tobler, D. J., Cuthbert, M. O., Greswell, R. B., Riley, M. S., Renshaw, J. C., Handley-Sidhu, S., and Phoenix, V. R. (2011). Comparison of rates of ureolysis between sporo-sarcina

- pasteurii and an indigenous groundwater community under conditions required to precipitate large volumes of calcite. *Geochimica et Cosmochimica Acta*, 75(11) :3290–3301.
- Tobler, D. J., Cuthbert, M. O., and Phoenix, V. R. (2014). Transport of *sporosarcina pasteurii* in sandstone and its significance for subsurface engineering technologies. *Applied geochemistry*, 42 :38–44.
- Tobler, D. J., MacLachlan, E., and Phoenix, V. R. (2012). Microbially mediated plugging of porous media and the impact of differing injection strategies. *Ecological engineering*, 42 :270–278.
- Torgal, F. P., Labrincha, J. A., Diamanti, M. V., Yu, C.-P., and Lee, H.-K. (2015). *Bio-technologies and biomimetics for civil engineering*. Springer.
- Torquato, S. (1991). Random heterogeneous media : microstructure and improved bounds on effective properties. *Appl. Mech. Rev*, 44(2) :37–76.
- Torquato, S. (2013). *Random heterogeneous materials : microstructure and macroscopic properties*, volume 16. Springer Science & Business Media.
- Umar, M., Kassim, K. A., and Chiet, K. T. P. (2016). Biological process of soil improvement in civil engineering : A review. *Journal of Rock Mechanics and Geotechnical Engineering*, 8(5) :767–774.
- Utili, S. and Nova, R. (2008). Dem analysis of bonded granular geomaterials. *International Journal for Numerical and Analytical Methods in Geomechanics*, 32(17) :1997–2031.
- Van Paassen, L. A. (2009). Biogrout, ground improvement by microbial induced carbonate precipitation.
- van Paassen, L. A., Ghose, R., van der Linden, T. J., van der Star, W. R., and van Loosdrecht, M. C. (2010). Quantifying biomediated ground improvement by ureolysis : large-scale biogrout experiment. *Journal of Geotechnical and Geoenvironmental Engineering*, 136(12) :1721–1728.
- van Paassen, L. A., van Loosdrecht, M., Pieron, M., Mulder, A., Ngan-Tillard, D., Van der Linden, T., et al. (2009). Strength and deformation of biologically cemented sandstone. In *ISRM Regional Symposium-EUROCK 2009*. International Society for Rock Mechanics.
- Venuleo, S., Laloui, L., Terzis, D., Hueckel, T., and Hassan, M. (2016). Microbially induced calcite precipitation effect on soil thermal conductivity. *Géotechnique Letters*.
- Wang, Y. and Leung, S. (2008a). Characterization of cemented sand by experimental and numerical investigations. *Journal of geotechnical and geoenvironmental engineering*, 134(7) :992–1004.
- Wang, Y.-H. and Leung, S.-C. (2008b). A particulate-scale investigation of cemented sand behavior. *Canadian Geotechnical Journal*, 45(1) :29–44.

- Wautier, A., Geindreau, C., and Flin, F. (2015). Linking snow microstructure to its macroscopic elastic stiffness tensor : A numerical homogenization method and its application to 3-d images from x-ray tomography. *Geophysical Research Letters*, 42(19) :8031–8041.
- Whiffin, V. S. (2004). *Microbial CaCO₃ precipitation for the production of biocement*. PhD thesis, Murdoch University.
- Whiffin, V. S., van Paassen, L. A., and Harkes, M. P. (2007). Microbial carbonate precipitation as a soil improvement technique. *Geomicrobiology Journal*, 24(5) :417–423.
- Xue-Hui, H., Jun-Xin, G., Feng-Bi, L., and Long, Y. (2014). Generalization of the expression of cementation radius in contact cement theory and its application. *Chinese Journal of Geophysics*, 57(4) :439–449.
- Yang, L. and Salvati, L. (2010). Small strain properties of sands with different cement types.
- Youssef, S., Maire, E., and Gaertner, R. (2005). Finite element modelling of the actual structure of cellular materials determined by x-ray tomography. *Acta Materialia*, 53(3) :719–730.
- Zell, C., Resch, M., Rosenstein, R., Albrecht, T., Hertel, C., and Götz, F. (2008). Characterization of toxin production of coagulase-negative staphylococci isolated from food and starter cultures. *International journal of food microbiology*, 127(3) :246–251.
- Zhao, Q., Li, L., Li, C., Li, M., Amini, F., and Zhang, H. (2014). Factors affecting improvement of engineering properties of micp-treated soil catalyzed by bacteria and urease. *Journal of Materials in Civil Engineering*, 26(12) :04014094.